EXPERIMENTAL INVESTIGATION OF THE SEISMIC BEHAVIOR OF PANEL BUILDINGS

A THESIS SUBMITTED TO
THE GRADUATE SCHOOL OF NATURAL AND APPLIED SCIENCE
OF
THE MIDDLE EAST TECHNICAL UNIVERSITY

BY

S. BAHADIR YÜKSEL

IN PARTIAL FULFILLMENT OF THE REQUIREMENTS FOR THE DEGREE OF
DOCTOR OF PHILOSOPHY
IN
THE DEPARTMENT OF CIVIL ENGINEERING

SEPTEMBER 2003

Approval of the Graduate School of Natural and Applied Sciences

Prof. Dr. Canan ÖZGEN
Director

I certify that this thesis satisfies all the requirements as a thesis for the degree of Doctor of Philosophy.

Prof. Dr. Mustafa TOKYAY
Head of Department

This is to certify that we have read this thesis and that in our opinion it is fully adequate, in scope and quality, as a thesis for the degree of Doctor of Philosophy.

Prof. Dr. Ergin ATIMTAY
Supervisor

Examining Committee Members

Prof. Dr. Engin KEYDER

Prof. Dr. Ergin ATIMTAY

Prof. Dr. Mehmet Emin TUNA

Prof. Dr. Tuğrul TANKUT (Disapproved)

Doç. Dr. Ali İhsan ÜNAY

ABSTRACT

EXPERIMENTAL INVESTIGATION OF THE SEISMIC BEHAVIOR OF PANEL BUILDINGS

YÜKSEL, S. Bahadır
Ph.D., Department of Civil Engineering
Supervisor: Prof. Dr. Ergin ATIMTAY

September 2003, 275 pages

Shear-wall dominant multi-story reinforced concrete structures, constructed by using a special tunnel form technique are commonly built in countries facing a substantial seismic risk, such as Chile, Japan, Italy and Turkey. In 1999, two severe urban earthquakes struck Kocaeli and Düzce provinces in Turkey with magnitudes (M_w) 7.4 and 7.1, respectively. These catastrophes caused substantial structural damage, casualties and loss of lives. In the aftermath of these destructive earthquakes, neither demolished nor damaged shear-wall dominant buildings constructed by tunnel form techniques were reported. In spite of their high resistance to earthquake excitations, current seismic code provisions including the Uniform Building Code and the Turkish Seismic Code present limited information for their design criteria. This study presents experimental investigation of the panel unit having H-geometry.

To investigate the seismic behavior of panel buildings, two prototype test specimens which have H wall design were tested at the Structural Mechanics

Laboratory at METU. The experimental work involves the testing of two four-story, 1/5-scale reinforced concrete panel form building test specimens under lateral reversed loading, simulating the seismic forces and free vibration tests. Free vibration tests before and after cracking were done to assess the differences between the dynamic properties of uncracked and cracked test specimens.

A moment-curvature program named Waller2002 for shear walls is developed to include the effects of steel strain hardening, confinement of concrete and tension strength of concrete. The moment-curvature relationships of panel form test specimens showed that walls with very low longitudinal steel ratios exhibit a brittle flexural failure with very little energy absorption.

Shear walls of panel form test specimens have a reinforcement ratio of 0.0015 in the longitudinal and vertical directions. Under gradually increasing reversed lateral loading, the test specimens reached ultimate strength, as soon as the concrete cracked, followed by yielding and then rupturing of the longitudinal steel. The displacement ductility of the panel form test specimens was found to be very low. Thus, the occurrence of rupture of the longitudinal steel, as also observed in analytical studies, has been experimentally verified. Strength, stiffness, energy dissipation and story drifts of the test specimens were examined by evaluating the test results.

Keywords: Reinforced Concrete, Shear Walls, Tunnel Form Buildings, Cyclic Loading, Moment-Curvature, Ductility.

ÖZ

PANEL BİNALARIN SİSMİK DAVRANIŞININ DENEYSEL ARAŞTIRILMASI

YÜKSEL, S. Bahadır
Doktora, İnşaat Mühendisliği Bölümü
Tez Yöneticisi: Prof. Dr. Ergin ATIMTAY

Eylül 2003, 275 sayfa

Şili, Japonya, İtalya ve Türkiye gibi potansiyel sismik risk altındaki ülkelerde özel tünel kalıp tekniği kullanılarak perde duvarlı çok katlı betonarme yapılar inşaa edilmektedir. 1999 yılında Kocaeli ve Düzce bölgelerinde 7.4 ve 7.1 büyüklüğünde iki şiddetli deprem meydana gelmiştir. Bu afetler büyük yapısal hasarlara, ciddi yaralanmalara ve pekçok can kaybına sebep olmuştur. Bu yıkıcı depremlerden sonraki araştırmalarda, yıkıldığı ya da hasar gördügü bildirilen tünel kalıp teknolojisi ile inşaa edilmiş perde duvarlı bina bulunmamaktadır. Tünel kalıp binaların deprem etkilerine karşı görünür yüksek dayanımlarına rağmen, deprem şartnamelerinde (Uniform Building Code ve Türk Afet Yönetmeliği) tunel kalıp binaların dizayn kriterleri hakkında çok kısıtlı bilgi mevcuttur. Bu çalışmada tünel kalıp ile yapılmış H şekilli taşıyıcı sistemlerin deneysel davranışının araştırması sunulmaktadır.

Panel form binaların sismik davranışını incelemek için H kesitindeki iki deney nümunesi ODTÜ Yapı Mekaniği Laboratuvarı'nda denenmiştir. Deneysel çalışma, iki adet dört katlı 1/5 ölçeğinde betonarme panel bina deney numunelerinin,

sismik kuvvetleri simule eden tersinir yatay yük altında denenmesi ve serbest titreşim deneylerini kapsamaktadır. Çatlamadan önceki ve sonraki serbest titreşim deneyleri, çatlamamış ve çatlamış dinamik tepkinin, dinamik özellikleri arasındaki farkı değerlendirmek için yapılmıştır.

Donatı çeliğinin pekleşmesi, betonda sargı etkisi ve betonun çekme dayanımını hesaba katan Waller2002 adında bir moment-eğrilik programı bu çalışmanın bir parçası olarak yazar tarafından geliştirilmiştir. Tunel kalıp deney nümunelerinin moment eğrilik ilişkileri, perde duvarda kullanılan çok düşük donatı oranlarında gevrek kırılmaların oluştuğunu göstermiştir.

Panel form deney nümunelerinin perde duvarları, yatayda ve düşeyde 0.0015 donatı oranına sahiptir. Yavaş yavaş artan tersinir yatay yük altında, deney numuneleri kırılma konumuna beton çatlar çatlamaz, donatının akması ve kopması ile kırılma konumuna ulaşmıştır. Tünel kalıp deney numunelerinin yerdeğiştirme sünekliği çok düşük gerçekleşmiştir. Böylece analitik çalışmalarda gözlenen düşey donatıda kopmanın oluşması deneysel olarak da doğrulanmıştır. Deney numunelerinin dayanımı, rijitliği, enerji tüketme kapasitesi ve göreli kat ötelenmeleri deney numuneleri değerlendirilerek incelenmiştir. Deney sonuçlarının değerlendirilmesiyle elemanların, dayanım, rijitlik, enerji tüketme ve göreli ötelenme özellikleri irdelenmiştir.

Anahtar Kelimeler: Betonarme, Perde Duvarlar, Tünel Kalıp Binalar, Tersinir Yükleme Moment-Eğrilik, Süneklik.

Dedicated to my father and mother Hüseyin and Şaziye YÜKSEL

ACKNOWLEDGEMENTS

This study was conducted under the supervision of Prof. Dr. Ergin Atımtay. I would like to convey my sincere appreciation to him for his helpful guidance and endless encouragement throughout this thesis. It was a great honor and opportunity having a chance to work with him.

Special thanks are due to Prof. Dr. Engin Keyder for his valuable suggestions and criticism.

I also would like to extend my thanks to the METU-Structural Mechanics Laboratory staff; Hasan Metin, Hasan Hüseyin Güner and Murat Pehlivan.

The financial support from the Scientific and Technical Research Council of Turkey (INTAG 561) is gratefully acknowledged.

Finally, I am deeply indebted to my sons, İsmail Emre and Hüseyin Eren, who gave a new meaning to my life, and to my wife for her endless support, encouragement, patience and love throughout this study.

TABLE OF CONTENTS

LIST OF TABLES

TABLE

LIST OF FIGURES

FIGURE

LIST OF SYMBOLS

A	Gross cross-sectional area
A_c	Area of the column section
b_w	Width of the wall
d	effective depth of the wall
E_c	Elastic modulus of concrete
E_s	Elastic modulus of steel
f_c	Concrete compressive strength
f_{ctf}	Flexural tensile strength of concrete
f_{sy}	Yield stress of steel
f_{su}	Ultimate stress of steel
H	Distance between the lateral load and base of the wall
I, I_g	Moment of inertia of the gross concrete section
I_{cr}	Moment of inertia of the cracked concrete section
L	The center-to-center distance between the members
l_p	Plastic hinge length at the base of the wall
M_{cr}	Moment corresponding to the flexural cracking of the wall
M_u	Ultimate moment
N	Axial load applied on the section
P	The lateral load
R_d	Response factor
$S(T)$	Spectrum coefficient
V	Shear force on the section
V_{cr}	Shear cracking strength
V_{fcr}	Shear corresponding to the flexural cracking of the wall
ϕ	Diameter of the bars

θ	Plastic hinge rotation
σ	Stress
ε_{sy}	Yield strain of steel
ε_{su}	Ultimate strain of steel
ε_{sp}	Steel strain hardening
ε_{cbot}	Bottom concrete strain of the section
Δ_y	Yield displacement
Δ_u	Ultimate displacement
μ_ϕ	Curvature ductility
μ_Δ	Displacement ductility
ϕ_y	Yield curvature
ϕ_u	Ultimate curvature
τ	Nominal shear stress
ν	Poisson's ratio
ρ	Reinforcement ratio
ρ_b	Boundary reinforcement ratio of shear wall
ρ_w	Web reinforcement ratio of shear wall

CHAPTER 1

INTRODUCTION

1.1 TUNNEL FORM SYSTEM

Tunnel form system is an industrialized construction technique, in which structural walls and slabs of the building are cast in one operation by using steel forms having accurate dimensions and plain surfaces. This construction system is composed of vertical and horizontal panel sets at right angles. Tunnel form buildings diverge from the other conventional reinforced concrete structures because of the lack of beams and columns. All the vertical members are made of shear walls and floor system is flat plate. These structures utilize all wall elements as primary load (wind and seismic as well as gravity) carrying members and loads are distributed homogeneously to the foundation.

Facade walls, stairs, landings, partition walls, chimneys, etc. are all produced as prefabricated elements and joined with the main structure which is cast in place. In general, all of the floor plans are the same, except in the basement. The story height may be different in the basement. This is due to the fact that the same steel tunnel forms are utilized in all of the stories. Walls and slabs, having almost the same thickness, are cast in a single operation. This reduces not only the number of cold-formed joints, but also the assembly time. The simultaneous casting of walls, slabs and cross-walls result in monolithic structures, which is assumed to provide high seismic performance and shows horizontal and vertical continuity.

This technology provides great advantages as compared to the conventional construction system, by eliminating scaffolding, plastering, making of formwork and simplifying certain operations of placement and striking of formwork, making and placement of reinforcement and placement of installations. The system on the whole, allows for a better organization of the construction activities enabling continuous flow of work, and a higher quality standard for the whole building. In tunnel form system, required strength is gained in a short time by curing concrete, therefore, forms can be removed at a very high speed and they can be erected again very quickly. In this way, construction is continued at a higher speed. The trend in present construction industry is reduction in construction time. Generally C25 is used as concrete standard. As reinforcement, steel wire mesh is used, which has a positive effect on workmanship. In tunnel form systems, by usage of iron sheets, plain surfaces are obtained. For this reason; tunnel form system does not need any other surfacing or plastering. Thus, desired finishing material can be used directly on the obtained surfaces.

Tunnel form system was first used in the fifties with timber forms in France and then produced as steel forms. After 1978, this industrialized construction technique was brought to Turkey. Today tunnel form system is the most preferred construction technique for mass housing or high rise building construction in Turkey. Nowadays, tunnel form system is used in Germany, North America, Italy, Israel, Turkey etc. totaling more than sixty countries. Most of these countries are in non-critical earthquake zones however; Japan, Italy, Chile and Turkey are exposed to substantial seismic risk. Turkey is a country having a high earthquake risk, i.e., 89% of population, 91% of land, 98% of the industry, and 92% of the dams are located in seismically active zones (Üzümeri et al., 1998). In spite of the abundance of such structures, limited research has been directed to their analysis, design and safety criteria. Behavior of tunnel form buildings under seismic ground motions is not a well-known subject due to lack of research. Presently in Turkey, considerable populations live and work in buildings built by tunnel form system. The unacceptable level of damage of these buildings under a probable earthquake will be an unaffordable burden for Turkey. Therefore, it becomes mandatory to make research and understand earthquake resistant design principles and the risk involved and, if necessary take precautions for tunnel form buildings.

Tendency of constructing high-rise buildings due to economic and social needs in Turkey causes the necessity of building seismic-resistant structures. Shear wall systems, due to their high lateral rigidity, are the best structural systems that satisfy this necessity.

To transfer information obtained from post earthquake evaluations to other geographic areas, variations in code requirements, construction practices, and earthquake ground motions must be considered.

1.2 SEISMIC BEHAVIOR OF REINFORCED CONCRETE SHEAR WALLS

Observations of structural failures due to earthquakes in the past 30 years convincingly demonstrate that shear walls offer the best protection for buildings in earthquake regions. An emerging philosophy for seismic design is to build stiff, but ductile structures with walls, rather than flexible and ductile structures without walls.

Since the late 19th century, reinforced concrete shear walls have been used in buildings to withstand earthquakes. The design concept was to make structures as stiff as possible. However, the effectiveness of such walls to resist earthquake was unclear because of a lack of proper analytical tool, and of reliable earthquake records.

Seismic design of civil engineering structures began in the 1950's when frame type structures were prevalent in buildings. Research in the ductility of beams and columns led to the use of ductile moment resisting frames for earthquake resistance. The whole design concept was to make a structure ductile so that it could dissipate earthquake energy. The ductility of such frames relied solely on the bending of frame members, while the shear action was considered to produce brittle failure and to be suppressed. The design concept is now being challenged because during an earthquake the performance of flexible structures has been found to be inferior to that of stiff structures.

Observations of building failures during earthquakes in the last 30 years show the superiority of stiff buildings with shear walls (Fintel, 1991). According to Fintel, who investigated and reported on the behavior of modern structures in dozens of earthquakes throughout the world since 1963,

> ”……not a single concrete building containing shear walls has ever collapsed. While there were cases of cracking of various degree of severity, no lives lost in these buildings. Of the hundreds of concrete buildings that collapsed, most suffered excessive inter-story distortions that in turn caused shear failure in the columns. Even where collapse of frame structures did not occur and no lives were lost, the large inter-story distortions of frames caused significant property damages. We can not afford to build concrete buildings meant to resist severe earthquake without shear walls.” (Fintel, 1991).

Superior earthquake resistance of concrete structures with walls was clearly demonstrated in 1985 by the dramatic comparison of the structural damages from two severe earthquakes of approximately equal magnitude, one in Mexico City and the other in Chile. In Mexico City, 280 multi-story frame buildings (six to fifteen stories) collapsed; none of them had shear walls. In contrast, the Chilean earthquake went almost unnoticed by the profession, because there were no dramatic collapses. The primary reason for the minimal damage in Chile was the widely used practice of incorporating concrete walls into their building to control drift. It is interesting to note that the detailing practice for shear walls in Chile generally does not follow the ductile detailing requirements of modern codes in seismic regions.

1.3 1985 CHILE EARTHQUAKE

On 3 March 1985, a strong earthquake of surface magnitude 7.8 occurred near the central coast of Chile (Wyllie et al., 1986). Recorded ground motions in Viña del Mar revealed a relatively long duration (45 sec between first and last peak of 0.05g), and peak ground acceleration of 0.36g. Peak spectral acceleration for the recorded ground motions exceeds 1.0g for 5% damping. The region affected included the city of Viña del Mar, where two hundred thirty-four buildings, ranging in height from 6 to 23 stories, were located at the time of the 1985 earthquake (Riddell et al., 1987). All buildings in this height range were constructed of reinforced concrete. One of the most notable features of Viña del Mar inventory was the predominance of structural systems that relied on structural walls to resist lateral and vertical loads. Of the 117 buildings for which structural or architectural drawings were available, only three could be classified as using moment-resisting frame systems for lateral load resistance. Structural walls were used to resist lateral and vertical loads in all other buildings. Following the 1985 earthquake, information was collected to evaluate the performance of the buildings in Viña del Mar. Reconnaissance reports (EERI, 1986) indicated that the stiff, shear wall structures constructed in Chile "performed extremely well", with little to no apparent damage in the majority of buildings. Later investigations (Wood et al., 1987) revealed that although the seismic code requirements in Chile are similar to those used for high seismic risk regions in the U.S., detailing requirements are less stringent.

Current Turkish seismic design codes (AY1997), classify Chilean structures as "bearing wall buildings". Design forces for such structures are substantially higher compared with ductile moment-resisting frames, or dual systems. Furthermore, ductile detailing and inspection are required to the same degree as for moment resisting frames and dual systems. The requirements appear to be inconsistent with observations from earthquake that occurred in Chile on the 3rd March of 1985.

The Chilean design philosophy (Wood et al., 1987) with respect to acceptable damage and safety for earthquake resistant design and construction is the same as that commonly expressed in Turkey: to prevent structural and non–structural damage in frequent minor intensity earthquakes; to prevent structural damage and minimize non-structural damage in the occasional moderate intensity earthquake; and to prevent the collapse of the building in rare high intensity earthquake. However, what constitutes a minor, moderate, or high intensity earthquake in Chile differs considerably from that in Turkey. Although no explicit bounds are established, earthquakes with magnitude of 6.0 to 7.0 (close to urban areas) are considered as minor intensity in Chile due to their frequent occurrence (Lomnitz, 1970). Earthquakes with magnitudes of 7.0 to 7.5 are generally considered to be moderate. Earthquakes with magnitudes greater than 7.5 are considered strong, and occur approximately every 20-25 years in Chile. This philosophy developed the limit excessive repair cost and risk to human safety in the frequent earthquakes in Chile (Wood and EERI, 1991).

Clearly, special attention must be paid to the earthquake threat when designing structures in this environment of frequent, strong ground motion. The Chilean experience with frequent strong earthquakes has led to a construction practice that differs from that used in many countries. In the early 1900’s both frame and wall constructions were common. The failure of some frame buildings during earthquakes in the 1930’s led subsequently to the almost exclusive use of structural walls for lateral load resistance (Wood et al., 1987). Chilean engineers, architects, and occupants became accustomed to the liberal use of structural walls in buildings. As multi-story construction began to evolve in the 1960’s the liberal use of structural walls continued. The amount of wall area in Chilean buildings is relatively large compared with buildings of similar height in seismic regions of Turkey. Walls occupied between 2 and 4 % of the floor area in approximately 70% of the buildings. Three percent wall area in each direction represented the population median. In most cases, the wall area was nearly evenly divided the longitudinal and transverse directions of the building. The ratio of wall area to floor area did not vary appreciably with the height of the building. As a result of the large area of structural walls, Chilean buildings tend to be very stiff. Periods of buildings in Viña del Mar were measured in two independent investigations after the 1985 earthquake (Calcagni and Saragoni, 1988) and (Midorikava, 1990). The data indicate that the period of shear wall buildings in Chile is likely to be less than N/20, where N is the number of stories and the period is reported in seconds.

On the basis of Municipality officials and their reports, the level of structural damage in each building was classified in four categories: None, Light, Moderate, and Severe. Basic information on the date of construction, building geometry, structural system, type of foundation, material properties, and extent of damage was available or 165 of the 234 buildings. Most of the buildings were designed for lateral forces comparable to those used in high seismic areas in the United States and Turkey. Of the 165 buildings for which data were available, five sustained severe damage during the 1985 earthquake. Four of these structures were repaired, and one was demolished 5 days after the earthquake. Eight buildings experienced moderate structural damage and light structural damage was observed in 21 buildings. One hundred thirty-one buildings, nearly 80% of the inventory, survived the earthquake with no structural damage. Approximately 180 deaths were recorded from the 6.8 million population of the region affected by the earthquake. In the communities of Viña del Mar and Valparaiso approximately 40 deaths were reported from the population of 550,000 (Wyllie et al., 1986).

1.4 OBSERVED BEHAVIOR OF TUNNEL FORM BUILDINGS IN THE MARMARA EARTHQUAKE

The development of codes for earthquake resistant design of buildings parallels major earthquakes causing damage and loss of lives. Post-earthquake studies to evaluate reasons for poor building performance during earthquakes are instrumental in the development and improvement of building codes. Good building performance during earthquakes, although often overlooked, instills confidence that provisions are adequate, and may even lead to relaxations in certain code requirements. Because of variations between Turkey and foreign code practices, evaluations of building behavior for earthquakes outside Turkey provide valuable insight into both Turkey and foreign code practices.

Hazardous earthquakes occurred in Turkey; Çaldıran-Muradiye (1976), Erzurum-Kars (1983), Malatya-Sürgü (1986), Erzincan (1993), Dinar (1995), Marmara (1999) and Düzce (1999). In recent earthquakes, it has been realized that inadequate lateral stiffness is the major cause of damage in buildings in Turkey. Reports and observations after the earthquakes indicated that the framed system structures constructed in Turkey showed poor performance. The structural type of almost all the collapsed and heavily damaged structures was framed systems. Dual systems performed much better behavior than framed systems. The occurrence of (M_w=7.4) Kocaeli and (M_w=7.1) Düzce earthquakes in Turkey in 1999 once again demonstrated the nondamaged and high performance conditions of reinforced concrete shear wall dominant structures commonly built by using the tunnel form technique.

After the Marmara Earthquake, attention was immediately focused on the seismic behavior of high-rise panel form structures. A mass housing development of dozens of high-rise buildings existed very close to the epicenter of the Marmara Earthquake, known as the Yahyakaptan Mass Housing Project. Therefore, the tunnel form building structures that are very close to the epicenter of the Marmara Earthquake (Yahyakaptan tunnel form structures) were tested by the horizontal seismic action imposed by the Marmara Earthquake. No damage on these high-rise panel form buildings was reported, except a few insignificant cracking. Yahyakaptan high-rise panel form buildings successfully passed the seismic test imposed by the Marmara Earthquake (Ünay et al., 2002).

In Turkey, collapse of panel form structures due to earthquakes has not occurred so far. This fact led many technical experts, as well as the public, to think that high-rise panel form buildings are earthquake safe building structures. This idea that came out spontaneously requires scientific research. Are panel form buildings, which have survived during the Marmara Earthquake undamaged, indeed earthquake safe structures?

1.5 OBJECTIVE AND SCOPE OF THE STUDY

Tunnel form technology has been used in every part of Turkey. Turkey is in an earthquake region where lots of faults pass through. How tunnel form buildings behave under seismic ground motions is not a well-known subject due to lack of sufficient research. Marmara and Düzce Earthquakes, on 17 August 1999 and 12 October 1999 respectively, show that structural walls are the most important part of the structure that reduce the damage of an earthquake on the structure and prevent collapse of the structure. Beyond this, buildings formed only with structural walls have shown very limited, or no damage due to earthquake loads.

The main objective of the research reported in this work was to study the behavior of the panel form buildings under reversed cyclic loading. To fulfill this objective, two four story 1/5-scale reinforced concrete panel form building test specimens were manufactured in the Structural Mechanic Laboratory at METU. The test specimens which were tested in the short dimension and the long dimension were identified as SPECIMEN1 (SP1) and SPECIMEN2 (SP2) respectively. Figure 1.1 shows a general view of the test specimens.

Figure 1.1 Front view and side view of the test specimens.

Test specimens that are seen in Figure 1.1 have been tested laterally in the vertical position by using the reaction wall and the strong floor. First SPECIMEN1 then SPECIMEN2 were tested. These specimens were tested under lateral reversed cyclic loading simulating the seismic forces. For both of the specimens two static and two dynamic tests were performed. Before the static test, free vibration tests were performed on the specimens to understand the dynamic properties for the uncracked cases such as periods, damping ratios etc. After the first dynamic test, test specimens were subjected to lateral reversed cyclic loading until some minor visible hair cracks occurred. Again a free vibration test was performed to realize differences between the dynamic properties of uncracked and cracked response. At the last stage specimens were loaded until failure occurred.

CHAPTER 2

LITERATURE SURVEY

To augment the work done in this study, relative to the cyclic loading of 1/5-scale reinforced concrete panel form buildings, a review of previous experimental and analytical investigations on shear walls was required. The scope of this chapter, therefore, deals with a literature review of related work done on the other shear walls. This investigation will provide information on the behavior of shear walls and their response to seismic loading conditions.

Paulay and Üzümeri (1975) reported the ductility characteristics of structural walls. They established a relationship between the curvature and displacement ductilities of walls with different wall lengths to aspect ratios. The range of required curvature ductilities for each aspect ratio and displacement ductility is derived from upper and lower estimate of plastic hinge length. The plastic hinge lengths are in turn a function of the wall dimensions or aspect ratio. It is understood that as shear walls become more slender they develop a greater plastic hinge length resulting in more rotational capacity and in turn greater ductility.

Park and Paulay (1975) contributed significantly to the development of capacity design procedures and important detailing concept for the design of shear wall systems. One of the consequences of concern over achieving large ductility led to the suggestion that the concentrated steel at the ends of the wall should be tied as columns. Confined concrete at the end of walls would increase the allowable strain in the compression zone of the wall where strains exceeding 0.004 are required to reach larger curvature ductilities. In addition, more closely spaced ties at the ends of walls prevent buckling of the concentrated vertical reinforcement.

Paulay (1980) reviewed a shear wall design philosophy for earthquake resisting shear walls, with emphasis on the desirable energy dissipation and structural properties. This study was one of the first researches to provide a design philosophy for shear walls including desirable energy dissipation and potential failure mechanism. In the light of these findings, it is important to note that ideas about designing structural walls have changed in the past 25 years.

Paulay, Priestly, and Synge (1982) have investigated the possibilities of achieving acceptable levels of energy dissipation in squat shear walls, mainly by flexural yielding of the reinforcement. A review of the possible failure modes was presented (diagonal tension failure, diagonal compression failure, sliding shear) along with the methods of prevention. Shear failures originating from diagonal tension or compression failure, limited ductility and dramatic degradation in strength and stiffness. For this reason, a more ductile flexural response is desired.

These researchers conducted an experimental program of four squat shear walls with a height-to-length ratio of 0.5. Two of the specimens had rectangular cross sections and the remaining included small flanges at the end of a central web wall. A rigid foundation was used to clamp the specimens to the laboratory floor, and a stiff top slab ensured an even distribution of the imposed displacements to the wall. The following observations, based on the experimental findings, were reported:

1. It is possible to ensure a predominantly flexural response, involving considerable yielding of the flexural reinforcement, for squat shear walls subjected to seismic loading.
2. Suppression of shear failure by diagonal tension or compression is a prerequisite for a flexural response and hence, significant energy dissipation.
3. Squat shear walls are likely to fail due to sliding shear along the base unless specially detailed or subjected to high axial loading. Sliding shear results in the most significant loss and strength.

4. Flanged walls are more seriously affected by sliding shear along interconnecting flexural cracks.
5. Diagonal reinforcement considerably improves the seismic response of squat shear walls.
6. The severity of sliding shear increases with increased ductility demand, with decreasing vertical reinforcement, and with a decrease of the flexural compression zone.

Cardenas, Hanson, Corley and Hognestad (1982) had an experimental research on the subject of strength of shear walls for high-rise and low-rise buildings. Six high-rise and seven low-rise shear walls were tested under combinations of lateral and axial loads at the laboratories of the Portland Cement Association. Variables were amount and distribution of vertical reinforcement and effect of moment to shear ratio. Test results indicated that flexural strength of rectangular shear walls could be calculated using the same assumptions as for reinforced concrete beams. Besides, the strength of high-rise shear walls containing minimum horizontal shear reinforcement was generally controlled by flexure. The results showed that both horizontal and vertical reinforcement contributed to the shear strength in low-rise shear walls. The background and development of Section 11.16, Special Provisions for Walls, of the ACI Building Code (ACI 318-71) were discussed. They also concluded that the shear strength of low-rise shear walls could be satisfactorily predicted by ACI-318-71 section 11.16, special provision for shear walls.

Tegos and Penelis (1988) have made an experimental investigation to study the behavior of short column and coupling beams reinforced with inclined bars under seismic conditions. A simple technique to prevent these elements from falling in premature splitting shear is tested for the first time. According to this technique, the main reinforcements are arranged at an inclination such as to form a rhombic truss. Test results show that inclined arrangements is one of the most effective ways to improve the seismic resistance of reinforced concrete low slenderness structural elements.

Wood (1989) investigated the results of 37 lateral load tests on structural walls. Lightly reinforced walls with low axial stresses are found to be vulnerable to failure caused by fracture of the main reinforcement. This mode of failure is of concern for the design of walls to resist seismic loads because some of the test specimens failed at overall drift ratios less than 2 percent. Based on the observed crack patterns on the structural walls, failure modes have been categorized as flexural failures and shear failures. The shear stress index was used to distinguish between shear and flexural modes. In more than one-half of the specimens that failed in flexure, reinforcing bars fractured, however, reinforcing bars fractured in none of the walls that failed in shear. Failures caused by fracture of the reinforcement were observed in walls with flexural-stress ratios less than 15 percent. Among the flexural failures, steel strain was used to identify the walls that were susceptible to fracture of the main reinforcement. The calculated steel strain in the extreme layer of reinforcement at the nominal flexural capacity of cross section was used. Fractured reinforcement was observed in test specimens that were not susceptible to shear failures and for which the calculated steel strains in the extreme layer of reinforcement exceeded 4 percent at the nominal flexural capacity. The two walls which had lowest longitudinal reinforcement ratios (ρ = 0.0027 and ρ=0.0031) failed by fracture of the tension reinforcement before crushing of the concrete. Except for these two walls, a flexural hinge developed in the other flexural failures. Walls with total longitudinal reinforcement ratios less than 1 percent were identified as being susceptible to fracture of the tensile reinforcement.

Lefas, Kostovos, and Ambraseys (1990) provide a means of understanding the behavior of shear walls. Their research began with a look into the strength, deformation characteristics, and failure mechanisms of reinforced concrete structural walls. Experimental work at Imperial College, England, was carried out on thirteen isolated cantilever reinforced concrete walls of aspect ratio of one, which were

750 mm wide × 750 mm high × 70 mm thick and aspect ratio two, which were 650 mm wide × 1300 mm high × 65 mm thick with a scale of 1:2.5. In all cases, the walls were monotonically connected to an upper and lower beam. The upper beam was 1150 mm long × 150 mm deep × 200 mm thick. The lower beam was essentially the same, except it was 300 mm deep. The upper beam functioned as an element through which the axial and horizontal loads were applied to the walls and as a case for the anchorage of the vertical bars and a lower beam was used to clamp the specimens to the laboratory floor, providing a rigid foundation. The vertical and horizontal reinforcement comprised high tensile deformed steel bars of 8 mm (f_{sy}=470 Mpa and f_{su}=565 Mpa) and 6.25 mm (f_{sy}=520 Mpa and f_{su}=610 Mpa) diameter, respectively. Additional horizontal reinforcement in the form of stirrups confined the wall edges. Mild steel bars of 4 mm (f_{sy}=420 Mpa and f_{su}=490 Mpa) diameter were used for this purpose.

The effect of parameters such as the height-to-width ratio, the axial load level, the concrete strength, and the amount of web horizontal reinforcement on wall behavior were investigated during those tests. Wall models were tested with load control under the combined action of a constant axial and horizontal loading monotonically, increasing up to failure using the test rig. The tests were performed for three levels of axial load corresponding to 0.0, 0.1, and 0.2 of the uniaxial compressive strength of the wall cross section that is equal to $0.85 \times f_c \times b_w \times h$. The researchers were able to draw some important conclusions:

1. It was observed that both vertical and horizontal displacements decrease as the axial load level increases, which also causes an increase in the horizontal load-carrying capacity and secant stiffness characteristics. This increment becomes more visible for high height-to-width ratios.
2. Uniaxial concrete strength characteristics within a range of 30 to 55 MPa do not affect the strength and deformation characteristics of the wall.
3. No significant effect of the horizontal web reinforcement was observed on shear capacity, which is in contrast to the expected case. Even the amount of horizontal web reinforcement used is half of the values specified by building codes; the failure load was not affected.

4. Decreasing the height to width ratio and increasing the axial load level extend the failure region. Failure of the walls occurred due to nearly vertical splitting of the compressive zone in the tip of the inclined (TYPE I) or the deepest flexural (TYPE II) crack, followed by splitting of the whole compressive zone.
5. Shear resistance is related with triaxial compressive stress conditions in compression zone of the base of the wall where flexural moment reaches its maximum value rather than the strength of the tensile zone of this section.
6. The failure region was more extensive by decreasing height-to-width ratio and increasing axial load.

Wood (1990) reviewed the results of 143 laboratory tests of low-rise walls to identify the sensitivity of the measured shear strength to experimental parameters, such as the loading history and the amount of web reinforcement. The nominal shear strength of reinforced concrete walls designed to resist seismic loads is defined in Appendix A of ACI 318-83 to be essentially the same as the nominal shear strength of reinforced concrete beams that are designed to resist gravity loads. Two quantities are used to define the nominal shear strength of both types of members, one attributed to the contribution of the web reinforcement and the other to the contribution of the concrete. This procedure has been defined as the modified truss analogy. The applicability of the modified truss analogy for low-rise structural walls subjected to earthquake-induced load has been questioned in discussions of the ACI Building Code and is evaluated in this paper. Procedures defined in Appendix A of ACI 318-83 were found to underestimate the strength of walls with more than 1.5 times the minimum web reinforcement ratio. A reasonable lower bound to the average shear stress resisted by the test specimens with distributed web reinforcement in orthogonal directions was $(f_c')^{1/2}/2$ MPa. The maximum average shear stress tended to increase with an increase in the amount of vertical reinforcement (longitudinal reinforcement in the boundary elements and vertical web reinforcement). The increase in shear strength attributed to the vertical reinforcement was approximated using a shear friction model. An upper limit of $5 \times (f_c')^{1/2} / 3$ MPa for the nominal shear strength was also established. A reasonable lower bound to the shear strength of low-rise walls with minimum web reinforcement was found to be $(f_c')^{1/2}/2$ MPa. The shear strength of the walls was observed to increase with an increase in the amount of vertical reinforcement in the web and boundary elements. A shear friction model was used to evaluate the shear strength provided by the vertical reinforcement.

Wood et al (1991) indicate that the El Faro building failed after the fracturing of the reinforcement in a first-story wall. The failure of El Faro provides convincing field evidence that brittleness of reinforced concrete members caused by under-reinforcement cannot be ignored when designing for earthquake resistance. El Faro building had extremely heavy structural damage during the Chile Earthquake in 1985, which provides an example of rare, documented failure of a structural wall system. It was an eight-story apartment building in Vina Del Mar in Chile which had equal wall area in orthogonal directions but the walls were not uniformly distributed around the perimeter. Large windows were located along the most damaged sides of the building. A large crack occurred in structural wall at the first story on this side. The wall separated along this crack and the portion of the building above the crack fell to the ground outside the lower portion. A series of linear and limit analyses were done by Sharon L. Wood in this paper to investigate the cause of the collapse of El Faro Building. Studies documented in this paper indicate that the building failed after longitudinal reinforcement fractured in a first-story wall. The calculated response of El Faro building was compared with that of four other buildings (Villa Real, Festival, Miramar, Sol) that survived the 1985 Chile Earthquake with light to moderate damage in Vina Del Mar.

Sharon L. Wood et al compared periods, base-shear strengths and mean drift ratios for these five buildings. The results indicate that the cause of the severe damage could not be due to the strength and stiffness characteristics because these characteristics are not comparable in all the five buildings. As a result it is understood that the main cause of the collapse was due to structural detail. From the moment curvature relationship the tensile strains in the boundary reinforcement exceed two times measured fractured strain of the reinforcement for a compressive strain of 0.003 in the concrete. The magnitude of the calculated strains indicates the possibility of rupture of reinforcement. The building collapsed after the longitudinal reinforcement fractured in a first story wall in structural wall system. Fracture susceptibility in the critical wall was exacerbated by the torsional response of the building. This paper indicates that lightly reinforced concrete structural walls are susceptible to brittle mode of failure due to fracture of the reinforcement.

Subedi (1991) proposed a method of analysis for reinforced concrete coupling beams that is component of coupled shear walls. This study is based on the subject of reinforced concrete coupled shear wall structures. First, some analyses are carried on coupling beams. Here, the behavior of coupling beams in the shear mode failure, known as diagonal splitting, is represented by a mathematical model, and a method for the ultimate strength analysis is presented. The proposed method of analysis for RC coupling beams is used to verify the results of nine beams tested by Thomas Paulay. Second, the ultimate strength calculations or reinforced concrete coupled shear walls are presented. Three modes of failure of reinforced concrete coupled shear wall structures, observed in micro-concrete models of 15 story structures were described. The method is proposed to predict the mode of failure and the ultimate strength of coupled shear wall structures. The method is based on the evaluation of the strengths of the coupling beams and the walls at the failure. Two lateral load cases have been considered: a point load at the top and a four-point equivalent triangular distribution. The proposed analysis and the test results are compared.

Pantazopoulou and Imran (1992) investigated the parameters that affect connection stiffness and shear resistance using experimental evidence and simple mechanical models. They found that for low reinforcement ratios such as those frequently used in designing slabs, the existing requirements for walls and diaphragms may overestimate the nominal shear resistance of connections by as much as 100 percent. The experimental evidence suggests that gravity loads and a cyclic load history further reduce the nominal resistance. They derived alternative design equations in this study using a plain-stress approach. They also showed that the results obtained for a range of reinforcement ratios corroborate the experimental findings.

Paulay and Priestley (1992) presented brief information about structural walls. Considerations of seismic design, which address mainly cantilever walls, were given. Common failure modes encountered in cantilever walls were also described. They also explain strategy in the positioning of walls, the establishment of a hierarchy in the development of strengths to ensure that brittle failure will not occur and preferred mode of energy dissipation in a predictable region.

Pilakoutas and Elnashai (1993) identified some of the common mistakes that could occur during the testing of reinforced concrete panels and gave an estimate of the errors involved. Furthermore, the success of such experimental work depends both on accurate representation of the intended boundary conditions, and the prudent interpretation of the testing results. A method that decomposes the shear and flexural components of deformation was given and the differences with other approaches were shown. From the preceding errors, the following conclusions were drawn: Forces, which are developed from the connection between loading jack and test specimen, may result in misleading conclusions. Load-controlled testing under monotonic loading is of limited use in drawing conclusions pertinent to seismic design. The method of calculating shear deformation in reinforced concrete panels should be carefully implemented to avoid large errors.

Paulay and Priestly (1993) carried out experimental and analytical studies on out-of-plane buckling of rectangular structural walls under severe earthquake loading. Wall stability becomes a concern when thin wall sections are subjected to high compressive strains, which could possibly lead to out-of-plane buckling. It is explained that this concern is based on concepts of Eulerian buckling of struts. An analytical approach was developed on the minimum required thickness in the vicinity of the flexural compression zones of ductile structural walls. This prevents the occurrence of out-of-plane buckling in the potential plastic region before the maximum estimated ductility is developed. The resulting solution of reducing the occurrence of instability was to limit the wall thickness, b_w, to about one-tenth the height of the wall in the first story. This research shows that out-of plane buckling of thin walls is more dependent on high inelastic tensile strains in the tensile steel. It is believed that upon initial moment reversal, all compressive stresses will be resisted by the steel because the cracks formed in the concrete due to the previous tensile cycle will not have completely been closed. The result may be flexural compressive force that does not coincide with the center of the wall thickness, b_w. This eccentricity together with small-dislocated concrete particles and unaligned crack surfaces could lead to instability. It was founded that the properties of inelastic buckling are mainly affected by wall length and previously experienced tensile strain rather than excessive compression strain.

Fintel (1993) presented a condensed report on the philosophy underlying the design for earthquake resistance of multi-story structures in reinforced concrete. The criteria for earthquake performance were discussed and behavior of structures under earthquake excitation was explained briefly. He noted that the evolution of earthquake engineering of buildings started in the 1950's when the ductile moment resistant frame was introduced. Most research during that period emphasized the importance of a ductile moment resisting frame to reduce seismic forces. Shear walls were expected to suffer severe damage stemming from their brittle response due to the fact that rigid structures attract higher seismic forces. It was concluded that severe damage could be expected in shear walls due to brittle response of the shear walls to in plane lateral forces. Based on this thinking, shear walls were considered undesirable for earthquake resistance, and buildings were built with moment resistance frames. However, recorded observations of severe earthquakes (e.g., Yugoslavia, 1963, Venezuela, 1967, California, 1971, Nicaragua, 1972, Romania, 1977, Mexico, 1985, Chile, 1985, and Armenia, 1988) over the past thirty years have shown otherwise. During these earthquakes, hundreds of concrete structures, based on moment resistant frames, collapsed due to excessive interstory distortions that caused failures of columns. However, buildings containing shear walls exhibited extremely good earthquake performance.

Many engineers confused ductility with flexibility (flexibility with ductility)) in the early days of seismic design, and as a result, a large number of buildings were built in a flexible manner. These structures were prone to large interstory drift leading to structural failure. The shear walls, on the other hand, were capable of resisting the interstory drift distortions associated with the seismic events noted above.

Incorporating shear walls to resist seismic actions requires the engineer to become aware of the potential failure mechanisms, and to control some of the undesired characteristics. An earthquake-resisting shear wall structure should ensure survival during the largest ground shaking that can be expected. It should also protect components of a building against all but superficial damage during more frequent disturbances of smaller intensity. Proper detailing will ensure structural survival through energy dissipation by hysteretic damping. Today shear walls are at the forefront for the earthquake resisting elements, and research has also tried to provide a degree of ductility.

Pilakoutas and Elnashai (1995) set out an experimental program to quantify the true ductility and energy absorption of reinforced concrete walls. Another series of wall tests commonly used to corroborate analytical models are the shear wall series tested by Pilakatus and Elnashai. Six isolated cantilever concrete walls, which have aspect ratio of 2 and scale 1:2.5, were tested under severe cyclic loading up to failure. The horizontal load was applied through the top beam, designed to spread the load over the wall panel. Displacements were imposed along the top slab in increments of 2 mm, consisting of two full cycles per displacement level. The cyclic loading was provided by displacement control, at a very slow rate. The displacements were incremented at 2-mm intervals with two full cycles at each displacement level.

Walls were designed in three pairs; each pair having equal flexural reinforcement but different shear reinforcement. Concentrated reinforcement in the boundary elements was used to maximize the flexural capacity, and the web reinforcement was kept nominal. Different amounts of shear reinforcement were used in each pair of walls to investigate the effect of various degrees of safety margins in shear. The shear reinforcement in the web walls was varied to investigate the effect of various degrees of safety margins in shear. The confinement of the boundary elements varied as a consequence of the variation in the shear reinforcement. As a result, the amount of confinement of the boundary region was also varied.

They found that the strength and deformational characteristics of specimens were not affected significantly by shear reinforcement in excess of the amount required to resist the maximum applied load. Concrete dilatation causes the extension of the wall in both the longitudinal and lateral direction. Considerable amount of extension of the wall in the vertical direction occurred due to excessive strains at the plastic hinge region. Shear force is carried by both the concrete in compression and the link reinforcement. Failure took place after the link reinforcement yielded and when the shear resistance of the concrete in compression was exceeded.

The researchers reported some of the following observations:

1. Failure mode depended mainly on the amount and distribution of the shear reinforcement.
2. The strength and deformational characteristics of the specimens were not affected significantly by the shear reinforcement in excess of the amount required to resist the maximum applied load.
3. Shear force was partly transmitted by the concrete in compression and partly by the horizontal (link) reinforcement that enables shear stresses to be resisted through the concrete in the tensile zone. Failure occurred after yielding of the links, and when the shear resistance of concrete in compression was exceeded.
4. Concrete dilatation following cracking caused the extension of the wall in both the longitudinal and lateral directions.
5. Significant extension of the wall in the vertical direction took place following yield due to the accumulation of irrecoverable strains mainly within the plastic hinge zone.

Pilakoutas and Elnashai (1995) evaluated the results that are presented in the companion paper “Cyclic Behavior of Reinforced Concrete Cantilever Walls, Part I: Experimental Results.” Evaluation of these results and comparisons with analytical predictions are made in this paper. Analytical techniques employed vary from linear elastic to nonlinear section analysis. In the first section of this paper, the stiffness characteristics were investigated, since this is the one of the most important parameters in earthquake-resistant code-based design. In the second section, the limit states of first yield and ultimate moments were investigated because of their significance in determining the actual capacity and ductility of members. Finally, the ductility and energy-dissipation aspects of the behavior were presented and discussed.

Aktan and Bertero (1995) evaluated the provisions of 1982 UBC, ACI 318-83, and ATC 3-06 pertaining to seismic shear design of slender walls in mid-rise construction. In the event of major ground shaking in regions of high seismic risk, the actual shear strength demand is expected to equal that associated with the axial-flexural supply. Thus, the codes minimum design requirements ought to insure that flexure, and not shear, will control the seismic response during the expected rare, major seismic event. The codes do not implement this condition. Expressions suggested by design documents for computing the shear strength of walls were evaluated by comparing the predicted and measured strengths of 10 wall specimens tested at Berkley. Although generally conservative, since code expressions do not incorporate the actual shear resisting mechanisms of walls under seismic effects, it is possible for the expressions to mislead the designer to poor shear design. Recommendations are formulated to improve the current shear design procedures by: (1) Relating the shear strength demands to the actual axial-flexural supply, and (2) Incorporating the actual shear resisting mechanisms in predicting shear strength supply of walls.

Sittipunt and Wood (1995) developed a procedure to assist the designer in evaluating the cyclic response of structural walls and identifying walls that are susceptible to undesirable modes of failure. Reinforced concrete walls, exposed to seismic loading, experience pinched hysteretic curves and poor energy dissipation characteristics, experience stiffness degradation with cycling, and may exhibit a sudden loss in lateral load capacity due to web crushing. The authors have suggested that these issues need to be considered in the design process and controlled by the use of diagonal reinforcement in the web. It has been identified as an efficient means of limiting shear distortions, increasing energy dissipation, and reducing the likelihood of shear failures in walls. Thirteen walls tested at the Portland Cement Association were investigated to illustrate the effect of web reinforcement arrangement under cyclic loading.

Failure of the specimens occurred by one of two methods: loss of flexural capacity caused by buckling or fracture of the longitudinal reinforcement, or a loss of shear capacity due to crushing of the concrete in the either boundary element of the web. In the current US building codes, the nominal shear strength of slender walls is assumed to increase in proportion to the amount of web reinforcement. However, many walls subjected to cyclic loading fail due to web crushing after yielding in flexure, which is not accounted for in the code. The results of the PCA tests show that increasing the amount of horizontal web reinforcement has a negligible influence on the hysteresis response of the walls. To study the influence of web reinforcement, six walls with varying arrangements were analyzed.

An increase in the horizontal web reinforcement and an increase in the vertical web reinforcement were not sufficient to improve the cyclic response of walls or reduce the shear distortion at the base. Anchoring with 0.30% of the web reinforcement was effective in reducing the average shear strain at the base. The unanchored bars could not yield at the base, however they were effective in controlling cracks widths. The increase in shear stiffness is, thus, due to aggregate interlock. The final two configurations utilized diagonal reinforcement of identical area. The diagonal reinforcement did not change the strength of the walls significantly, but the hysteric response was more rounded and the shear stiffness did not degrade appreciably. This significant improvement occurs because the diagonal reinforcement runs nearly perpendicular to web cracks. After cracking, most of the force is carried across the cracks by diagonal reinforcement in direct tension. In walls with only vertical and horizontal reinforcement, the reinforcement is inclined to the cracks and the force transmitted across the cracks is carried by dowel action. This is characteristic to stiffness degradation. Therefore, utilizing diagonal reinforcement in webs subjected to reversed loading conditions provided an improvement in the response and should be used in the design process.

Tassios, Moretti and Bezas (1996) in their study presented the results of an experimental program on coupling beams under cyclic loading. They tested ten specimens with five different reinforcement layouts and two different shear ratios (which are α_s=0.50 and 0.83) with scale 1:2. The effect of various layouts of reinforcement on the hysteretic response of “short” (α_s=0.50) and “medium” (α_s=0.83) coupling beams has been investigated. The performance of the specimens according to their ductility has been classified. This paper offers quantitative evidence for the selection of layouts of reinforcement other than the conventional or bidiagonal ones, depending on the shear ratio of the coupling beams. Moreover, the stiffness degradation of coupling beams can be evaluated and possibility used for a more pragmatic estimation of the reduction of bending moments of the main walls.

Grupta and Rangen (1998) tested eight high-strength concrete (HSC) isolated cantilever structural walls under the combined action of in-plane axial and horizontal loads. In addition, they presented the analytical studies on the strength of reinforced concrete structural walls, which also predict the ultimate and failure modes. Test specimens were one-third scale model, which have overall length of 1000 mm with 75 mm thick and 375×100 mm edge elements. The dimension of the top beam and the bottom (foundation) beam were selected such that they did not suffer premature failure and that they were stiffer than the wall. The 28-day concrete compressive strength of the test specimens was 70 MPa. The maximum size of aggregate was 7 mm in order to ensure good compaction of concrete in the test specimens. The test wall specimens were cast horizontally in timber molds. The specimen dimensions achieved were within 0.5 percent accuracy. Test parameters investigated were the longitudinal reinforcement ratio, transverse reinforcement ratio, and axial load level. The ultimate loads and failure load obtained by the analytical study of Grupta and Rangen show good correlation with not only the results of their studies but also with those available in the literature.

Paulay (1999) reviewed elementary but largely forgotten principles, relevant to the seismic behavior of structural systems comprising elements with very different characteristics. In such structures the displacement at the ultimate limit state may be associated with very different displacement ductility demands imposed on constituent elements. He showed how, by simulating nonlinear ductile structural response with bilinear modeling, the unavoidable restriction on the system ductility capacity, necessary to protect elements with the smallest displacement potential, can be readily determined. To illustrate the applications of fundamental principles a few simple examples are presented. The exploitation of the principles presented in structures with restricted ductility and very different plastic mechanisms is illustrated.

Balkaya and Kalkan (2002) investigated the applicability and accuracy of inelastic pushover analysis in predicting the seismic response of tunnel form building structures. The contribution of transverse walls and slab-wall interaction during the 3D action, the effects of 3D and 2D modeling on the capacity-demand relation, as well as diagram flexibility, torsion and damping effects were investigated. Two different buildings having similar plan and sections with different story levels were analyzed by utilizing the 3D and 2D finite element models with the use of the developed isoparametric shell element. This paper also makes comparisons between the conventional 2D solutions and the applied 3D analyses of presented case studies and illuminates the reasons for their differences. In general, total resistance capacities of the three dimensionally analyzed structures were observed to be more than that of two dimensionally modeled cases. This study showed that the applied methodology has a considerable significance for predicting the actual capacity, failure mechanism, and evaluation of the seismic response of tunnel form buildings.

Balkaya and Kalkan (2003) investigated the consistency of empirical equations in current seismic code provisions related to dynamic properties of shear-wall dominant buildings constructed by using tunnel form techniques. For that reason, a total of 80 different building configurations were analyzed by using three-dimensional finite-element modeling and a set of new empirical equations was proposed. It is demonstrated that current earthquake codes overestimate the performed finite-element analysis results for rectangular plans and most of the time underestimate them for square plans. The recommended empirical equations are presented in detail in this paper and are considered to be appropriate for the estimation of the period of tunnel form building structures for 2-15 story levels with various architectural configurations. The results of the analyses demonstrated that given formulas including new parameters provide accurate predictions for the broad range of different architectural configurations, roof heights and shear-wall distributions, and may be used as an efficient tool for the implicit design of these structures.

CHAPTER 3

TEST SPECIMENS AND EXPERIMENTAL TECHNIQUE

3.1 GENERAL

This chapter contains details pertaining to the test specimens. It includes the design of panel form test specimens, the construction process, the properties of the materials used, description of the test setup, loading system and the testing facility. It also includes instrumentation utilized during the test and test procedure.

The main objective of the research reported in this thesis is to study the behavior of panel form structures under seismic action. Since system testing is expensive and time-consuming, test specimens had to be designed and detailed carefully, construction of the test specimens had to be planned considering all the details and instrumentation had to be designed considering the main objectives for this experimental research.

The experimental study conducted by the author was a part of research program sponsored by National Science and Technical Research Council of Turkey (TUBİTAK-İNTAG 561).

3.2 TEST SPECIMENS

3.2.1 General

The experimental work described in the following involves the testing of two four-story 1/5-scale reinforced concrete panel form building test specimens under lateral reversed cyclic loading, simulating the seismic forces and free vibration tests. 1/5-scale reinforced concrete panel form building test specimens were manufactured at the Structural Mechanic Laboratory at METU. The test specimens tested in short dimension and long dimension were identified as SPECIMEN1 (SP1) and SPECIMEN2 (SP2), respectively. The photograph in Figure 3.1 demonstrates the actual size and general view of the test specimens. The photograph was taken at the end of construction and prior to any test preparations.

Figure 3.1 General view of the test specimens.

Test specimens that are seen in Figure 3.1 have been tested vertically by using the reaction wall and the strong floor. First, SP1, then SP2 was tested. These specimens were tested under lateral reversed cyclic loading, simulating the seismic forces. For both of the specimens two static and two dynamic tests were performed. Before the static tests, free vibration tests were performed on the specimens to understand the dynamic properties of uncracked dynamic response. After the first dynamic test, test specimens were subjected to lateral reversed cyclic loading until some minor visible hair cracks occurred. Again a free vibration test was performed on the panel form test specimens to realize the differences between the dynamic properties of uncracked and cracked response. At the last stage, specimens were loaded until failure occurred.

3.2.2 Dimensions of the Test Specimens and the Formwork

The experimental work described in the following involves the testing of two four-story 1/5-scale reinforced concrete panel form building test specimens under lateral reversed cyclic loading, simulating the seismic forces and free vibration tests. SP1 was tested along short dimension and SP2 was tested along long dimension. All specimens were cast vertically by using 1/5-scale steel forms. The steel formwork was manufactured from 2.5 mm thick steel plates. Steel plates were assembled with bolts, forming the formwork. The 1/5-scale steel forms of the specimens were manufactured with an error of 1/10 of one millimeter. The forms were stiff enough to avoid any deformations during the molding process.

The plan view of the test specimens is given in Figure 3.2 (All dimensions given in this study are in mm). The two sectional drawings, I-I and II-II are given in Figure 3.3 and Figure 3.4, respectively. Each test specimen has 880×2000 mm plan dimensions. There was an empty space of 870 mm between two specimens. Both specimens were manufactured on the same foundation with 2.4 m width, 3.2 m length and 0.4 m thickness. There was a 200 mm thick slab at the fourth story to prevent the local deformations while loading the test specimens under reversed cyclic loading at this level.

The specimens were monolithically connected to the upper extra slabs and the foundation. The upper slabs also functioned both as the elements through which horizontal loads were applied to the specimens and as cages for the anchorage of the vertical bars. The top slabs of the specimens were heavily reinforced with $\phi 8$ reinforcing bars. It consisted of top and bottom reinforcement in both directions with a bar spacing of 100 mm. The ends of the bars had an anchorage length of 100 mm in the form of a 90-degree bend. This heavy reinforcement in the top slab was required to ensure stiff slab members so that failure would be concentrated in the wall members. The clear cover for the reinforcement was 40 mm in the top slab. The self-weight of the top slab contributed an additional 7.48 kN of axial load.

The foundation was utilized to clamp down the specimens to the laboratory floor, simulating a rigid foundation. Forming the foundation constituted the first phase of the construction of the panel form test specimens. The second phase of the construction consisted of casting the walls and slabs of the test specimens. The final phase of the test specimens included the construction of the top slab. Wall thickness was 40 mm, slab thickness was 30 mm and story heights were 650 mm. The shear wall consisted of an H beam cross-section. The two flange walls were 620 mm high × 40 mm thick × 2000 mm long. The web walls were 620 mm high × 40 mm thick × 800 mm long. The ratio of the wall area to the floor area was 10.91%. Total overall heights of the specimens were 2770 mm.

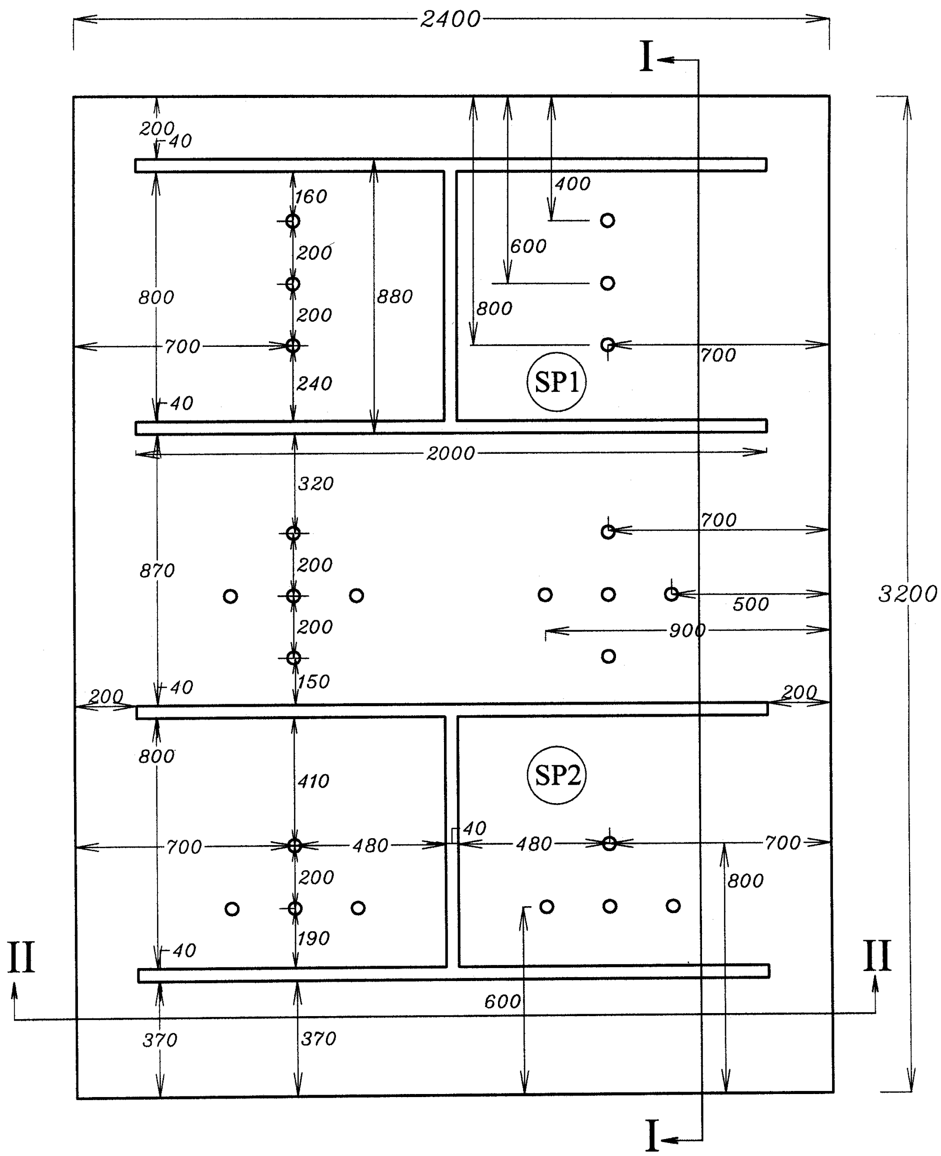

Figure 3.2 Plan views of the test specimens.

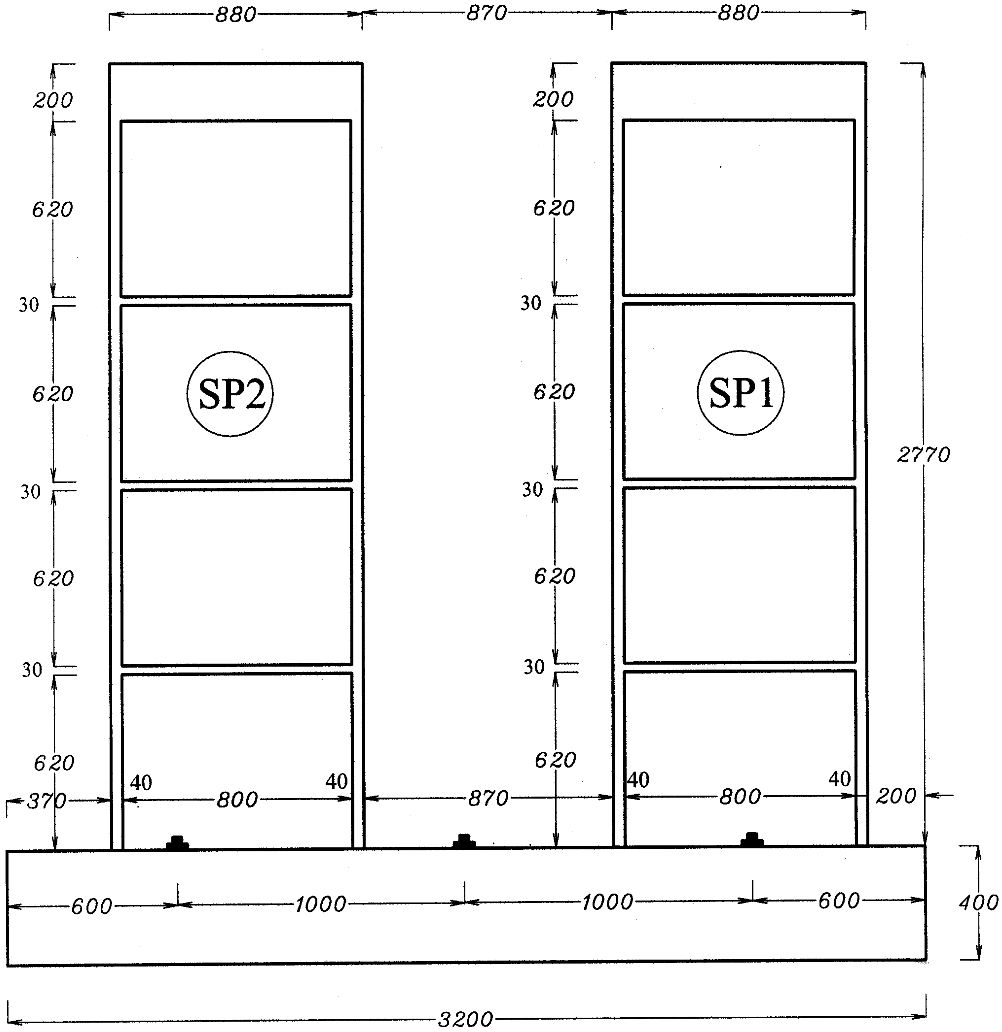

Figure 3.3 Sections I-I of the test specimens.

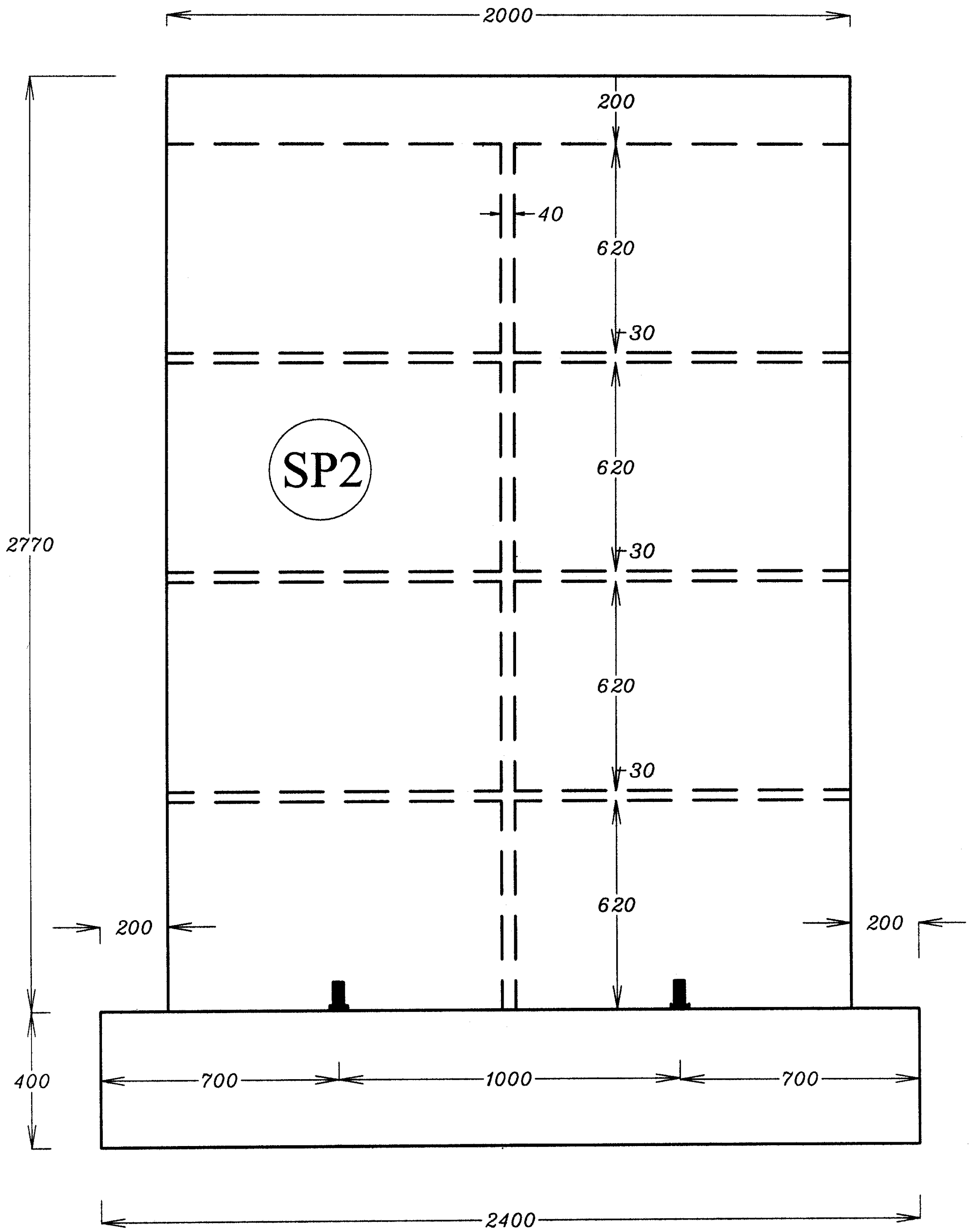

Figure 3.4 Sections II-II of the test specimens.

3.2.3 Details of the Test Specimens

The dimensions of the test specimens are given in Section 3.1.1. The dimensions and detailing of the reinforcement are chosen to reflect the common deficiencies encountered in practice in Turkey. According to AY (1997) the minimum reinforcement ratio for shear walls is 0.0025. However if the ratios of wall area to building plan area satisfy some requirements stated in AY (1997), the minimum reinforcement ratio for shear walls in this situation is $\rho_{min} = 0.0015$. The ratios of wall area to building plan area satisfy requirements stated in AY (1997). To provide minimum reinforcement ratio for shear walls in the vertical and horizontal directions respectively$\rho_{hmin} = \rho_{vmin} = 0.0015$; 2 mm diameter one-layer mesh reinforcement was used. The spacing of the wall reinforcement is 50 mm in both directions. There are 40ϕ2/50 mm bars in each flange and 17ϕ2/50 mm bars in the web in the longitudinal direction of the walls. The longitudinal reinforcement of the shear walls was spliced at foundation level. 97ϕ2.5/50 mm dowels cast in the foundation had a length of 80ϕ (80×2.5 mm = 320 mm). The longitudinal reinforcement of the shear walls was spliced at floor level with a splice length of 50ϕ (50×2 mm = 100 mm). No splice problem was faced during the experiments at those locations. In none of the tests bond slip of the reinforcement was evident.

In slabs, 2.5 mm diameter one-layer mesh reinforcement was used. The spacing of the slab reinforcement was 50 mm in both directions. One-layer mesh reinforcement was placed in the middle of the slabs. The ends of the bars had an anchorage length of 50 mm in the form of a 90-degree bend. The reinforcement ratio for slabs along the long and short dimensions was 0.0025%. Reinforcement patterns and loading directions of SP1 and SP2 are given in Figure 3.5 and Figure 3.6, respectively. The reinforcement pattern of the slabs is given in Figure 3.7.

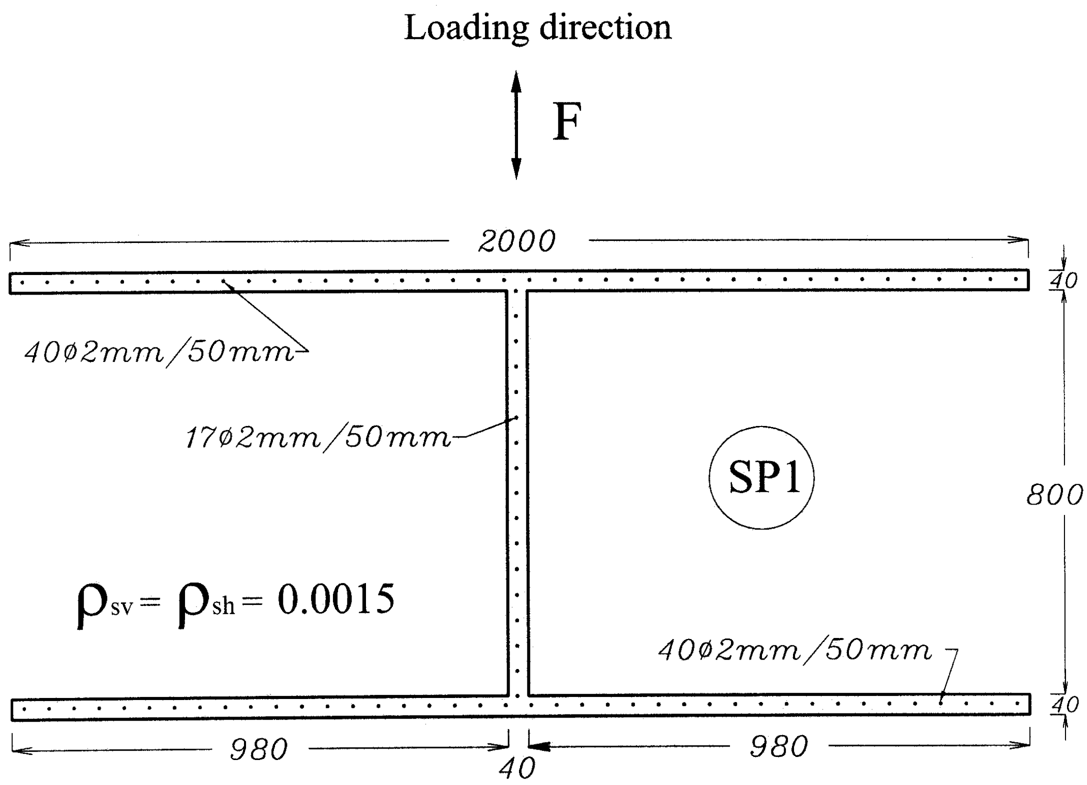

Figure 3.5 Reinforcement pattern and loading direction of SP1.

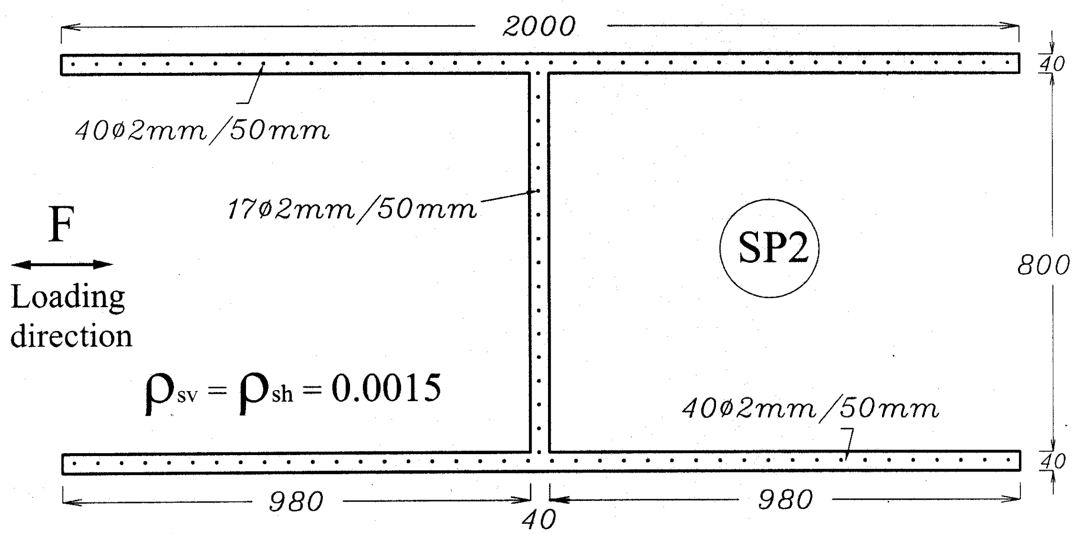

Figure 3.6 Reinforcement pattern and loading direction of SP2.

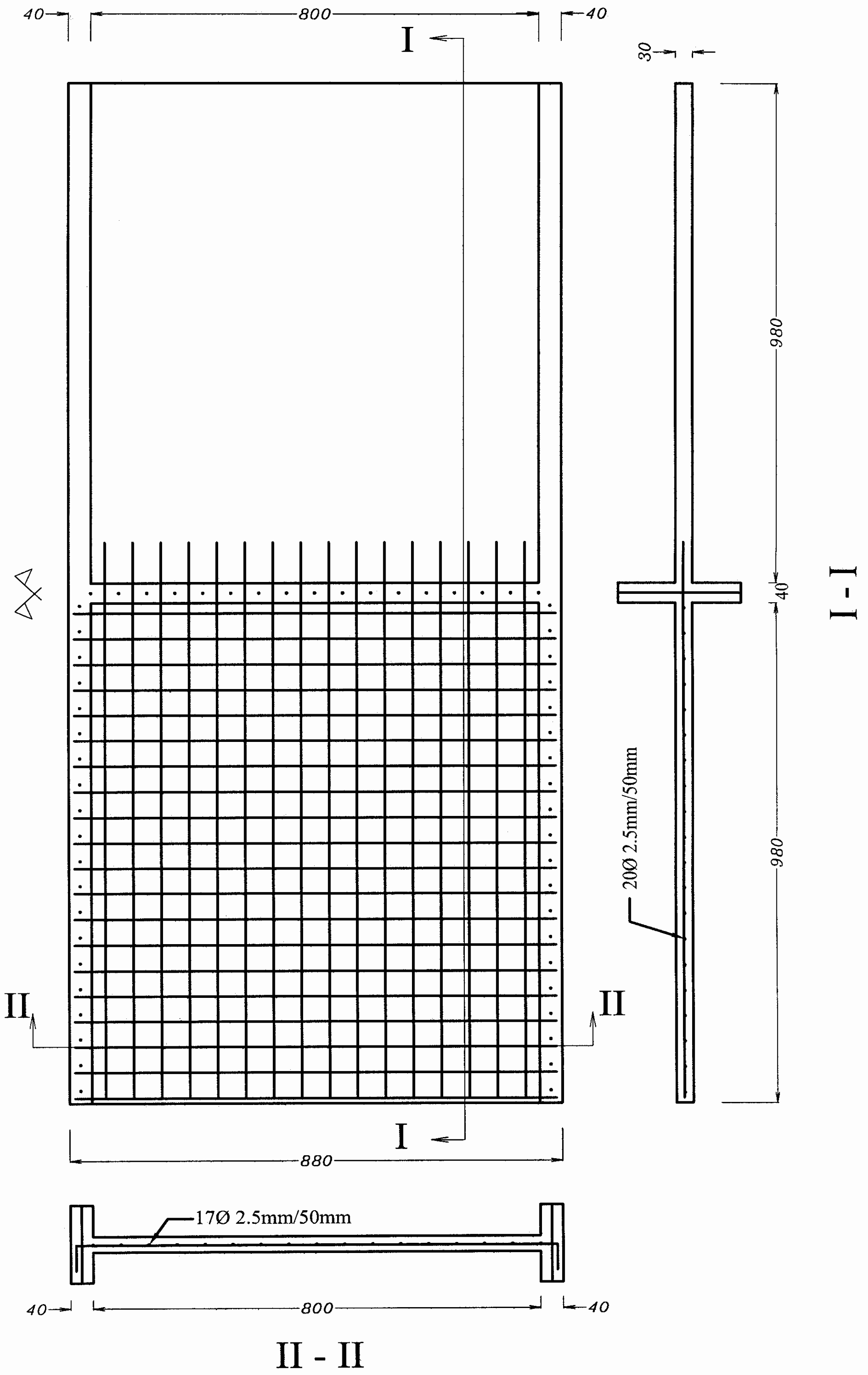

Figure 3.7 Reinforcement pattern of the slabs.

3.3 FOUNDATION OF THE TEST SPECIMENS

Forming the foundation constituted the first phase of the construction of the panel form test specimens. One-meter distance between the holes on the strong floor led to a design of a big foundation that has a length of 3.2 m, width of 2.4 m, and thickness of 0.4 m. This foundation enabled to place two 1/5-scale reinforced concrete panel form buildings on the same foundation. The foundation can be fixed to the strong floor at six points for SP1 and four points for SP2 by means of 50 mm diameter and 1.5 m length high strength steel bolts. Plan view, cross section I-I and cross section II-II of the foundation are given in Figure 3.8.

Steel forms were prepared for molding of the foundation concrete. Approximately $3m^3$ of concrete was required for the production of the foundation. The weight of the foundation was 77 kN. Ready mixed concrete was ordered from a local ready mix plant company. Before placing the concrete, the cavities inside the forms were cleaned and greased to facilitate their removal when concrete was set. A general view of the foundation's steel formwork and reinforcement pattern are shown in Figure 3.9. Figure 3.10 shows a general view of molding the ready mixed concrete of the foundation. Mechanical vibration was used for the compaction of the concrete. This mechanical vibration was imparted by means of a vibrator, which operated with the help of an electric motor. Nine cylinder specimens were taken for the quality control of concrete. At the conclusion of testing, compression cylinder tests were conducted on standard (150 mm × 300 mm) concrete cylinders batched from the truck. The cylinders were tested at 28 days at a loading rate of 0.005 mm/s. The grade of the ordered ready mixed concrete was C25, which should have a compressive strength of 25 MPa at 28 days. According to the standard cylinder tests, the concrete of the foundation had a final strength of 44 MPa.

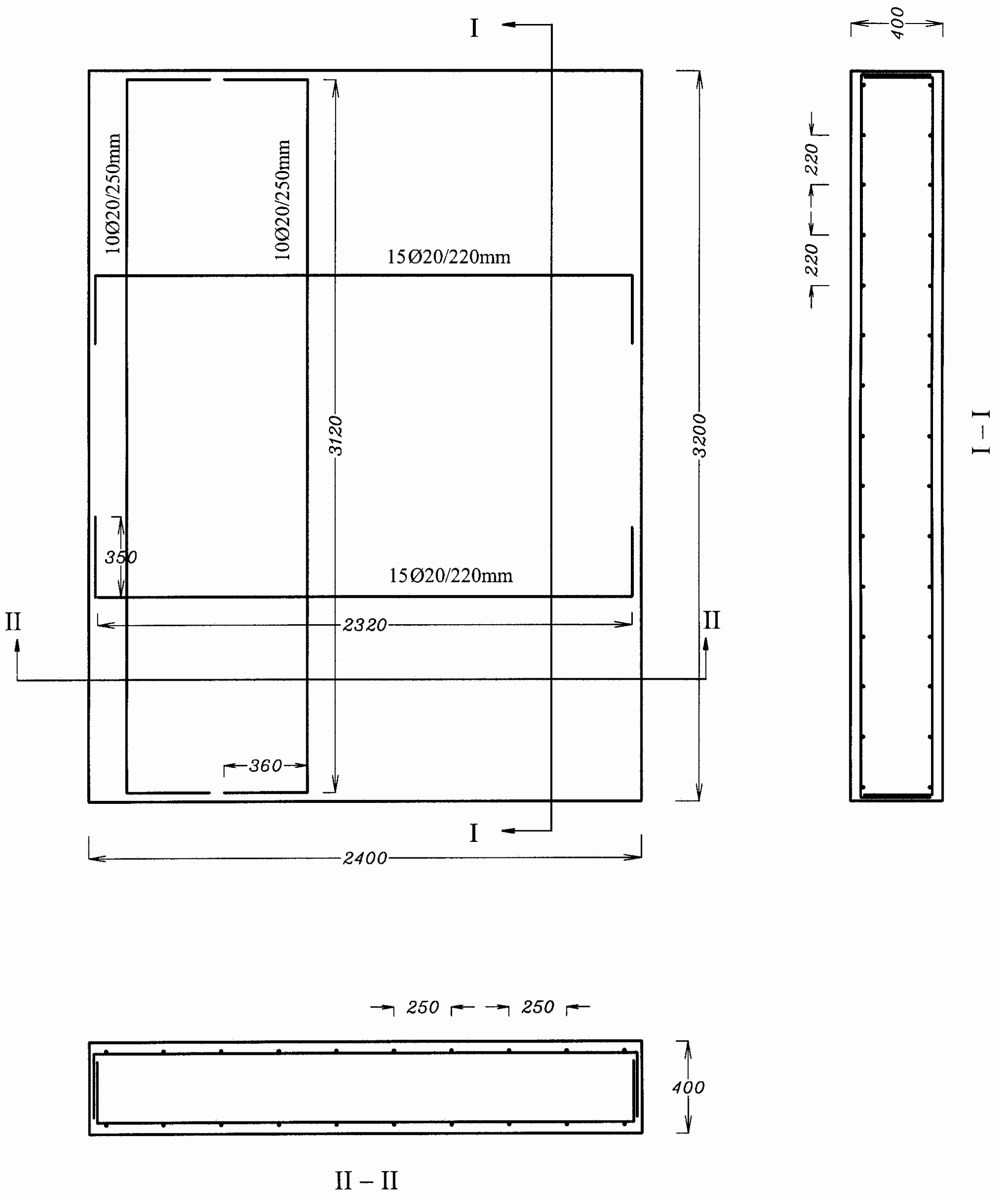

Figure 3.8 Plan view, Section I-I and Section II-II of the foundation.

Figure 3.9 A general view of the foundation's steel formwork and reinforcement pattern.

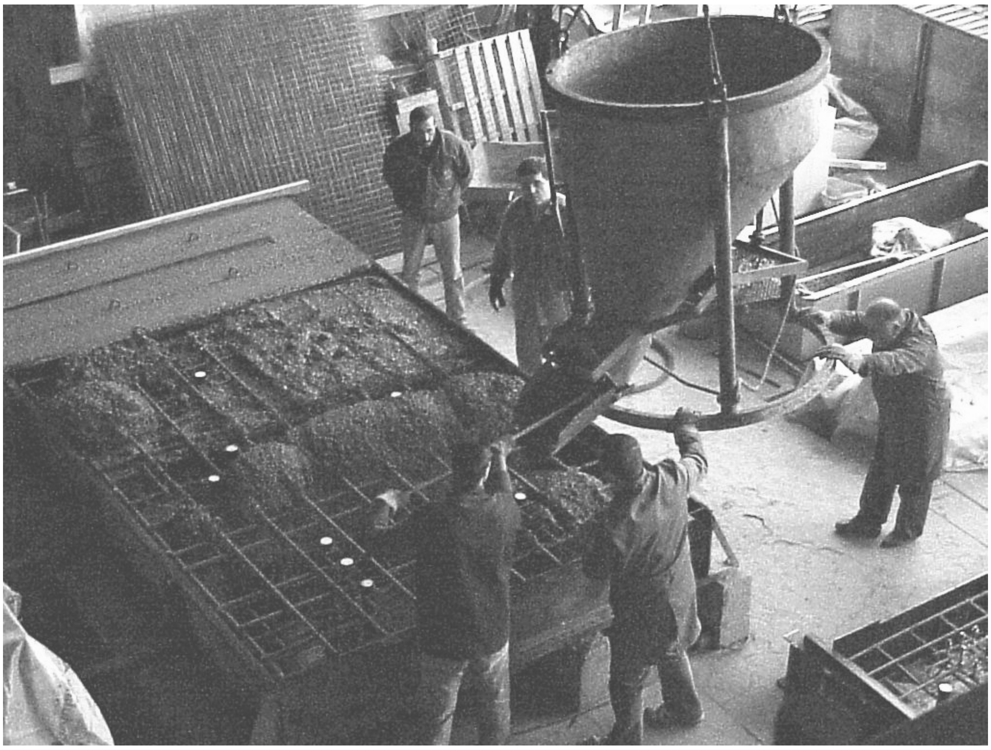

Figure 3.10 A general view of molding the ready mixed concrete of the foundation.

The foundation of the test specimens were heavily reinforced with twenty-millimeter diameter S420 type deformed bars. In short direction 20ϕ20/250 mm deformed bars were used and in long direction 30ϕ20/220 mm deformed bars were used. These reinforcements were placed on bottom and top faces of the foundation to resist the reversed cycling of the testing load. The clear cover for the foundation reinforcement was 40 mm. This heavy reinforcement causes the reinforcement ratio for the foundation along the long and short dimensions to be 0.73% and 0.82%, respectively, which was required to ensure stiff foundation so that premature failure would not occur in foundation.

An important step was to place the dowels prior to casting. To transmit the loads of test specimens to the foundation, 2.5 mm diameter mesh reinforcements, which have 50 mm × 50 mm spacing, were used as dowels. To provide adequate development length, these dowels were extended into footing 30 mm. They were tied to the reinforcement of the foundation. They also extended into the walls 200 mm, that is 100 times that of the wall's bar diameter (100 ×2.0 mm = 200 mm). Plan view, Section I-I and Section II-II of the foundation and dowels are given in Figure 3.11.

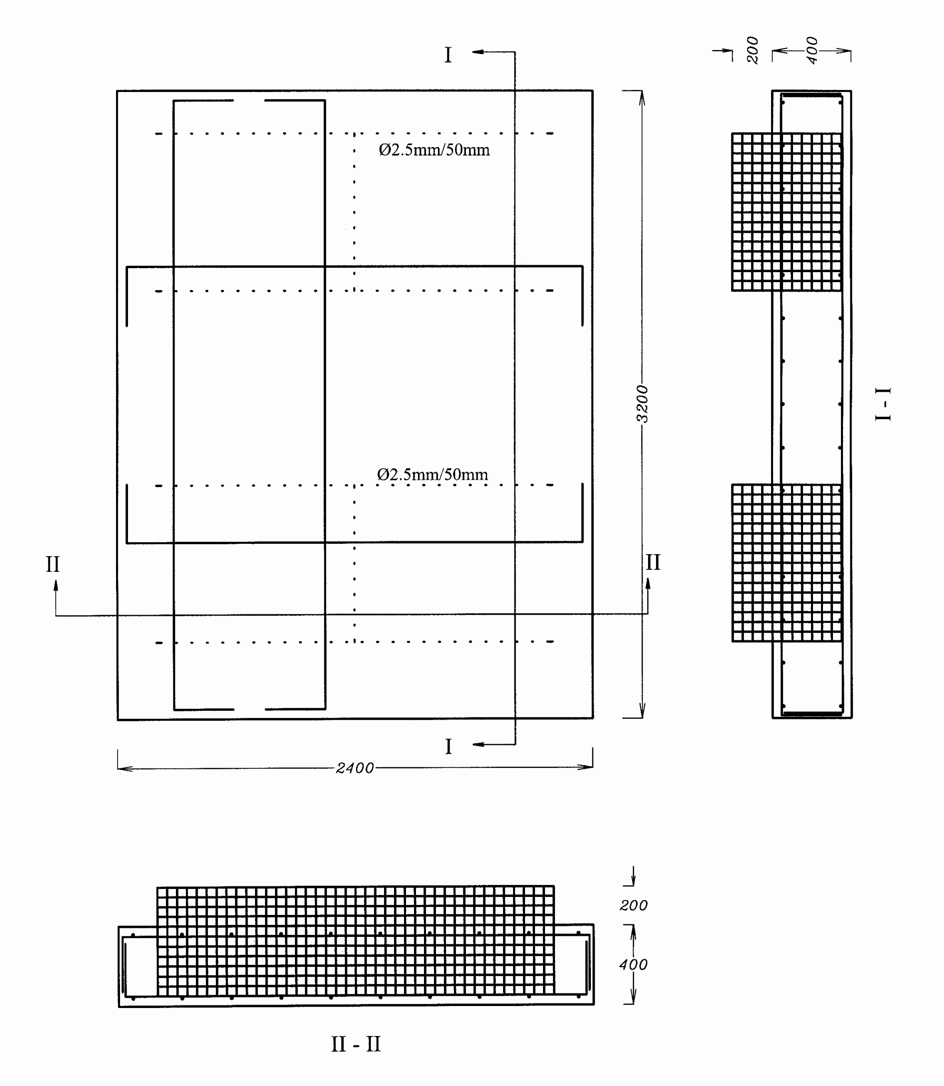

Figure 3.11 Plan view, Section I-I and Section II-II of the foundation and dowels.

3.4 MATERIALS

Reinforced concrete panel form specimens were cast monolithically in the vertical direction. The concrete of the 1/5-scale reinforced concrete panel form specimens was produced at the structural Mechanics Laboratory of METU. A concrete mixture with a maximum aggregate size of 7 mm and cement content of about 436 kg/m^3 were used in the panel form test specimens. According to Turkish Seismic Code (AY-1997) in high seismic zones minimum C20 must be used. The average 28 days characteristic cylinder strength of concrete must be more than 200 kg/cm^2. The target compressive cylinder strength of the 1/5-scale reinforced concrete panel form specimens was more than 20 MPa. The concrete mix for the walls required a special order that would provide an increased flow of the concrete so that it would penetrate through the thin wall members. Prior to casting, superplasticizer (sikament300) was added to bring the slump up to 200 mm. The superplasticizer improved the floor of the concrete while improving the strength and hardening time of the concrete. Table 3.1 gives the mixture proportions of concrete for the 1/5-scale reinforced concrete panel form specimens. Materials used in the mixture are given by weight for 1 m^3 concrete. The cylinders from the panel form test specimens were tested on the day of testing. At the test day of SP1 and SP2, the strength of concrete was 35 MPa.

Special attention was given to curing. Curing was done by covering the specimens with wet burlap which kept the concrete moist and as near as possible to the ideal temperature for chemical hydration.

At least nine standard cylinder test specimens were taken from each batch in order to determine the concrete strength. The test cylinders were 150 mm in diameter and 300 mm in height. The test cylinders were kept under the same moist curing conditions as the test specimens. Each time, three cylinders were tested to obtain the average strength of concrete.

Table 3.1 Mix design of the panel form specimen (weight for 1 m^3 of concrete).

	Weight (kg)	**Proportions by weight (%)**
Cement	436	19.05
0-3 mm Aggregate	864	37.75
3-7 mm Aggregate	745	32.55
Water	240	10.48
Sikament 300	4	0.17
Total	2289	100.00

Two different sizes of plain reinforcing bars were used in the panel form test specimens. In each shear wall 2 mm diameter mesh reinforcement and in slabs 2.5 mm diameter mesh reinforcement were used. The reinforcement of all specimens was prepared from the same batch of steel. Six test coupons were randomly taken to determine the stress-strain relationship of the steel used. The coupons were tested in tension. The properties of reinforcing bars used in the panel form test specimens are listed in Table 3.2. The reinforcing bars were not heat-treated and did not respond with a flat yield plateau.

Table 3.2 Mechanical properties of reinforcing bars.

Steel No	f_{sy}(MPa)	f_{su} (MPa)	ε_{su}
ϕ2	540	600	0.025
ϕ2.5	540	600	0.025

3.5 INSTRUMENTATION

In the instrumentation of the panel form test specimens, LVDTs (Linear Variable Displacement Transducers) and electrical DG (dial gages) were used for displacement measurements and load cell was used for load measurement. Load measurements were made using a 110 kN compression-tension load cell. Loading of the panel form test specimens consisted of increasing horizontal cyclic displacements of the top slab. The magnitude of applied load was measured with 110 kN tension-compression load cell that was connected to the hydraulic jack and the data acquisition system. Deformations were measured by LVDTs with 200, 100 and 50 mm strokes and dial gages with 50, 20 and 10 mm strokes.

In each static test, voltage signals coming from the transducers were recorded by a data acquisition system and the results were then directed to a personal computer. With the help of a personal computer, voltage outputs were converted to displacement and load values i.e. voltage outputs from the instrumentation were fed into a data acquisition system, from which all signals were directed to a personal computer. A computer program written at METU stored the data as force and displacement. This program also monitored the data as numbers and graphics on the screen.

In all tests in this study, the displacement of each story was measured with respect to the foundation. These readings would be used to construct load-displacement and load-inter-story drift curves. The lateral displacements of the test specimens at each floor level were measured by means of displacement transducers. Shear deformations were measured on both the first and the second story walls in the static tests of SP1. Shear deformations were measured on the first story walls in the static tests of SP2. In the specimens, average shear deformations of the wall panels were measured by means of diagonally placed displacement transducers. Transducers were located 100 mm away from the corner of the walls. The reason for choosing this location was to avoid localized effects like crushing of concrete during the experiment. Strains were measured on both faces of the walls at the base, which would enable the calculation of the curvature.

The rigid body rotations and displacement of the foundation and reaction wall were measured by means of mechanical dial gages in all tests. Two gages in horizontal direction, two gages in lateral direction and two gages in vertical direction were mounted on the foundation and reaction wall. These gages were monitored manually. The readings were acquired at the end of each cycle. In all tests no appreciable movement was observed in these dial gages ($\Delta \approx 1/50$mm), which meant that in the load range applied during the test, no appreciable movement occurred either at the foundation or at the reaction wall in all tests. Moreover, all measurements on the test specimens were taken relative to the foundation. Therefore, rigid body movements would not affect the readings of the test specimens.

3.6 TEST SETUP AND LOADING SYSTEM

The testing apparatus required for the reversed cyclic loading of the panel form test specimens is explained in detail in this section. The testing system consisted of the strong floor, reaction wall, loading equipment, instrumentation and the data acquisition system.

The Structural Mechanics Laboratory of METU has a strong floor for fixing the test specimens to the test floor. This floor has a thickness of 600 mm. Additionally a working drift (gallery) lies under the strong floor that enables to work under the floor easily. Holes are left on the floor, which allow fixing of the test specimens to the floor. Totally, 48 holes are lined up as two rows with 1-meter spacing. The distance between the rows is also 1 meter. The diameter of these holes is 150 mm.

The foundation of the test specimen was fixed to the strong floor by means of specially produced high strength steel bolts (Dywidag). These bolts had a diameter of 50 mm. 6 and 4 holes were used to fasten the footing to the strong floor for testing the SP1 and SP2, respectively. The footing had to be anchored with a uniform force to the floor. To accomplish this, a pre-tensioning system was built from steel sections. First, all Dywidags were tensioned with this system up to 120 kN. Then, the bolts were tightened at their stretched position. After bolting, the tension force was released from the Dywidags. All the Dywidags were tightened almost by the same amount of force in this way.

To make vertical testing of the specimens' possible, there was a need for a reaction wall that provides lateral loading. In the laboratory, a reaction wall was fixed to the strong floor by means of totally 8 Dywidags. The total height of the reaction wall was 4.58 m. There are totally 14 holes on the wall that are spaced at two columns and seven rows. These holes match correctly the holes on the floor; in other words, the distance between two columns is 1 m. Also, the length between the rows is 610 mm. Front view, top view and side view of the reaction wall are given in Figure 3.12, Figure 3.13and Figure 3.14, respectively.

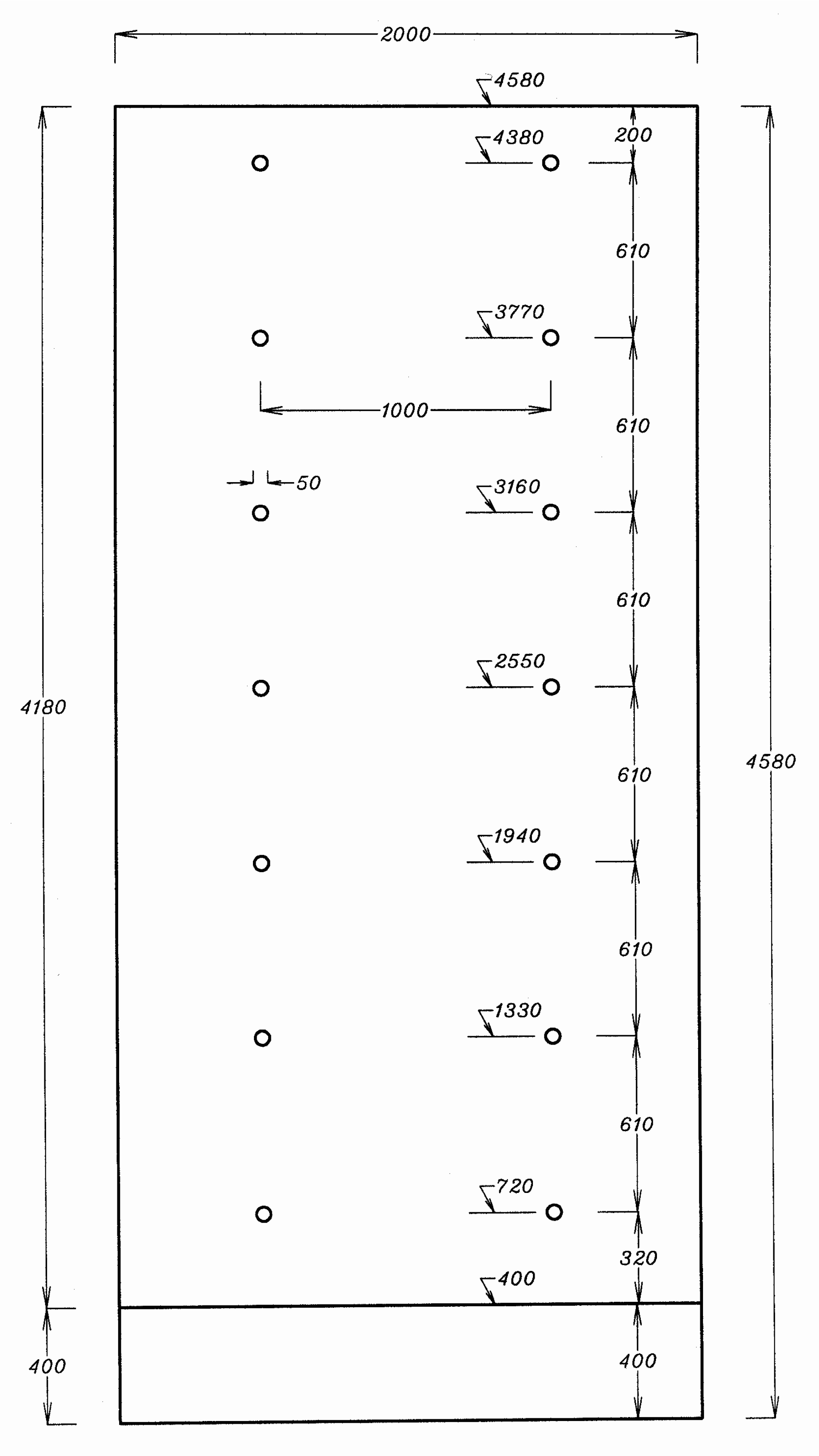

Figure 3.12 Front view of the reaction wall.

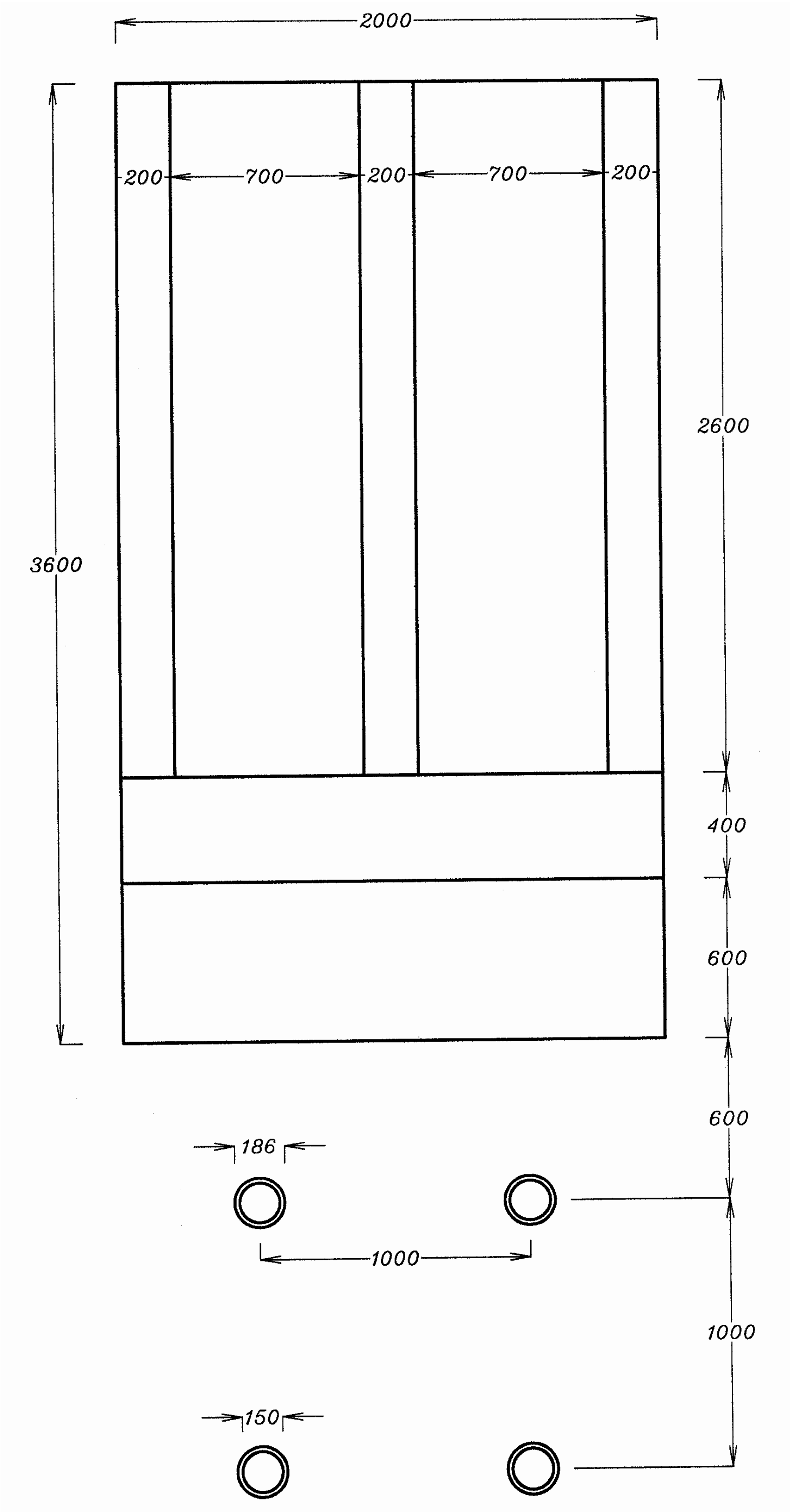

Figure 3.13 Plan view of the reaction wall and gallery holes.

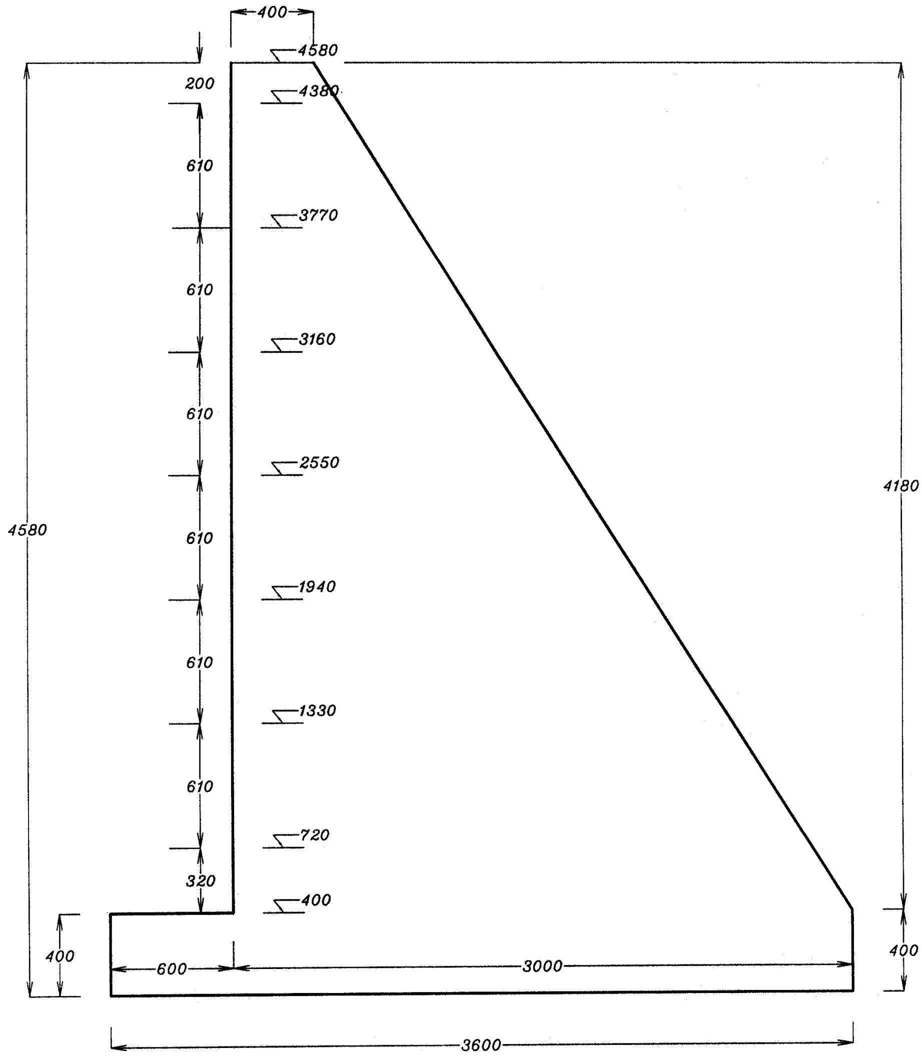

Figure 3.14 Side view of the reaction wall.

The lateral loading system had to be fixed perpendicularly to the reaction wall and the extra slab of the test specimen. This loading system consisted of hinges at the ends, a load cell and a hydraulic jack (cylinder). This loading system had to enable the loading jack to come exactly to the center-point of the fourth story slab. Therefore, this system had to be freely moveable on the reaction wall allowing accurate positioning. For this reason, a rail system was designed using heavy steel sections. Photographs of the front view and side view of the interface system between the reaction wall and lateral loading are given in Figures 3.15 and 3.16, respectively. The top and bottom part of the system consisted of build-up box sections welded to two U200 steel sections. To enable sliding, two U140 steel sections were put together with a space in between. The width of this space was 40 mm. U140 steel sections were strengthened by welding 6×1 mm steel plates to the flanges. The sliding system was welded to the top and bottom heads to form the left and right columns. These columns enable sliding up and down directions. In order to allow movement in horizontal direction, the same sliding mechanism was placed on the steel columns. A 400×400 mm steel plate with a thickness of 30 mm was attached on this mechanism. This plate allowed fixing the hinge of the lateral loading system.

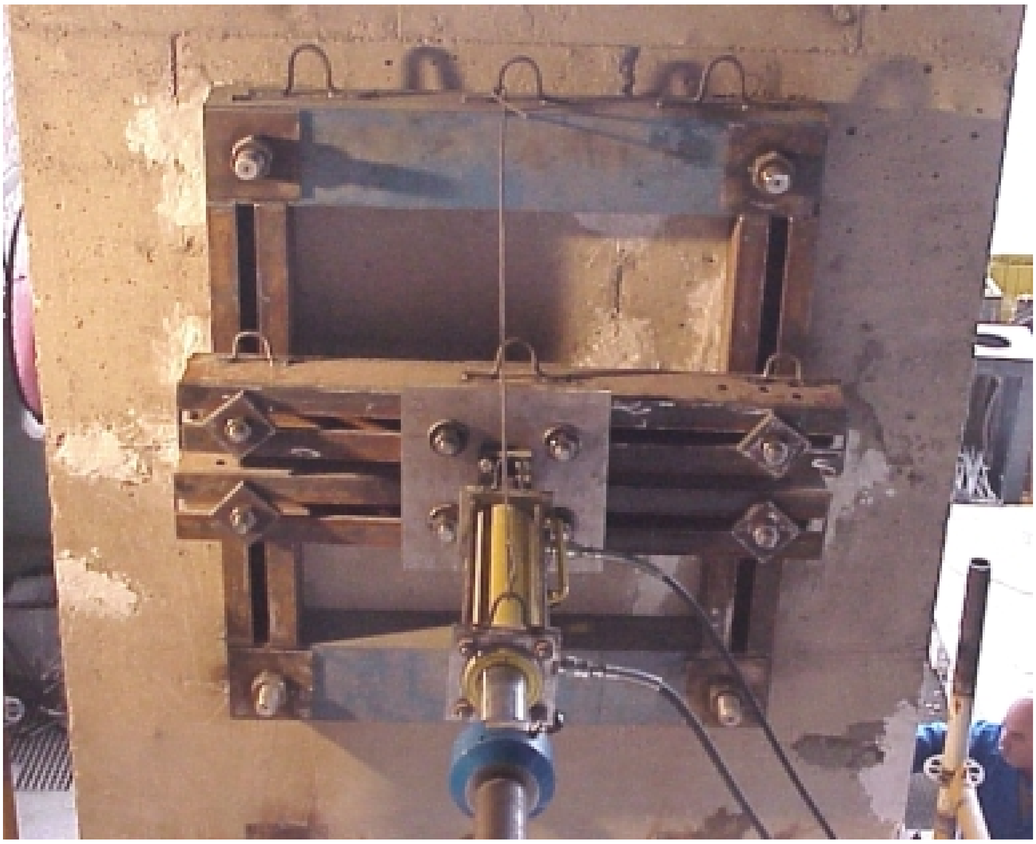

Figure 3.15 Front view of the interface system between the reaction wall and lateral loading.

Figure 3.16 A general view of the lateral loading system.

The lateral load was applied at the fourth story floor level through a hydraulic jack. Before molding of the concrete of the extra slab on the fourth story, a steel plate was placed at the face of the exterior joint. This steel plate was welded to the longitudinal lateral reinforcement of the extra slab to transmit the lateral load from the hydraulic jack safely during the cyclic loading. A load cell was connected in front of the hydraulic jack in order to measure the magnitude of the applied lateral load. A steel stiffened pipe was put between the load cell and test specimens to fill the gap between the reaction wall and the test specimens. This pipe was welded to the steel plate at the joint. At both ends of this loading system, hinges were placed to ensure axial load application. A general view of the loading system is given in Figure 3.16.

A general view of the test setup, loading system, instrumentation, reaction wall and data acquisition system for static test of SP1 and SP2 are shown in Figure 3.17 and Figure 3.18, respectively.

Figure 3.17 A general view of the test setup for the static tests of SP1.

Figure 3.18 A general view of the test setup for the static tests of SP2.

3.7 TEST PROCEDURE

Following the curing period, the specimens were carried to the front of the reaction wall where they would be tested. They were positioned carefully so that they were exactly perpendicular to the reaction wall. Afterwards, they were fixed to the strong floor by means of Dywidags. Specimens were whitewashed in order to be able to monitor the cracks more clearly during the test. Then, dial gages, LVDTs and the load cell were mounted to the test specimens and their connections to the data acquisition system were established. Moreover, concrete cylinders were tested in order to get the compressive strength of the specimens.

Loading a specimen to a predetermined level and then unloading to a zero level constitutes a half cycle loading. In each half cycle, the direction of the lateral loading was changed. The addition of a reversed half cycle to a half cycle represents a full cycle. All specimens were tested under reversed cyclic lateral loading. During the test, top displacement versus lateral load diagram was monitored. At each maximum load level of half cycles, cracks were marked on the specimens and notes were taken describing the observations.

CHAPTER 4

TEST RESULTS AND OBSERVED BEHAVIOR OF SPECIMEN1

4.1 INTRODUCTION

This chapter summarizes the instrumentation on SP1 for the first and second static tests, qualitative and quantitative experimental results and behavior of the panel form test specimen, SP1. The quantitative results will include lateral displacement curves of each story, story drift ratios with the applied lateral force, shear deformation and moment curvature curves. The qualitative results will be presented in the form of photographs of the SP1 taken during testing, displaying the crack patterns, cracking and/or crushing locations, and the state of the SP1 at failure. In the instrumentation of the SP1 for the static tests LVDTs (Linear Variable Displacement Transducer), electronic and mechanical dial gages were used for displacement measurements and load cell was used for load measurements. Load measurements were done using a 110 kN compression-tension load cell.

4.2 STATIC TEST ON UNDAMAGED SPECIMEN1

After the free vibration test was done on the undamaged SP1, the reversed cyclic static test was applied. The aim of this test was to investigate the behavior of the SP1 up to cracking.

In the first static test, lateral deformations were measured by dial gages with a 20 mm strokes at the fourth story and dial gages with 10 mm strokes at the third, second and first stories. To measure possible torsional rotation, two LVDTs with 50 mm strokes were placed at the fourth story at the right and left edges of the specimen. No appreciable torsional rotation was observed in the first static test, which meant that no out of plane deformation occurred during the first static test. Average shear deformations of the walls were measured on both the first and second stories by means of diagonally placed dial gages with 50 mm strokes. For this purpose, dial gages with 50 mm strokes were used. Dial gages were located 100 mm away from the corner. The reason for choosing this location was to avoid localized effects like crushing of concrete during the experiment. The north flange is the wall near the reaction wall. The south flange is the wall further from the reaction wall. Figure 4.1 shows a general view of the test setup, loading system, instrumentation, reaction wall and data acquisition system for SP1 for the first static test. Figure 4.2 shows the details of the test setup, loading system and instrumentation for SP1 for the first static test. The plan view of the test setup, loading system and instrumentation for SP1 for the first static test is given in Figure 4.3.

Figure 4.1 A general view of the test setup, loading system, instrumentation, reaction wall and data acquisition system for SP1 for the first static test.

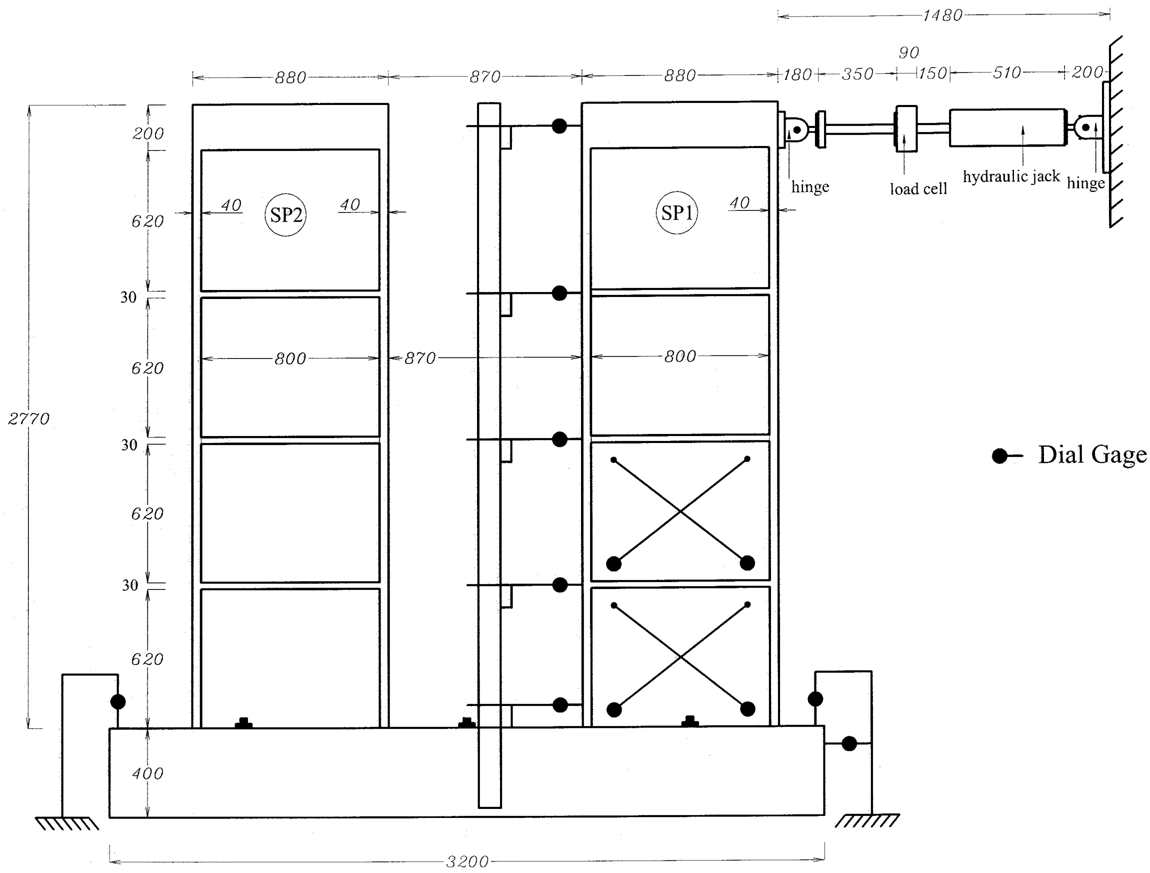

Figure 4.2 Details of the test setup, loading system and instrumentation for SP1 for the first static test.

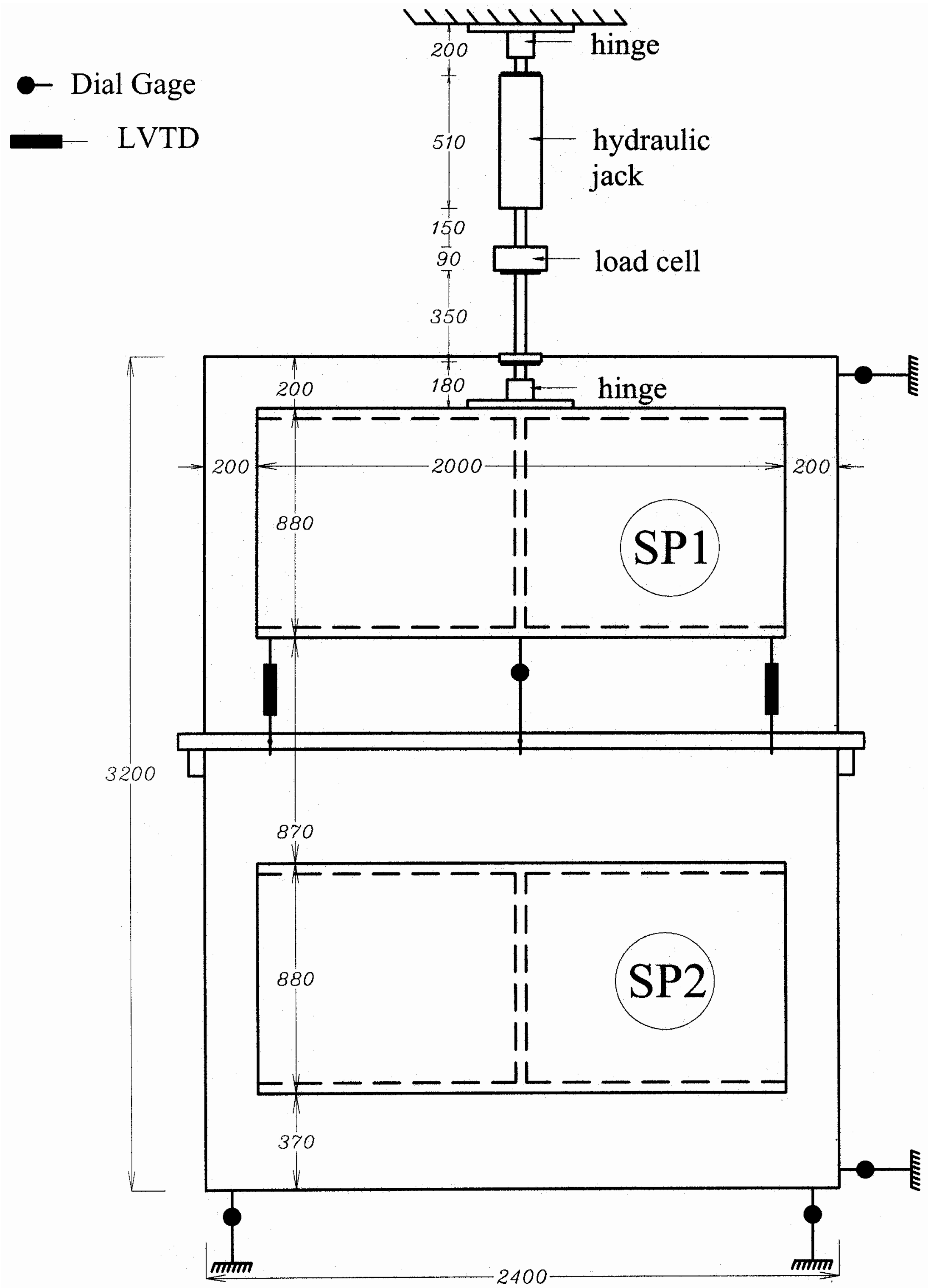

Figure 4.3 Plan view of the test setup, loading system and instrumentation for SP1 for the first static test.

4.2.1 Load-Deformation Response of the Undamaged SP1

This section presents the response of the panel form test specimen SP1 for the first static test under the reversed displacements. The undamaged SP1 was loaded under the lateral loading history presented in Figure 4.4. This first static test was load-controlled test that consisted of five full reversed cycles. In the first two cycles 20 kN lateral load was applied to the SP1, then the load was increased by 5 kN in each cycle up to 35 kN.

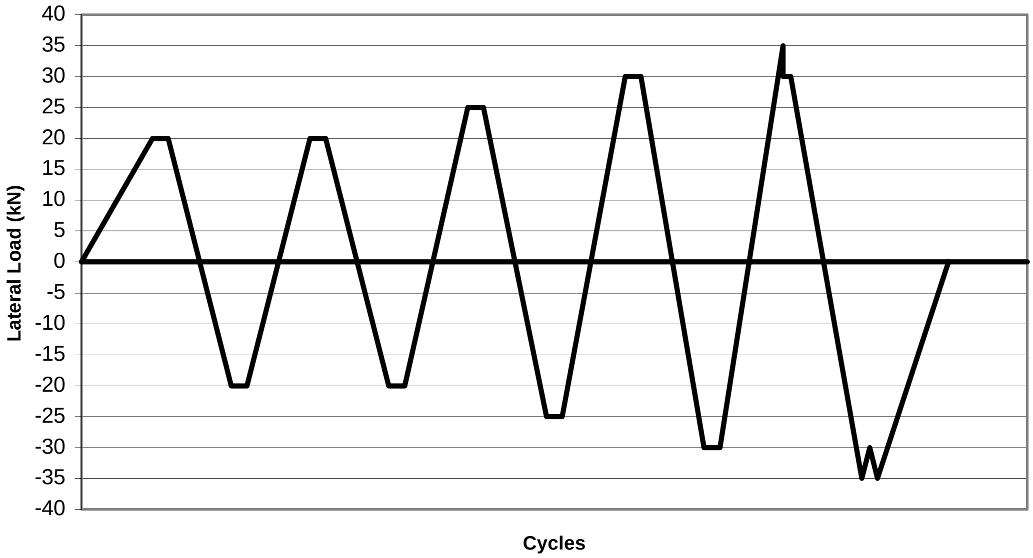

Figure 4.4 Lateral load history of test specimen SP1 for the 1st static test.

In Figure 4.5, Figure 4.6, Figure 4.7 and Figure 4.8 load-displacement curves are presented for the first, second, third and fourth stories, respectively.

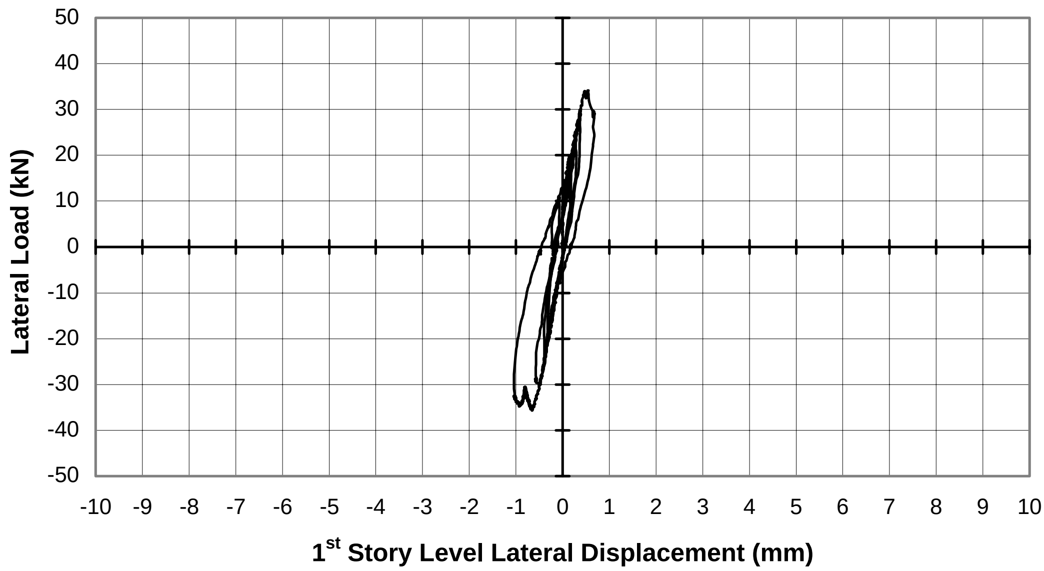

Figure 4.5 Lateral load-displacement curve of the 1st story for the 1st static test, SP1.

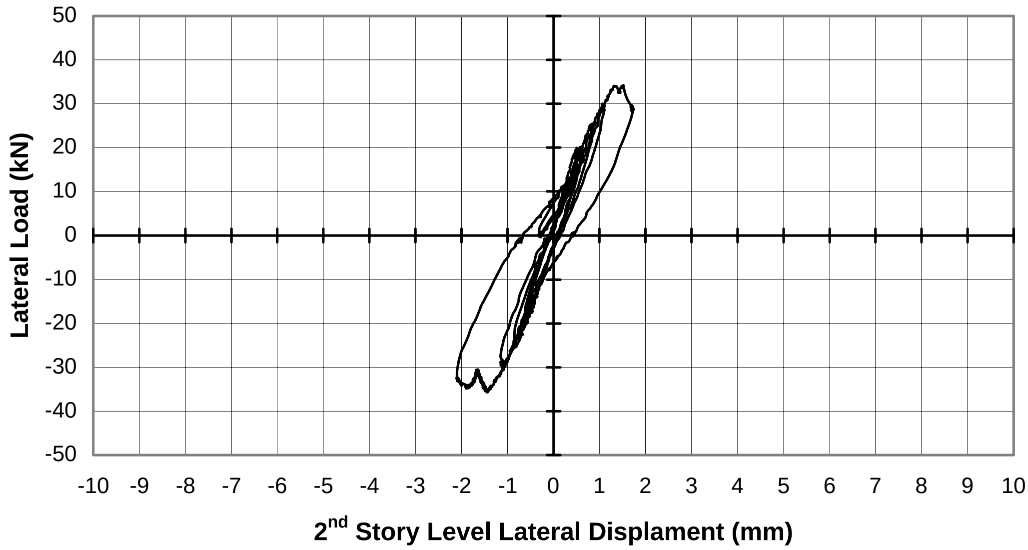

Figure 4.6 Lateral load-displacement curve of the 2nd story for the 1st static test, SP1.

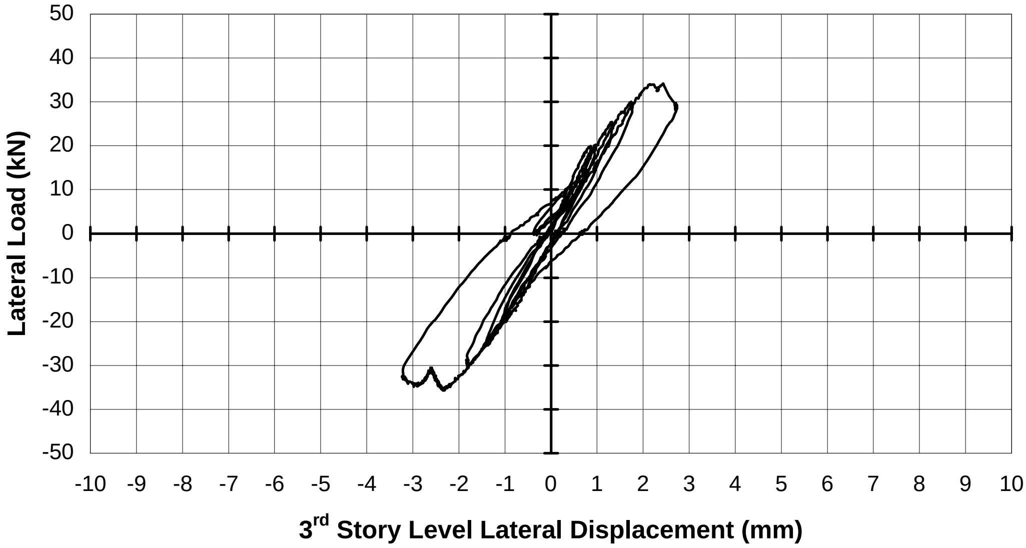

Figure 4.7 Lateral load-displacement curve of the 3rd story for the 1st static test, SP1.

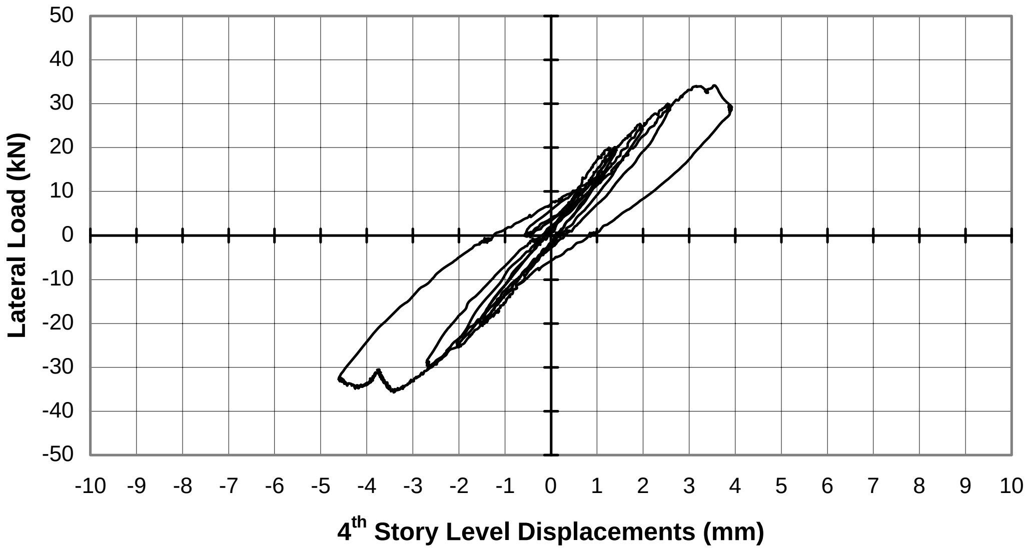

Figure 4.8 Lateral load-displacement curve of the 4th story for the 1st static test, SP1.

For the 1st static test of SP1, the top deflections are summarized in Table 4.1.

Table 4.1 Summary of the top deflection of the 1st static test of SP1.

Half cycle No	Maximum top displacement (mm)	Lateral load (kN)
1	1.27	20
-1	-1.46	-20
2	1.40	20
-2	-1.52	-20
3	1.96	25
-3	-2.00	-25
4	2.53	30
-4	-2.66	-30
5	3.89	35
-5	-4.60	-35

The maximum lateral load applied to SP1 for the 1st static test was 35 kN. At this load level, the maximum top displacement of the SP1 was 4.6 mm.

The drift ratio of each story is calculated and plotted against the applied lateral load. The displacements in these curves are relative and normalized with respect to the story height. Variations of the 1st, 2nd, 3rd, and 4th story drift ratios for the first static test of SP1 are presented in Figure 4.9, Figure 4.10, Figure 4.11 and Figure 4.12, respectively.

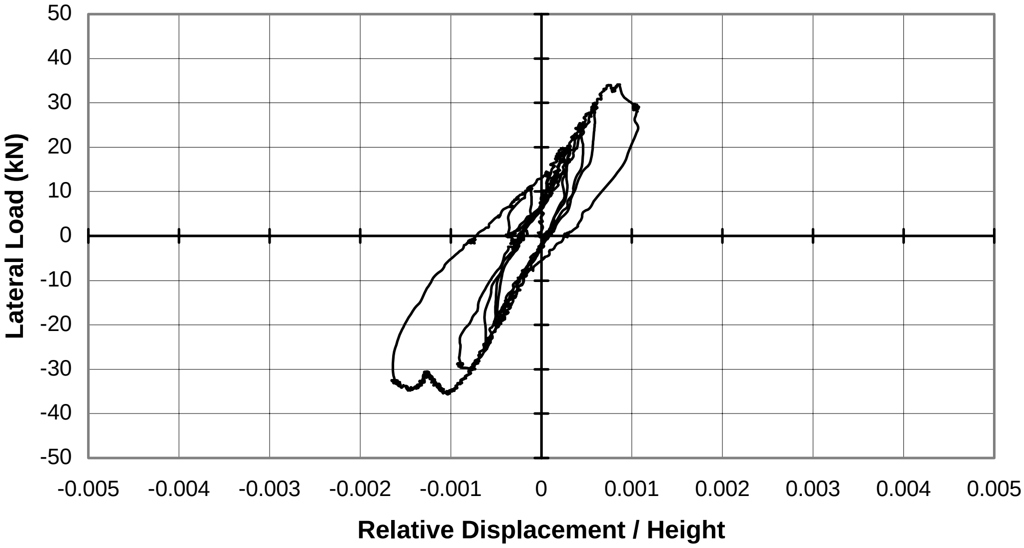

Figure 4.9 Variation of the 1st story drift ratio with the applied load, for the 1st static test, SP1.

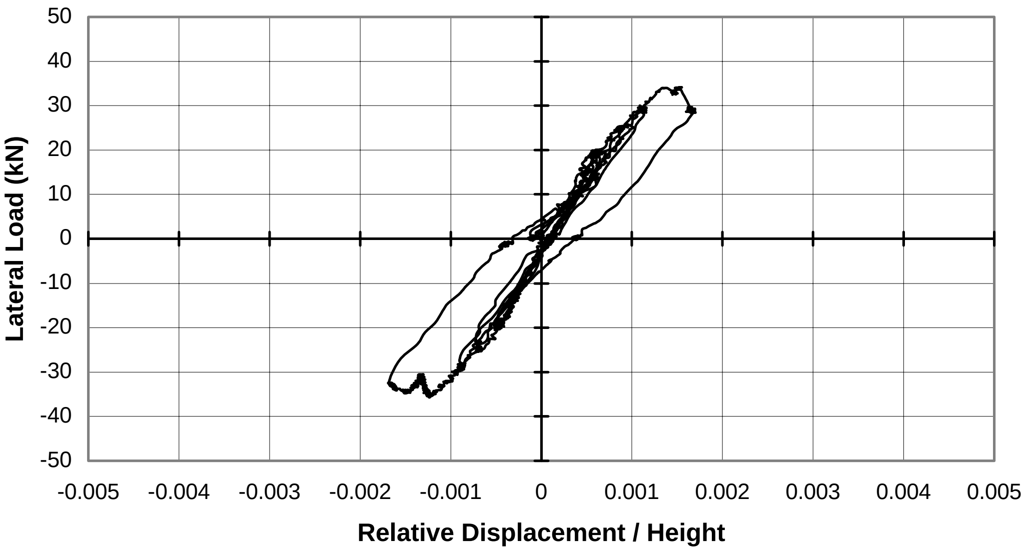

Figure 4.10 Variation of the 2nd story drift ratio with the applied load, for the 1st static test, SP1.

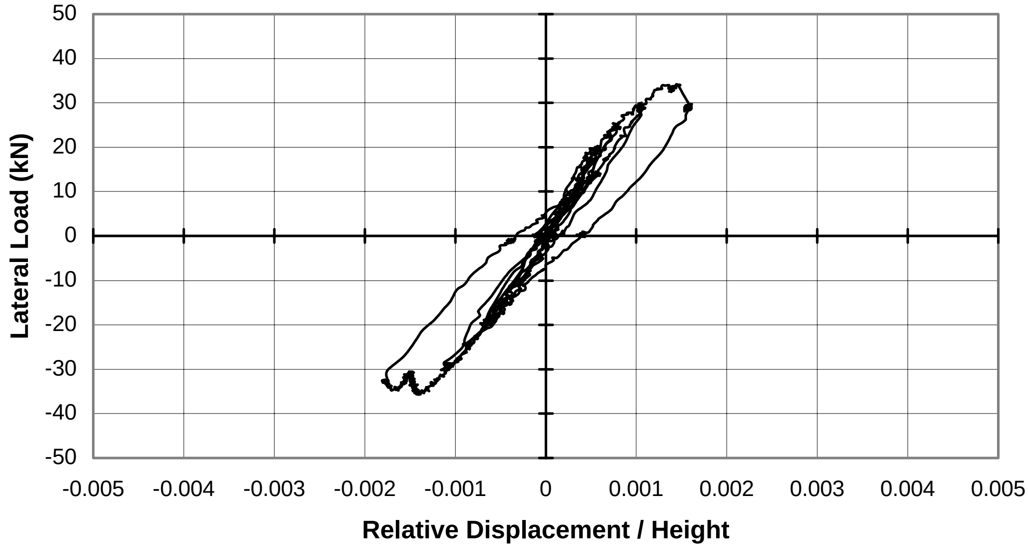

Figure 4.11 Variation of the 3rd story drift ratio with the applied load, for the 1st static test, SP1.

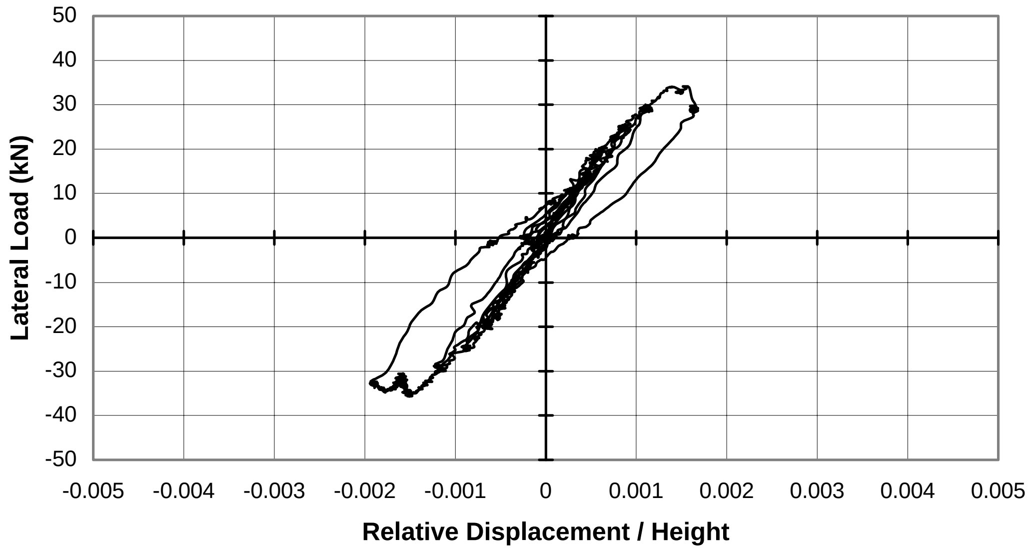

Figure 4.12 Variation of the 4th story drift ratio with the applied load, for the 1st static test, SP1.

4.2.2 Cracking Characteristics of the Undamaged SP1

In the first two cycles, SP1 was loaded up to 20 kN, then in the third, fourth and fifth cycles 25 kN, 30 kN and 35 kN lateral loads were applied to SP1, respectively. The first four cycles remained in the elastic range. While testing, observations show that all the cracks in the flange were horizontal and identical at the end of each cycle. Flange cracks propagated from the boundaries of the flange towards the centers.

In the first two cycles, SP1 was loaded up to 20 kN. The flange, which is close to the reaction wall, is defined as the north flange and the flange, which is away from the reaction wall, is defined as the south flange for the panel form test specimen, SP1. The first cracks exhibited by the structure were horizontal flexural cracks at the slab wall joint at the north flange of the first story occurring in the 1st positive half cycle when the lateral load reached 17 kN. Figure 4.13 shows crack pattern on the north flange during the 1st positive half cycle. This horizontal crack started at the left side of the wall flange and progressed toward the center. When the two cycles were completed, this crack length was 740 mm, which was approximately 655-660 mm above the foundation. Figure 4.14 shows crack pattern on the north flange during the 2nd positive half cycle.

In the second negative half cycle, a horizontal flexural crack occurred at the slab wall joint at the south flange of the first story. This horizontal crack started at the right side of the wall flange and progressed towards the center. Figure 4.15 shows the crack pattern on the south flange after the 2nd cycle finished. When the two cycles were completed, this crack length was 440 mm long, which was approximately 655-660 mm above the foundation.

In the third cycle, 25 kN lateral load was applied to the SP1. A horizontal crack was observed at the wall foundation joint at the north face of the SP1 in the third cycle. Figure 4.16 shows the crack at the foundation wall joint after the 3rd cycle finished. When the 3rd cycle was completed, the horizontal wall slab cracks progressed towards the centers in both faces of the SP1.

30 kN lateral load was applied to the SP1 at the fourth cycle. Here flange cracks at the slab wall joint at the north flange of the first story propagated from the right edge to the center of the flange and another horizontal crack started at the left edge, which propagated towards the center, and these two cracks joined in the 4^{th} positive half cycle. This crack was again 645-650 mm above the foundation level but this crack propagated from the right edge to the center of the flange. Figure 4.17 shows the crack pattern on the north flange after the 4^{th} cycle was completed. In the 4^{th} negative half cycle, a new horizontal crack started to occur at the right edge of the south flange at the first story wall-slab joint. Figure 4.18 shows the front view of the crack pattern on SP1 during the 4^{th} negative half cycle of the first static test. At this cycle also another joint crack at the second story was observed in the negative direction of this cycle. It was 330 mm long and approximately 130-132 mm above the foundation level.

At the 5^{th} cycle, the maximum applied lateral load was 35 kN in both directions. At the 5^{th} positive half cycle when the lateral load was increased up to 35 kN, the lateral load suddenly dropped to 30 kN due to the tension crack at the tension side which ran across the entire flange. This was a horizontal flexural cracking on the north flange and it was 380 mm above the foundation level. Figure 4.19 shows the crack pattern on the south flange after the 5^{th} cycle was ended. Also an inclined crack was observed at the web of SP1. Crackings on each side of the web were identical. These shear cracks were visible on both sides of the web wall. Figure 4.20 shows the crack pattern on the web after the fifth positive half cycle was over.

At the 5^{th} negative half cycle again when the lateral load reached up to 35 kN, it suddenly dropped to 30 kN due to tension crack at the south flange which comprised the entire flange. Then lateral load was then again increased to 35 kN. Figure 4.21 shows the crack pattern at the south flange after the 5^{th} negative half cycle was over. This was a horizontal flexural cracking on the south flange and it was 400 mm above the foundation level.

These horizontal flexural cracking on the north and south flanges, which were 380 mm and 400 mm above the foundation level respectively, were due to probability of defects (like voids, large aggregates, local cracks etc.) and low reinforcement ratio. Placing of the concrete of the panel form test specimens was achieved in stages, therefore, while placing and compaction of the concrete, weak construction surfaces occurred. While loading the test specimens, tension cracks occurred at these weak surfaces such as foundation wall joints and first story slab wall joints, which were 380-400 mm above the foundation level.

Figure 4.13 Crack pattern on the north flange during the 1st positive half cycle, 1st static test, SP1.

Figure 4.14 Crack pattern on the north flange during the 2nd positive half cycle, 1st static test, SP1.

Figure 4.15 Crack pattern on the south flange after the 2nd cycle finished, 1st static test, SP1.

Figure 4.16 Crack at the foundation wall joint after the 3rd cycle finished, 1st static test, SP1.

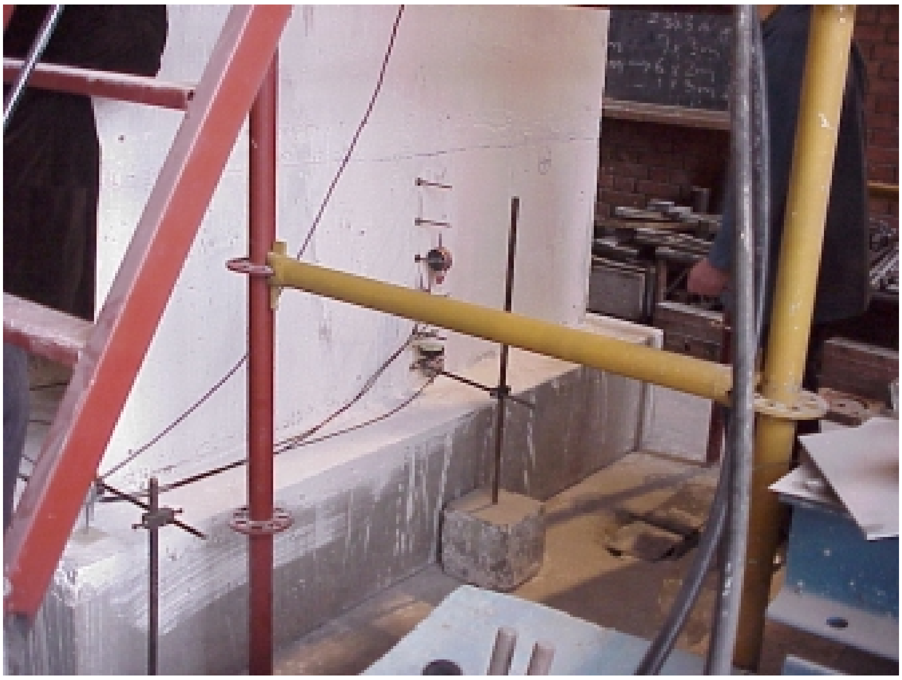

Figure 4.17 Crack pattern on the north flange after the 4th cycle finished, 1st static test, SP1.

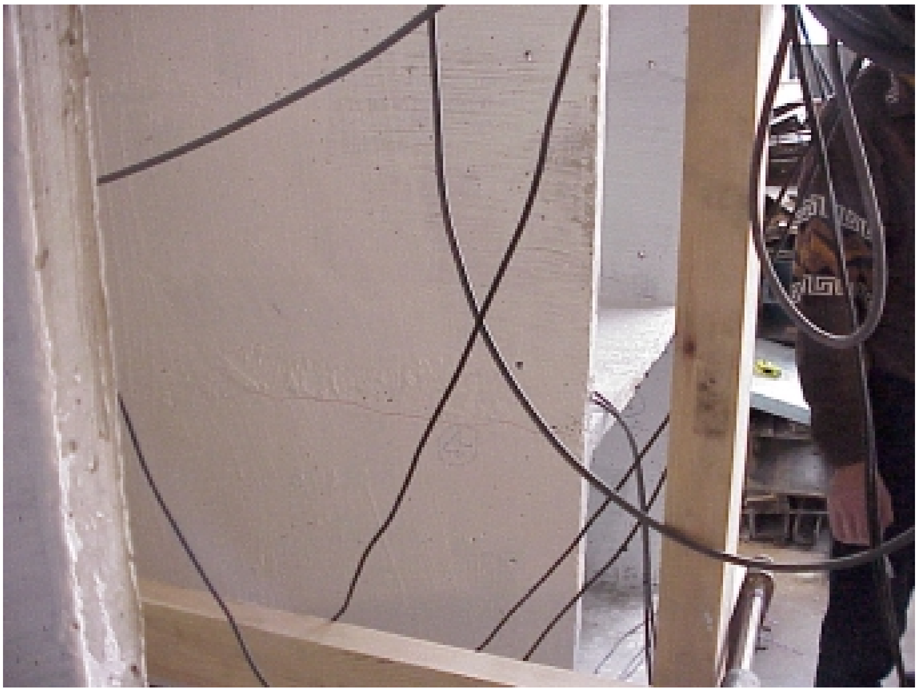

Figure 4.18 Front view of the crack pattern on SP1 during the 4th negative half cycle, 1st static test, SP1.

Figure 4.19 Crack pattern on the south flange after the 5th cycle finished, 1st static test, SP1.

Figure 4.20 Crack pattern on the web after the 5th positive half cycle finished, 1st static test, SP1.

Figure 4.21 Crack pattern at the south flange after the 5th negative half cycle finished, 1st static test, SP1.

4.3 STATIC TEST ON THE DAMAGED SPECIMEN1

After the free vibration tests were done on the damaged SP1, the reversed cyclic static test was applied again. The aim of this test was to investigate the behavior of SP1 up to the failure.

In the second static test, lateral deformations were measured by LVDTs with 50 mm strokes at the fourth, third, second and first stories. To measure possible torsional rotation, two LVDTs with 100 mm strokes were placed at the fourth story at the right and the left edges of the specimen. No appreciable torsional rotation was observed in the first static test. Average shear deformations of the walls were measured on both the first and second stories by means of diagonally placed dial gages with 50 mm strokes. For this purpose, dial gages with 50 mm strokes were used, which were located 100 mm away from the corner. The reason for choosing this location was to avoid localized effects like crushing of concrete during the experiment. Figure 4.22 shows the details of the test setup, loading system and instrumentation for SP1 for the second static test. The plan view of the test setup, loading system and instrumentation for SP1 for the second static test are given in Figure 4.23.

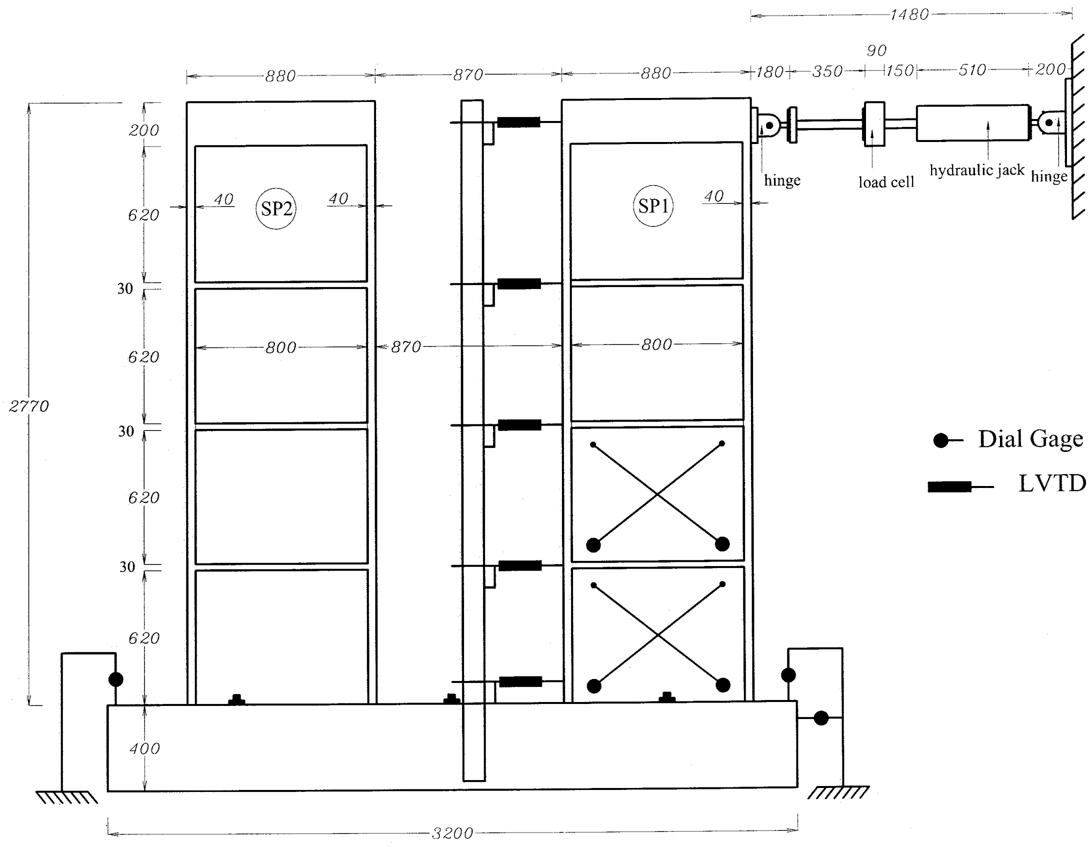

Figure 4.22 Details of the test setup, loading system and instrumentation for SP1 for the second static test.

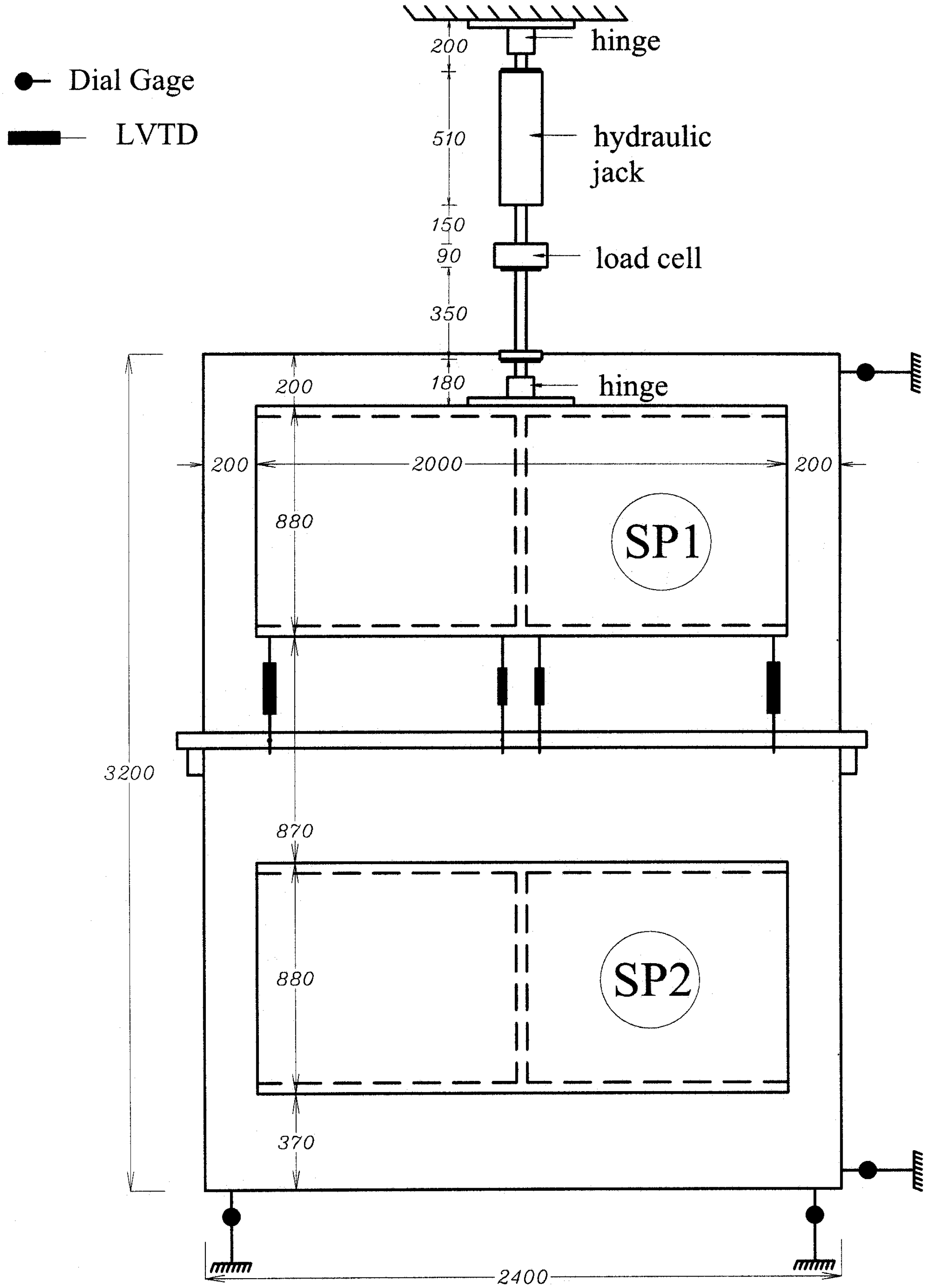

Figure 4.23 Plan view of the test setup, loading system and instrumentation for SP1 for the second static test.

4.3.1 Load-Deformation Response of the Damaged Specimen1

This section presents the response of the panel form test specimen SP1 for the second static test under the cyclic displacements as recorded.

The damaged SP1 was loaded under the lateral loading history presented in Figure 4.24. This 2nd static test was again load-controlled test that consisted of two full reversed cycles. In the first cycle 35 kN lateral load was applied to SP1. In the 2nd cycle lateral load was increased to 40 kN. These two cycles remained in the inelastic range.

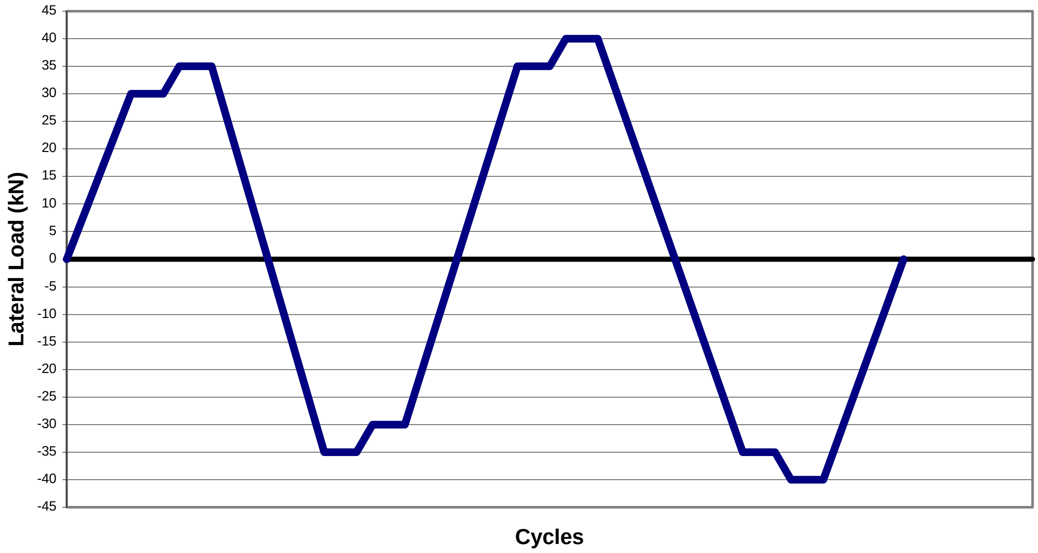

Figure 4.24 Lateral load history of test specimen SP1 for the 2nd static test.

In Figure 4.25, Figure 4.26, Figure 4.27 and Figure 4.28 load-displacement curves are presented for the first, second, third and fourth stories respectively for the 2nd static test for SP1.

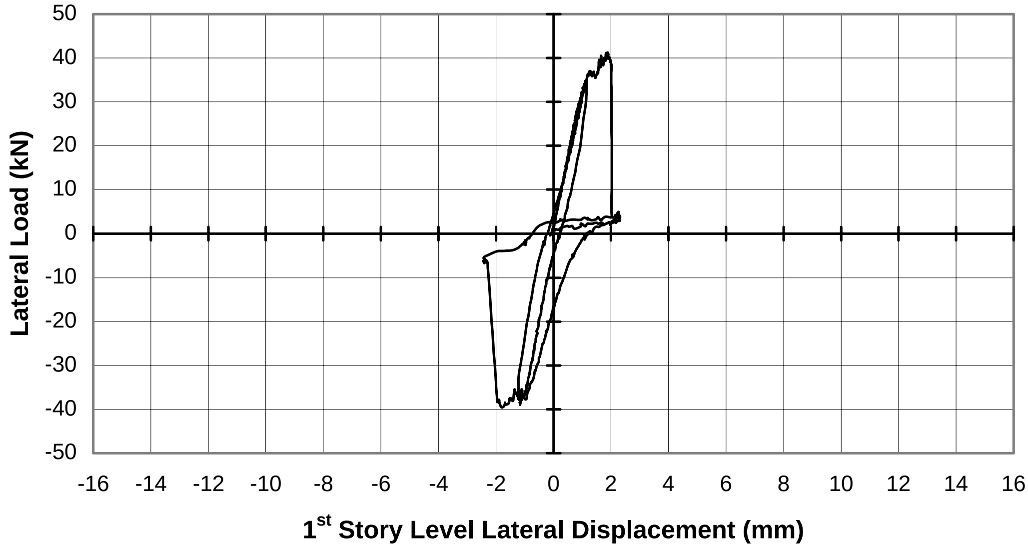

Figure 4.25 Lateral load-displacement curve of the 1st story for the 2nd static test, SP1.

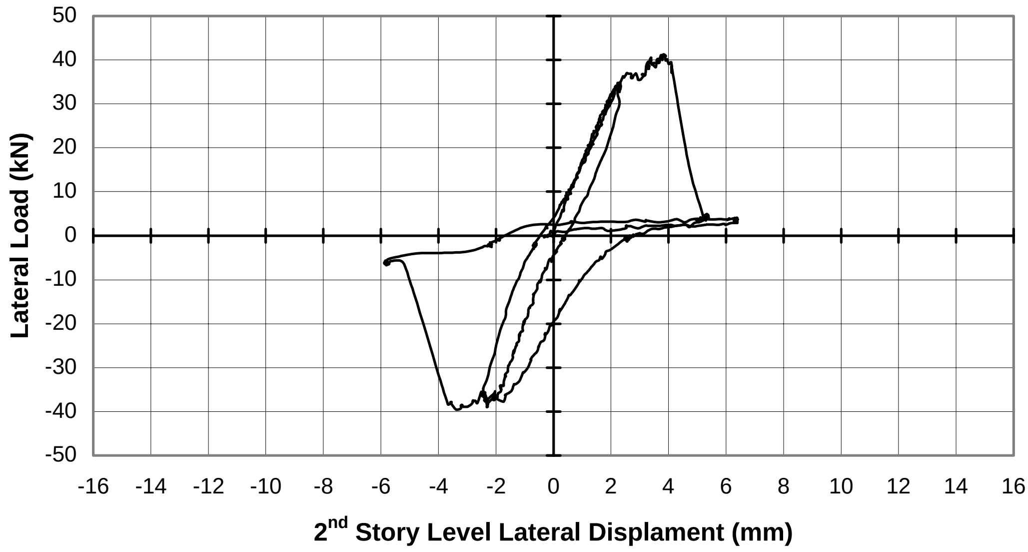

Figure 4.26 Lateral load-displacement curve of the 2nd story for the 2nd static test, SP1.

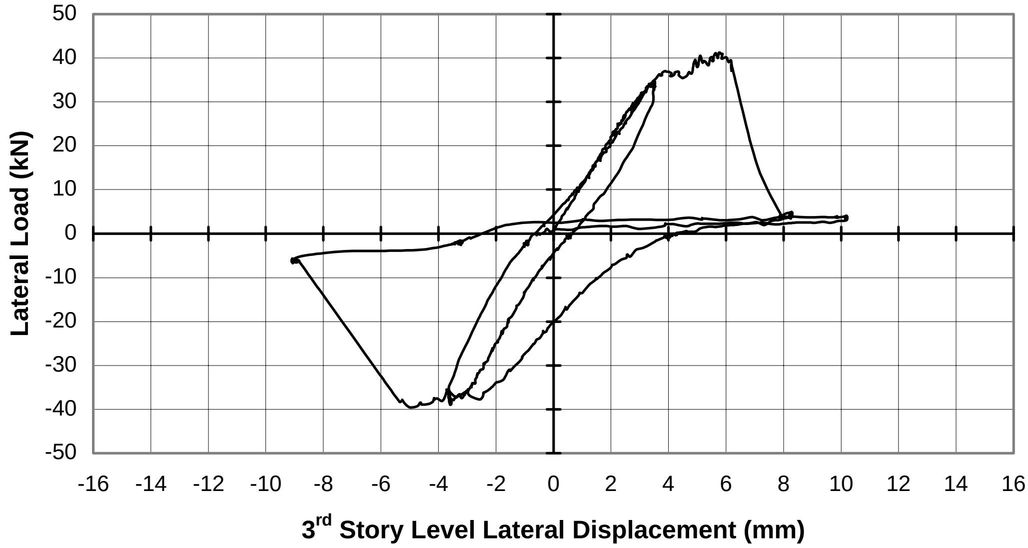

Figure 4.27 Lateral load-displacement curve of the 3rd story for the 2nd static test, SP1.

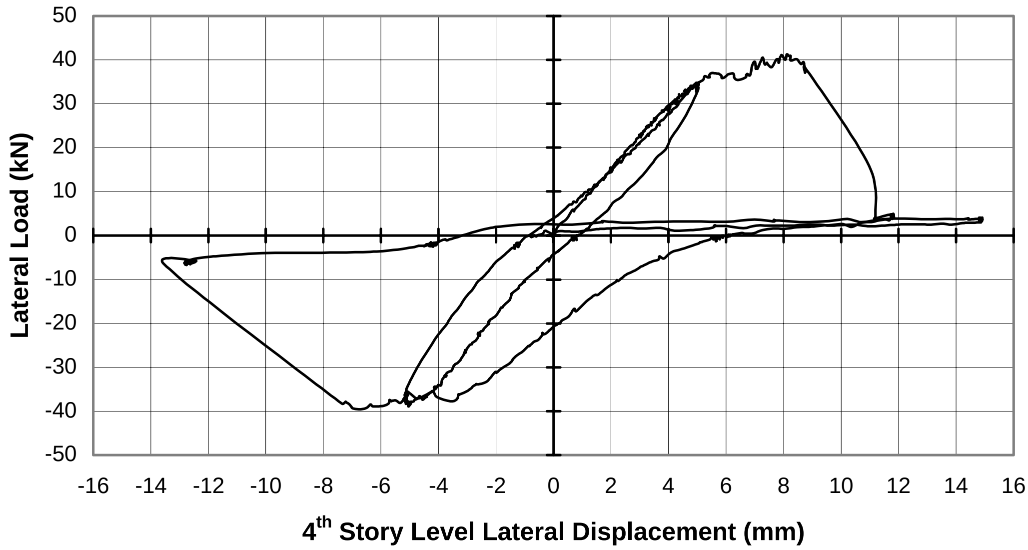

Figure 4.28 Lateral load-displacement curve of the 4th story for the 2nd static test, SP1.

For the 1st static test of SP1, the top deflections are summarized in Table 4.2. The maximum lateral load applied to SP1 for the 2nd static test was 40 kN. At this load level, the top displacement of SP1 was 8.6 mm.

Table 4.2 Summary of the top deflection of the 2nd static test of SP1.

Half cycle No	Maximum top displacement (mm)	Lateral load (kN)
1	5.32	35
-1	-5.37	-35
2	8.6	40
-2	-7.3	-40

The drift ratio of each story is calculated and plotted against the applied lateral load. Variations of the 1st, 2nd,3rd, and 4th story drift ratios for the 2nd static test of SP1 is presented in Figure 4.29, Figure 4.30, Figure 4.31 and Figure 4.32, respectively.

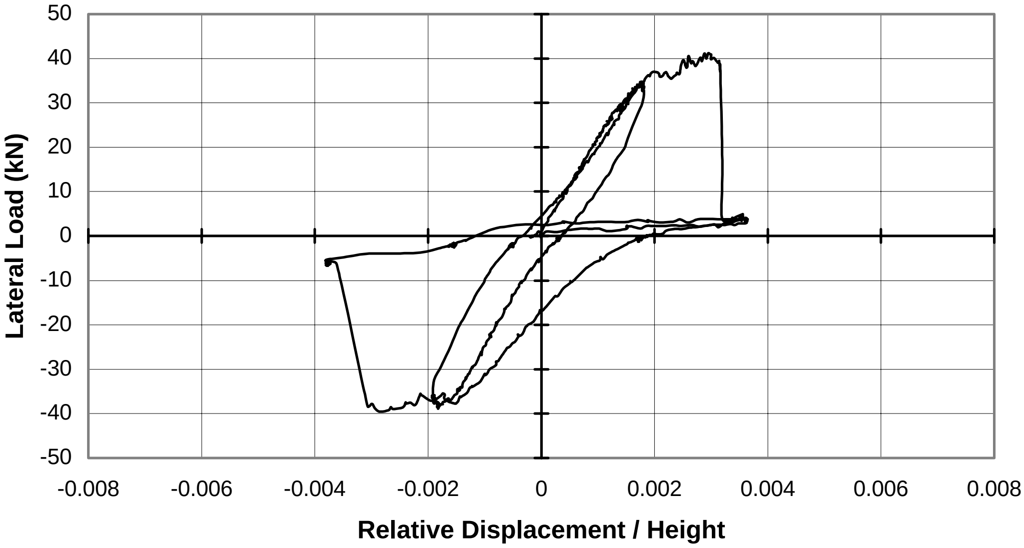

Figure 4.29 Variation of the 1st story drift ratio with the applied load, for the 2nd static test, SP1.

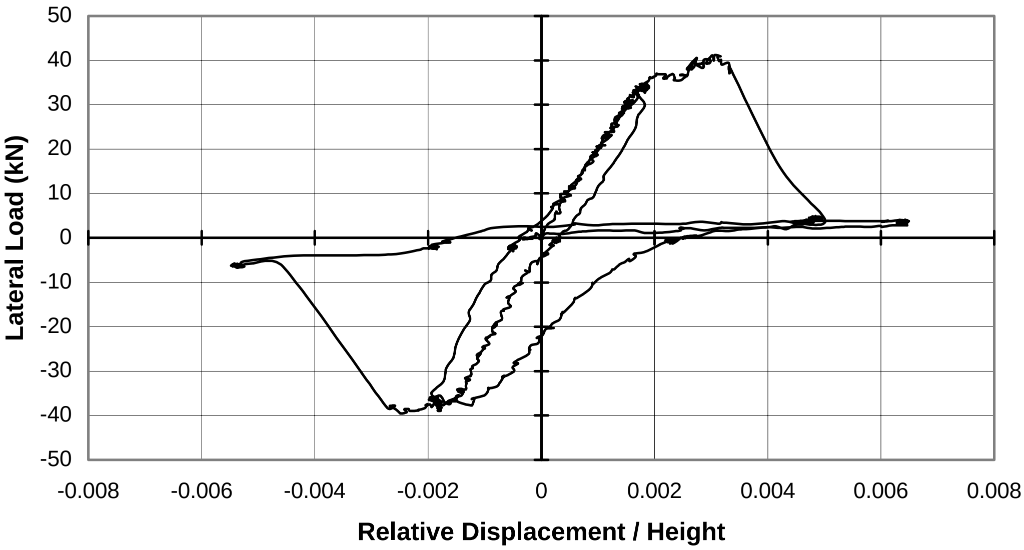

Figure 4.30 Variation of the 2nd story drift ratio with the applied load, for the 2nd static test, SP1.

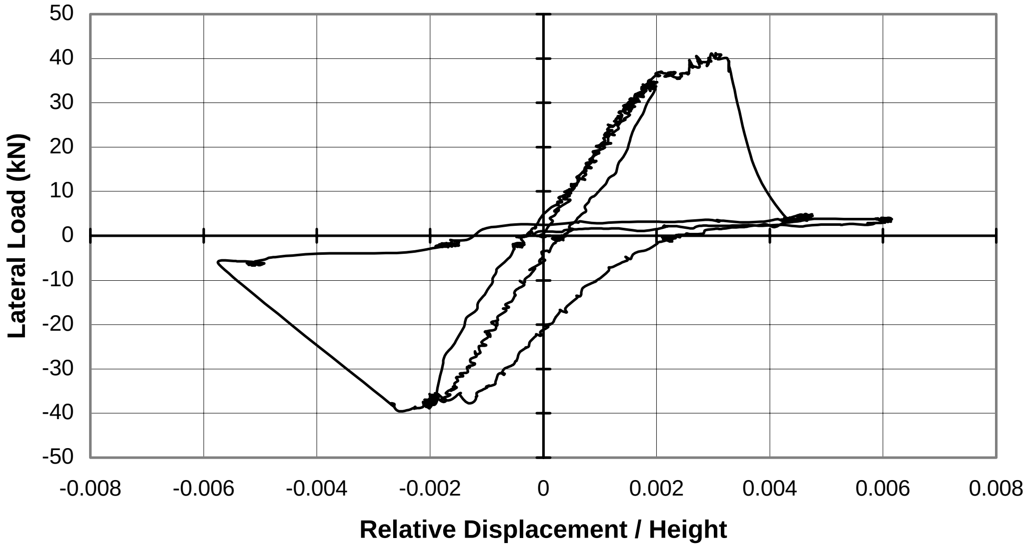

Figure 4.31 Variation of the 3rd story drift ratio with the applied load, for the 2nd static test, SP1.

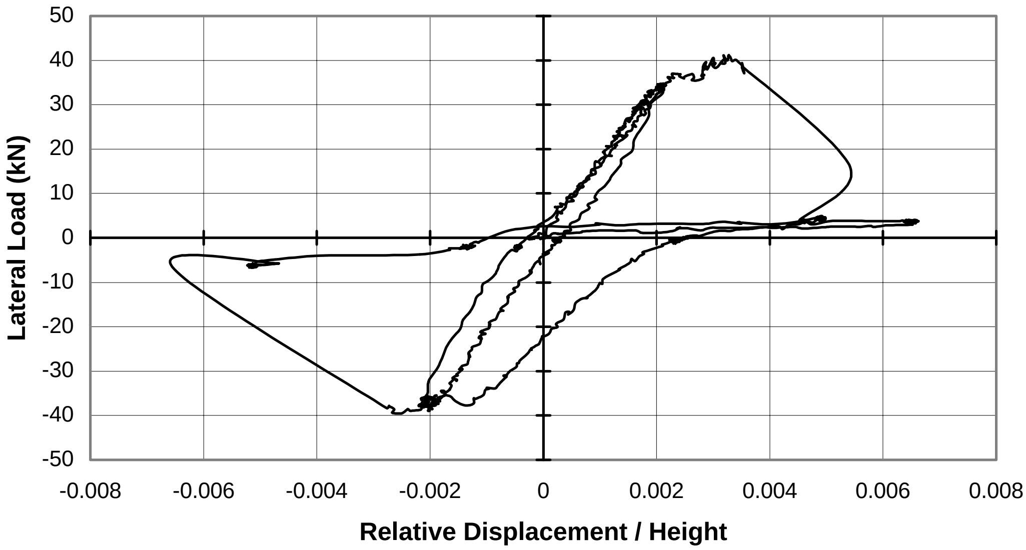

Figure 4.32 Variation of the 4th story drift ratio with the applied load, for the 2nd static test, SP1.

4.3.2 Cracking and Failure Characteristics of the Damaged SP1

The second static test was load-controlled that consisted of two full-reversed cycles. In the first cycle, 35 kN lateral load was applied to SP1. In the second cycle, lateral load was increased up to 40 kN. After the first positive half cycle, shear cracks developed at the wall web. This crack inclined 30 degrees to the horizontal. Crackings on each side of the web were identical and crackings in the flanges were essentially identical at the end of each cycle. While testing, observations show that all the cracks in the flange are horizontal.

Horizontal cracks that occurred at the north flange of SP1 in the 1st static test which were 380 mm above the foundation level of the first story wall-slab joint propagated along the entire flange and the crack width increased. Also, a new inclined shear crack occurred on the web of SP1. This shear crack was inclined 45 degrees to the horizontal and it was visible on both sides of the web wall. The photograph in Figure 4.33 depicts the state of the web wall after the 1st positive half cycle.

In the 1st negative half cycle, lateral load was again increased up to 35 kN. In the 1st positive half cycle, 35 kN lateral load was applied to SP1. In the 1st static test, the horizontal crack which occurred 400 mm above the foundation level of the 1st story wall-slab joint at the south flange of SP1 propagated along the entire south flange. These crack widths increased. Also a new horizontal flange crack occurred 160 mm above the foundation level at the south flange. At the end of this cycle, this crack ran across the entire south flange. An inclined shear crack occurred on the web of the specimen. This shear crack was visible on both sides of the web wall. Figure 4.34 shows the crack pattern on the web after the 1st negative half cycle was completed.

At the 2nd positive half cycle, the maximum applied load was 40 kN. In this cycle a new horizontal flexural crack at the north flange occurred 490 mm above the foundation level when the horizontal lateral load was just more than 35 kN. When the lateral load was increased up to 40 kN all the reinforcement ruptured suddenly 380 mm above the foundation level at the north flange. Figure 4.35 shows the crack pattern at the north flange at the end of the 2nd positive half cycle.

At the 2nd negative half cycle, lateral load increased up to 40 kN. When the horizontal lateral load was just more than 35 kN, a horizontal flexural crack 420 mm above the foundation level occurred at the south flange of SP1. This horizontal flange crack occurred at the right edge of the flange and propagated towards the center. The crack length was 480 mm. When the lateral load reached 40 kN, all the reinforcement in the south flange ruptured suddenly 380 mm above the foundation level. Figure 4.36 shows the crack pattern at the south flange when the 2nd negative half cycle ended. Figure 4.37 shows the crack pattern on the web of SP1 after the 2nd negative half cycle. At this stage, the second static test for the damaged SP1 was over.

The failure of SP1 was due to the rupturing of the longitudinal reinforcement bars in the flange. The failure was very unpredictable and brittle. In the 2nd positive half cycle when the lateral load reached up to 40 kN, all the longitudinal reinforcement in the north flange ruptured 380 mm above the foundation level. Figure 4.39 shows the photograph of the reinforcement rupturing at the north flange of SP1 after the 2nd static test. In the 2nd negative half cycle, again all the longitudinal reinforcement in the south flange ruptured 380 mm above the foundation level at the lateral load level of 40 kN. Figure 4.40 shows the photograph of the reinforcement rupturing at the south flange of SP1 after the 2nd static test. All the mesh reinforcement in the flange ruptured below the welded points of the longitudinal and the horizontal reinforcement. Crushing of the concrete was not observed in the static tests of SP1.

The moment at the failure surface, which was approximately 400 mm above the foundation level, was 85% of the maximum moment. Deformation was accumulated on the failure surface. If the reinforcement ratio had been higher, it might have prevented the failure at the cracking location. More horizontal cracks might have occurred near or at the maximum moment regions. Due to low longitudinal reinforcement ratio, as soon as the concrete cracked at the weak surface, longitudinal reinforcements yielded and ruptured at these crack surfaces. If the longitudinal reinforcement ratio had been higher, longitudinal reinforcement would not have yielded and ruptured as soon as concrete cracked 380-400 mm above the foundation and new horizontal cracks would have occurred near or at the maximum moment regions. Plastic hinge and crushing of concrete would have occurred according to the amount of longitudinal reinforcement ratio. The failure of SP1 would have been at the maximum moment region.

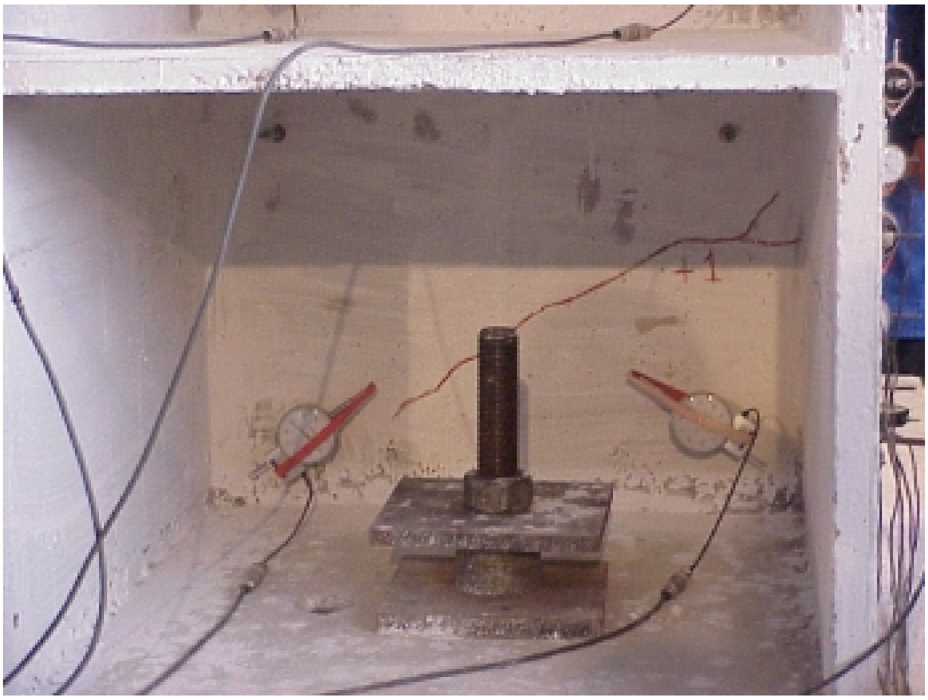

Figure 4.33 Crack pattern on the web after the 1st positive half cycle finished, 2nd static test, SP1.

Figure 4.34 Crack pattern on the web after the 1st negative half cycle finished, 2nd static test, SP1.

Figure 4.35 Crack pattern at the north flange after the 2nd positive half cycle finished, 2nd static test, SP1.

Figure 4.36 Crack pattern at the south flange after the 2nd negative half cycle finished, 2nd static test SP1.

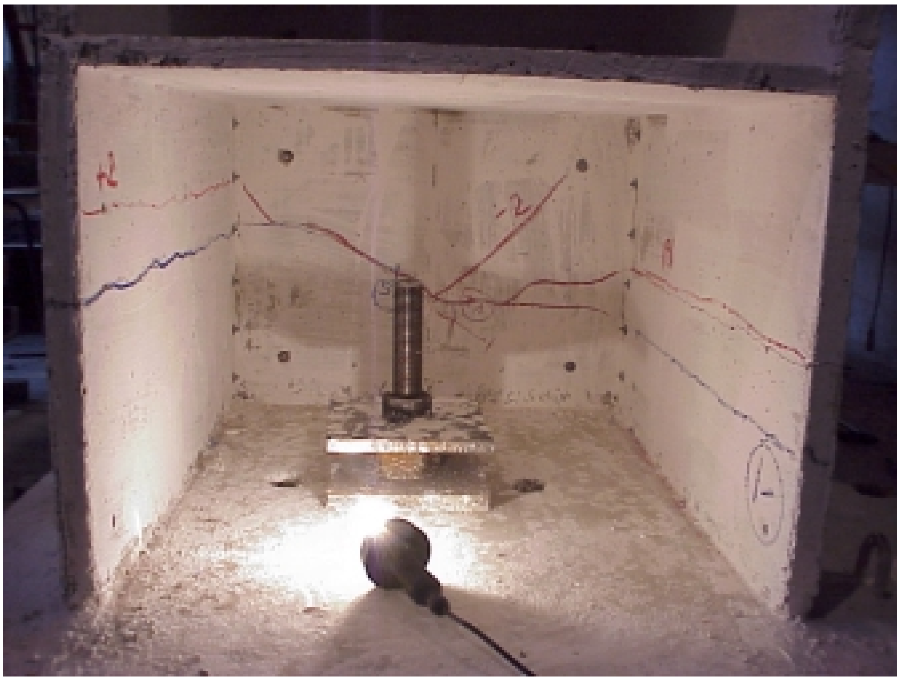

Figure 4.37 Crack pattern on the web of SP1 after the 2nd negative half cycle, 2nd static test.

Figure 4.38 Photograph of the reinforcement rupturing at the north flange of SP1 after the 2nd static test.

Figure 4.39 Photograph of the reinforcement rupturing at the south flange of SP1 after the 2nd static test.

CHAPTER 5

TEST RESULTS AND OBSERVED BEHAVIOR OF SPECIMEN2

5.1 INTRODUCTION

This chapter summarizes the instrumentation on SP2 for the first and second static tests, qualitative and quantitative experimental results. The same instrumentation technique was used on SP2 as used on SP1 explained in Chapter 4.1.

5.2 STATIC TEST ON THE UNDAMAGED SPECIMEN2

Before investigation on the elastic behavior of SP2, free vibration tests on the undamaged SP2 were done. After that, reversed cyclic test was applied to SP2.

In the first static test, lateral deformations were measured by dial gages with two 20 mm strokes at the fourth story and dial gages with 10 mm strokes at the third, second and first stories. Due to the importance of the fourth story, for lateral displacement measurements, two 20 mm strokes dial gages were placed at the fourth story. Average shear deformations of the walls were measured on the first story walls by means of diagonally placed dial gages with 50 mm strokes. Dial gages were located 100 mm away from the corners. The reason for choosing this location was to avoid localized effects like crushing of concrete during the experiment. Figure 5.1 shows a general view of the test setup, loading system, instrumentation, reaction wall and data acquisition system for SP2 for the first static test. Figure 5.2 shows the details of the test setup, loading system and instrumentation for SP2 for the first static test. Plan view of the test setup, loading system and instrumentation for SP2 for the first static test is given in Figure 5.3.

Figure 5.1 A general view of the test setup, loading system, instrumentation, reaction wall and data acquisition system for SP2 for the 1st static test.

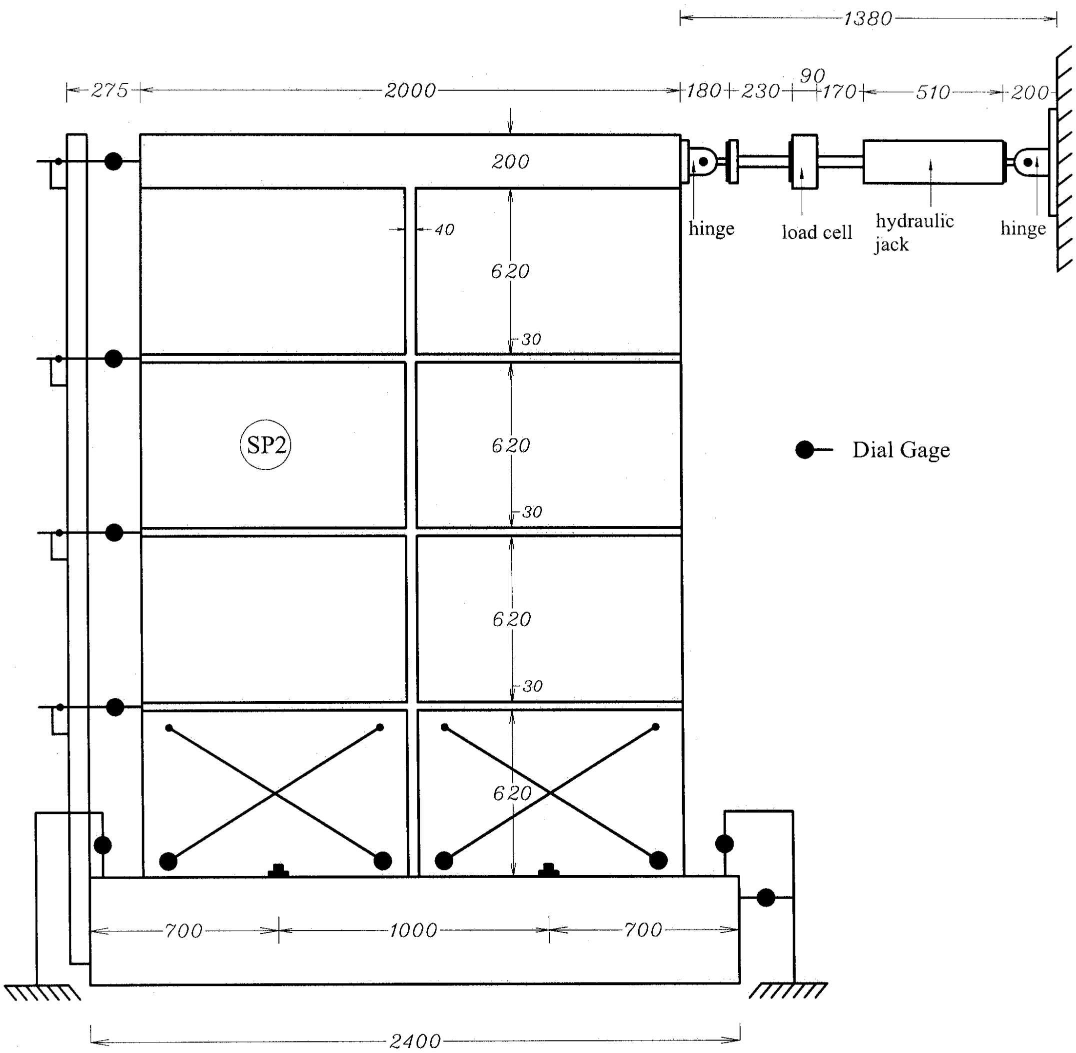

Figure 5.2 Details of the test setup, loading system and instrumentation for SP2 for the 1st static test.

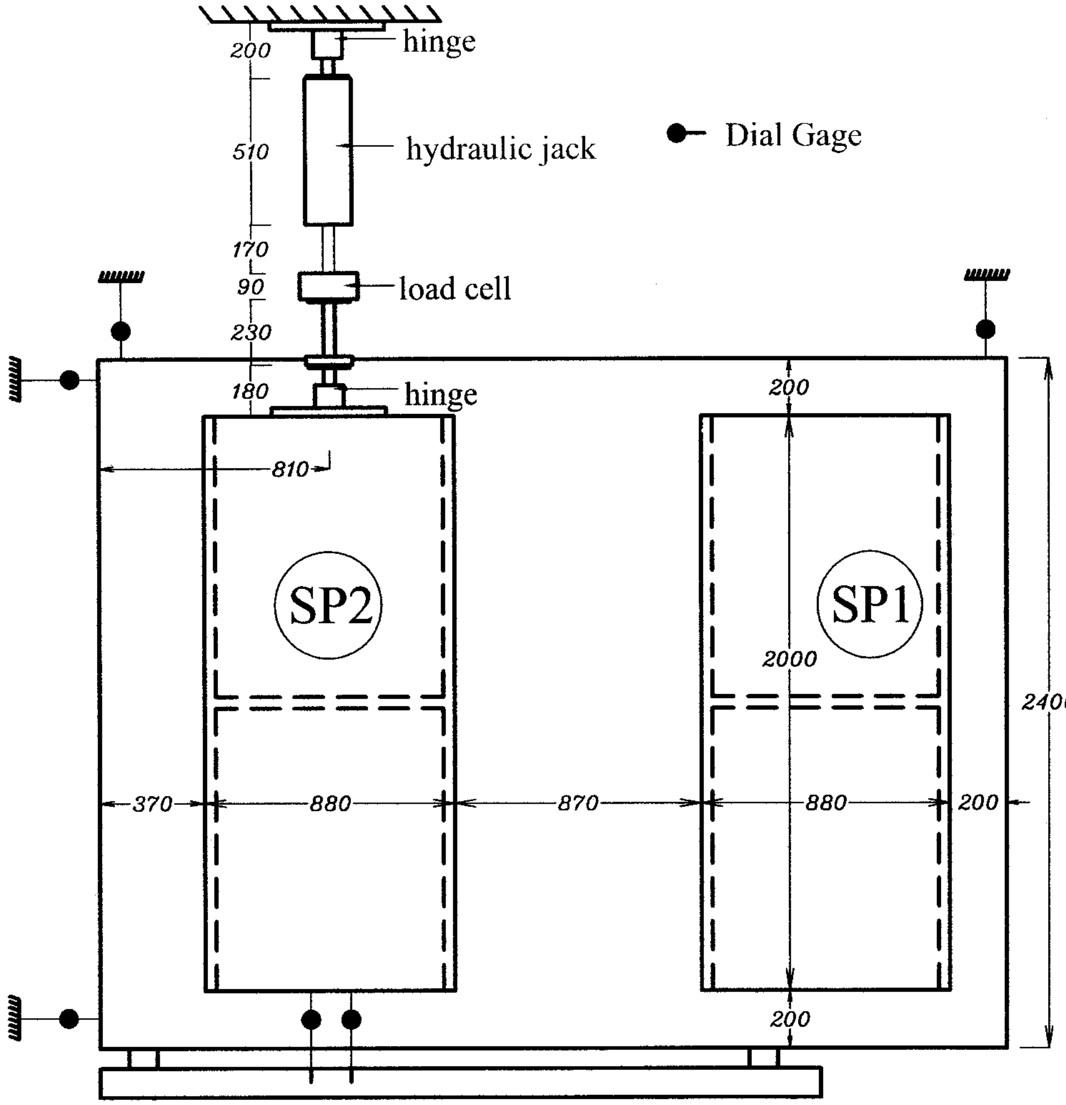

Figure 5.3 Plan view of the test setup, loading system and instrumentation for SP2 for the 1st static test.

5.2 1 Load-Deformation Response of the Undamaged Specimen2

This section presents the response of the panel form test specimen SP2 for the first static test under the cyclic displacements. The undamaged SP2 was loaded under the lateral loading history presented in Figure 5.4. This 1st static test was load-controlled test that consisted of five full reversed cycles. In the first cycle 10 kN lateral load was applied to SP2, then the load was increased by 5 kN in each cycle up to 30 kN.

The maximum lateral load applied to SP2 for the first static test was 33 kN. At this load level, the top displacement of SP2 was 1.142 mm. In Figure 5.5, Figure 5.6, Figure 5.7 and Figure 5.8 load-displacement curves are presented for the 1st, 2nd, 3rd and 4th stories, respectively.

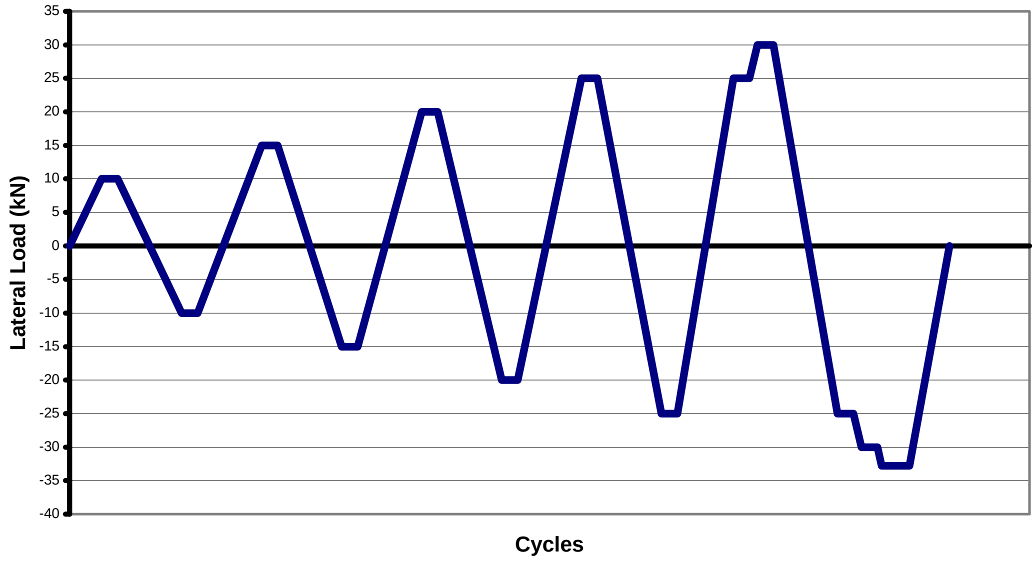

Figure 5.4 Lateral load history of the test specimen SP2 for the 1st static test.

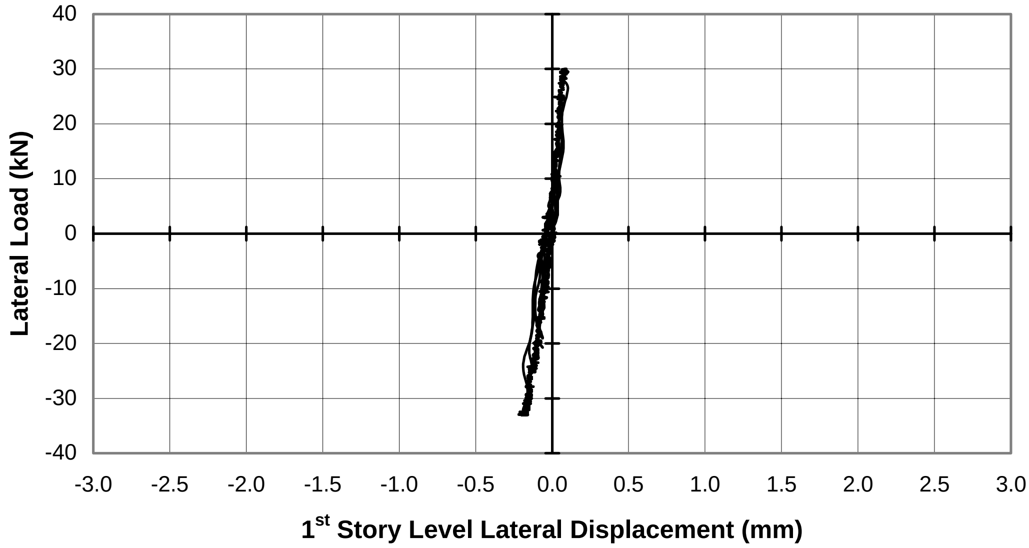

Figure 5.5 Lateral load-displacement curve of the 1st story for the 1st static test, SP2.

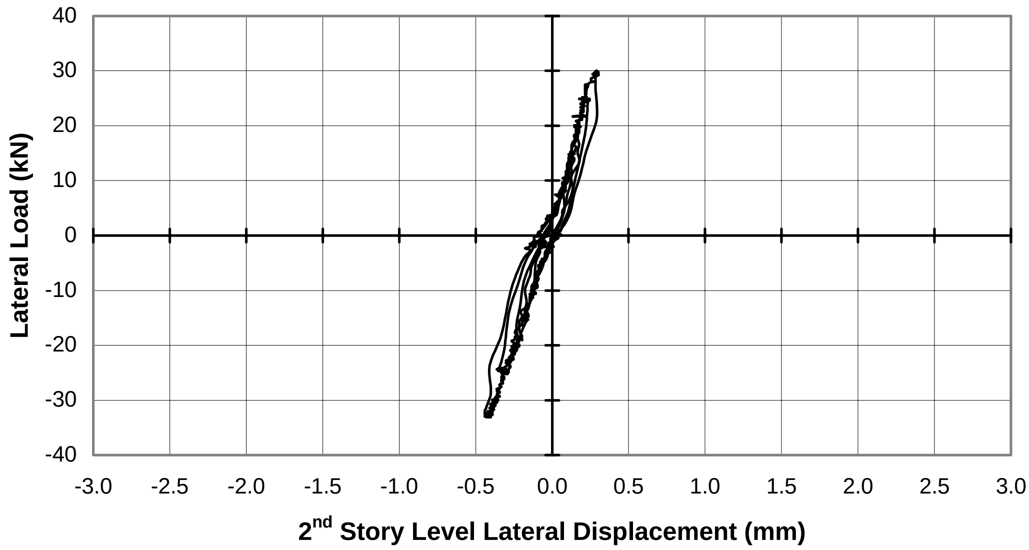

Figure 5.6 Lateral load-displacement curve of the 2nd story for the 1st static test, SP2.

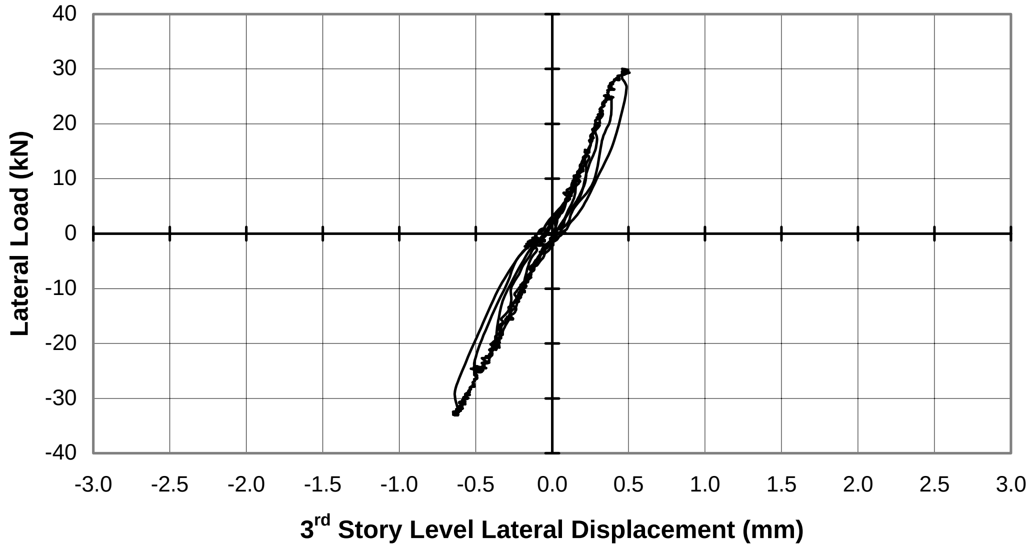

Figure 5.7 Lateral load-displacement curve of the 3rd story for the 1st static test, SP2.

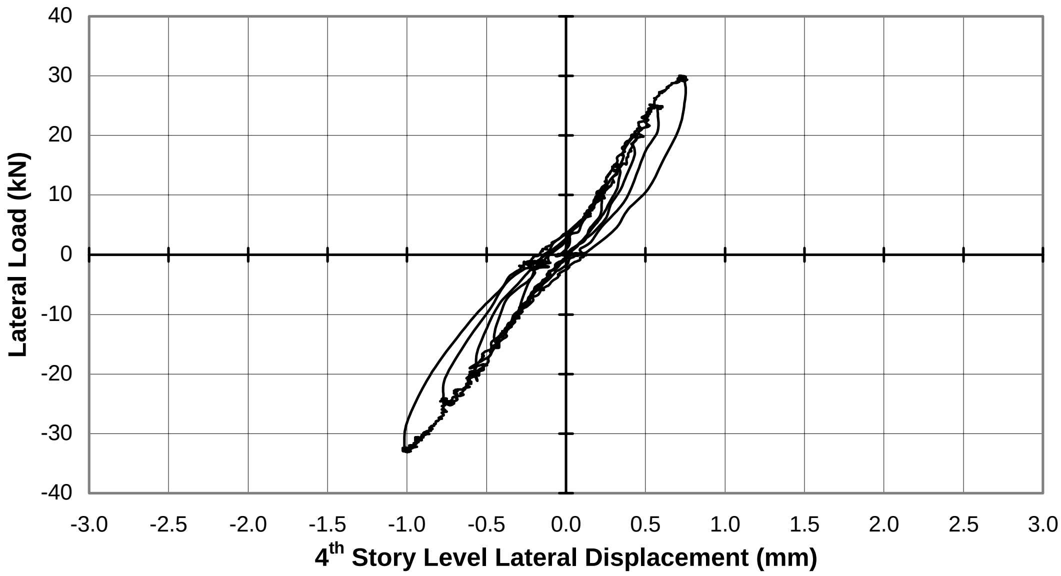

Figure 5.8 Lateral load-displacement curve of the 4th story for the 1st static test, SP2.

For the 1st static test of SP2 the top deflections are summarized in Table 5.1. The maximum lateral load applied to SP2 for the 2nd static test was 30 kN. At this load level, the top displacement of SP2 was 1.016 mm.

Table 5.1 Summary of the top deflection of the 1st static test of SP2.

Half cycle No	Maximum top displacement (mm)	Lateral load (kN)
1	0.234	10.0
-1	-0.322	-10.0
2	0.352	15.0
-2	-0.498	-15.0
3	0.498	20.0
-3	-0.664	-20.0
4	0.654	25.0
-4	-0.830	-25.0
5	0.810	30.0
-5	-1.016	-30.0

The drift ratio of each story is calculated and plotted against the applied lateral load. Variations of the 1st, 2nd, 3rd, and 4th story drift ratios for the first static test of SP2 are presented in Figure 5.9, Figure 5.10, Figure 5.11 and Figure 5.12, respectively.

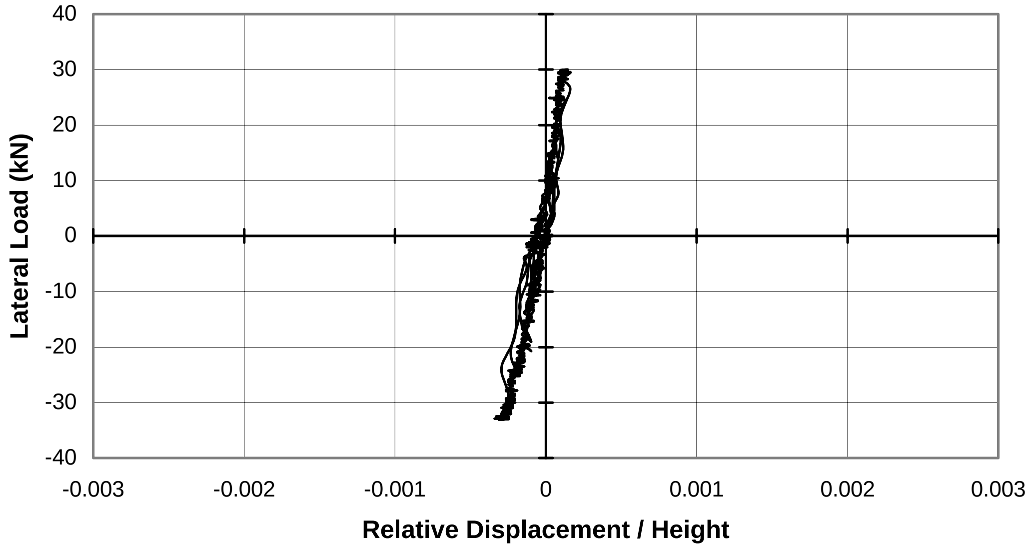

Figure 5.9 Variation of the 1st story drift ratio with the applied load, for the 1st static test, SP2.

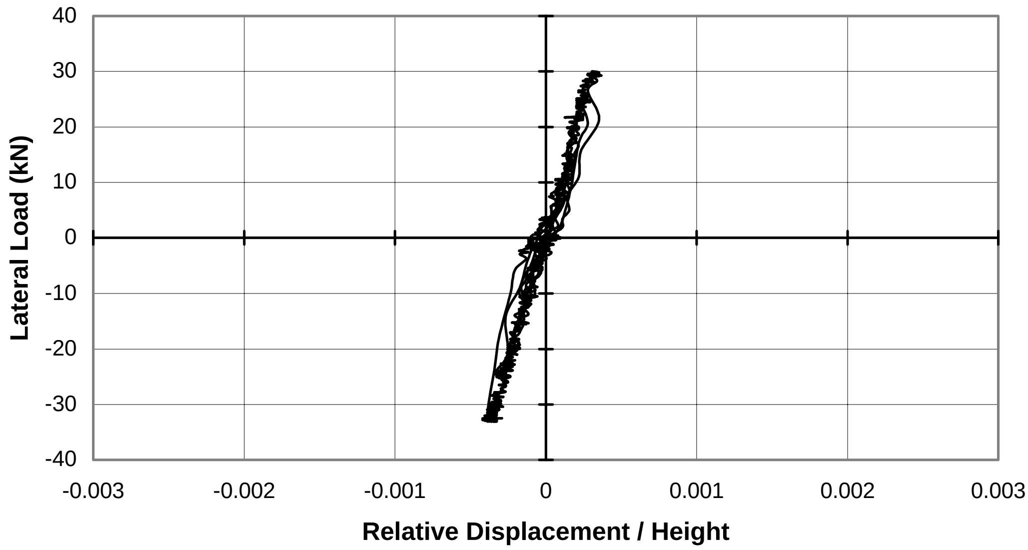

Figure 5.10 Variation of the 2nd story drift ratio with the applied load, for the 1st static test, SP2.

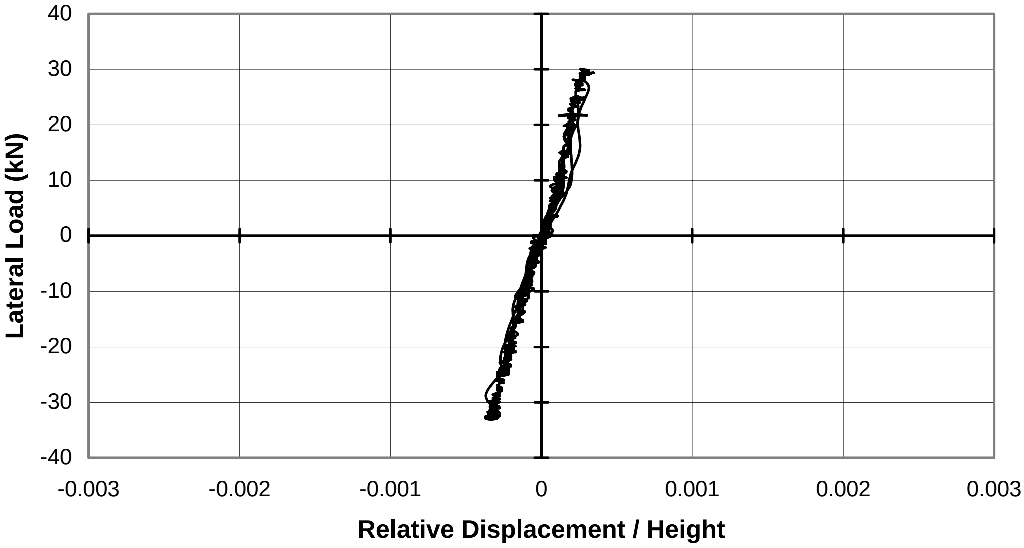

Figure 5.11 Variation of the 3rd story drift ratio with the applied load, for the 1st static test, SP2.

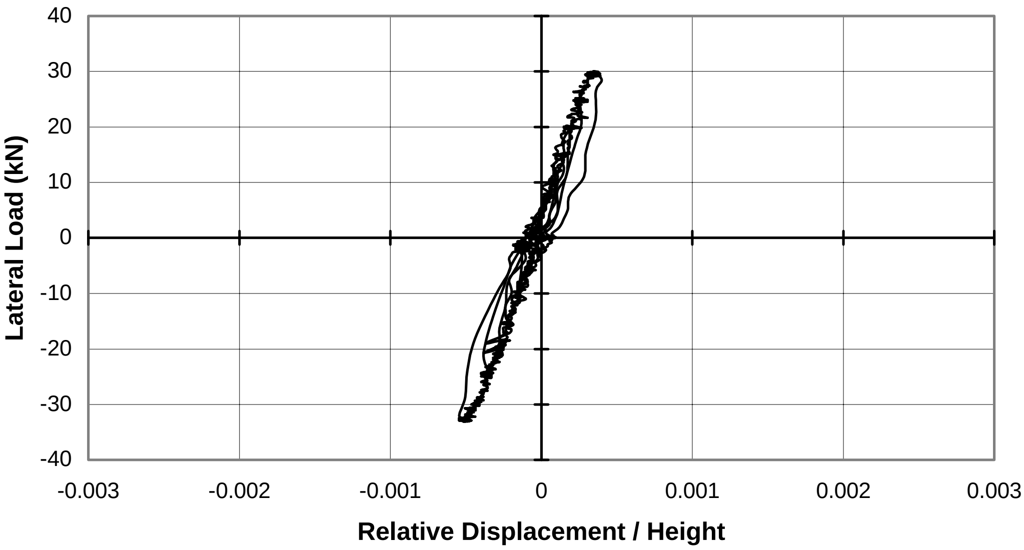

Figure 5.12 Variation of the 4th story drift ratio with the applied load, for the 1st static test, SP2.

5.2.2 Cracking and Crushing Characteristics of the Undamaged Specimen2

Cracking in the flanges were essentially identical at the end of each cycle. While testing, observations show that all the cracks in the flanges were horizontal. Flange cracks propagated from the boundaries of the flange towards centers. All five cycles remained in the linear elastic range. Applied lateral loads were 10 kN, 15 kN, 20 kN, 25 kN, and 30 kN for the 1st, 2nd, 3rd, 4th, and 5th cycles, respectively, for the first static test of SP2.

In the second cycle, SP2 was loaded up to 15 kN. The first cracks exhibited by the structure were horizontal flexural cracks at the foundation wall joint of both flanges at the tension side. These horizontal cracks were hairline cracks that started at the tension side of the wall flange and propagated towards the center. Crack pattern at the foundation-wall joint after the 2nd positive half cycle for the 1st static test on SP2 is shown in Figure 5.13. When the two cycles were completed, this crack occurred also at the other edges. These horizontal cracks started to occur at the edges of the wall flange and propagated towards the center.

At the 3rd cycle 20 kN lateral load was applied to SP2. The crack at the foundation-wall joint propagated towards the center of SP2. Crack patterns at the foundation-wall joint after the 3th positive and negative half cycles are shown in Figures 5.14 and 5.15, respectively, for the 1st static test on SP2.

25 kN lateral load was applied to SP2 at the fourth cycle. When the 4th cycle was completed the horizontal foundation wall cracks propagated towards the center in both faces of SP2. The first four cycles remained in the linear elastic range.

At the 5th positive half cycle 30 kN lateral load was applied. At the 5th positive half cycle while lateral load was just more than 25 kN, a sudden tension crack occurred at the 1st story wall-slab construction joint and lateral load stayed constant, then lateral load was increased up to 30 kN. This flexural crack occurred at the slab-wall construction joint at the tension side. It started to occur at the tension side at the boundaries of SP2 and propagated towards the center. The crack pattern at the first story slab-wall joint after the 5th positive half cycle for the 1st static test on

SP2 is shown in Figure 5.16. At the negative 5th half cycle the maximum applied lateral load was 32.65 kN. At the 5th negative half cycle when the lateral load was just more than 25 kN again a tension crack occurred at the tension side at the1st story wall-slab construction joint. When the lateral load was more than 30 kN the tension crack propagated through neutral axis and when the lateral load reached 32.8 kN the 1st static test was ended.

Figure 5.13 Crack pattern at the foundation-wall joint after the 2nd positive half cycle for the 1st static test on SP2.

Figure 5.14 Crack pattern at the foundation-wall joint after the 3rd positive half cycle for the 1st static test on SP2.

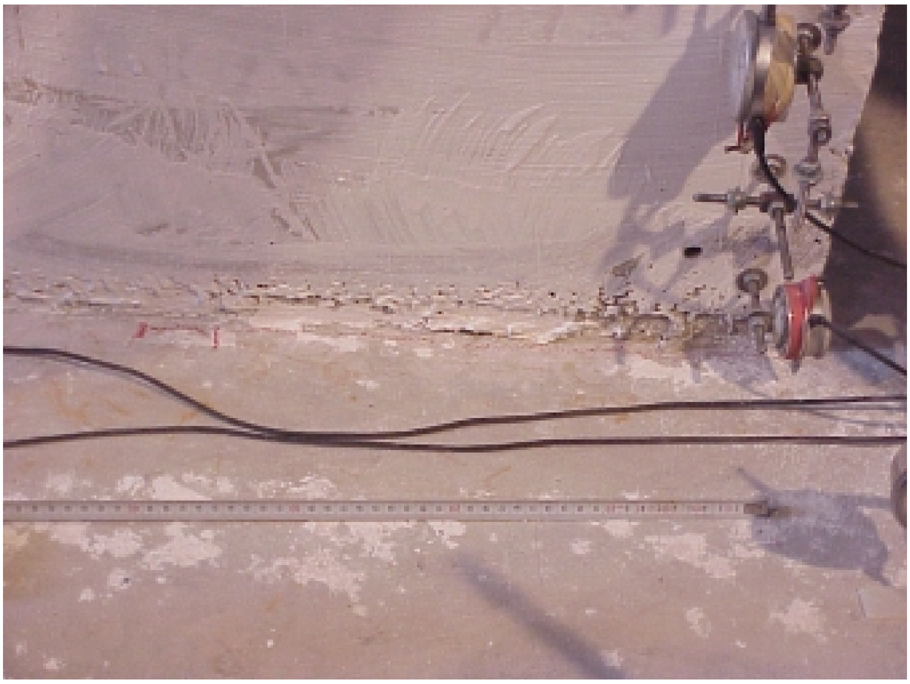

Figure 5.15 Crack pattern at the foundation-wall joint after the 3rd negative half cycle for the 1st static test on SP2.

Figure 5.16 Crack pattern at the first story slab-wall joint after the 5th negative half cycle for the 1st static test on SP2.

5.3 STATIC TEST ON THE DAMAGED SPECIMEN2

After the free vibration tests were done on the damaged SP2, the reversed cyclic static test was applied again. The aim of this test was to investigate the behavior of SP2 up to failure.

In the 2nd static test lateral deformations were measured by LVDTs with 50 mm strokes at the 4th, 3rd, 2nd and 1st stories. Average shear deformations of the walls were measured on both the first and second stories by means of diagonally placed dial gages with 50 mm strokes. For this purpose, dial gages with 50 mm strokes were used. Dial gages were located 100 mm away from the corner. The reason for choosing this location was to avoid localized effects like crushing of concrete during the experiment. Figure 5.17 shows the details of the test setup, loading system and instrumentation for SP2 for the 2nd static test. The plan view of the test setup, loading system and instrumentation for SP2 for the 2nd static test are given in Figure 5.18.

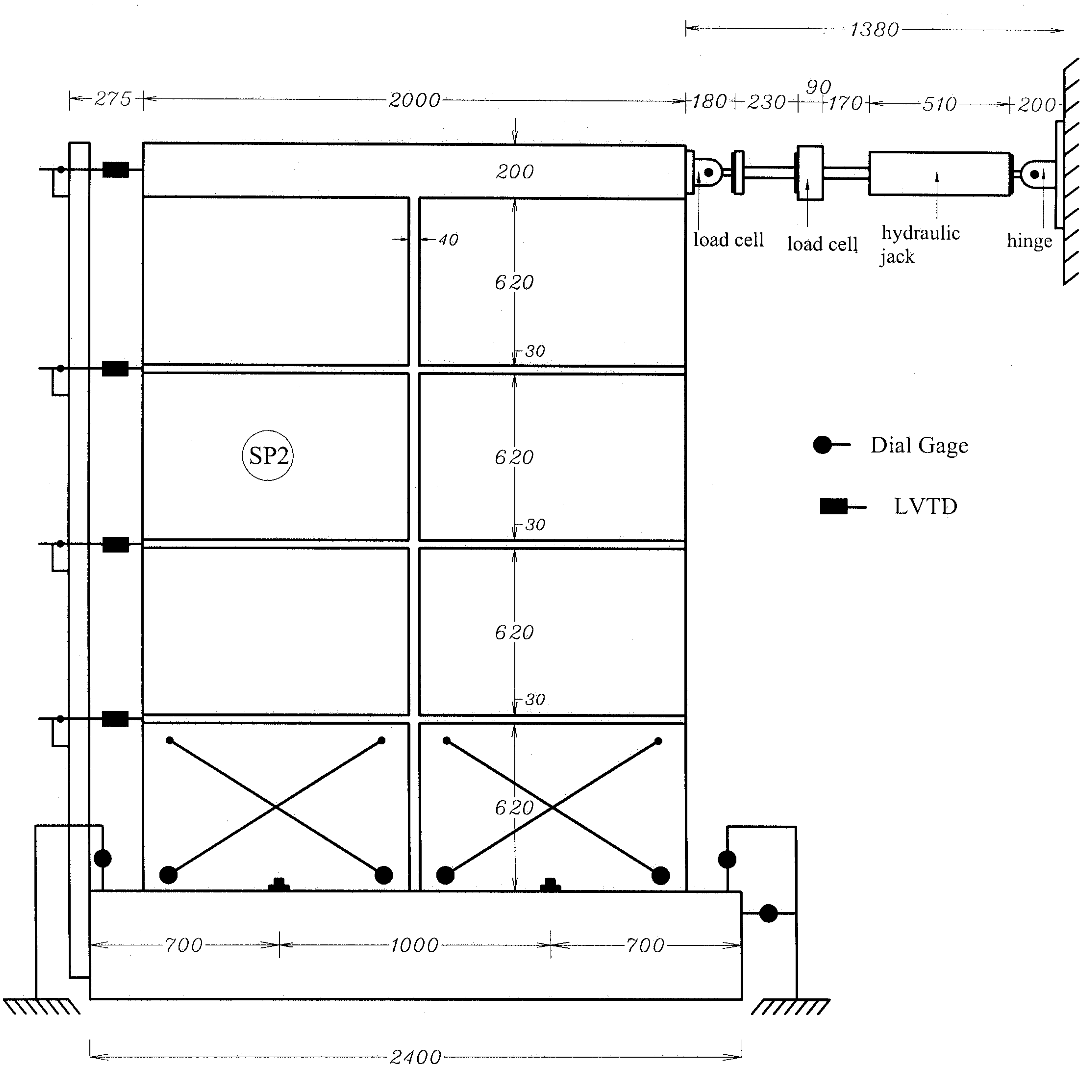

Figure 5.17 Details of the test setup, loading system and instrumentation for SP2 for the 2nd static test.

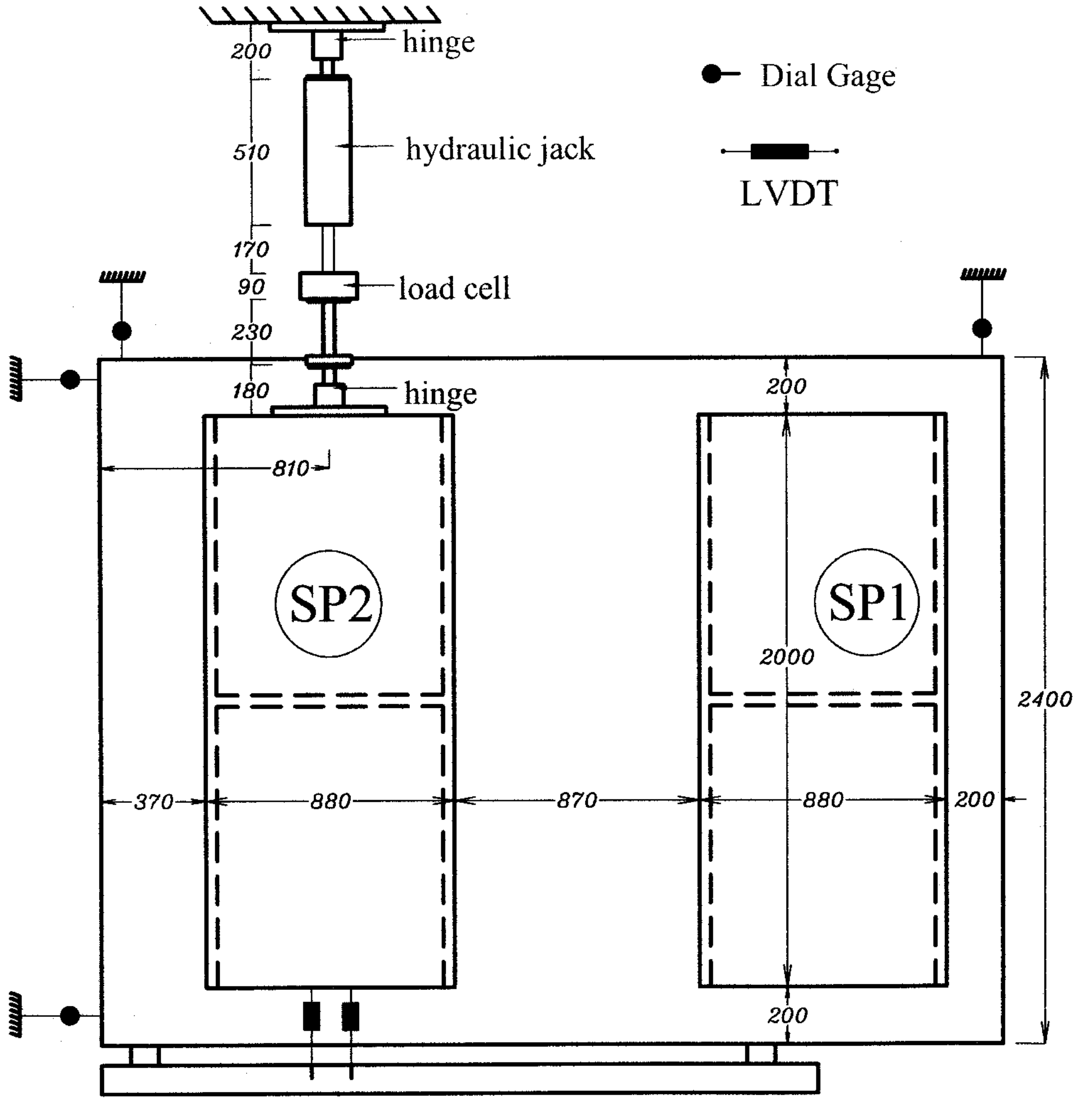

Figure 5.18 Plan view of the test setup, loading system and instrumentation for SP2 for the 2nd static test.

5.3.1 LOAD-DEFORMATION RESPONSE OF DAMAGED SPECIMEN2

This section presents the response of the panel form test specimen SP2 for the 2nd static test under the cyclic displacements.

The damaged SP2 was loaded under the lateral loading history presented in Figure 5.19. This 2nd static test was again a load-controlled test that consisted of five full reversed cycles. Applied lateral loads were 20 kN, 40 kN, 60 kN, 70 kN, and 80 kN for the 1st, 2nd, 3rd, 4th, and 5th cycles, respectively, for the 2nd static test of SP2.

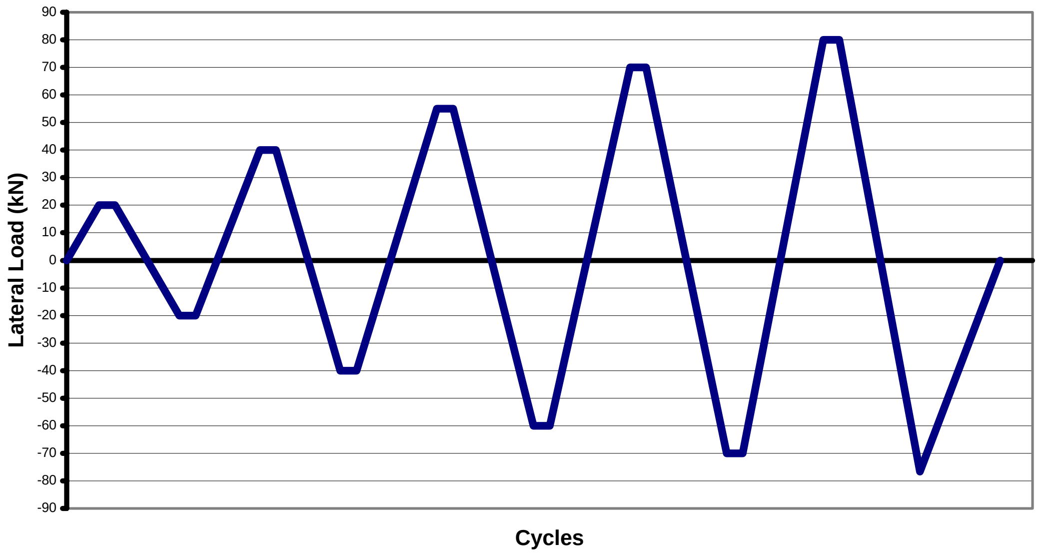

Figure 5.19 Lateral load history of SP2 for the 2nd static test.

The maximum lateral load applied to SP2 for the 2nd static test was 35kN. At this load level, the top displacement of SP2 was 4.5 mm. In Figure 5.20, Figure 5.21, Figure 5.22 and Figure 5.23 load-displacement curves are presented for the 1st, 2nd, 3rd and 4th stories, respectively, for the 2nd static test for SP2.

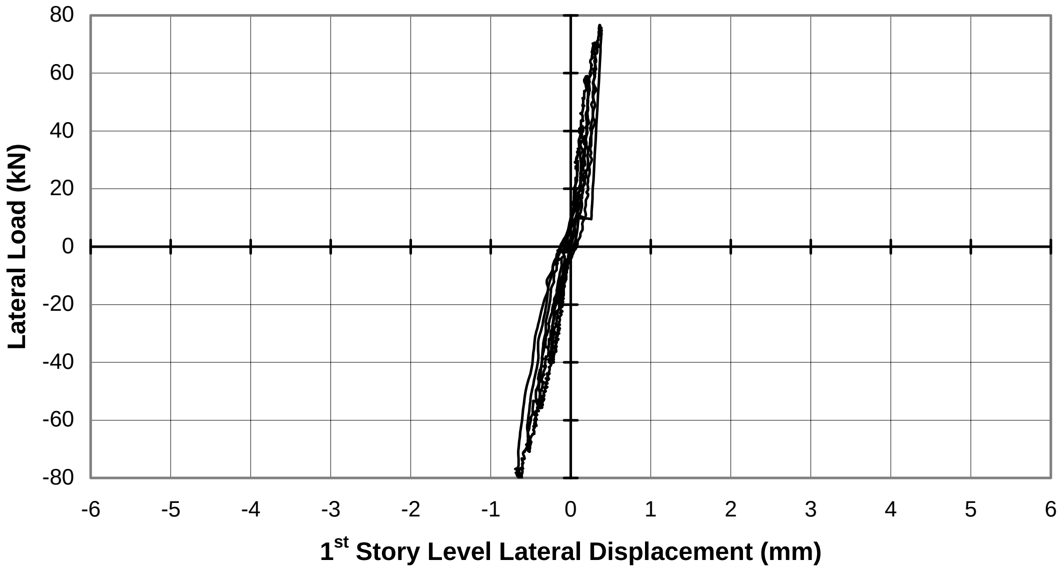

Figure 5.20 Lateral load-displacement curve of the 1st story for the 2nd static test, SP2.

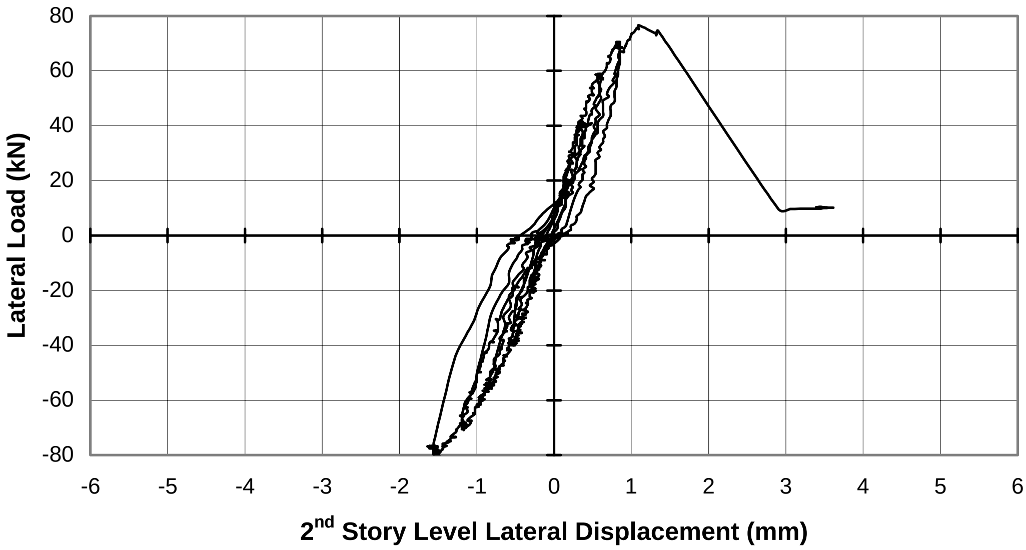

Figure 5.21 Lateral load-displacement curve of the 2nd story for the 2nd static test, SP2.

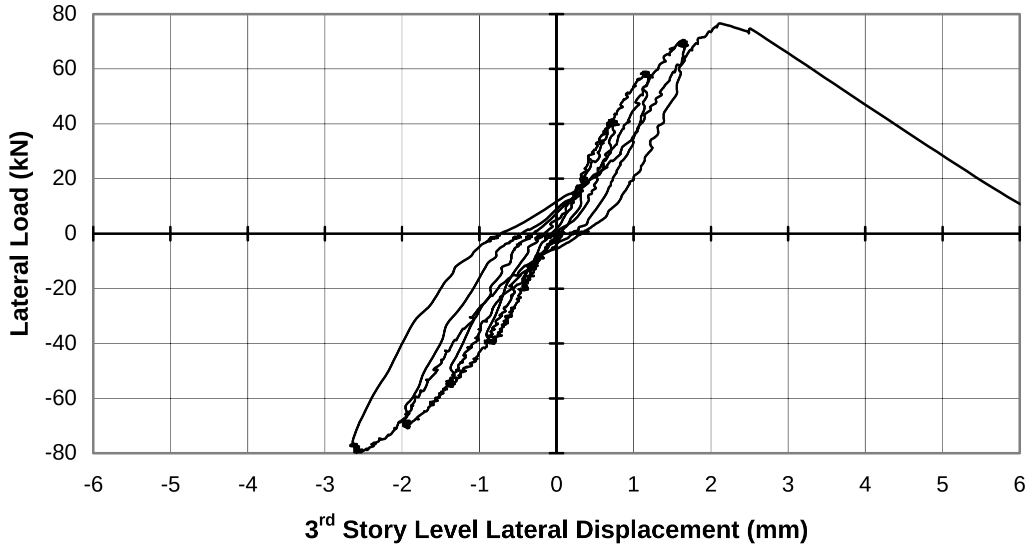

Figure 5.22 Lateral load-displacement curve of the 3rd story for the 2nd static test, SP2.

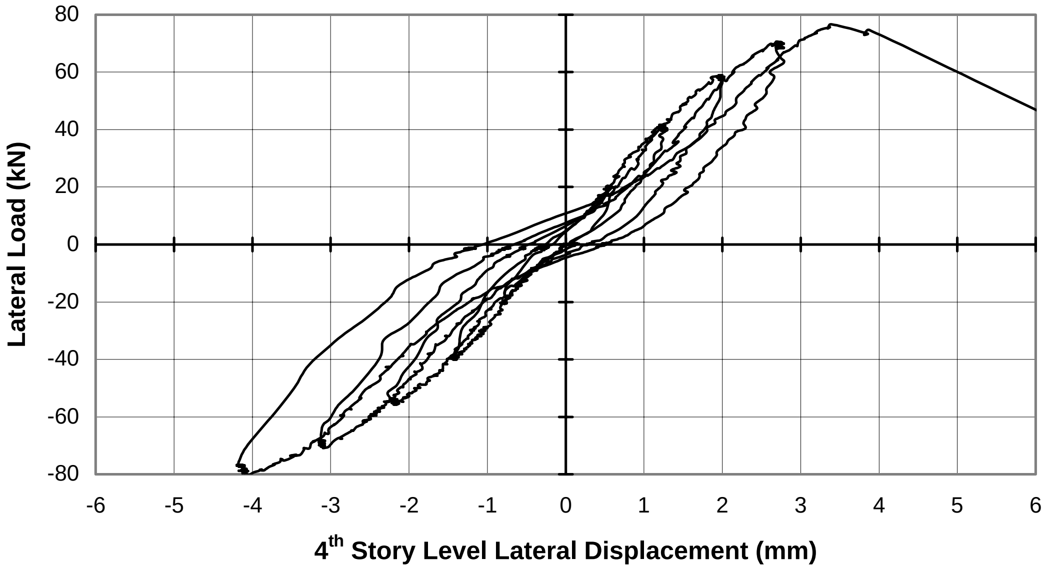

Figure 5.23 Lateral load-displacement curve of the 4th story for the 2nd static test, SP2.

For the 2nd static test of SP2, the top deflections are summarized in Table 5.2. The maximum lateral load applied to SP2 for the 2nd static test was 80 kN. At this load level, the top displacement of SP2 was 4.1 mm.

Table 5.2 Summary of the top deflection of the 2nd static test of SP2.

Half cycle No	Maximum top displacement (mm)	Lateral load (kN)
1	0.780	20.0
-1	-0.510	-20.0
2	1.390	40.0
-2	-1.220	-40.0
3	-2.195	55.0
-3	-1.976	-55.0
4	3.080	70.0
-4	-2.685	-70.0
5	4.100	80.0
-5	3.200	-80.0

The drift ratios of each story are calculated and plotted against the applied lateral load. Variations of the 1st, 2nd,3rd, and 4th stories drift ratios for the 2nd static test of SP2 are presented in Figure 5.24, Figure 5.25, Figure 5.26 and Figure 5.27, respectively.

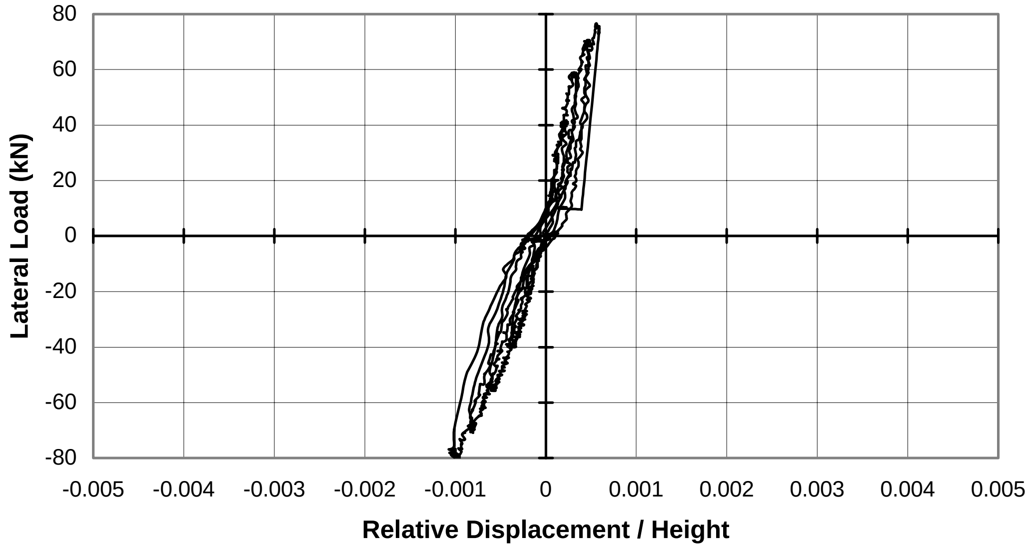

Figure 5.24 Variation of the 1st story drift ratio with the applied load, for the 2nd static test, SP2.

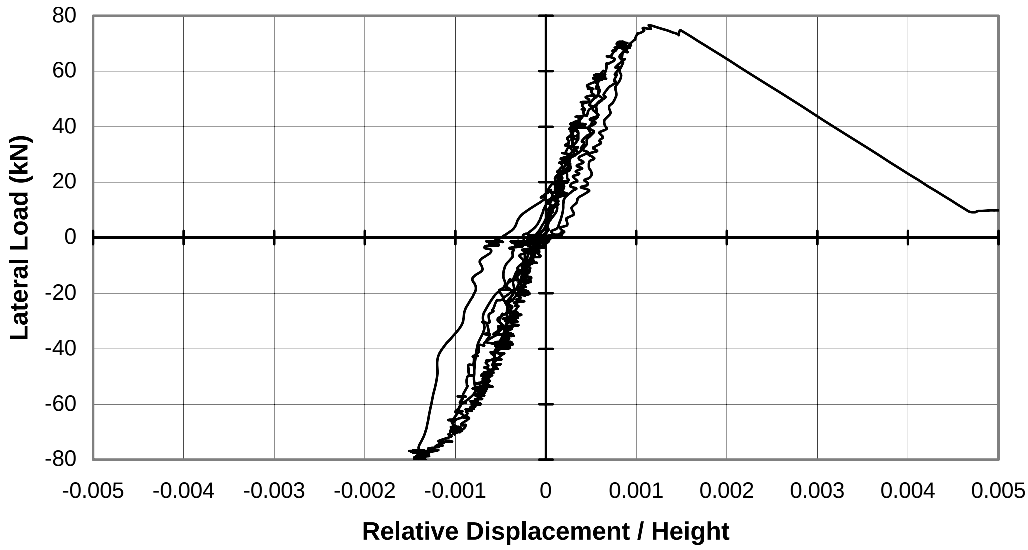

Figure 5.25 Variation of the 2nd story drift ratio with the applied load, for the 2nd static test, SP2.

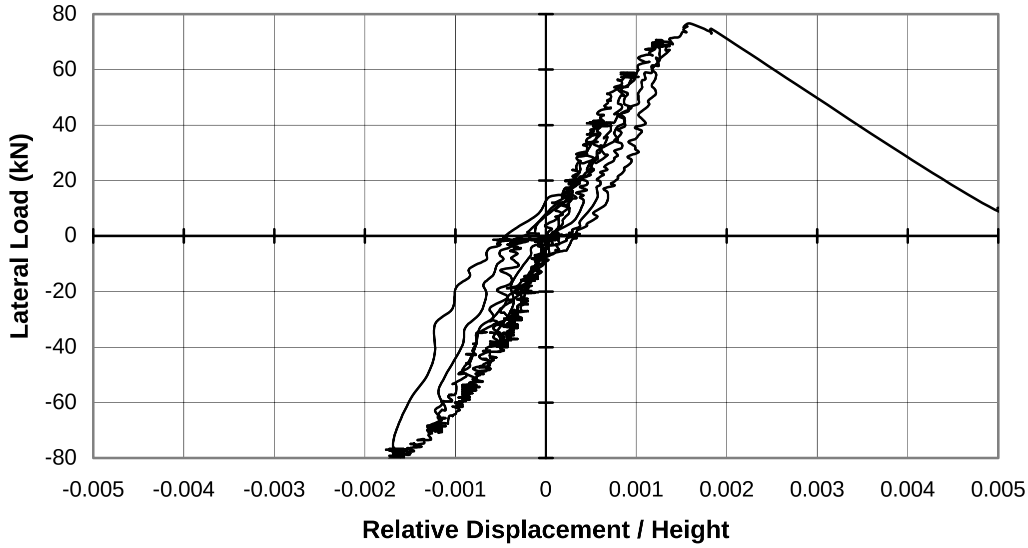

Figure 5.26 Variation of the 3rd story drift ratio with the applied load, for the 2nd static test, SP2.

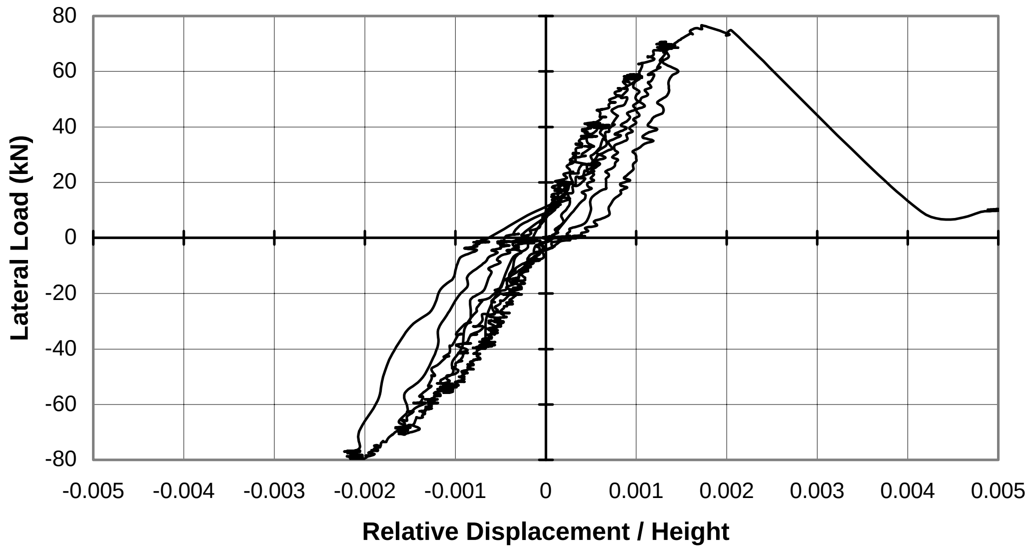

Figure 5.27 Variation of the 4th story drift ratio with the applied load, for the 2nd static test, SP2.

5.3.2 Cracking and Failure Characteristics of the Damaged SP2

Cracking in the flanges were essentially identical at the end of each cycle. While testing, observations show that all the cracks in the flange were horizontal flange cracks. Inclined cracks due to shear were not observed in the static tests of SP2. The main crack was the first story wall-slab construction joint crack at the flanges of the panel form test specimen SP2. These flange cracks propagated from the boundaries of the flange towards the center. In the first cycle 20 kN lateral load was applied to SP2. In the second cycle lateral load was increased up to 40 kN. Figure 5.29 shows the crack pattern at the first story slab-wall joint after the 2nd positive half cycle for the 2nd static test on SP2.

At the 3rd cycle lateral load was 60 kN. At the 3rd cycle a new horizontal crack occurred at the second story wall-slab construction joint. Figure 5.29 shows the crack pattern at the first and second story slab-wall joints after the 3rd negative half cycle for the 2nd static test on SP2. Lateral load was increased up to 70 kN at the fourth cycle. Figures 5.30 and 5.31 show the crack patterns at the first story slab-wall joint after the 4th positive half cycle for the 2nd static test on SP2. Figures 5.32 and 5.33 show the crack patterns at the first story slab-wall joint after the 4th negative half cycle for the 2nd static test on SP2. In the last cycle, lateral load was increased up to 80 kN. At the 5th positive half cycle when the lateral load reached 80 kN all the reinforcement in the tension side wall ruptured suddenly. Figures 5.34, 5.35 and 5.36 show the crack patterns at the first story slab-wall joint after the 5th positive half cycle for the 2nd static test on SP2. At the 5th negative half cycle when the lateral load was again 80 kN all the reinforcement in the other side flange ruptured. Figure 5.37 shows the crack pattern at the first story slab-wall joint after the 5th negative half cycle for the 2nd static test on SP2. After that the second static test was ended for the damaged SP2.

Figure 5.28 Crack pattern at the first story slab-wall joint after the 2nd positive half cycle for the 2nd static test on SP2.

Figure 5.29 Crack pattern at the first and second story slab-wall joint after the 3rd negative half cycle for the 2nd static test on SP2.

Figure 5.30 Crack pattern at the first story slab-wall joint after the 4th positive half cycle for the 2nd static test on SP2.

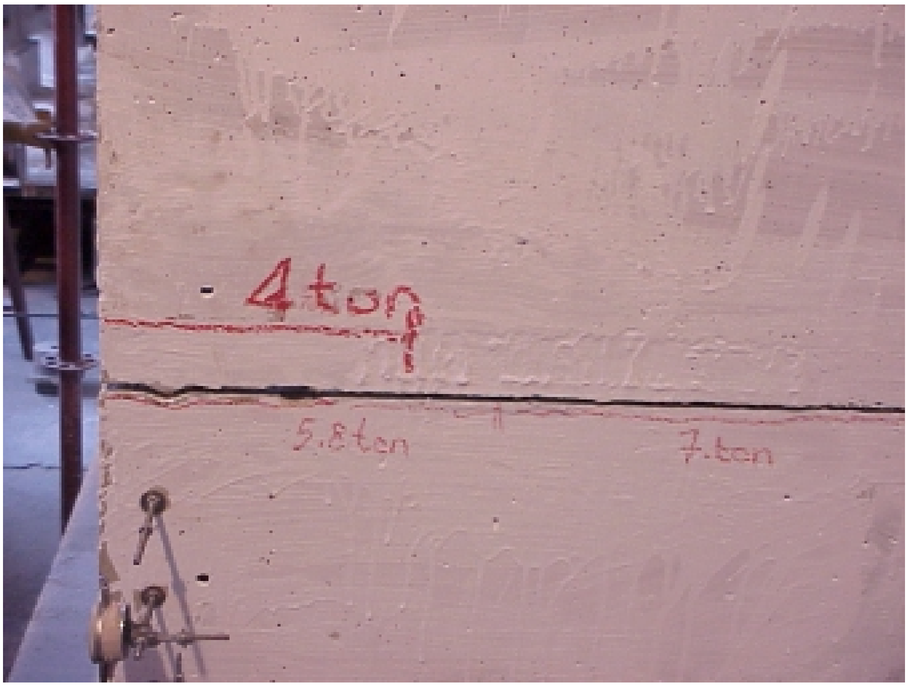

Figure 5.31 Crack pattern at the first story slab-wall joint after the 4th positive half cycle for the 2nd static test on SP2.

Figure 5.32 Crack pattern at the first story slab-wall joint after the 4th negative half cycle for the 2nd static test on SP2.

Figure 5.33 Crack pattern at the first story slab-wall joint after the 4th negative half cycle for the 2nd static test on SP2.

Figure 5.34 Crack pattern at the first story slab-wall joint after the 5th positive half cycle for the 2nd static test on SP2.

Figure 5.35 Crack pattern at the first story slab-wall joint after the 5th positive half cycle for the 2nd static test on SP2.

Figure 5.36 Crack pattern at the first story slab-wall joint after the 5th positive half cycle for the 2nd static test on SP2.

Figure 5.37 Crack pattern at the first story slab-wall joint after the 5th negative half cycle for the 2nd static test on SP2.

SP2 failed due to rupturing of the longitudinal mesh reinforcement of flanges at the first story wall-slab construction joint. This failure occurred in a very sudden and unpredictable manner. All the mesh reinforcement in the flange ruptured below the welded point of the longitudinal and the horizontal reinforcement. Crushing of the concrete was not observed in the static tests of SP2.

CHAPTER 6

TEST PROCEDURE AND RESULTS OF DYNAMIC EXPERIMENTS

6.1 GENERAL

In this chapter, the test procedure and the results of dynamic experiments of SP1 and SP2 are presented in detail. For each specimen, free vibration tests were performed to determine the dynamic properties of the specimens and were compared with the undamaged and damaged cases.

In the free vibration tests, specimens were pulled back with the help of a hydraulic jack, a load cell and the reaction wall. Specimens were released suddenly by a quick release mechanism. When the specimens were released, the accelerometer, which was placed at the fourth story, recorded the acceleration data. With the help of stored acceleration data, the natural periods and damping ratios were evaluated.

The free vibration tests were first performed on SP1 and then on SP2. The undamaged SP1 was pulled with 10 kN and 15 kN lateral forces and then released suddenly by a quick release mechanism to determine its natural period and damping ratio. After these free vibration tests, the first static tests were performed on SP1 by applying reversed cyclic lateral loading simulating the earthquake forces up to cracking. The same free vibration tests were performed on the damaged SP1. In addition to these tests, SP1 was pulled with 0.35 mm and 0.50 mm top displacements and then released to determine natural periods and damping ratios of the damaged specimens. The same procedure was then applied to SP2.

Figures 6.1 and 6.2 show a general view of the test setup, loading system, instrumentation, reaction wall and data acquisition system for the dynamic test of SP1 and SP2, respectively. Also general views of the quick release mechanisms of SP1 and SP2 for the dynamic tests are given in Figures 6.3 and 6.4, respectively.

Figure 6.1 A general view of the test setup, loading system, instrumentation, and reaction wall and data acquisition system for the dynamic tests of SP1.

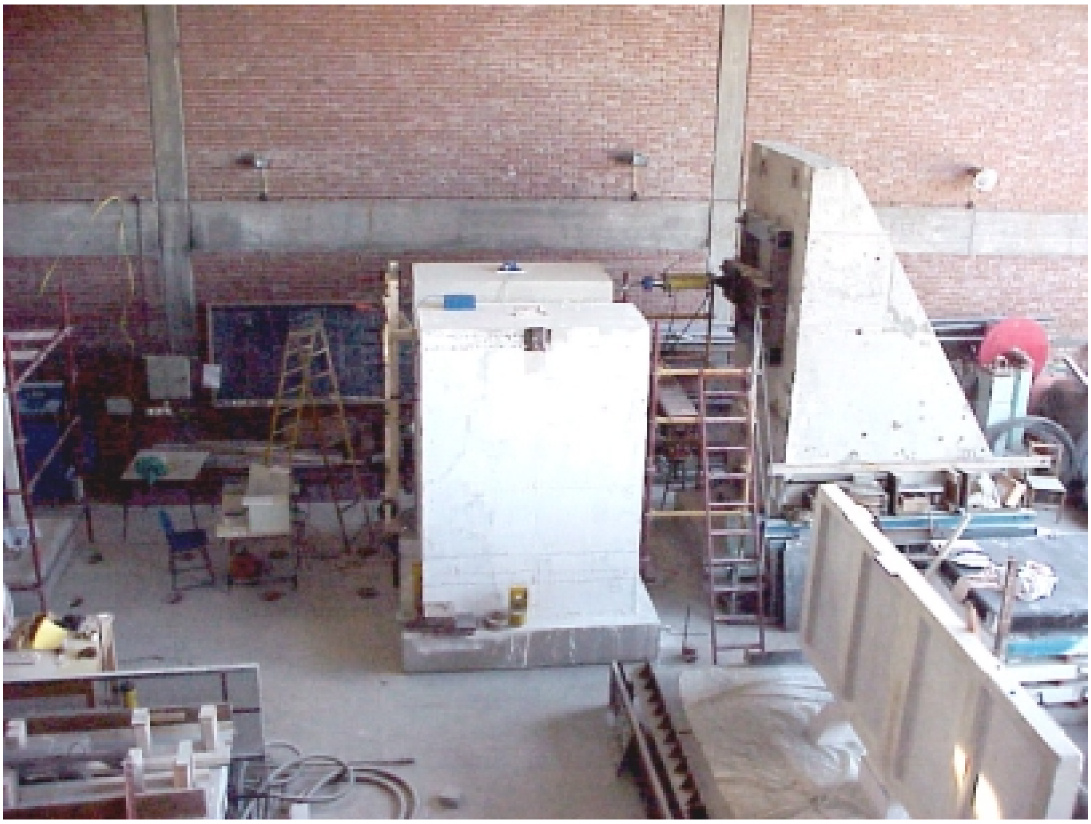

Figure 6.2 A general view of the test setup, loading system, instrumentation, and reaction wall and data acquisition system for the dynamic tests of SP2.

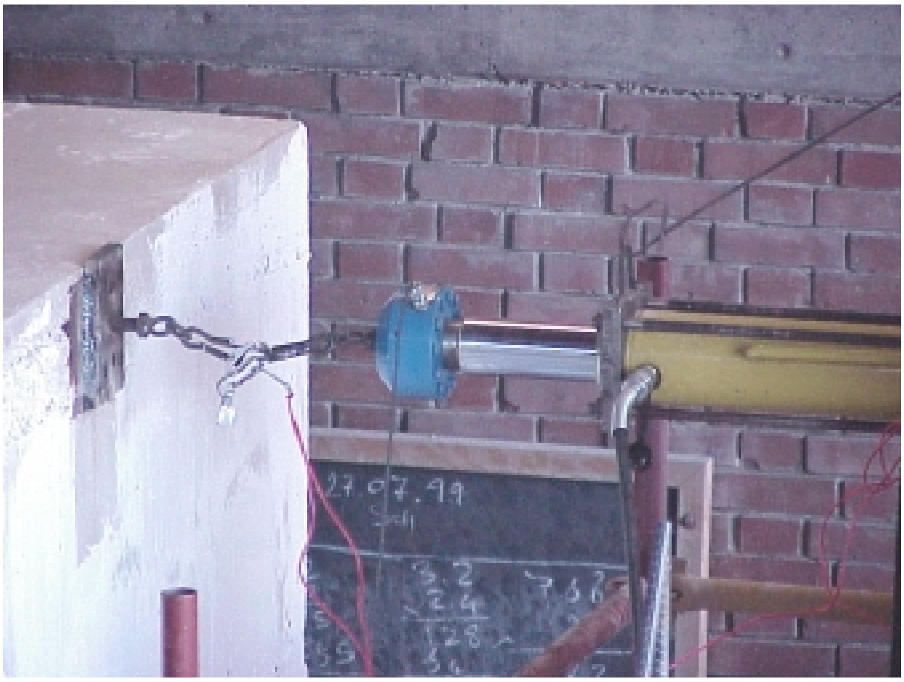

Figure 6.3 A general view of the quick release mechanism for the dynamic test of SP1.

Figure 6.4 A general view of the quick release mechanism for the dynamic test of SP2.

6.2 HALF-POWER BANDWIDTH

An important property of the frequency response curve for the deformation response factor (R_d) is shown in Figure 6.5, where the half-power bandwidth is defined. If ω_a and ω_b are frequencies on either side of the resonant frequency ω_n at which the amplitude is $1/\sqrt{2}$ times the resonant amplitude, then for small ζ

$$\frac{\omega_b - \omega_a}{\omega_n} = 2\zeta \tag{6.1}$$

This result was derived in Chopra (1995) in detail and ζ can be written as

$$\zeta = \frac{\omega_b - \omega_a}{2\omega_n} \qquad \text{or} \qquad \zeta = \frac{f_b - f_a}{2f_n} \tag{6.2}$$

where $f = \omega/2\pi$ is the cyclic frequency. This important result enables evaluation of damping from vibration tests without knowing the applied force.

The natural frequency and damping ratio can be determined from the frequency response curve. The damping ratio is calculated by using Equation 6.2, and the frequencies f_a and f_b are determined from the experimental curve as illustrated in Figure 6.6. Although Equation 6.2 was derived from the frequency-displacement curve for a constant-amplitude harmonic force, it is approximately valid for the other response curves as long as the structure is lightly damped. All the calculations for damping ratio in this study were performed based on Equations 6.1 and 6.2.

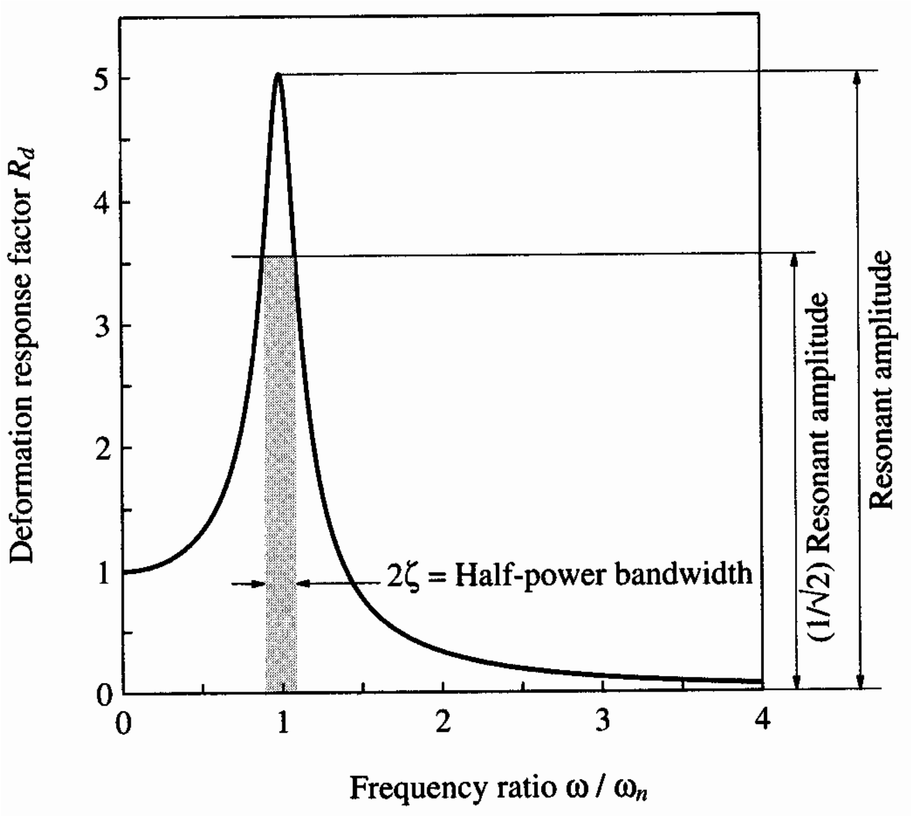

Figure 6.5 Definition of half-power bandwidth.

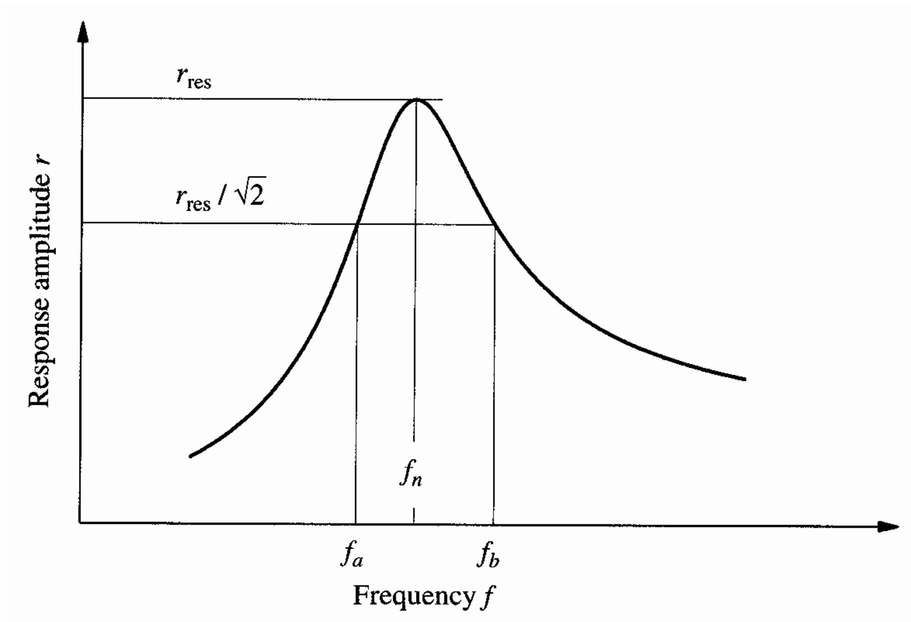

Figure 6.6 Evaluating damping ratio from frequency-response curve.

6.3 DYNAMIC TEST ON THE UNDAMAGED SP1

The acceleration, calculated period and damping ratio of SP1 is along the short dimension because SP1 is pulled and released suddenly along that dimension. Figure 6.7 shows the details of the test setup, loading system and instrumentation for the dynamic test of SP1. As can be seen in Figure 6.7, SP1 was pulled back with the help of a hydraulic jack and the lateral load was measured by the load cell. Also displacements corresponding to applied lateral force can be determined with the help of dial gages that were placed on the story levels.

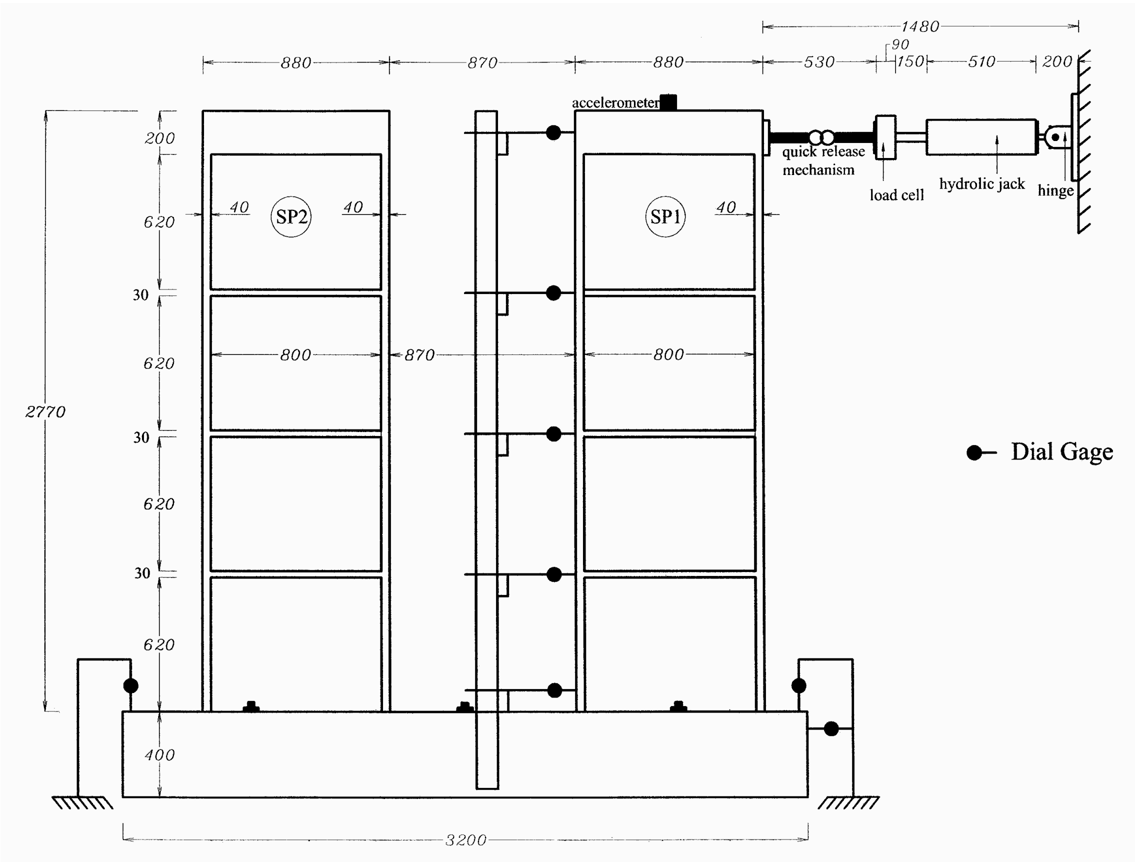

Figure 6.7 Details of the test setup, loading system and instrumentation for the dynamic test of SP1.

Two hundred acceleration data were stored per second by accelerometer in the dynamic test on the undamaged SP1. It was first pulled back with F=10 kN lateral force and then released suddenly. The acceleration time graph for this case is given in Figure 6.8. Fast Fourier transformation of acceleration was taken. Frequency response curve for this case is given in Figure 6.9.

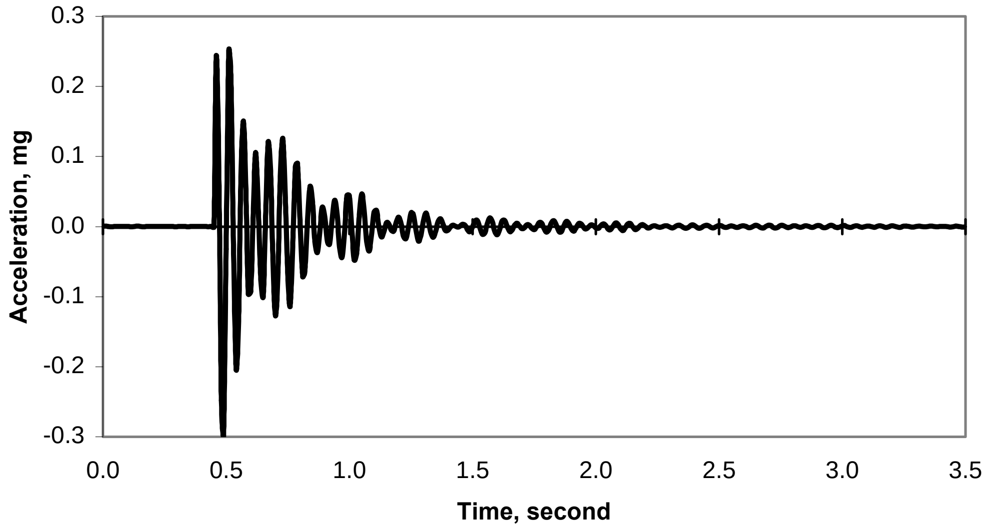

Figure 6.8 Acceleration-time graph for the dynamic test of undamaged SP1 (F=10 kN lateral force).

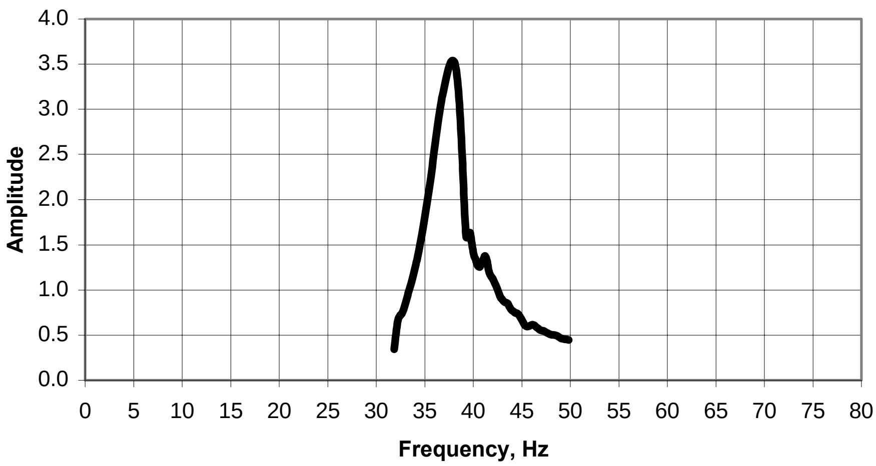

Figure 6.9 Frequency response curve for the dynamic test of undamaged SP1 (F = 10 kN lateral force).

The natural period vibration is 0.0264 sec, the natural cyclic frequency is 37.91 Hz and the damping ratio is 0.039 for the undamaged SP1 when it was pulled back with F=10 kN lateral force.

After SP1 was pulled back with F = 10 kN lateral force, the same experiment was performed with F = 15 kN lateral force. It was pulled back with F = 15 kN lateral force and released suddenly by a quick release mechanism and acceleration data was stored. Acceleration time graph and frequency response curve for the undamaged SP1 are given in Figures 6.10 and 6.11, respectively, when SP1 was pulled back with F = 15 kN lateral force.

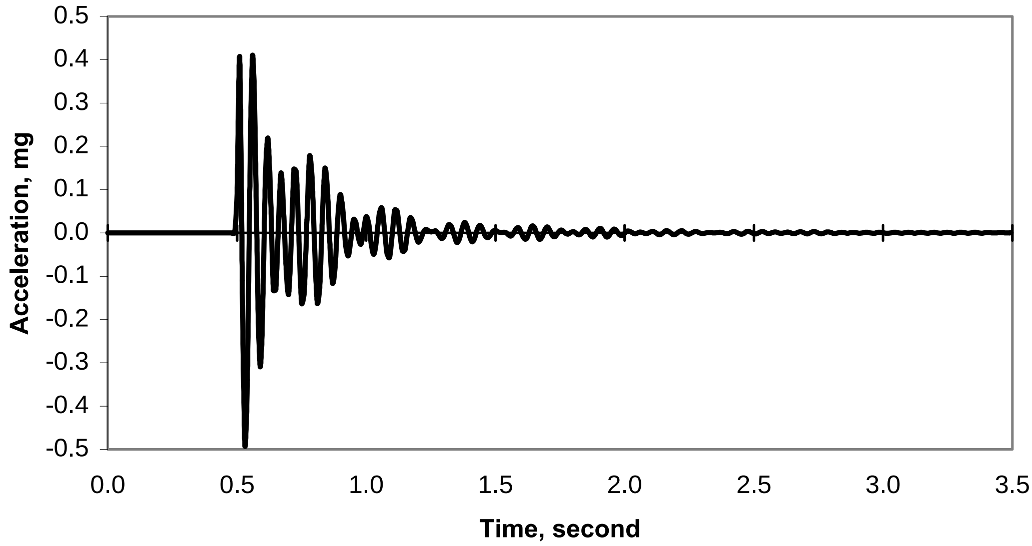

Figure 6.10 Acceleration-time graph for the dynamic test of the undamaged SP1 (F=15 kN lateral force).

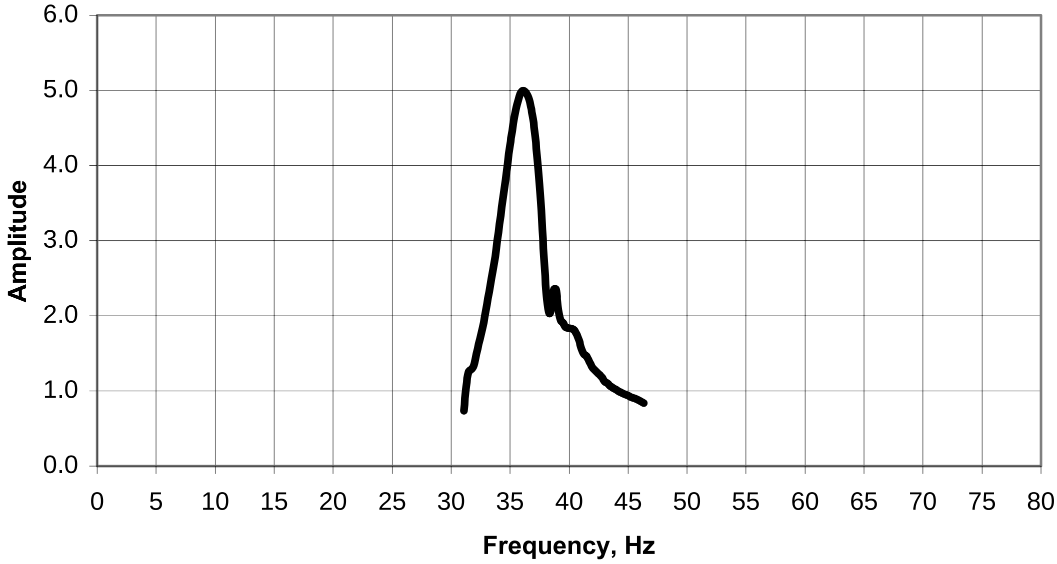

Figure 6.11 Frequency response curve for the dynamic test of the undamaged SP1 (F=15 kN lateral force).

The natural period vibration was 0.0276 sec, the natural cyclic frequency was 36.17 Hz and the damping ratio was 0.0455 for the undamaged SP1 when it was pulled back with F = 15 kN lateral force. The summary of the dynamic properties of the undamaged SP1 is given in Table 6.1.

Table 6.1 Dynamic properties of the undamaged SP1.

Case	Frequency, Hz	Natural period, sec	Damping ratio
F = 10 kN lateral force	37.91	0.0264	0.039
F = 15 kN lateral force	36.17	0.0276	0.045
Mean value	37.04	0.0270	0.042

It is seen from Table 6.1 that the mean values of the natural period and damping ratio are 0.027 sec and 0.042, respectively, for the free vibration tests on the undamaged SP1.

6.4 DYNAMIC TEST ON THE DAMAGED SP1

After dynamic tests on the undamaged SP1, reversed cyclic lateral loading which simulates the earthquake forces was applied to SP1 in the first static tests. The same free vibration tests were performed on this damaged SP1.

The damaged SP1 was pulled with 10 kN, 15 kN lateral forces and 0.35 mm and 0.50 mm lateral top displacements, then was released suddenly by the quick release mechanism to determine its natural period and damping ratio, and to compare them with the undamaged case.

One hundred acceleration data were stored per second by the accelerometer in the dynamic test on the damaged SP1. The acceleration time graph and the frequency response curve are given in Figures 6.12 and 6.13, respectively, when the damaged SP1 was pulled back with F = 10 kN lateral force.

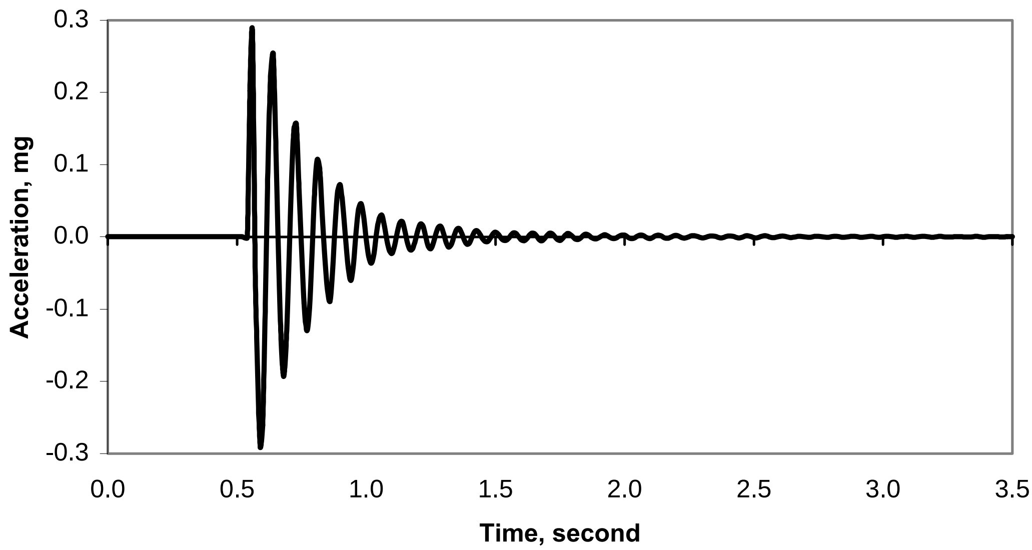

Figure 6.12 Acceleration-time graph for the dynamic test of the damaged SP1 (F=10 kN lateral force).

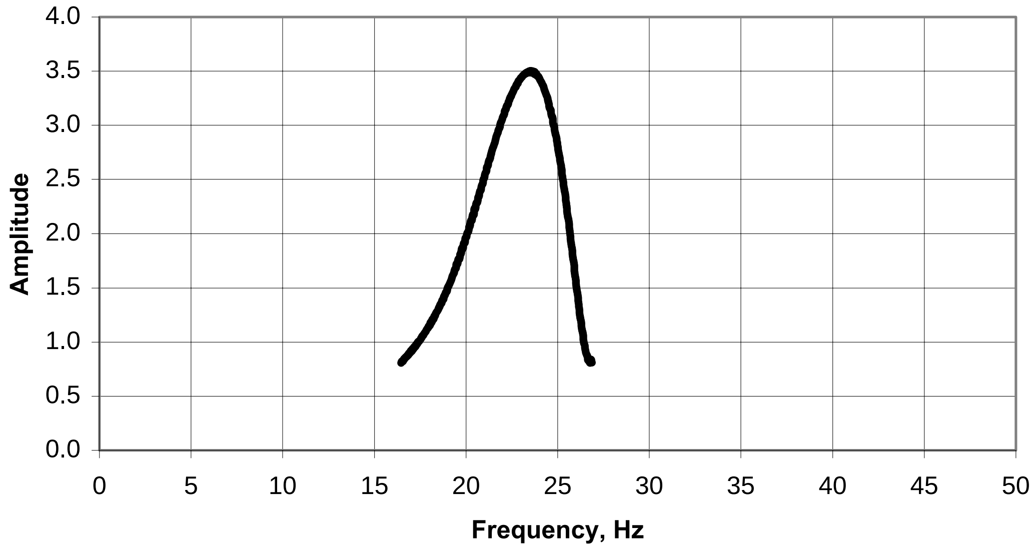

Figure 6.13 Frequency response curve for the dynamic test of the damaged SP1 (F=10 kN lateral force).

The natural period vibration was 0.0421 sec, the natural cyclic frequency was 23.736 Hz and the damping ratio was 0.090 for the damaged SP1 when it was pulled back with F=10 kN lateral force.

The acceleration time graph and the frequency response curve are given in Figures 6.14 and 6.15 when the damaged SP1 was pulled back with F=15 kN lateral force.

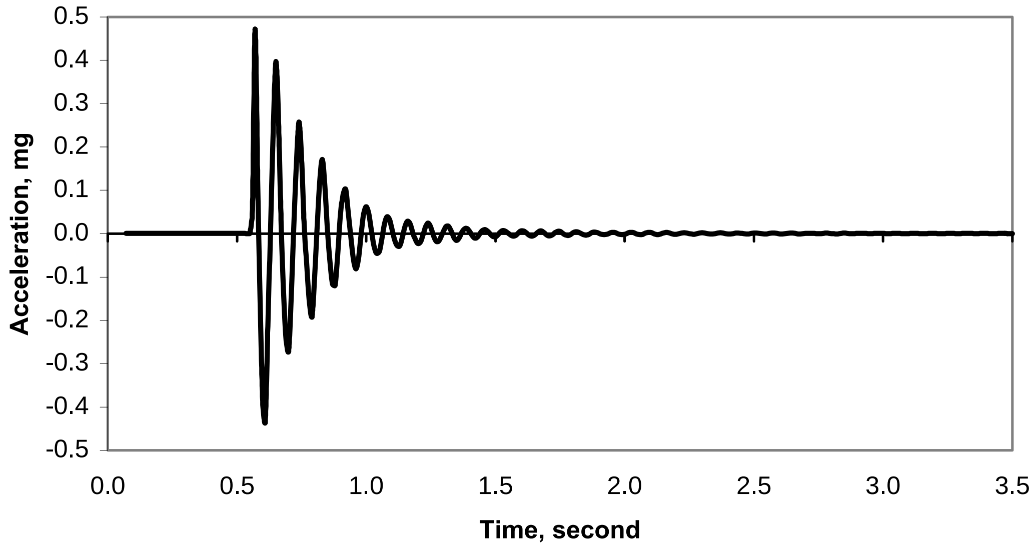

Figure 6.14 Acceleration-time graph for the dynamic test of the damaged SP1 (F=15 kN lateral force).

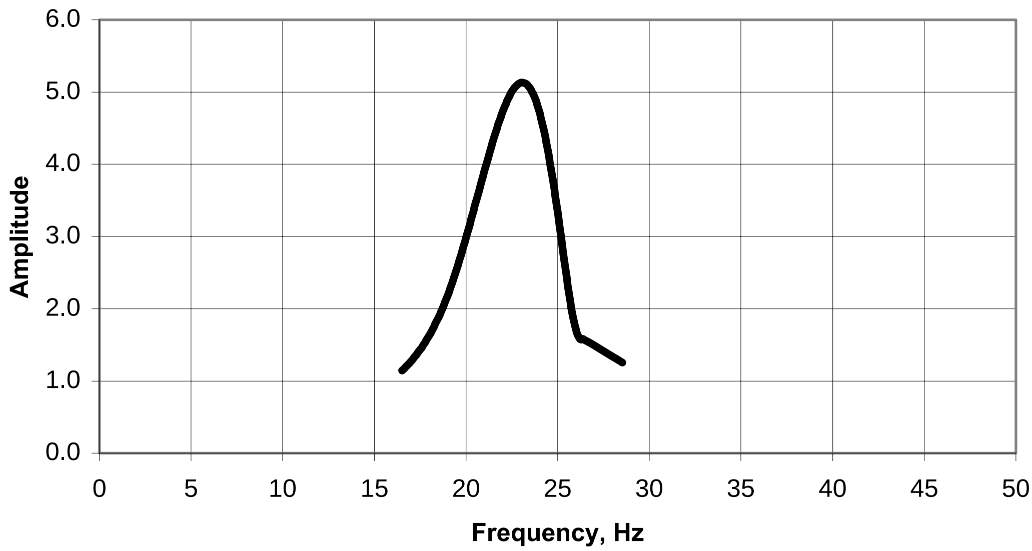

Figure 6.15 Frequency response curve for the dynamic test of the damaged SP1 (F=15 kN lateral force).

The natural period vibration was 0.0430 sec, the natural cyclic frequency was 23.253 Hz and the damping ratio was 0.092 for the damaged SP1 when it was pulled back with F=15 kN lateral force.

The acceleration time graph and the frequency response curve are given in Figures 6.16 and 6.17 when the damaged SP1 was pulled back with 0.35 mm top displacement.

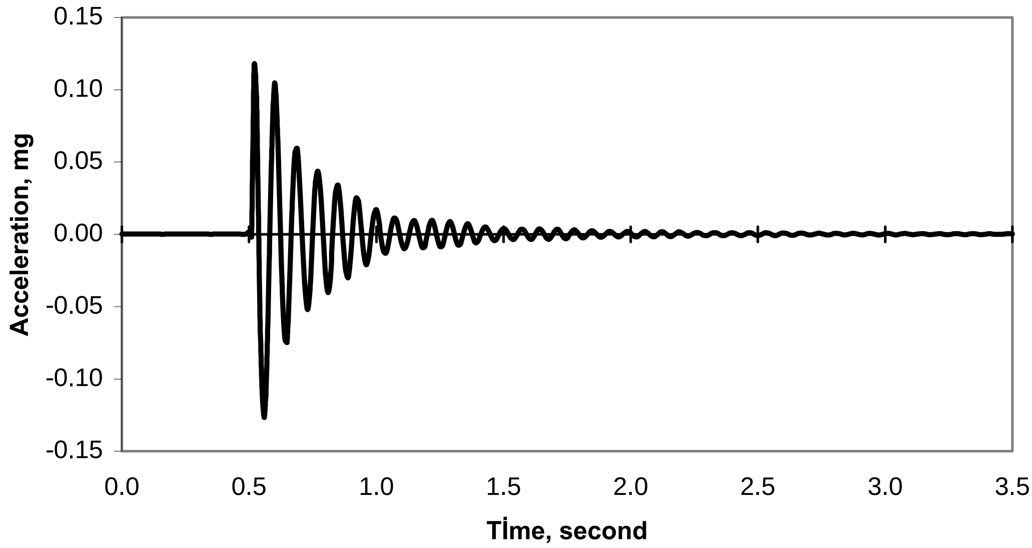

Figure 6.16 Acceleration-time graph for the dynamic test of the damaged SP1 (Top displacement=0.35 mm).

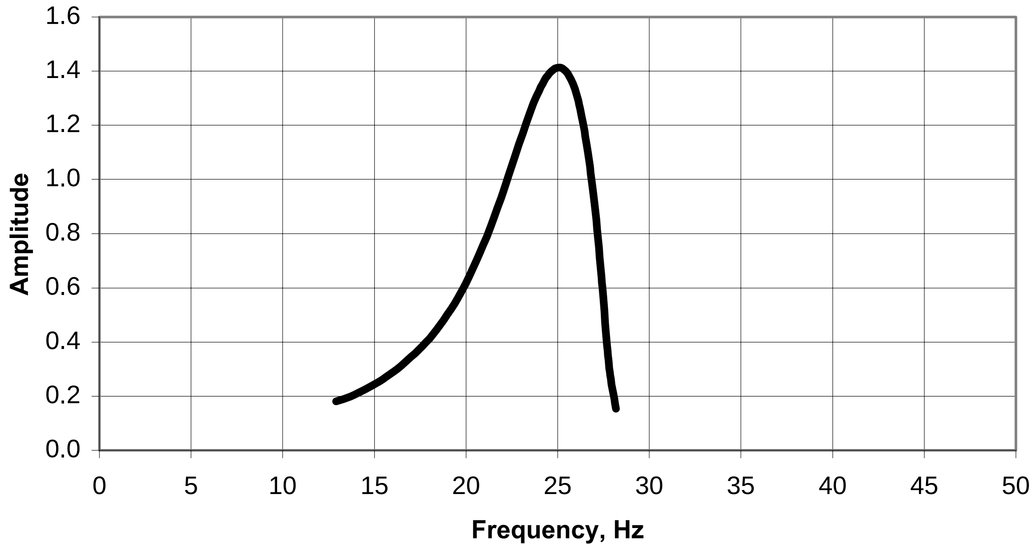

Figure 6.17 Frequency response curve for the dynamic test of the damaged SP1 (Top displacement = 0.35 mm).

The natural period vibration was 0.040 sec, the natural cyclic frequency was 25.05 Hz and the damping ratio was 0.091 for the damaged SP1 when it was pulled back with 0.35 mm lateral top displacements.

The acceleration time graph and the frequency response curve are given in Figures 6.18 and 6.19 when the damaged SP1 was pulled back with 0.50 mm top displacement.

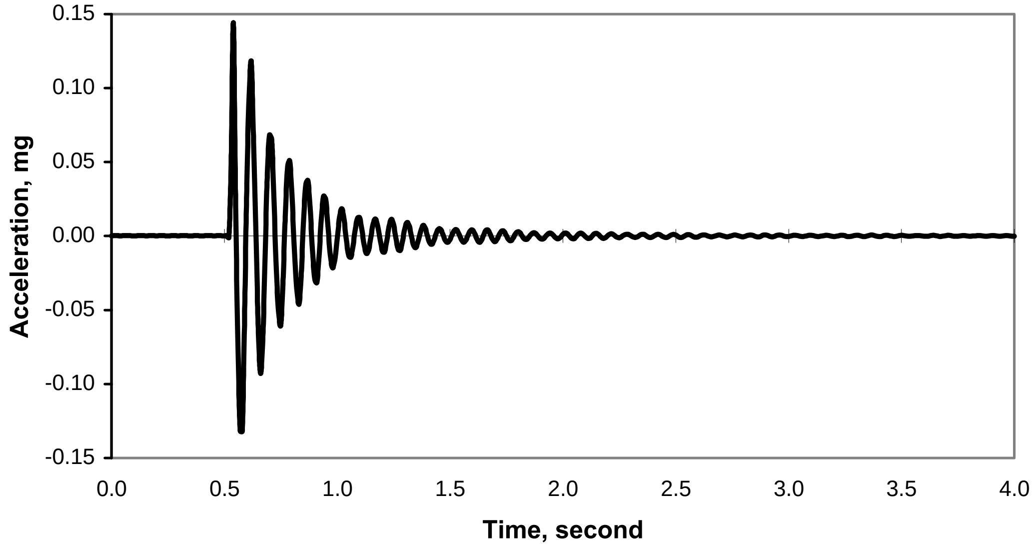

Figure 6.18 Acceleration-time graph for the dynamic test of the damaged SP1 (Top displacement = 0.50 mm).

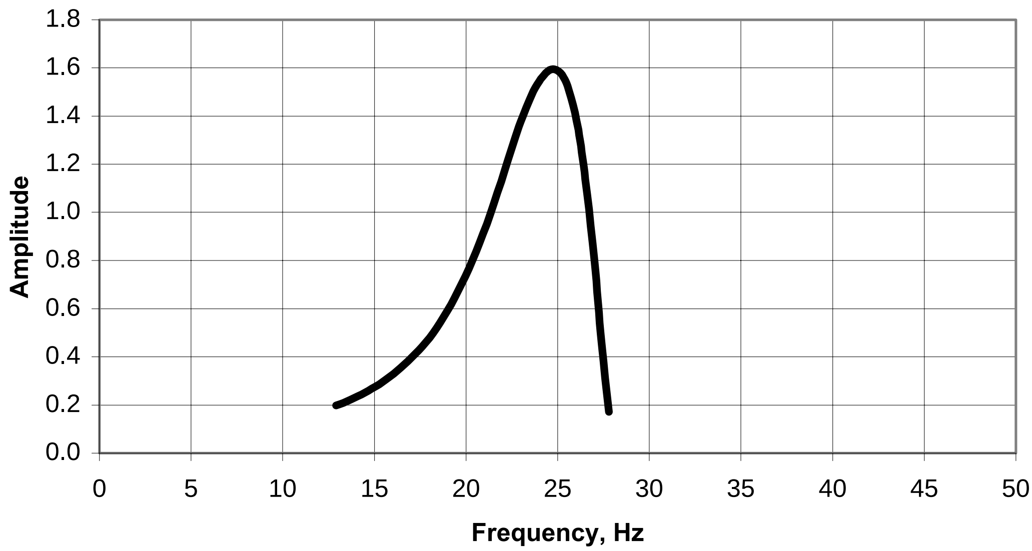

Figure 6.19 Frequency response curve for the dynamic test of the damaged SP1 (Top displacement = 0.50 mm).

The natural period vibration was 0.0405 sec, the natural cyclic frequency was 24.657 Hz and the damping ratio was 0.093 for the damaged SP1 when it was pulled back with 0.50 mm lateral top displacements. Table 6.2 shows the summary of the dynamic properties of damaged SP1.

Table 6.2 Dynamic properties of damaged SP1.

Case	Frequency, Hz	Natural period, sec	Damping ratio
F = 10 kN Lat. force	23.736	0.0421	0.0933
F = 15 kN Lat. force	23.253	0.0430	0.0917
Top disp = 0.35 mm	25.050	0.040	0.0929
Top disp = 0.50 mm	24.657	0.041	0.0957
Mean values	24.174	0.041	0.0934

The free vibration tests on the undamaged SP1 show that the mean values of the natural period and damping ratio are 0.027 sec and 0.042, respectively. In the free vibration tests of the damaged SP1 the mean values of the natural period and damping ratio were 0.041 and 0.0934. The natural period of free vibration increases 0.041 / 0.027 = 1.518 times and damping ratios increase 0.093 / 0.042 = 2.224 times from the undamaged case to the damaged case for SP1.

6.5 DYNAMIC TEST ON THE UNDAMAGED SP2

SP2 was pulled along the long dimension and released suddenly so that the acceleration, calculated period and damping ratio of SP2 were along that dimension. Figure 6.20 shows the details of the test setup, loading system and instrumentation for the dynamic test of SP2. As can be seen in Figure 6.20, SP2 was pulled back with the help of a hydraulic jack and the lateral load was measured by load cell. SP2 was first pulled back with F = 10 kN lateral force and then released suddenly. Two hundred acceleration data were stored per second by the accelerometer in the dynamic tests of the undamaged SP2 as was done for the undamaged SP1. The acceleration time graph and the frequency response curve for this case are given in Figure 6.21 and Figure 6.22, respectively.

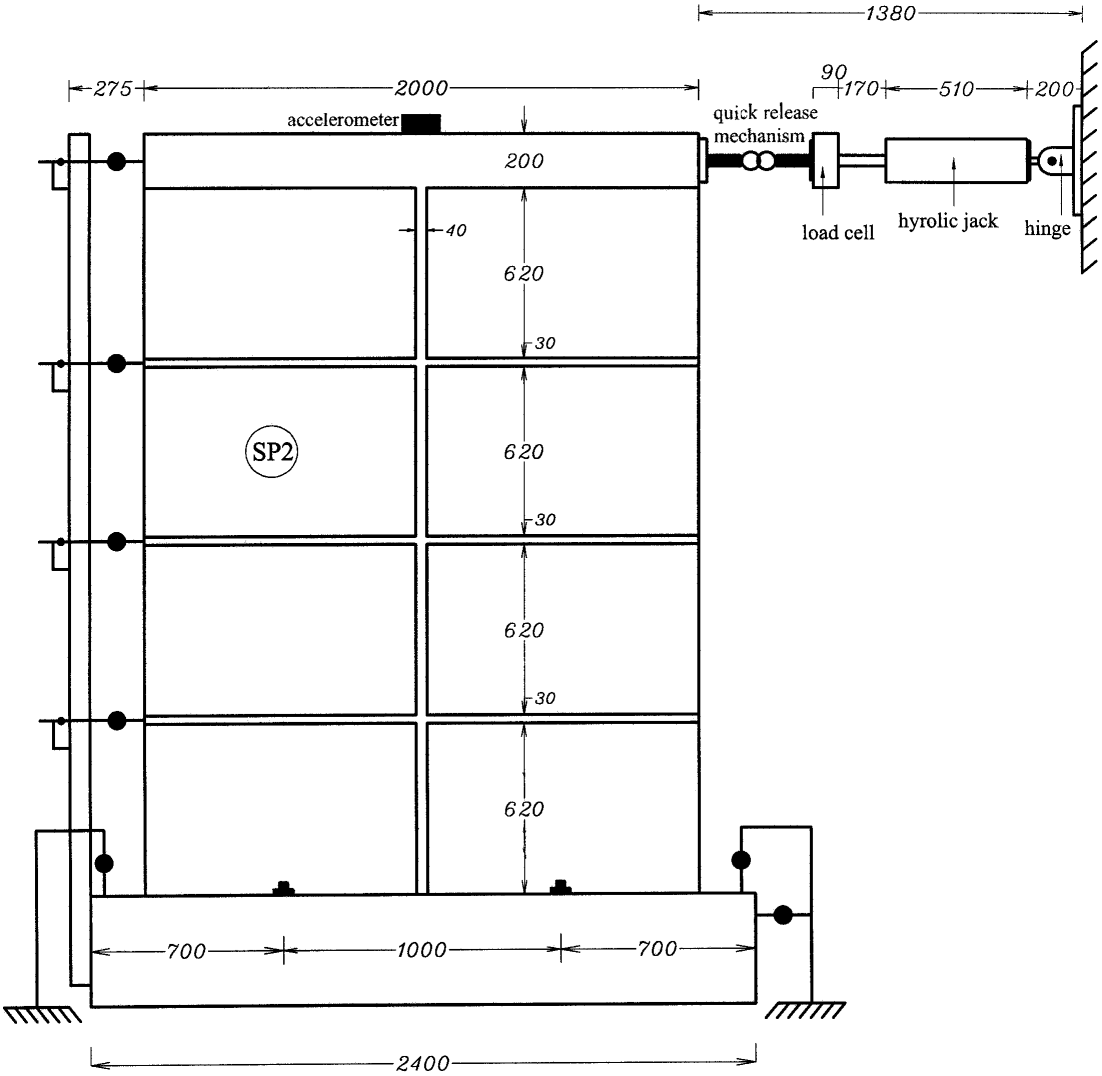

Figure 6.20 Details of the test setup, loading system and instrumentation for the dynamic test of SP2.

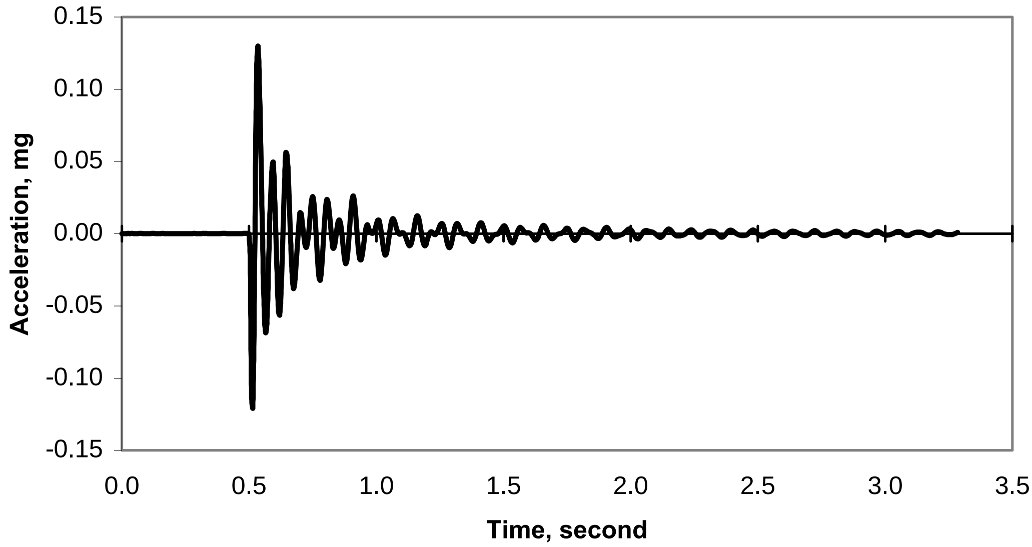

Figure 6.21 Acceleration-time graph for the dynamic test of the undamaged SP2 (F = 10 kN).

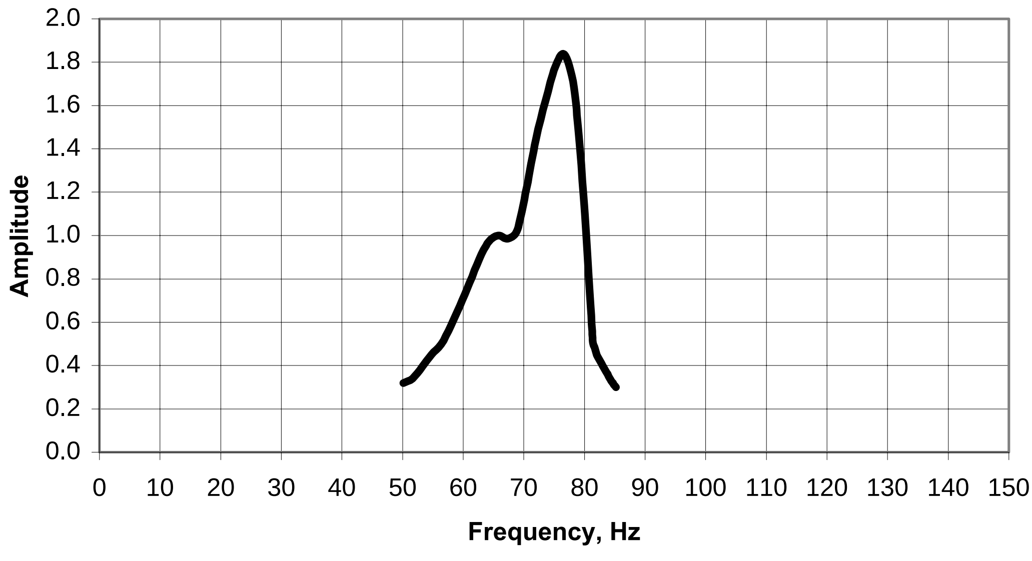

Figure 6.22 Frequency response curve for the dynamic test of the undamaged SP2 (F = 10 kN).

The natural period vibration was 0.013 sec, the natural cyclic frequency was 76.71 Hz and the damping ratio was 0.055 for the undamaged SP2 when it was pulled back with F = 10 kN lateral force.

After SP2 was pulled back with F = 10 kN lateral force, it was pulled back with F= 15 kN lateral force and released suddenly by the quick release mechanism and acceleration data were stored. Acceleration time graph and frequency response curve for the undamaged SP2 are given in Figures 6.23 and 6.24, respectively.

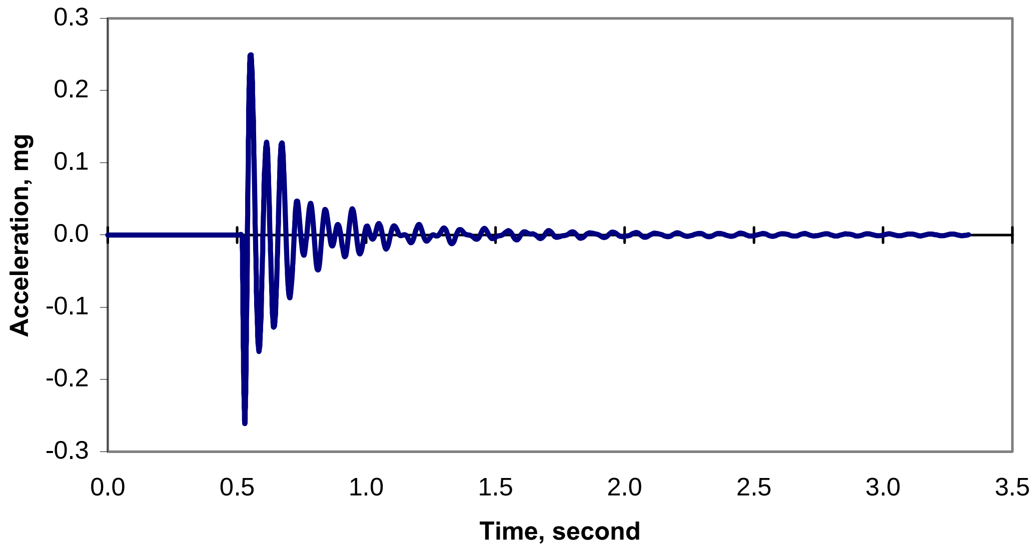

Figure 6.23 Acceleration-time graph for the dynamic test of the undamaged SP2 (F=15 kN).

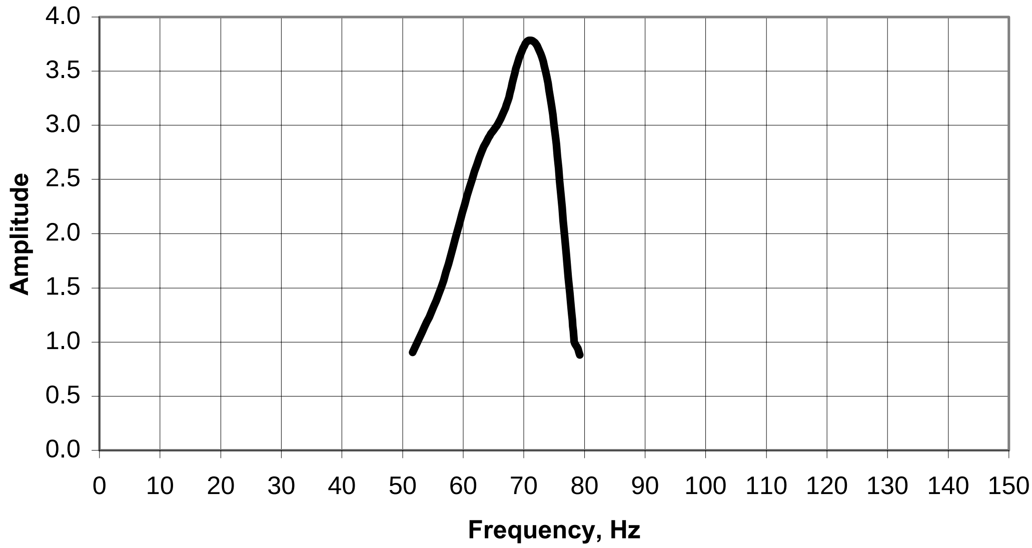

Figure 6.24 Frequency response curve for the dynamic test of the undamaged SP2 (F = 15 kN).

The natural period vibration was 0.0142 sec, the natural cyclic frequency was 70.45 Hz and the damping ratio was 0.092 for the undamaged SP2 when it was pulled back with F = 15 kN lateral force.

The acceleration time graph and the frequency response curve are given in Figures 6.25 and 6.26 when the undamaged SP2 was pulled back with F = 20 kN lateral force.

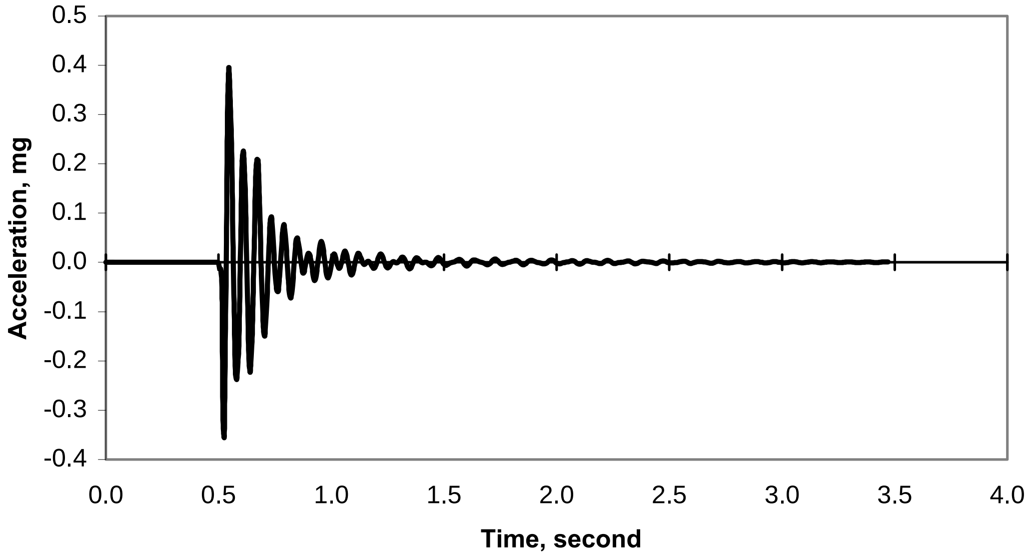

Figure 6.25 Acceleration-time graph for the dynamic test of the undamaged SP2 (F = 20 kN).

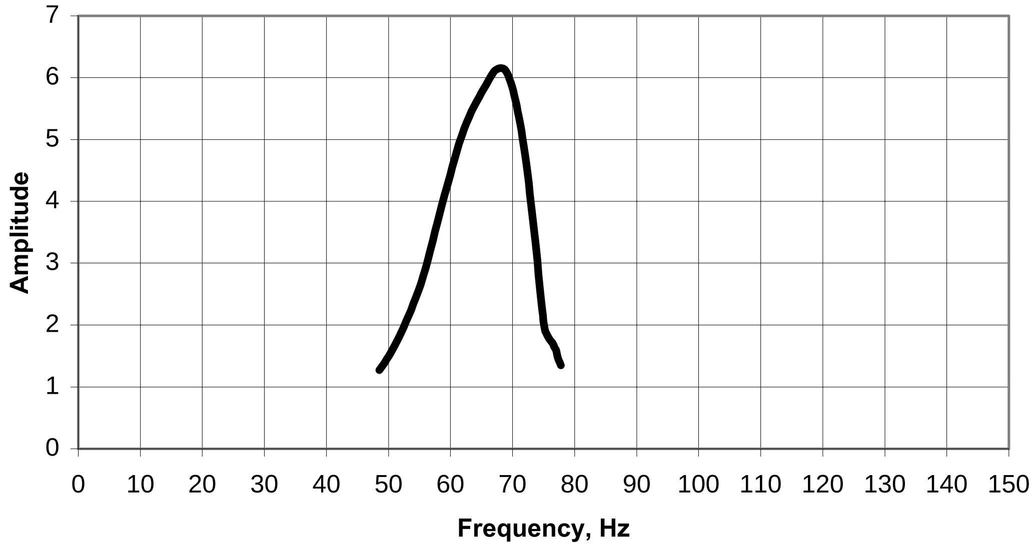

Figure 6.26 Frequency response curve for the dynamic test of the undamaged SP2 (F = 20 kN).

The natural period vibration was 0.0148 sec, the natural cyclic frequency was 67.31 Hz and the damping ratio was 0.094 for the undamaged SP2 when it was pulled back F = 20 kN lateral force.

The acceleration time graph and the frequency response curve are given in Figures 6.27 and 6.28 when the undamaged SP2 was pulled back with F = 20 kN lateral force again.

Experiments by using 20 kN by pulling back were done twice. The forces are shown in Table 6.3 as F1 and F2.

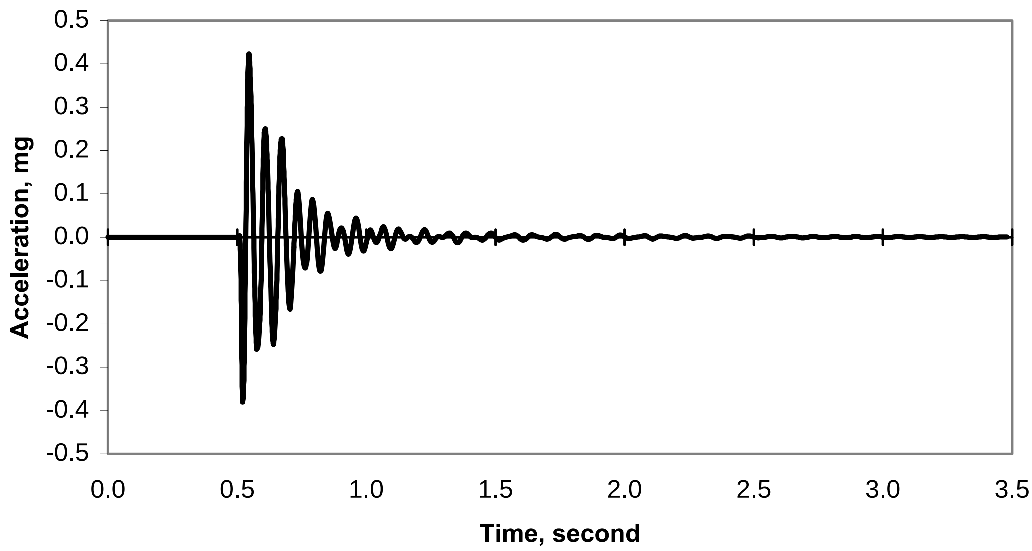

Figure 6.27 Acceleration-time graph for the dynamic test of the undamaged SP2 (F = 20 kN).

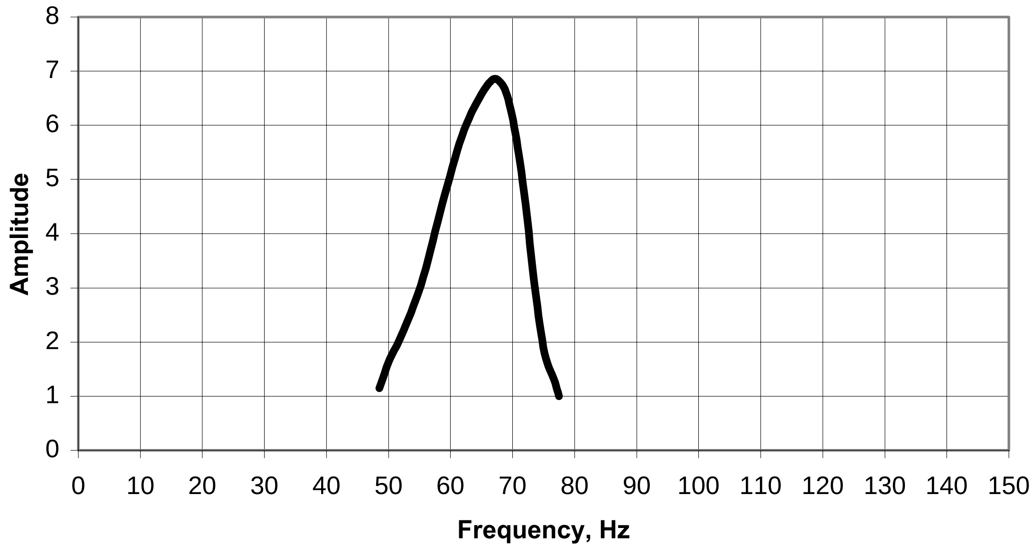

Figure 6.28 Frequency response curve for the dynamic test of the undamaged SP2 (F = 20 kN).

Table 6.3 shows the summary of the dynamic properties of the undamaged SP2.

Table 6.3 Dynamic properties of the undamaged SP2.

Case	Frequency, Hz	Natural period, sec	Damping ratio
F = 10 kN Lat. force	76.71	0.0130	0.0550
F = 15 kN Lat. force	70.45	0.0142	0.0919
F1 = 20 kN Lat. force	67.31	0.0148	0.0935
F2 = 20 kN Lat. force	67.31	0.0148	0.0916
Mean values	70.45	0.0142	0.0923

6.6 DYNAMIC TEST ON THE DAMAGED SP2

After the dynamic tests on the undamaged SP2 were completed, reversed cyclic lateral loading which simulates the earthquake forces was applied to SP2 in the first static tests. The same free vibration tests were performed on this damaged SP2.

The damaged SP2 was pulled with 10 kN, 15 kN and 20 kN lateral forces and was released suddenly by the quick release mechanism to determine its natural period and damping ratio and to compare them with the undamaged case.

The acceleration time graph and the frequency response curve are given in Figures 6.29 and 6.30 when the damaged SP2 was pulled back with F = 10 kN lateral force.

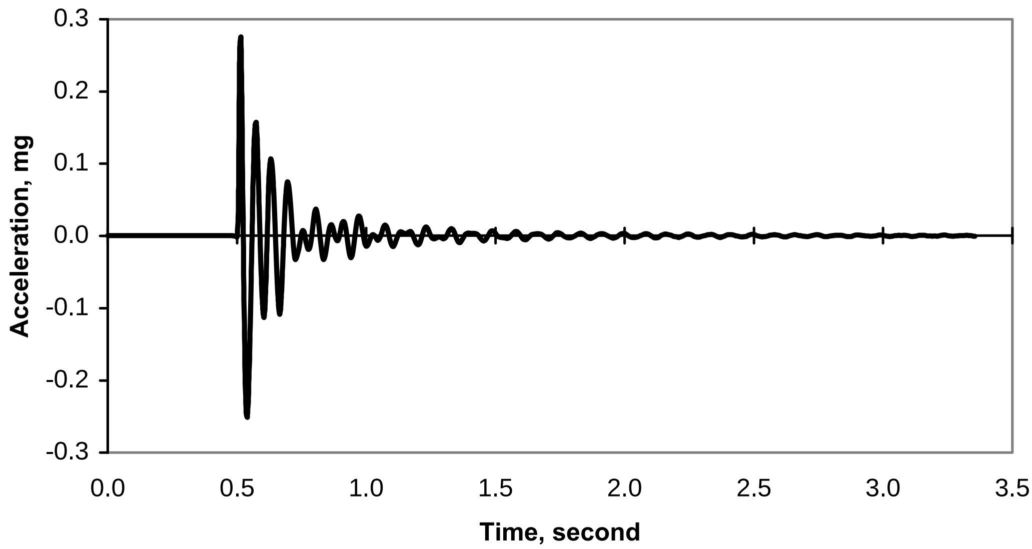

Figure 6.29 Acceleration-time graph for the dynamic test of the damaged SP2 (F = 10 kN).

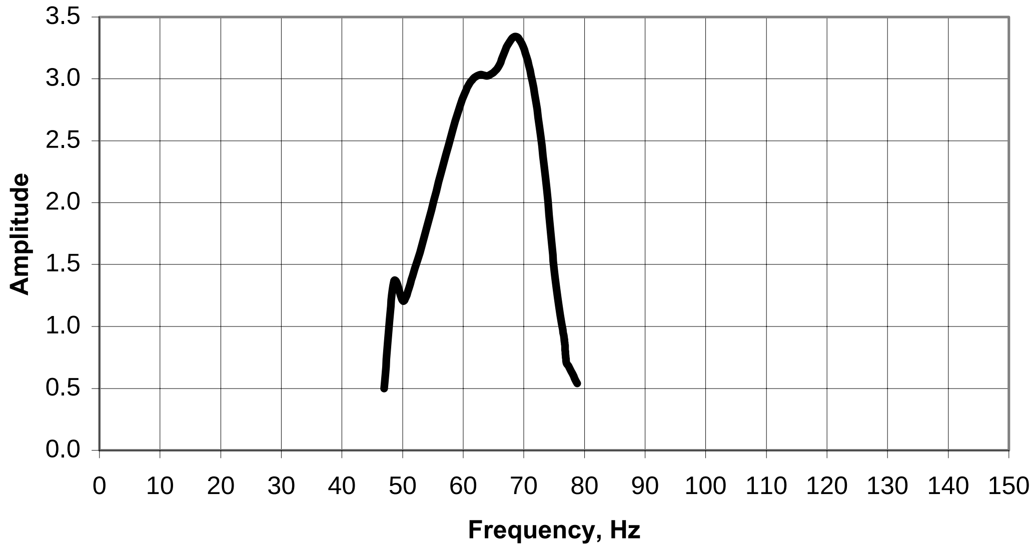

Figure 6.30 Frequency response curve for the dynamic test of the damaged SP2 (F = 10 kN).

The natural period vibration was 0.0145 sec, the natural cyclic frequency was 68.885 Hz and the damping ratio was 0.117 for the undamaged SP2 when it was pulled back F= 10 kN lateral force.

The acceleration time graph and the frequency response curve are given in Figures 6.31 and 6.32 when the undamaged SP2 was pulled back with F = 15 kN lateral force.

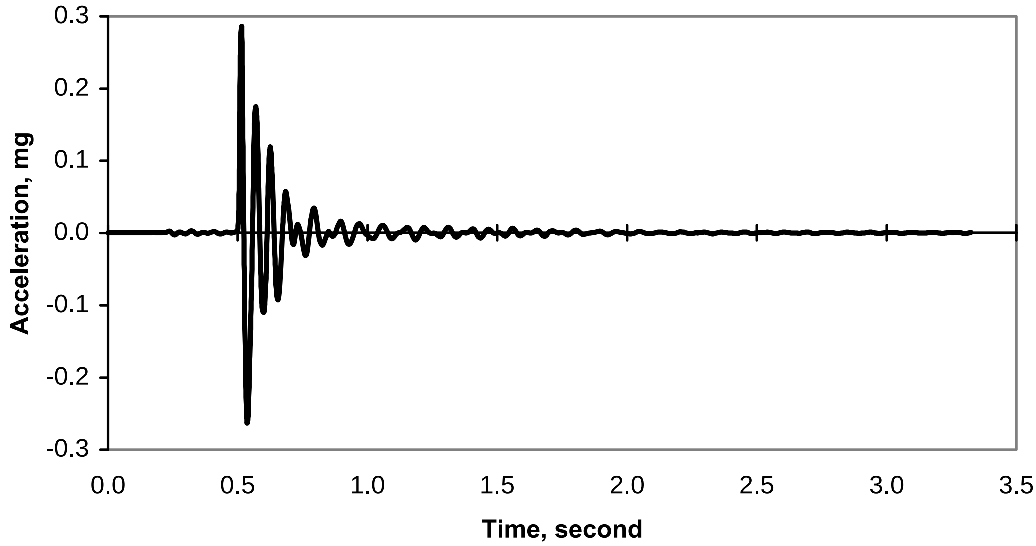

Figure 6.31 Acceleration-time graph for the dynamic test of the damaged SP2 (F = 15 kN)

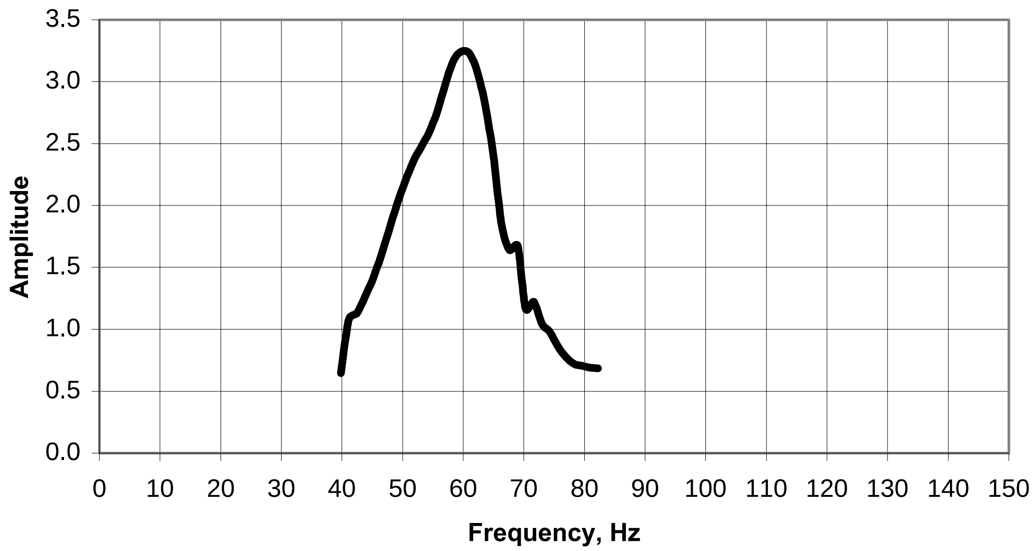

Figure 6.32 Frequency response curve for the dynamic test of the damaged SP2 (F = 15 kN).

The natural period vibration was 0.0168 sec, the natural cyclic frequency was 59.7 Hz and the damping ratio was 0.117 for the undamaged SP2 when it was pulled back F = 15 kN lateral force.

The acceleration time graph and the frequency response curve are given in Figures 6.33 and 6.34 when the undamaged SP2 was pulled back with F = 20 kN lateral force.

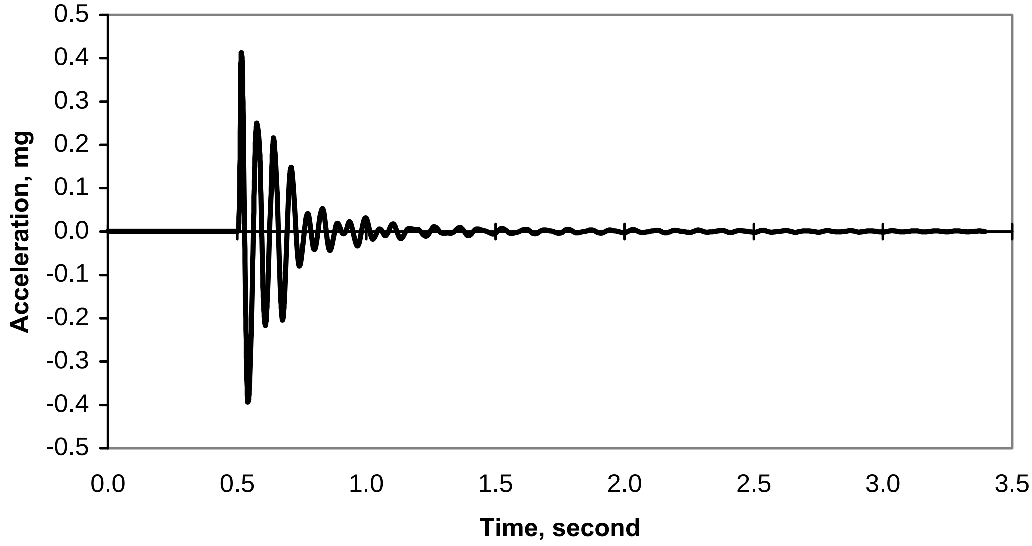

Figure 6.33 Acceleration-time graph for the dynamic test of the damaged SP2 (F = 20 kN).

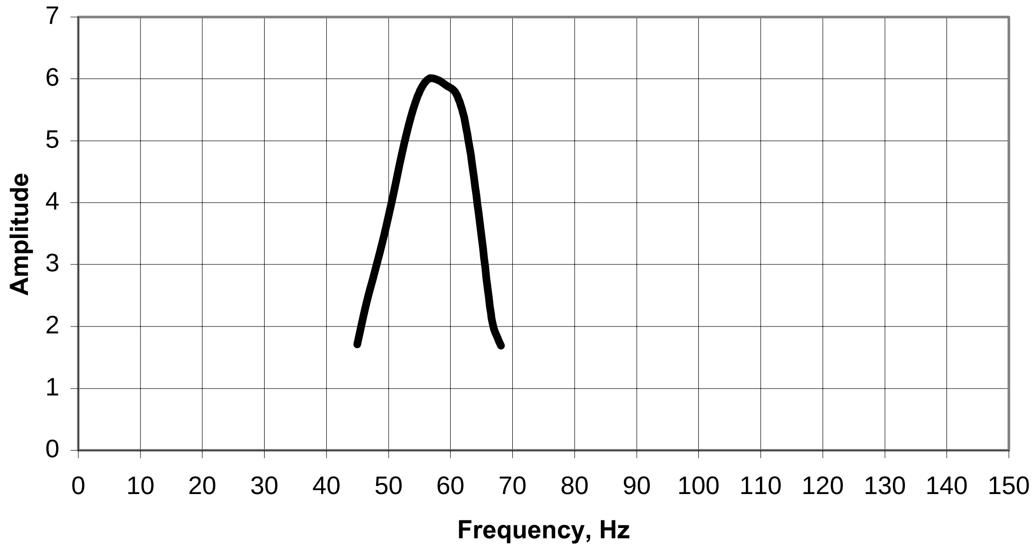

Figure 6.34 Frequency response curve for the dynamic test of the damaged SP2 (F = 20 kN).

The natural period vibration was 0.0177 sec, the natural cyclic frequency was 56.534 Hz and the damping ratio was 0.112 for the undamaged SP2 when it was pulled back F= 20 kN lateral force.

The acceleration time graph and the frequency response curve are given in Figures 6.35 and 6.36 when the damaged SP2 was pulled back with F = 20 kN lateral force.

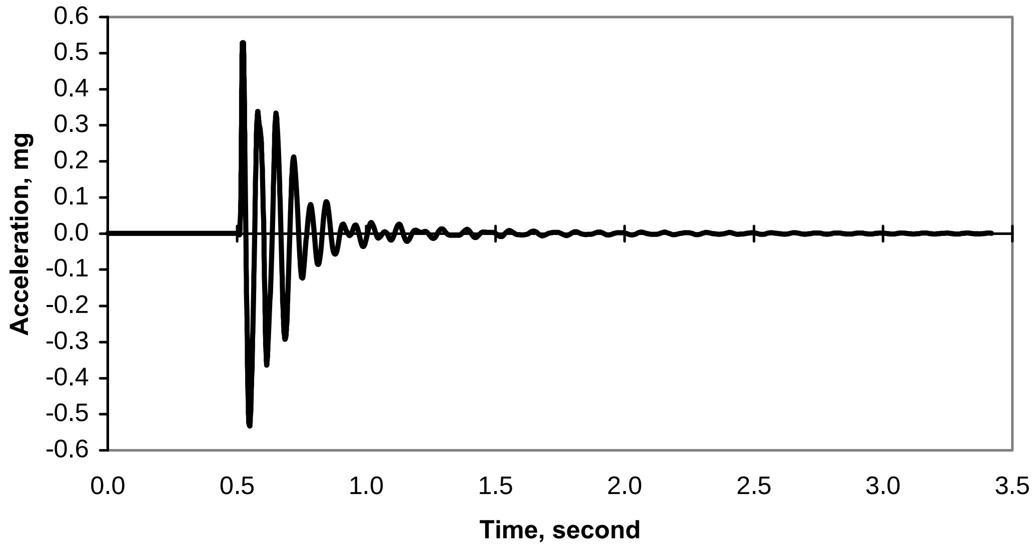

Figure 6.35 Acceleration-time graph for the dynamic test of the damaged SP2 (F = 20 kN).

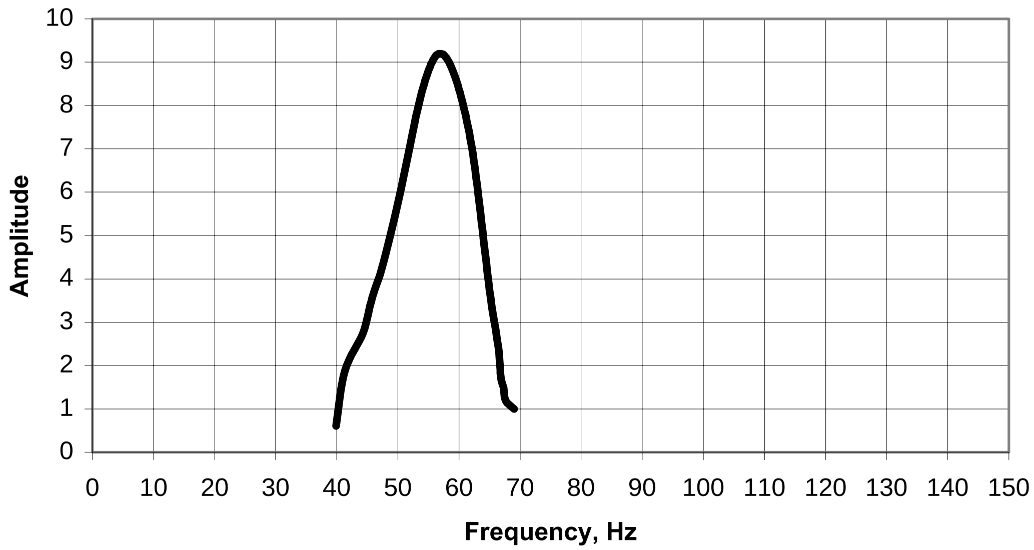

Figure 6.36 Frequency response curve for the dynamic test of the damaged SP2 (F = 20 kN).

The natural period vibration was 0.0174 sec, the natural cyclic frequency was 57.6 Hz and the damping ratio was 0.112 for the undamaged SP2 when it was pulled back F= 20 kN lateral force. Table 6.4 shows the summary of the dynamic properties of the damaged SP2.

Table 6.4 Dynamic properties of damaged SP2

Case	Frequency,	Natural period, sec	Damping ratio
F = 10 kN Lat. force	68.885	0.0145	0.1173
F = 15 kN Lat. force	59.705	0.0168	0.1172
F1 = 20 kN Lat. force	56.534	0.0177	0.1122
F2= 20 kN Lat. force	56.123	0.0178	0.1122
Mean values	60.310	0.0167	0.1147

The free vibration tests on the damaged SP2 show that the mean values of the natural periods and damping ratios are 0.0142 and 0.0923, respectively. In the free vibration tests of the damaged SP2 the mean values of the natural period and damping ratios were 0.0167 and 0.1147. The natural period increases 0.0167 / 0.05628= 1.077 times and damping ratio increases 0.0167 / 0.0142 = 1.176 times from the undamaged case to the damaged case for SP2.

6.7 COMPARISON OF THE DYNAMIC TEST RESULTS

Table 6.5 shows the summary of dynamic properties of the test specimens. In the first dynamic tests on SP1 the natural period and damping ratio are found to be 0.0270 sec and 0.039, respectively, for the uncracked case. The second dynamic tests on SP1 show that the natural period and damping ratio increase up to 0.041 sec and 0.0935, respectively, for the cracked case. The natural period increases 0.041 / 0.027 = 1.518 times and damping ratio increases 0.0935 / 0.039 = 2.397 times from the uncracked case to the cracked case for SP1.

For SP2 the natural period and the damping ratio in the first dynamic test are found to be 0.0142 sec and 0.0934, respectively. The natural period and the damping ratio of SP2 in the second dynamic tests increase up to 0.0167 sec and 0.1125, respectively, for the cracked case. The natural period and the damping ratio increase 0.0167 / 0.0142 = 1.176 and 0.1125 / 0.0934 = 1.2045 times, respectively, from the first dynamic test to the second dynamic test on SP2.

The increment of the natural period and the damping ratios from the first dynamic test to the second dynamic test on SP1 is considerable, but it is negligible for SP2. It is seen from Table 6.5 that after cracking the natural period of vibration increases.

Table 6.5 Dynamic properties of the panel form test specimens.

CASE	Natural period	Damping ratio
1st dynamic test on SP1	0.0270	0.0390
2nd dynamic test on SP1	0.0410	0.0935
1st dynamic test on SP2	0.0142	0.0934
2nd dynamic test on SP2	0.0167	0.1125

Spectrum coefficient S(T), which is defined in Turkish Earthquake Code (AY-1997), is defined by Equations 6.3 and illustrated in Figure 6.37,

$S(T) = 1 + 1.5\ T / T_A$ $\quad (0 \leq T \leq T_A)$ $\quad$ (6.3a)

$S(T) = 2.5$ $\quad (T_A \leq T \leq T_B)$ $\quad$ (6.3b)

$S(T) = 2.5\ (T_B / T_1)^{0.8}$ $\quad (T_B < T)$ $\quad$ (6.3c)

where, T_A , T_B : spectrum characteristic periods which depend on the local soil class. T_A and T_B are given in Table 6.6.

Table 6.6 Spectrum characteristic periods (T_A, T_B) in AY-1997

Local soil class	T_A (second)	T_B (second)
Z1	0.10	0.30
Z2	0.15	0.40
Z3	0.15	0.60
Z4	0.20	0.90

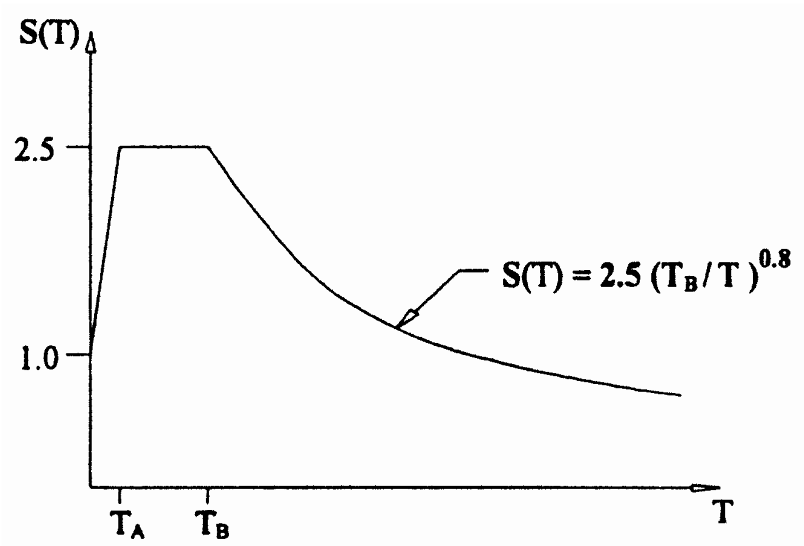

Figure 6.37 Response spectrum shape in AY-1997.

Tunnel form buildings are very stiff structures, therefore natural period of vibrations of the tunnel form structures are generally smaller than 0.10 seconds. It is seen from the response spectrum shape that after cracking the spectrum values of the tunnel form buildings increase due to increasing of the natural period of vibration. Earthquake forces on the tunnel form buildings also increase after cracking of the wall section. It can be concluded that a tunnel form building is not safe, after concrete cracking, during an earthquake.

6.8 EIGENVALUE ANALYSIS FOR THE PANEL FORM TEST SPECIMENS

Mode superposition analysis was performed on the test specimens to determine the frequencies, periods, mode shapes, modal displacements and mass participation ratios. Test specimens were modeled by using the finite element techniques and wide-column-frame analogy. A general-purpose finite element program called SAP2000 was used.

6.8.1 Finite Element Modeling

In this study shear walls and slabs are modeled by using a rectangular mesh of isotropic shell elements of four joint formulations, which combine the membrane and plate-bending behavior. This shell element activates all six degrees of freedom at each of its connected joints. Each shell element has its own local coordinate system for defining material properties, mass, loads, and for interpreting output.

In order to satisfy adequate accuracy for the test specimens, the walls are divided into elements having dimensions of 158.75 mm × 200 mm and the floor slabs are divided into elements having dimensions of 168 mm × 200 mm, as shown in Figure 6.38. The result of the eigenvalue analysis by using finite element method is given in Table 6.7. Fundamental periods of vibration of the specimens for 1st, 2nd, and 3rd modes are given in Figures 6.39, 6.40 and 6.41, respectively.

Table 6.7 The result of the eigenvalue analysis for finite element modeling

Mode Number	Frequency (cycles/sec)	Period (second)	Mode Shape
1	37.593	0.0266	Translation along short dimension
2	45.871	0.0218	Torsional motion
3	61.350	0.0163	Translation along long dimension

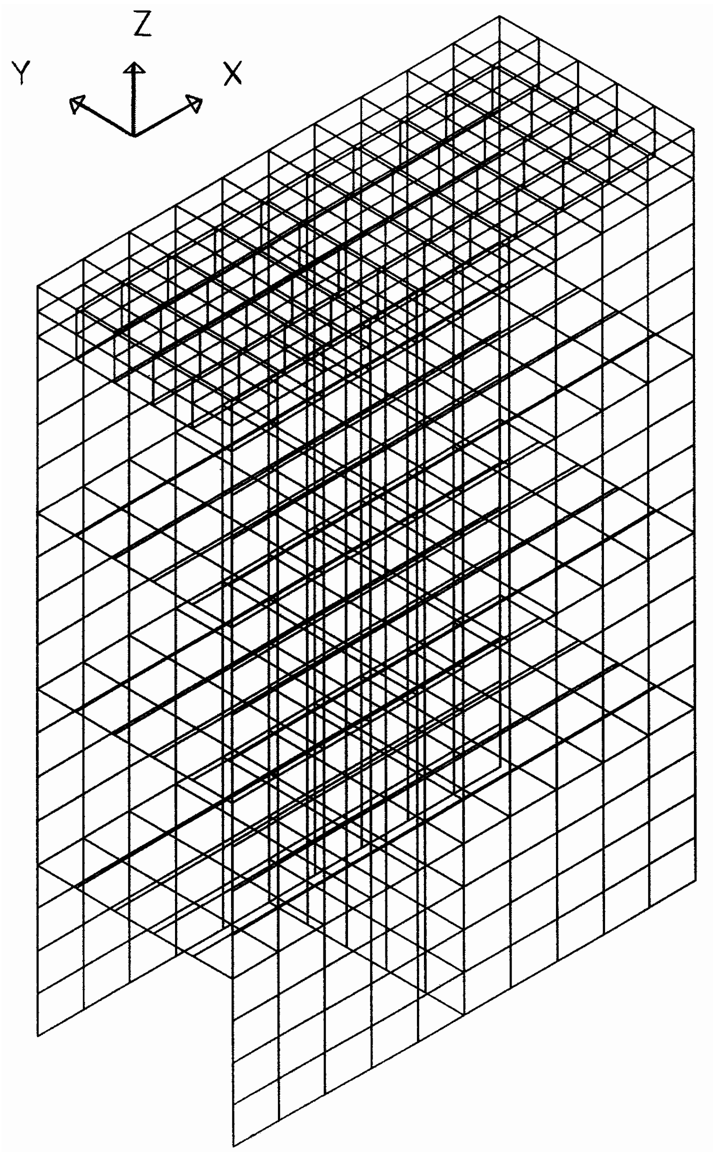

Figure 6.38 Finite Element Modeling of the panel form test specimens.

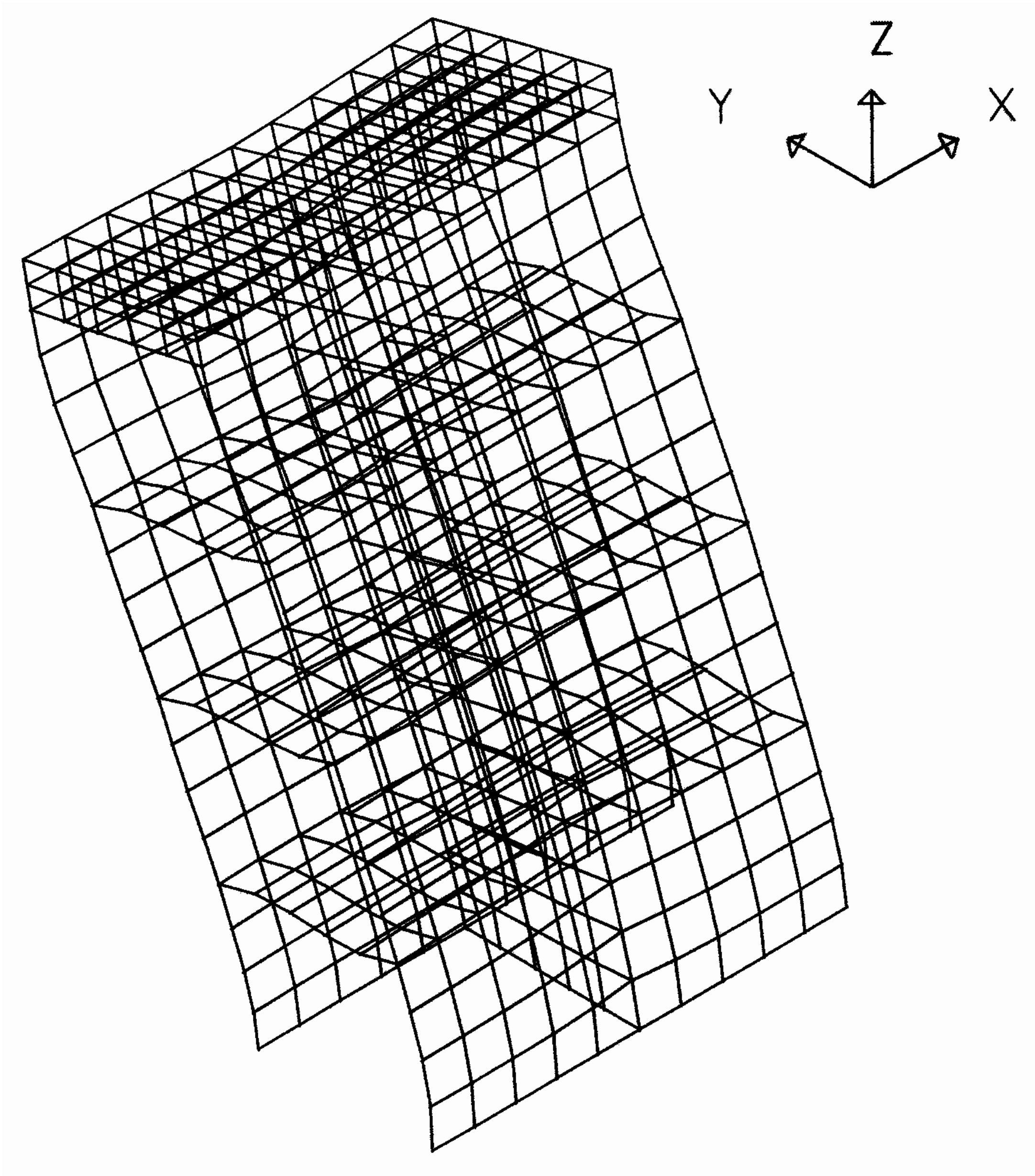

Figure 6.39 Fundamental period of vibration of the specimens for translation motion in short dimension (1st mode).

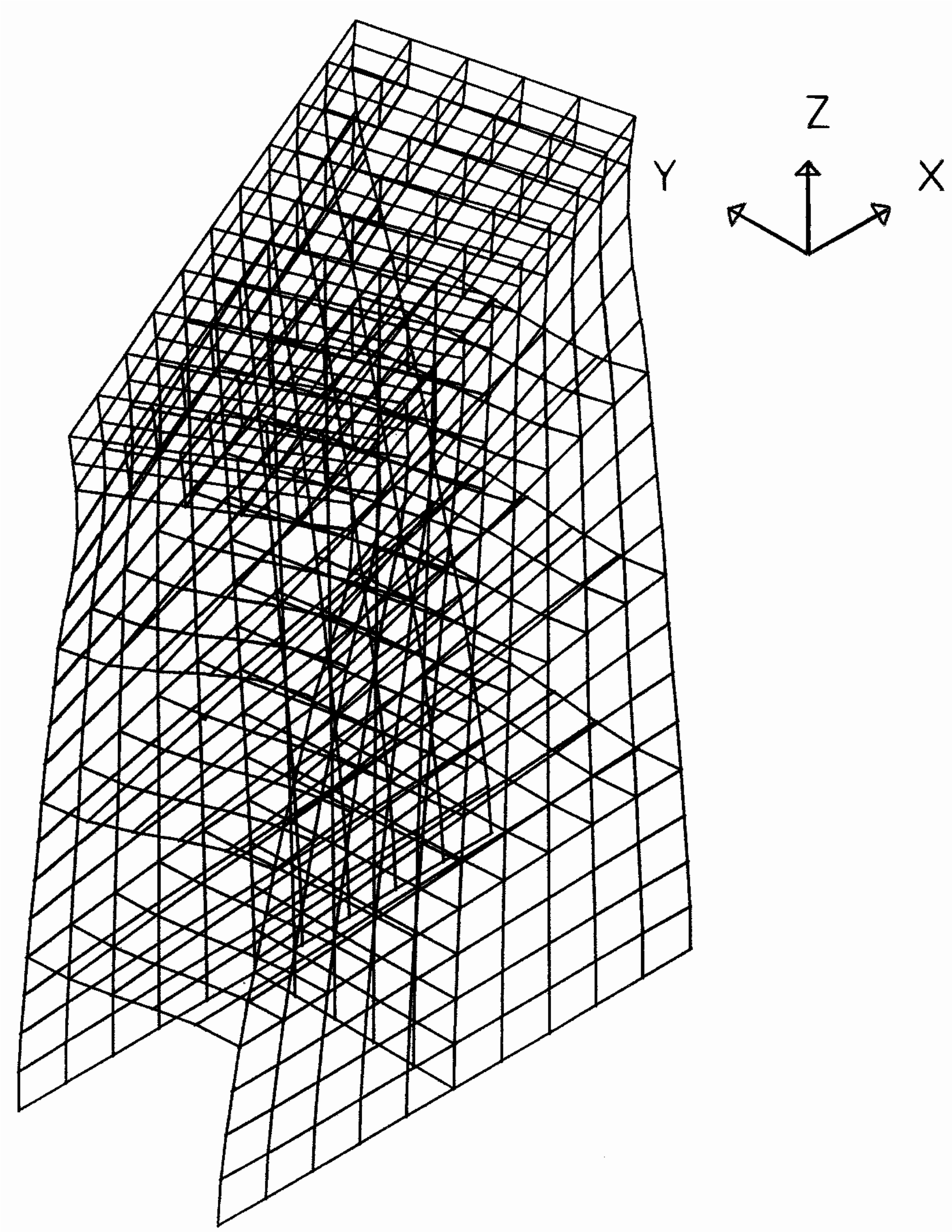

Figure 6.40 Fundamental period of vibration of the specimens for torsional motion (2^{nd} mode).

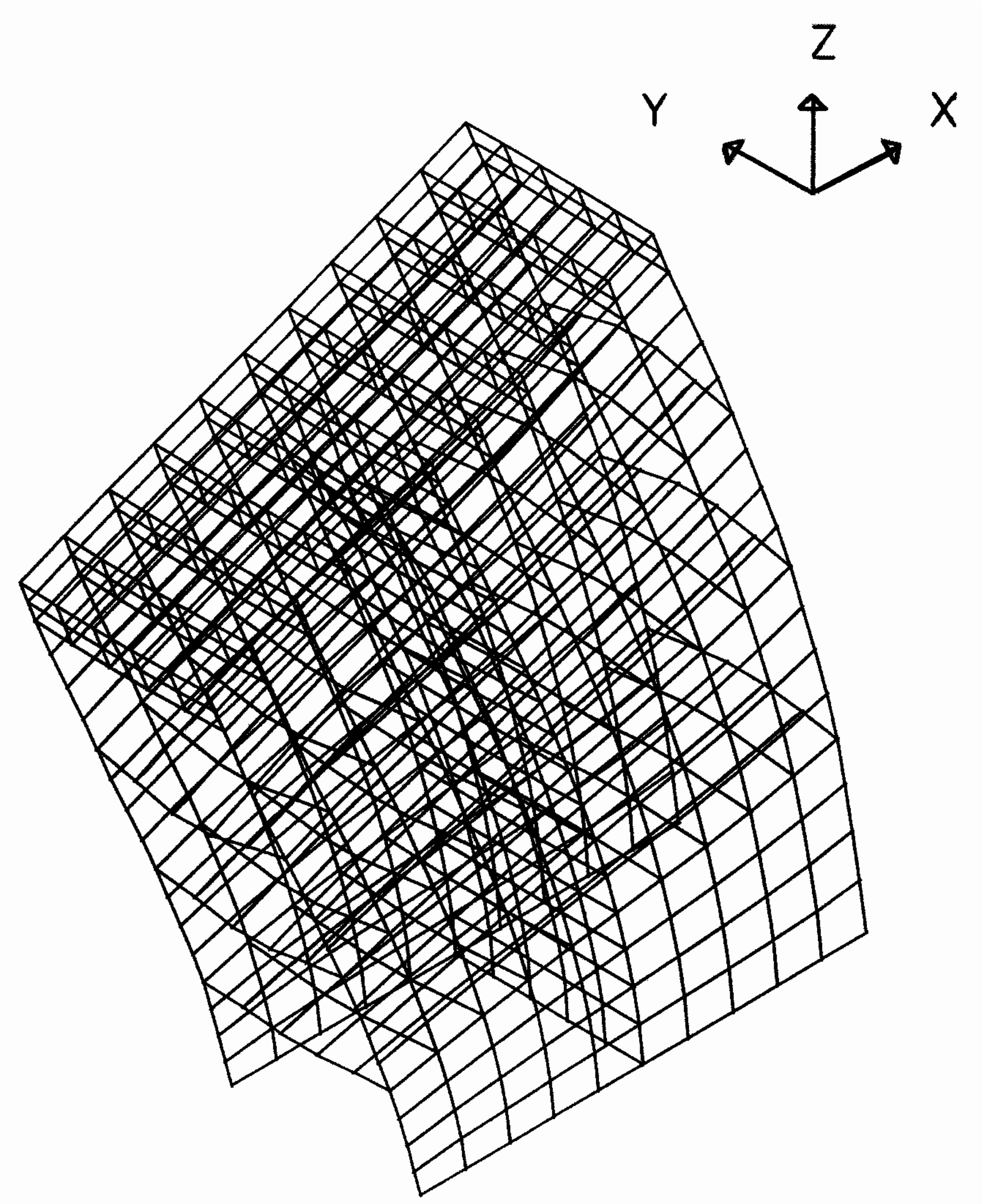

Figure 6.41 Fundamental period of vibration of the specimens for translation motion in long dimension (3rd mode).

6.8.2 Wide Column Analogy

In high-rise structures, modeling of concrete shear wall structures with finite element method becomes a time consuming process. In addition, the use of this method on complex shear wall structures is still prohibitive in terms of cost. Therefore, design engineers prefer equivalent frame method. In this study, samples, which are constructed with shell elements in the previous section, are modeled according to the frame method by use of SAP2000 as shown in Figure 6.42. Each shear wall is considered as a column placed at the center of gravity of the wall, each column connected to the other columns by an infinitely rigid beam. Each column is assumed to have the sectional properties of the wall.

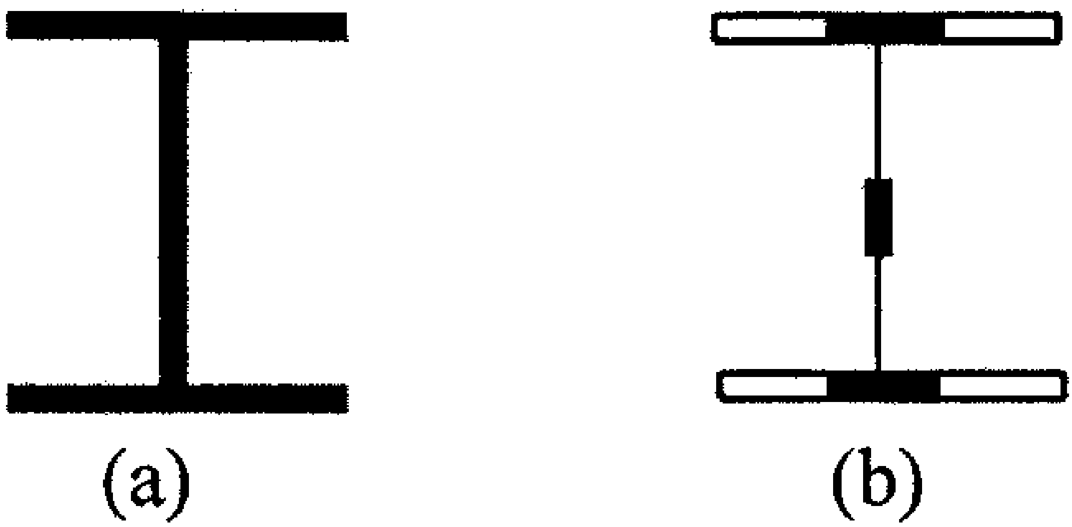

Figure 6.42 Wide-column frame modeling of the panel form test specimens.

After modeling of equivalent frame, actual sectional properties of structural walls and beams are assigned to line columns and connecting beams. One additional assumption that deserves special attention concerns the calculation of the structural properties of a concrete member. The cross-sectional area and the flexural stiffness are based on the gross concrete sections.

Theoretically, rigid arms are assumed to have infinite moments of inertia and sectional area. However, extremely large areas can create errors or large inaccuracies in the results. Therefore, although the program used allows infinite rigid arms, perfect rigidity is not applied to avoid unexpected errors. Area and moments of inertia of the rigid arms are determined according to the following formulas proposed (Mattachoine, 1991);

$$A_e = 100 \times (e/f)$$
$$I_e / I_f = 100 \times (e/f)^3 + 300\,(e/f)^2 + 300\,(e/f)$$

where,

e : length of stiff-ended section

f : half length of connected beam

A_e : area of stiff-ended section

I_e : moments of inertia of stiff ended section

A_f : area of connecting beam

I_f : moments of inertia of connecting beam

Because of their inherent economy, “Flat Slabs” are widely used in shear wall structures, in particular apartment buildings. In addition to carrying the floor loads, they also act as rigid horizontal diaphragms. Rigid-floor behavior is modeled by generating a joint in the plane of the diaphragm. Translational mass values and rotational mass value around out-of-plane axis are assigned to the master joints according to the procedure stated by the structure analysis program.

The result of the eigenvalue analysis by using wide column frame analogy is given in Table 6.8.

Table 6.8 The result of the eigenvalue analysis for wide column frame modeling.

Mode number	Frequency (cycles/sec)	Period (second)	Mode Shape
1	34.554	0.0289	Torsional motion
2	38.895	0.0257	Translation along short dimension
3	51.894	0.0193	Translation along long dimension

The first mode is torsional motion, the second and third modes are translational motion along the short and long dimensions, respectively if the panel form test specimens are modeled by wide column frame analogy. However, when the panel form test specimens are modeled by the finite element method, the first mode is translational motion along the short dimension, the second mode is torsional motion and the third mode is translational motion along the long dimension.

Table 6.9 shows the comparisons of the results of eigenvalue analysis. They are obtained by the finite element method and wide column frame analogy for the translational motion along short and long dimensions.

Table 6.9 Comparisons of the results of eigenvalue analysis that are obtained by finite element method and wide column frame analogy for the transnational motion along short and long dimension.

Mode shape	Natural period (sec) by wide column frame analogy	Natural period (sec) by finite element method
Translational motion along short dimension	0.0257	0.0218
Translational motion along long dimension	0.0193	0.0163

Natural vibration period obtained by using wide column analogy is 17.9 % greater than that obtained by using the finite element method for the translational motion along the short dimension. Also, natural vibration period obtained by using wide column analogy is 18.4 % grater than that obtained by using the finite element method for the translation motion along the long dimension.

6.8.3 Comparison of the Results of Free Vibration Test, Finite Element Method and Wide Column Analogy

Table 6.10 shows the comparisons of the results of fundamental period of vibrations obtained by dynamic tests finite element method and wide column frame analogy for the translational motion along short and long dimension.

Table 6.10 Comparisons of the fundamental period of vibrations of experimental and analytical results for the uncracked case.

Mode shape	Natural period (sec) by wide column frame analogy	Natural period (sec) by finite element method	Natural period (sec) by dynamic tests
Translational motion along short dimension	0.0257	0.0218	0.0270
Translational motion along long dimension	0.0193	0.0163	0.0142

In the free vibration tests of the test specimens the natural vibration along the short dimension and long dimension are found as 0.0270 sec and 0.0142 sec, respectively, for the uncracked case as seen in Table 6.9. The natural periods of vibration are found 0.0218 sec and 0.027 sec by wide column frame analogy and finite element method, respectively, for the uncracked case. Natural periods of vibration along the short dimension found by using wide column analogy and finite element method are 4.82 % and 19.62 % less than that found by dynamic tests, respectively. Natural periods of vibration along the long dimension found by using wide column analogy and finite element method are 26.43 % and 12.89 % greater than that found by dynamic tests.

The results can be summarized as follows:

Dynamic tests are performed on panel form units to determine the natural periods in X and Y directions of the cross-section. The panel form test units are modeled by the computer by using the Finite Element Technique and the Wide Column Analogy Technique. Theoretical natural periods are calculated. Natural periods obtained by using the finite element method, wide column analogy, and free vibration test from the dynamic experiments represent an agreement with acceptable errors. Experimentally found and theoretically calculated natural periods are almost the same. This fact proves a very important point that the computer models used satisfactorily reflect the realistic dynamic behavior of panel structures. The finite element model is commonly accepted to be realistic, but the wide column analogy is not as readily accepted. The dynamic analyses prove that the wide column analogy could also determine natural periods very close to the experimentally found correct values. The wide column analogy is a very valuable analytical tool for structural analysis. It reduces the two-dimensional panels to one-dimensional structural elements. Thus the panel structure can be modeled and analyzed as a framed structure. The framed structure, of course, is a method of analysis, which the design engineers are very familiar with.

CHAPTER 7

A MOMENT-CURVATURE PROGRAM FOR STRUCTURAL WALLS

7.1 INTRODUCTION

Shear wall cross-sectional dimensions, reinforcement detailing and the location of the confined sections are different those in actual columns and beams. Therefore some problems can arise in deriving moment-curvature relationships for shear walls. Available computer programs that are used to obtain the moment-curvature diagram have limited capacity in the modeling of reinforced concrete sections for shear walls. For example the available moment-curvature program Response (2000), which, is available on the web address of (http://www.ecf.utoronto.ca/~bentz/r2k.htm) does not have an option for the modeling of confined concrete. Therefore, the moment-curvature response of structural walls, which have confined end regions, cannot be predicted by using this program. For this purpose the computer program Waller2002, which includes the effects of steel strain hardening, confinement of concrete, and tension strength of concrete in deriving the moment-curvature relationship of shear walls, has been developed. The basic assumptions and algorithms of this program have been explained in detail. The results given by the Waller2002 for two cases where the longitudinal boundary reinforcement is not confined using transverse reinforcement are compared with those obtained from Response2000. Four shear wall cases were investigated by changing the longitudinal and transverse reinforcement ratio in the boundary element.

7.2 BASIC ASSUMPTIONS FOR DERIVING THE MOMENT CURVATURE RELATIONSHIP

Axial load-moment-curvature relationships (N-M-ϕ) for reinforced concrete structural walls have been calculated on the basis of following assumptions:

(a) Strain was assumed to be directly proportional to the distance from the neutral axis; height to length ratio H_w/l_w of walls is taken to be greater than two.

(b) Effect of shear was neglected.

(c) Perfect bond between steel and concrete is assumed.

(d) Longitudinal bars are taken not to buckle.

(e) Characteristic values are used for material strengths.

(f) The axial load was assumed to act through the centroid of the wall cross section.

(g) The model proposed by Hognestad (1951) was used for unconfined concrete under compression. The stress-strain curve of the Hognestad model is shown in Figure 7.1.

The initial part of the curvature is a second-degree parabola, expressed by Equation 7.1 (in this study SI units are used).

$$f_c = f_c'' \times \left[\frac{2\,\varepsilon_c}{\varepsilon_0} - \left(\frac{\varepsilon_c}{\varepsilon_0} \right)^2 \right] \tag{7.1}$$

where f_c is the stress, f_c'' is $0.85 \times f_{ck}$, f_{ck} is the compressive cylinder strength of concrete, ε_c is the strain value and ε_0 is the peak strain value of the stress-strain curve which is $\varepsilon_0 = 2 \times f_c''/E_c$, and E_c is the modulus of elasticity for concrete. The recommended formula for calculation of E_c is given in Equation 7.2.

$$E_c = 12680 + 460 \times f_c'' \tag{7.2}$$

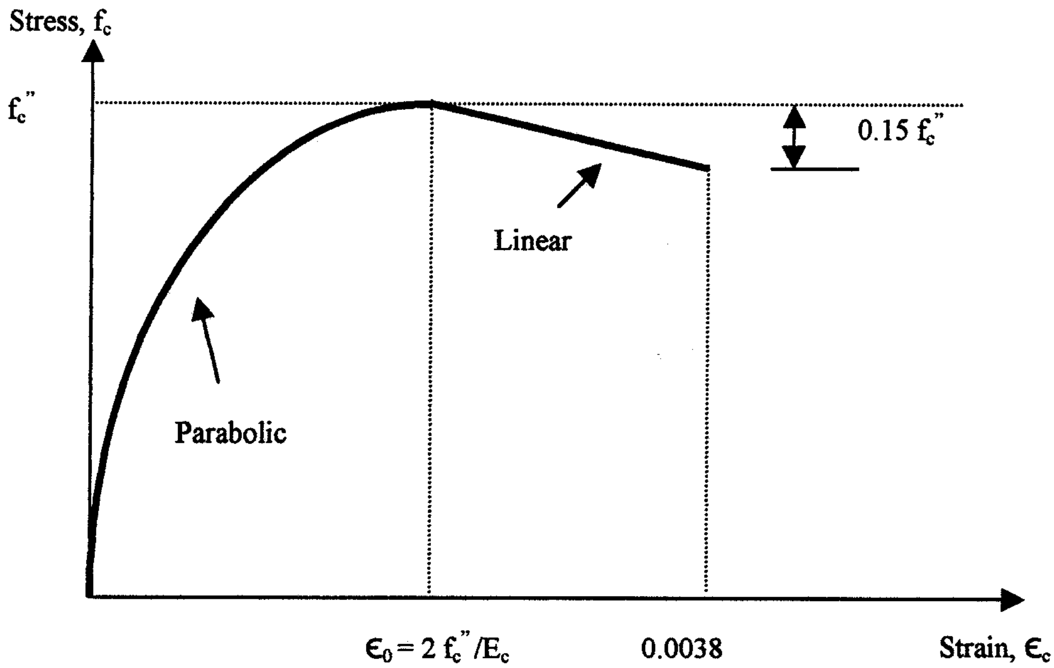

Figure 7.1 Hognestad stress-strain curve for unconfined concrete.

Between the strains corresponding the maximum stress, ε_0 and the ultimate strain, ε_{cu} the stress-strain relationship is assumed to be a descending straight line.

$$f_c = f_c''[1 - z(\varepsilon_c - \varepsilon_0)] \tag{7.3}$$

where z defines the slope of the assumed linear falling branch as

$$z = \frac{0.15}{0.038 - \varepsilon_0} \tag{7.4}$$

(h) The confined-concrete model proposed by Saatçioğlu and Razvi (1992) was used for confined region under compression. The model is based on the computation of confinement pressure starting from the material and geometric properties of confinement regions. The model incorporates the effect of unequal confinement pressures in two orthogonal directions and the superposition of pressures resulting from different types of confinement reinforcement.

Figure 7.2 illustrates the stress-strain curve of the Saatçioğlu and Razvi (1992) model for confined concrete. The model consists of a parabolic ascending branch, followed by a linear descending segment and a residual strength. Equation 7.5 describes the ascending branch of the Saatçioğlu and Razvi model for confined concrete.

$$f_c = f_{cc}'\left[2\left(\frac{\varepsilon_c}{\varepsilon_{coc}}\right)-\left(\frac{\varepsilon_c}{\varepsilon_{coc}}\right)^2\right]^{1/(1+2K)} \leq f_{cc}' \tag{7.5}$$

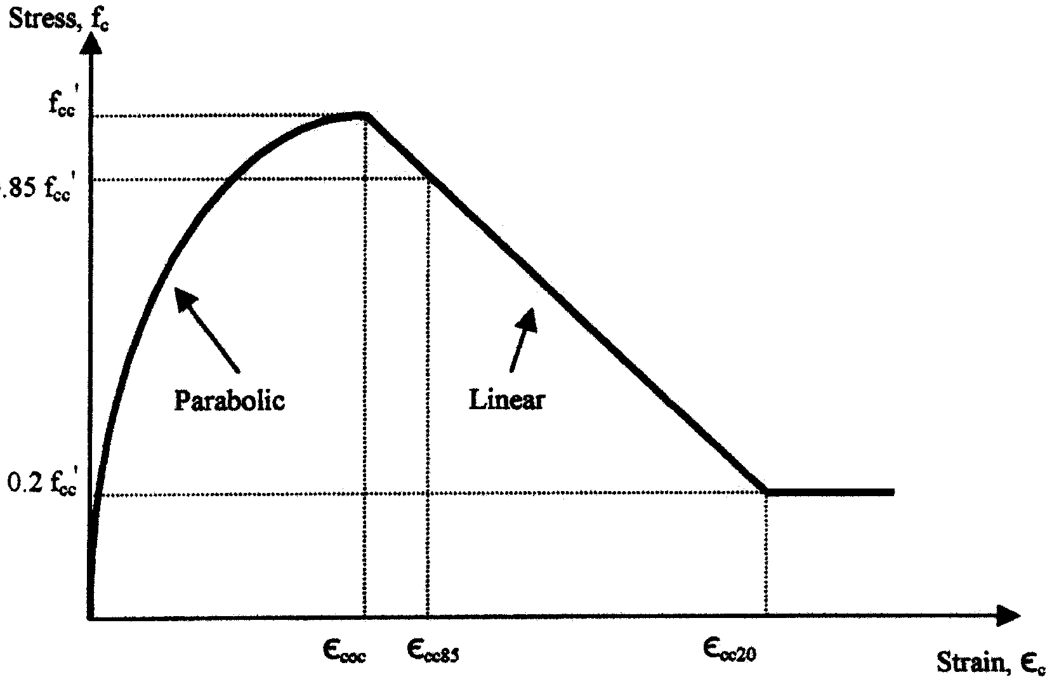

Figure 7.2 Stress-Strain curve of the Saatcioğlu and Ravzi model.

where f_c is the stress, ε_c is the strain, f_{cc}' is the confined concrete strength and ε_{coc} is the corresponding strain and K is a constant calculated considering the hoop spacing, spacing of laterally supported longitudinal reinforcement, equivalent uniform pressure, strength of unconfined concrete and the width and depth of the confined area. When the maximum stress is reached, the curvature follows the descending path, which can be described by Equation 7.6.

$$f_c = f_{cc}' \left[1 - z\left(\varepsilon_c - \varepsilon_{coc}\right)\right] \geq 0.2\, f_{cc}' \tag{7.6}$$

where parameter z defines the slope of the linear descending part. A constant residual strength is assumed at 20% strength level.

$$z = \frac{0.15}{\varepsilon_{cc85} - \varepsilon_{coc}} \tag{7.7}$$

(i) The bilinear model proposed by Rüsch (1963) was used to consider the tension strength of concrete. Since the tensile strength of concrete is very low and concrete cracks at low strains, tensile strength is generally neglected in strength calculations. However the structural walls which are a component of the tunnel form buildings have low reinforcement ratios and very high depth that result in a very large cracking moment as the ultimate moment in certain cases, hence the tensile strength of concrete becomes significant. Figure 7.3 shows the assumed stress-strain diagram for concrete in tension. The tensile strength of concrete is taken as $f_{ct} = 0.35\ (f_c)^{1/2}$ in calculations.

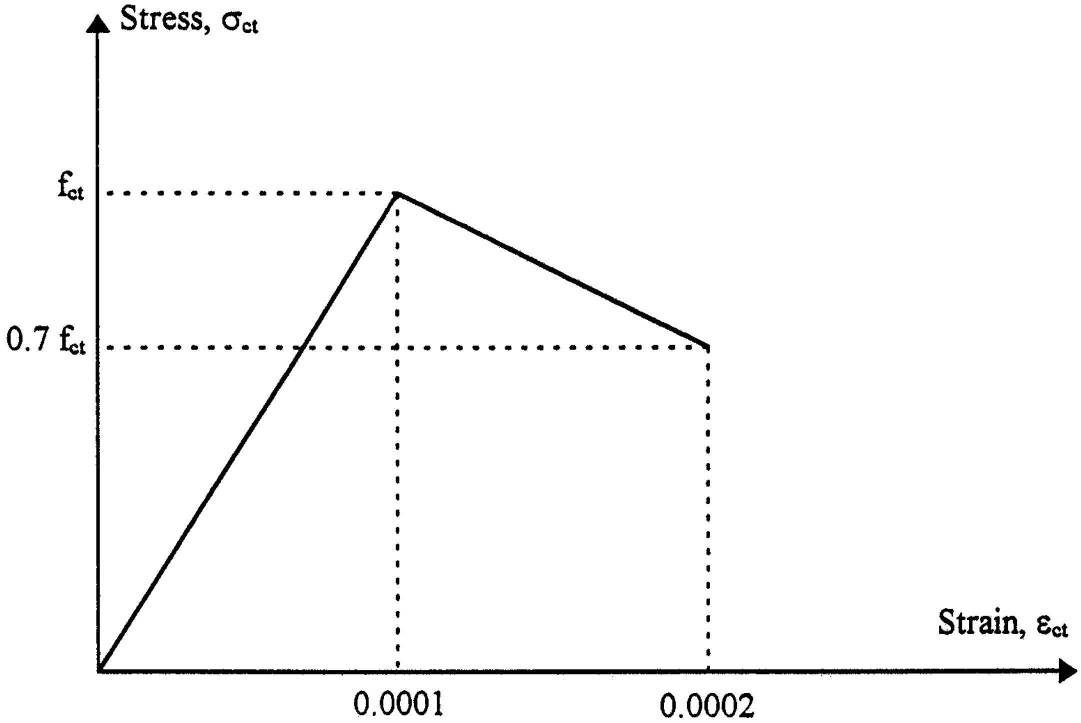

Figure 7.3 Assumed stress-strain diagram for concrete in tension.

(j) The stress-strain relation of the reinforcing steel is assumed to be identical under compression and tension. In the case study S500 mesh reinforcement was used for the web reinforcement and S420 was used for the boundary and confinement reinforcement for all the case studies. Figure 7.4 and Figure 7.5 show the stress-strain relationships of S420 and S500 type reinforcement, respectively. The mechanical properties of the S420 and S500 type reinforcement which is specified in TS500 (2000) were given in Table 7.1. The modulus of elasticity of steel is taken as E_s=200 GPa for the calculations.

Table 7.1 Mechanical properties of the S420 and S500 type reinforcement.

Steel Type	f_y(MPa)	f_{su}(MPa)	ε_{sy}	ε_{sp}	ε_{su}
S420	420	525	0.0021	0.01	0.1

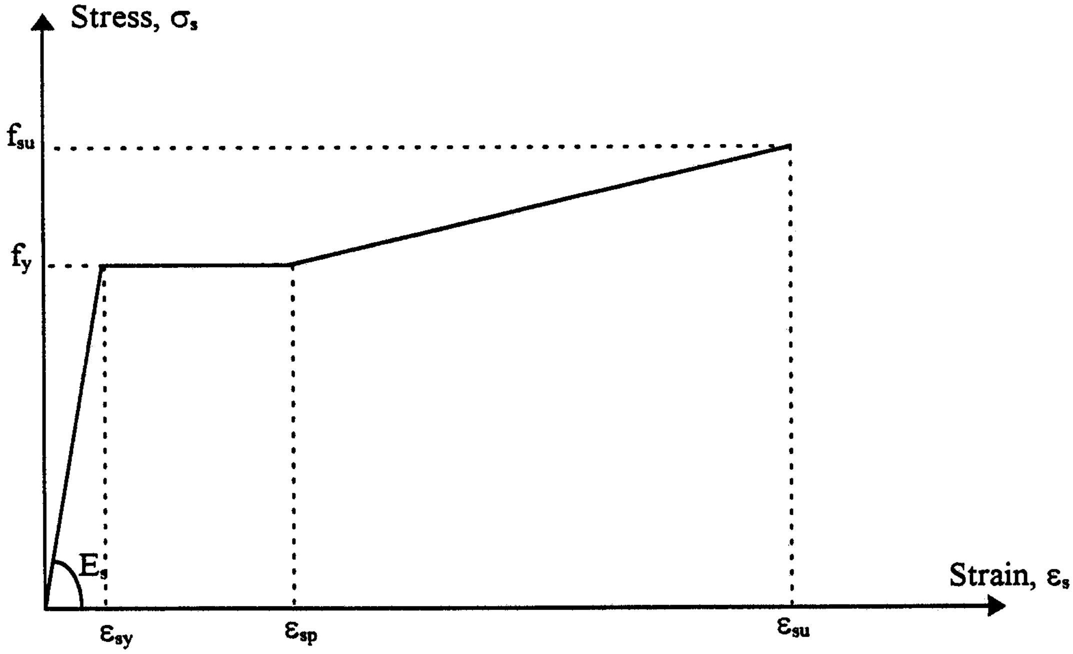

Figure 7.4 Assumed tri-linear stress-strain curve for S420 type reinforcement.

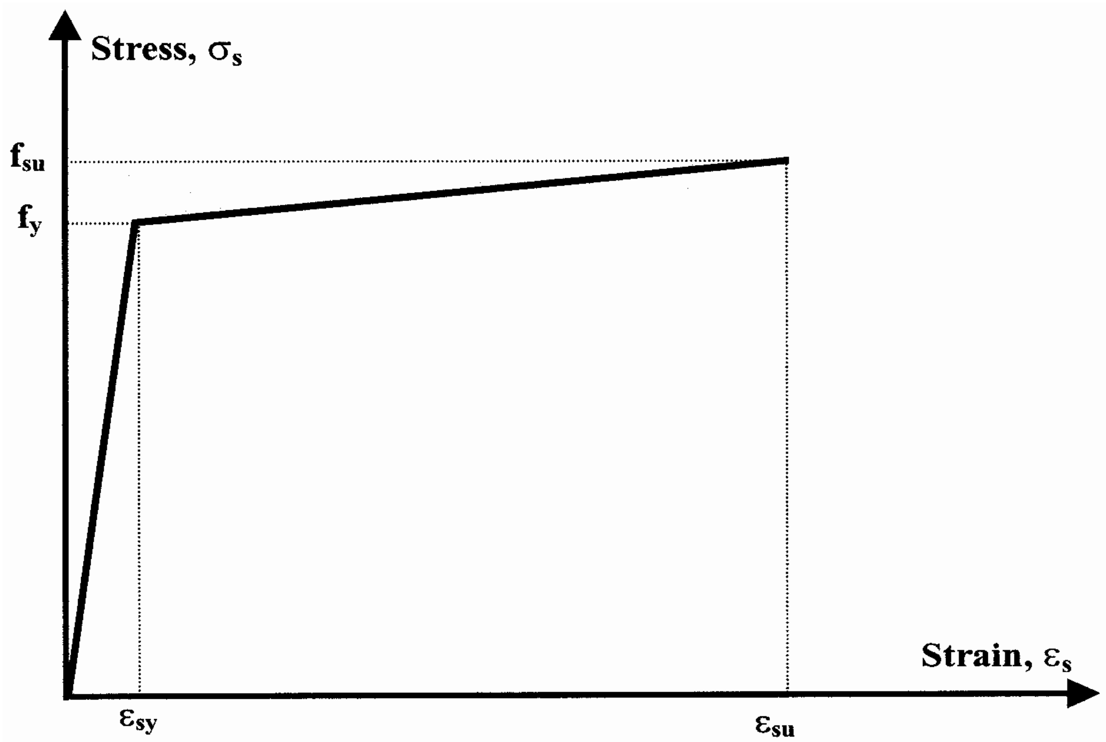

Figure 7.5 Assumed bi-linear stress-strain curve for S500 type reinforcement.

7.3 BASIC ALGORITHM

The cross section is idealized as a series of unconfined and confined concrete rectangular layers and steel layers that are each parallel to the neutral axis. It is assumed that the strain in each layer is uniform and equal to the actual strain at the center of the layer. The stress will also be taken as uniform over the layer and found from the assumed stress-strain relations. The force in each layer is found by multiplying the stress in the layer by the area of the layer. The moment contribution is found by multiplying the layer force by the distance between the middle of the layer and the plastic centroid of the cross-section. The stress resultants are determined by evaluating the forces in each layer of concrete and each layer of reinforcement. Obviously the idealization becomes more accurate as the layers become narrower, so layers of 1 mm thickness are used in this study. The theoretical moment curvature relation for a given axial load level can be determined by increasing the concrete strain in the extreme compression fiber. Iteration was started with a low extreme concrete fiber strain. This is a rather small strain value for concrete in compression. The analysis procedure involves the following steps:

1) Assign an initial value for the compressive strain at the extreme concrete fiber. An initial top strain value of -0.00001 is assigned in this study. However, in the analysis of some sections the force equilibrium cannot be found for small values of top strain, like -0.00001. In order to prevent this situation, the program finds the smallest top strain value at which the force equilibrium is satisfied and takes this value as the initial top strain and continues the process.

2) Assume a neutral axis depth. The depth of neutral axis is iterated starting from an initial value of 4 times the depth of the section until the force equilibrium is reached.

3) Calculate strains at the middle of each fiber.

4) Use stress-strain models for confined and unconfined concrete to determine the stress values at each fiber.

5) Determine the longitudinal steel strains from similar triangles of the strain diagram.

6) With the steel strain at each level, steel stresses are determined from the stress-strain diagram of steel. Forces in steel in each level are obtained by multiplying these stresses by the respective steel areas.

7) On the compression side, with the concrete strains at each fiber, concrete stresses are determined by entering the stress-strain curves of confined or unconfined concrete. Forces in confined and unconfined concrete fibers are obtained by multiplying these stresses by respective areas.

8) On the tension side, tensile stresses at each fiber are obtained by entering the stress strain curve of concrete in tension. Forces in concrete on the tension side are obtained by multiplying these stresses by the filament area.

9) Compute the sum of the internal forces and compare this with the external axial force. If the difference is less than or equal to 0.1%, results are acceptable. Otherwise, the position of the neutral axis is changed (go to step 2) until equilibrium is satisfied.

10) Calculate moment and curvature values. After the neutral axis depth corresponding to an extreme fiber strain is found, the total moment is calculated by summing up the fiber moments and the moments of longitudinal reinforcements about the plastic centroid of the section. Fiber moments are calculated by multiplying the fiber force by the distance from the middle of fiber to the geometric center of the section. Curvature is obtained by dividing the top fiber strain by the neutral axis depth. Top strain, bottom stain and the neutral axis depth are written corresponding to the moment-curvature values on the 'output sheet'.

11) Set the new concrete strain and go back to the step 2. Top strain value is assigned increasing the previous top strain value by 0.00001. When the force equilibrium at a top strain cannot be found, the program ends the process.

7.4 CURVATURE DUCTILITY

The most common and desirable sources of inelastic structural deformations are rotations in potential plastic hinges. Therefore, it is useful to relate section rotations per unit length (i.e., curvature) to causative bending moments. Curvature ductility ratios are calculated by dividing ultimate curvatures by yield curvatures and expressed as:

$$\mu_\phi = \phi_u / \phi_y \qquad (7.8)$$

The moment-curvature relation of a wall or wall system analyzed can be idealized by an approximated elastoplastic or bilinear moment-curvature relation in order to find the curvature ductility in a simpler way of solution. First yield is defined as the moment and curvature corresponding to $\varepsilon_y = f_y / E_s$, where the bottom tensile reinforcement starts to yield. For shear wall sections where there are many steel layers the yield curvature ϕ_y has to be defined. While assuming the bilinear relation, one must determine the yield curvature and corresponding yield moment to be used for this relation. In order to find this yield curvature, an approximation is made as described below.

- A tangent line is drawn to the first yield point on the moment-curvature diagram.
- The second line is drawn assuming the approximate increasing linear path after the yield point on the moment-curvature diagram.
- The yield curvature and the corresponding moment is found as the point where these two lines intersect.

The approximation procedure and the bilinear curve obtained are shown in Figure 7.6.

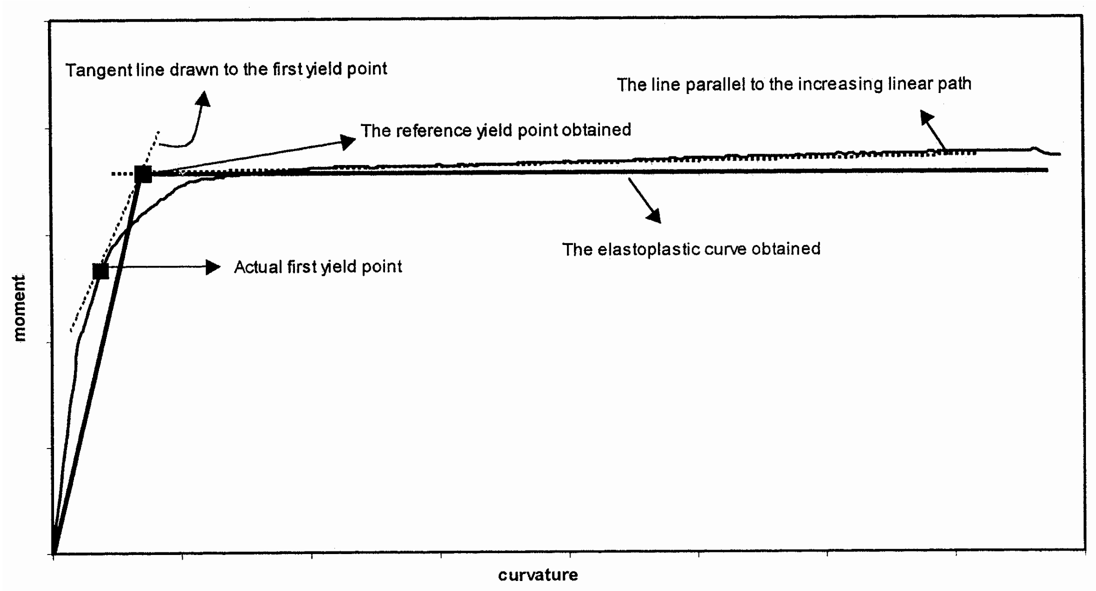

Figure 7.6 Determination process for bilinear moment-curvature diagram.

It is obvious that the yield curvature obtained from this assumption is a higher value from the first yield point, however especially in structural walls, this may be a good approximation as the walls are reinforced all along the wall length and so there is more than one layer of steel in the tension zone.

7.5 CASE AND VERIFICATION STUDIES

Four cases were investigated in this study. The analyses were based on a shear wall 4.6 m long and 200 mm wide, with f_{ck} = 20 MPa. The axial load compressive stress (N/A_g) was 2.17 MPa corresponding to an axial load ratio of $N/f_{ck}A_g$ = 0.108. In all cases boundary elements are provided at a distance of $l_u = 0.206 \times l_w$ = 950 mm from each end of the wall. The spacing of the longitudinal boundary reinforcement is 150 mm. Web reinforcement ratio is taken as 0.25% for shear walls in all cases for this study. To provide 0.25% web reinforcement ratio in the vertical and horizontal directions, 7 mm diameter two-layer mesh reinforcement (S500) was used in the web regions for shear walls. The spacing of longitudinal and vertical web reinforcement is 150 mm. The reinforcement characteristics and details of the shear walls are given in Table 7.2 and illustrated in Figure 7.7.

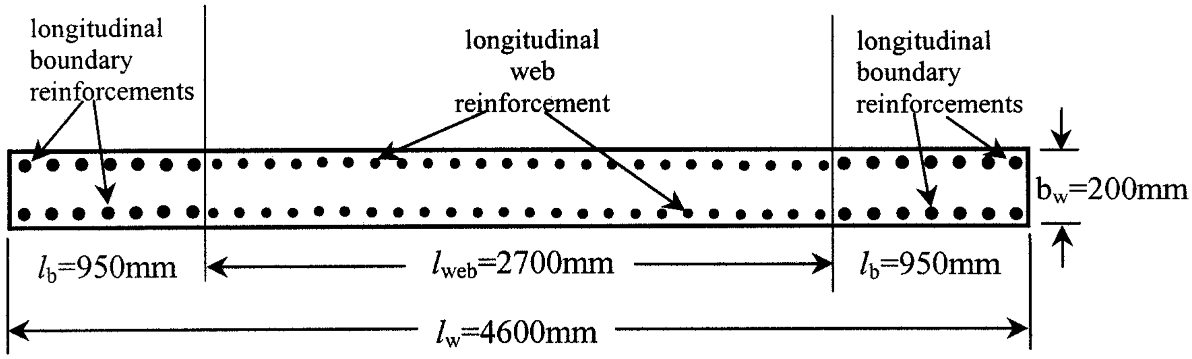

Figure 7.7 Reinforcement details of the shear walls for case studies.

Table 7.2 Reinforcement details of the shear walls.

Wall code	Flexural boundary reinforcement	Flexural boundary reinforcement ρ_b percent (%)	Transverse reinforcement in boundary element	Transverse reinforcement ratio in boundary element
SW1	14ϕ14(S420)	0.234	ϕ8/75mm(S420)	0.564%
SW2	14ϕ20(S420)	0.478	ϕ8/75mm(S420)	0.564%
SW3	14ϕ14(S420)	0.234	No confinement in boundary element	No confinement in boundary element
SW4	14ϕ20(S420)	0.478	No confinement in boundary element	No confinement in boundary element

The longitudinal boundary reinforcement ratio is 0.234% for Shear Wall 1 (SW1) and Shear Wall 3 (SW3). The longitudinal boundary reinforcement ratio is increased twice (0.478%) for boundary elements in Shear Wall 2 (SW2) and Shear

Wall 4 (SW4) to study the effect of the longitudinal boundary reinforcement ratio of shear walls. 8 mm diameter transverse reinforcement with 75 mm spacing is used to confine the boundary elements in SW1 and SW2. The reinforcement detail for confined boundary regions of SW1 and SW2 is shown in Figure 7.8. The transverse reinforcement ratio is 0.564% for boundary elements in these two walls. Boundary elements in Shear Wall 3 and Shear Wall 4 are not confined so as to be able to observe the confinement effect in shear walls.

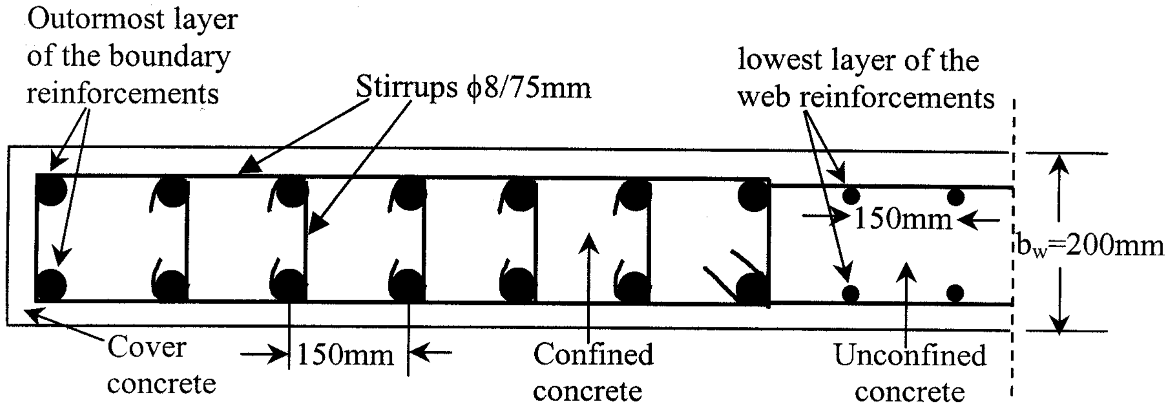

Figure 7.8 Reinforcement detail for confined boundary regions of SW1 and SW2.

7.6 SHEAR WALL 1 (SW1)

For this first case a detailed explanation was presented about the moment curvature diagram and relationship to be able to show the behavior of the wall. The calculated response of SW1 is summarized in Table 7.3 and illustrated in Figure 7.9.

Figure 7.9 Moment-curvature diagram of the SW1.

Table 7.3 The summary of the calculated response of the SW1.

ε_{top}	ε_{bottom}	ϕ(rad/km)	M(kNm)	Comments
-0.00036	0.00021	0.124	4171	Concrete cracks
-0.00106	0.00214	0.695	6812	Bottom steel yields
-0.00132	0.00301	0.941	7509	All boundary reinforcements yield
-0.0148	0.00367	1.119	7717	Web reinforcement starts to yield
-0.00278	0.01016	2.814	8397	Strain hardening at bottom steel
-0.0038	0.01553	4.202	8558	Cover crushing starts
-0.01555	0.06927	18.439	8800	1^{st} web reinforcement rupture
-0.01636	0.07332	19.495	8708	2^{nd} web reinforcement rupture
-0.01722	0.07763	20.619	8623	3^{rd} web reinforcement rupture
-0.01821	0.08268	21.933	8545	4^{th} web reinforcement rupture
-0.01955	0.08917	23.635	8476	5^{th} web reinforcement rupture
-0.02084	0.09543	25.277	8411	6^{th} web reinforcement rupture
-0.02119	0.09683	25.656	8415	Ultimate curvature
Yield curvature (ϕ_y) = 0.868 rad/km				Curvature Ductility Ratio (μ_ϕ) = 29.56

For a large moment the concrete remains uncracked. Cracking marks the points where the moment-curvature relationship begins to change its slope. The initial change in slope immediately after cracking is rather small. When the applied moment is greater than 7509 kN all the boundary reinforcement in the tension side yields. After that the web reinforcements start to yield, strain hardening starts at the outermost longitudinal boundary reinforcement and the moment curvature diagram get rounded in nature. We can see from the moment curvature diagrams that there is a small change for moment corresponding to the extreme compression fiber strain -0.0038 (ϕ=4.202 rad/km M=8558 kNm). When the extreme compression fiber strain reaches -0.0038 the unconfined cover concrete start to crush. After a small decrease in moment, it starts to increase again slowly according to the ductility of the section. After the spalling of the top cover concrete is completed, cover crushing continues at the edges of confined boundary regions. At a moment of 8800 kNm the strain in the lowest layer of the web reinforcement (S500) is predicted to be 0.0501. This value of strain will cause rupture of this reinforcement. Five more web reinforcements reached their ultimate strain (ε_{su}=0.05) and ruptured consecutively as can be observed from the moment-curvature diagram. At a curvature value of 25.656 rad/km the strain in the outermost layer of the longitudinal boundary reinforcement (S420) is 0.097. Rupture of this reinforcement defines the capacity of the member. At this stage cover concrete with a length of 678 mm (82% of the neutral axis depth) from the compression edge of the wall spalled. Confined concrete in the confined boundary region was not crushed. Failure of the Shear Wall 1 occurs by rupturing of the reinforcement rather than by crushing of the concrete.

7.7 SHEAR WALL 2 (SW2)

The moment curvature curve of the SW1 and SW2 is plotted on the same graph to be able to compare the effect of longitudinal boundary reinforcement ratio in shear walls that have confined boundary elements at each end of the wall. The calculated response of SW2 is summarized in Table 7.4 and illustrated in Figure 7.10.

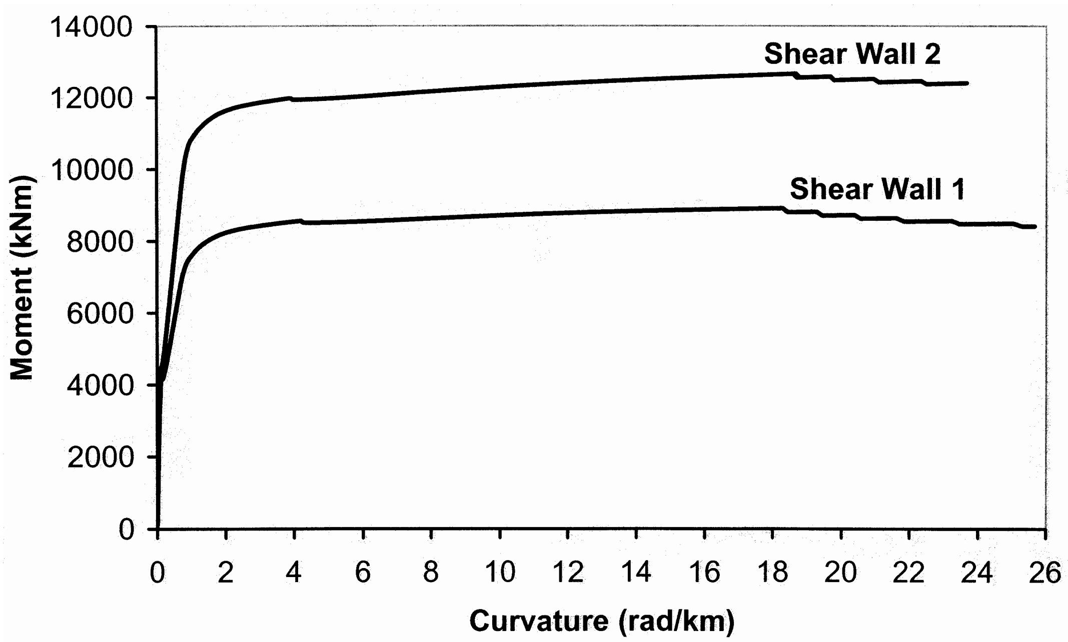

Figure 7.10 Moment curvature diagram of SW1 and SW2.

Table 7.4 The summary of the calculated response of the SW2.

ε_{top}	ε_{bottom}	ϕ(rad/km)	M(kNm)	Comments
-0.00035	0.00021	0.122	4487	Concrete cracks
-0.00119	0.00214	0.725	9595	Bottom steel yields
-0.0015	0.00304	0.988	10796	All boundary reinforcements yield
-0.0167	0.00373	1.175	11043	Web reinforcement yields
-0.00301	0.0102	2.873	11827	Strain hardening at bottom steel
-0.0038	0.01421	3.915	11975	Cover crushing starts
-0.01679	0.06961	18.783	12546	1st web reinforcement rupture
-0.01775	0.07388	19.92	12479	2nd web reinforcement rupture
-0.01874	0.07825	21.085	12417	3rd web reinforcement rupture
-0.02003	0.08357	22.522	12366	4th web reinforcement rupture
-0.02119	0.08766	23.662	12394	Ultimate curvature
Yield curvature (ϕ_y) = 0.905 rad/km			Curvature ductility ratio (μ_ϕ) = 26.15	

The overall behavior of SW1 and SW2 is identical. Failure occurs similar to SW1 by rupturing of the lowest four layers of web reinforcement and the outermost level of longitudinal boundary reinforcement. At this stage the cover concrete with a length of 735mm (82% of the neutral axis depth) from the compression edge of the wall spalled. Confined concrete in the confined boundary region was not crushed.

As a result of two times, increase in the longitudinal boundary reinforcement ratio, a 40% increase in moment capacity is observed. However the ductility of the system reduces slightly. There is a 4.3% increase in yield curvature. The ultimate curvature and curvature ductility ratios decrease 7.8% and 11.5%, respectively.

7.8 SHEAR WALL 3 (SW3) and SHEAR WALL 4 (SW4)

SW3 and SW4 are analyzed with both Waller2002 and Response2000. Two moment curvature curves obtained from these programs were plotted on the same graph to be able to examine the differences. It is seen from Figure 7.11 that the moment curvature curves obtained by these programs are close to each other. The small difference at ultimate curvature is due to the models used for unconfined concrete. The Hognestad model and parabolic models are used in Waller 2002 and Response2000, respectively.

The overall behavior of SW3 and SW4 is almost the same. The behavior of SW3 and SW4 is explained and calculated responses are summarized in Table 7.5 and Table 7.6, respectively, according to the output of Waller2002. For SW1 and SW3 at the bottom concrete strain of 0.00021 concrete cracks and the slope of moment curvature curves is changed. Before the unconfined cover concrete crushes (ε_{contop}=-0.0038) all the longitudinal boundary reinforcement and the outermost mesh reinforcement yield. Even strain hardening starts at the bottom layer of the longitudinal boundary reinforcement in both cases. Both shear walls show brittle failure and their failure occurs by crushing of the concrete, reinforcement rupture does not occur in either case.

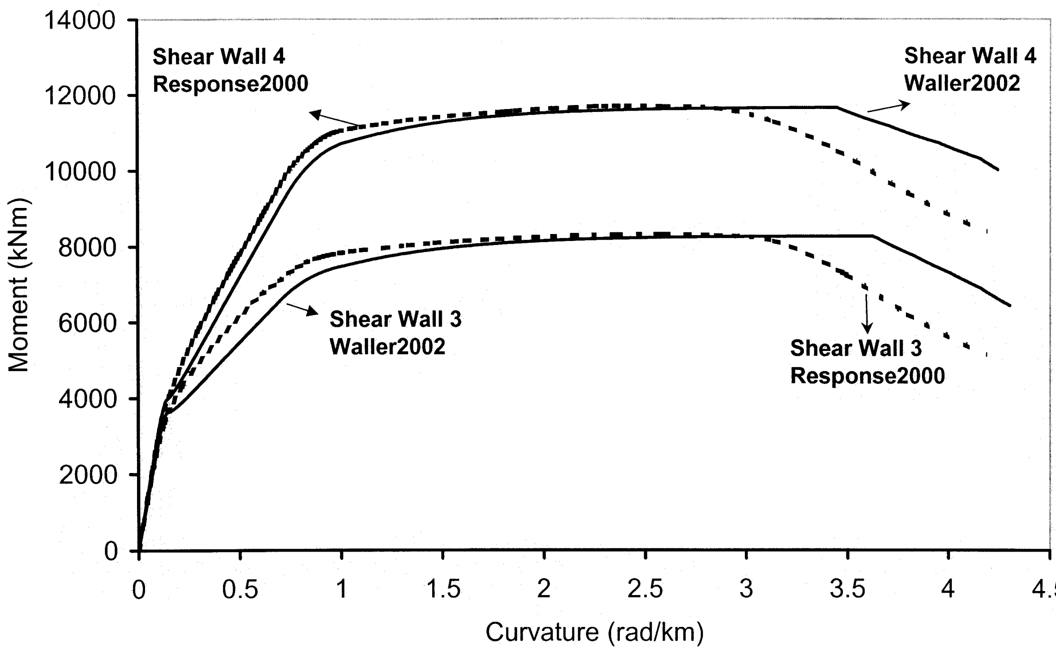

Figure 7.11 Moment curvature diagram of SW3 and SW4.

For this case that the longitudinal end reinforcement is not confined by lateral reinforcement, and a two times, increase in the longitudinal end reinforcement ratio causes a 40.9% increase in moment capacity. Furthermore, there is also an 8.7% increase in yield curvature and 4% decrease in ultimate curvature, which results in an 11.6% decrease in the curvature ductility ratio.

Table 7.5 The Summary of the Calculated Response of the Shear Wall 3.

ε_{top}	ε_{bottom}	ϕ(rad/km	M(kNm**)**	Comments
-0.00044	0.00021	0.141	3612	Concrete cracks
-0.00117	0.00213	0.718	6671	Bottom steel yields
-0.00144	0.00303	0.973	7429	All boundary reinforcements yield
-0.0016	0.00368	1.147	7644	Web reinforcement starts to yield
-0.00311	0.01015	2.822	8251	Strain hardening at bottom steel
-0.0038	0.01286	3.623	8265	Cover crushing starts
-0.00388	0.0129	3.647	8205	Ultimate curvature
Yield curvature (ϕ_y) = 0.833 rad/km			Curvature ductility ratio (μ_ϕ) = 4.38	

Table 7.6 The Summary of the calculated response of the Shear Wall 4.

ε_{top}	ε_{bottom}	ϕ(rad/km	M(kNm**)**	Comments
-0.00043	0.00021	0.14	3956	Concrete cracks
-0.00128	0.00215	0.745	9474	Bottom steel yields
-0.00159	0.00305	1.01	10717	All boundary reinforcements yield
-0.00176	0.00373	1.192	10967	Web reinforcement starts to yield
-0.00338	0.01041	2.999	11635	Strain hardening at bottom steel
-0.0038	0.01205	3.445	11653	Cover crushing starts
-0.0396	0.01215	3.503	11524	Ultimate curvature
Yield curvature (ϕ_y) = 0.906 rad/km			Curvature ductility ratio (μ_ϕ) = 3.87	

7.9 MOMENT-CURVATURE RESPONSE OF THE PANEL FORM TEST SPECIMENS

In this part, moment-curvature response of the panel form test specimens SP1 and SP2 are obtained both by the Waller2002 and Response2000. The results obtained by the computer programs Waller2002 and Response2000 are compared and discussed. Characteristic compression strength and tension strength of the concrete are taken as 35 MPa and 2.07 MPa, respectively. The shape of the stress-strain diagram of the concrete under compression and tension are as given in Figure 7.1 and 7.3. ε_y = 0.00275, ε_u = 0.025, f_{sy} = 550 MPa and f_{su}=600 MPa are the yield strain, ultimate strain, yield strength, ultimate strength values of the reinforcing steel, respectively. Rupturing of the longitudinal reinforcement occurred for both SP1 and SP2. While evaluating the computer output results, it is realized that for both SP1 and SP2 rupturing of the longitudinal reinforcement occurred. A detailed investigation and nomenclatures of the moment-curvature response of the panel form tests are given in Chapter 8.

7.10 COMPARISON OF THE MOMENT-CURVATURE RESPONSE OF SP1 BY WALLER2002 AND RESPONSE2000

Moment-curvature diagram of SP1 obtained by Waller2002 is shown in Figure 7.12. It is seen from Figure 7.12 that cracking moment is much too higher than the yield moment and ultimate moment. When the steel strain at the tension flange reaches the ultimate steel strain (ε_{su} = 0.025), all the steels in the flange ruptured. The moment and curvature values are 86 kNm and 28.2 rad/km, respectively. Moment-curvature diagram of SP1 obtained by Response2000 is shown in Figure 7.13. Ultimate strain of the reinforcing steel is taken as ε_y = 0.025 again in the moment-curvature program Response2000. However, when the steel strain at the tension side flange reaches the half of the rupture strain value (0.025/2=0.0125) all the steels in the tension side flange seem to rupture at the moment and curvature values of 88 kNm and 13.8 rad/km, respectively. This result is wrong and has to be investigated. Figure 7.14 shows the comparison of the moment-curvature diagram of SP1 obtained by Response2000 and Waller2002.

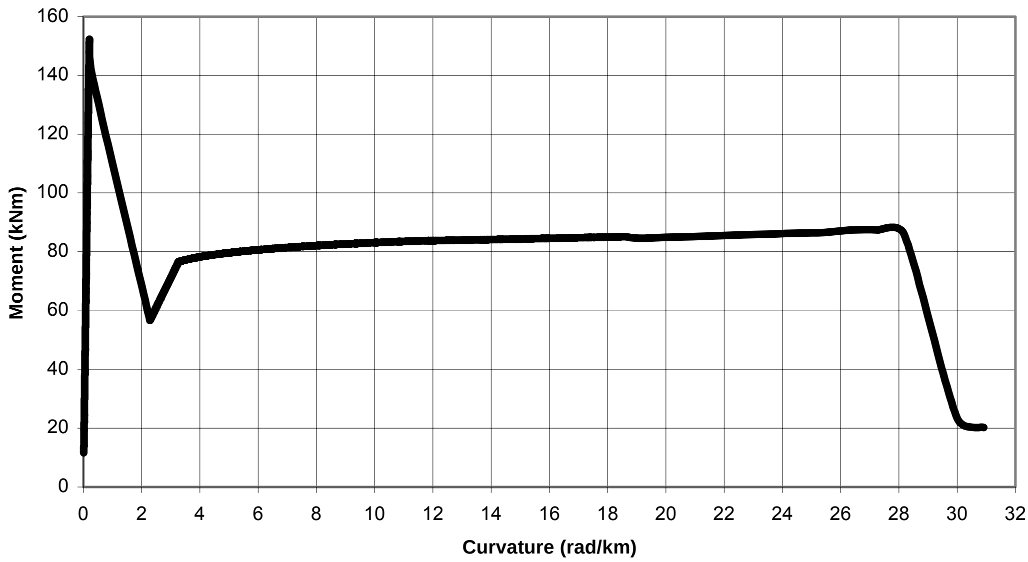

Figure 7.12 Moment-curvature diagram of SP1 obtained by Waller2002.

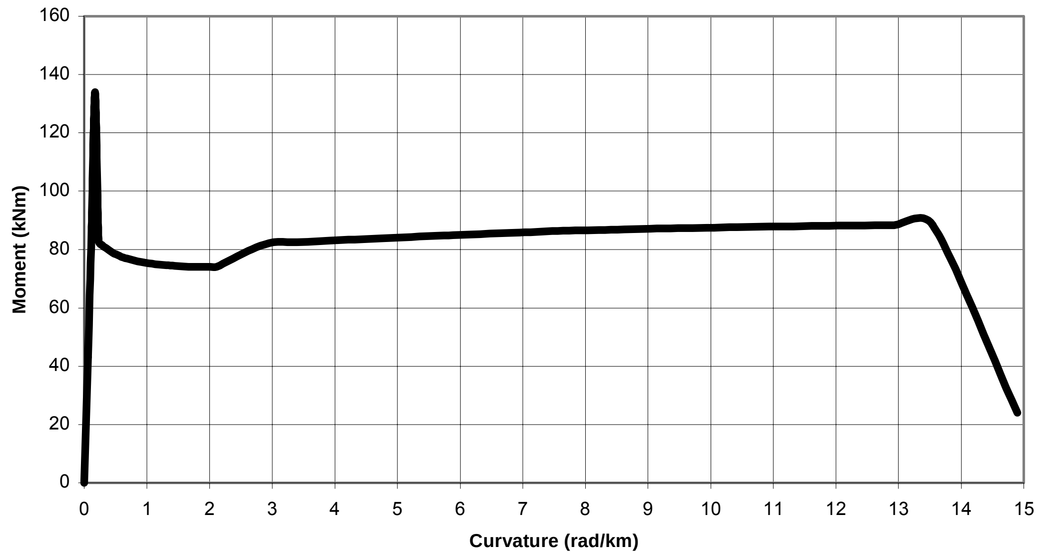

Figure 7.13 Moment-curvature diagram of SP1 obtained by Response2000 (ultimate strain of reinforcing steel is 0.025).

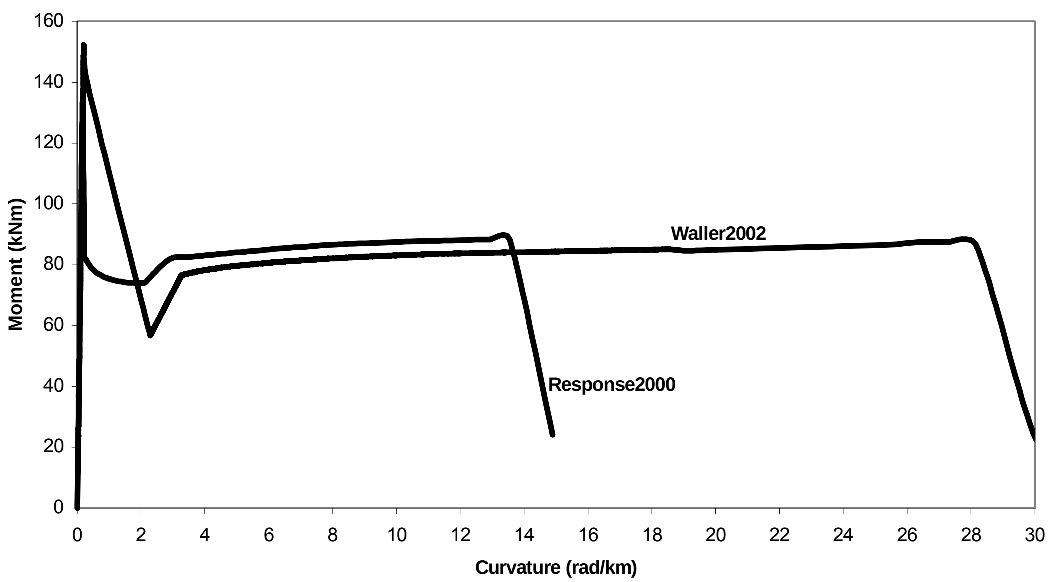

Figure 7.14 Comparison of moment-curvature diagram of SP1 obtained by Response2000 and Waller2002.

In the manual of Response2000 this unexpected situation is stated as in the Response 2000 user manual:

> “**Things that Response2000 is poor at now:**
>
> Problem with elastic-to-rupture materials. For materials that display linear elastic behavior to the point of rupture, Response-2000 will produce very conservative results. The problem is that the program assumes that the strain at a crack must be able to twice the average strain for the crack check. To account for this, increase the strain at rupture for the material to twice the measured value and the same ultimate stress. That is, give the material a “yield plateau that reaches to twice the yield strain.”

SP1 is reanalyzed again by Response2000 by multiplying the rupture strain of reinforcing steel by two (0.025×2 = 0.05). Figure 7.15 shows the moment-curvature diagram of SP1 obtained by Response2000 when the rupture strain of reinforcing steel is taken as 0.05. It is seen that from the comparisons of the moment-curvature diagrams of SP1 obtained by Response2000 and Waller2002 that the two graphs are identical provided that the input values of the rupture strain is modified by multiplying by two in the Response2000 as shown in Figure 7.16.

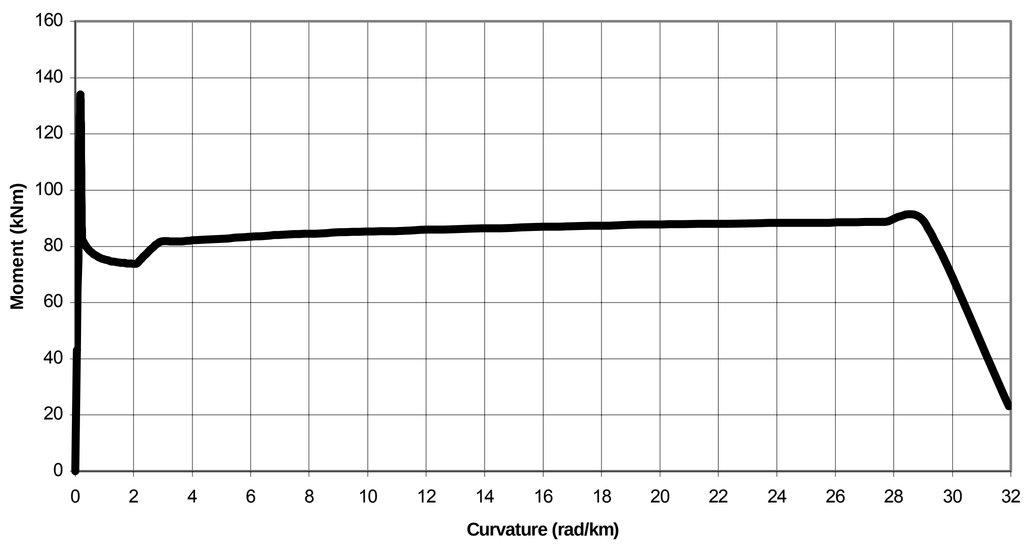

Figure 7.15 Moment-curvature diagram of SP1 obtained by Response2000 (rupture strain of reinforcing steel is 0.05).

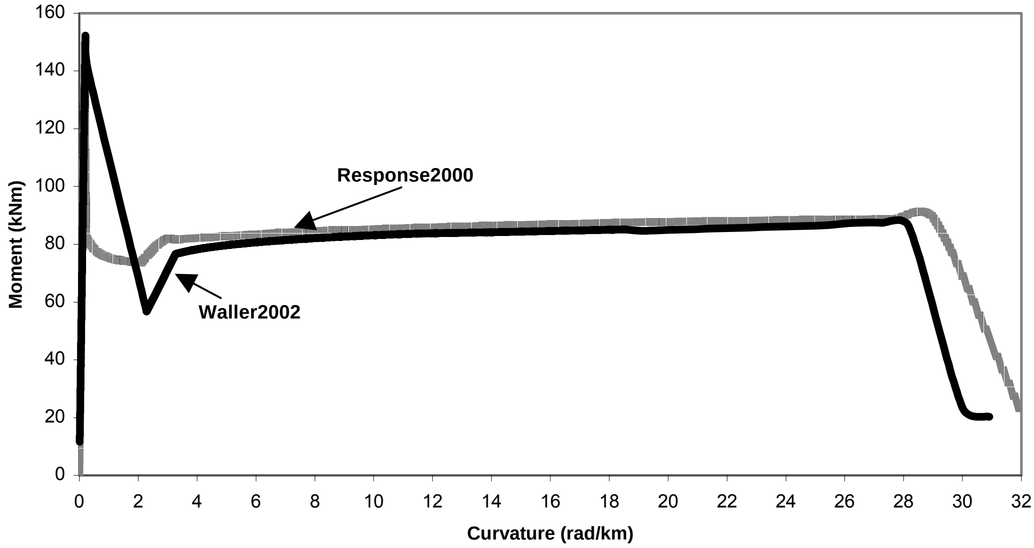

Figure 7.16 Comparison of moment-curvature diagram of SP1 obtained by Response2000 and Waller2002.

7.11 COMPARISON OF THE MOMENT-CURVATURE RESPONSE OF SP2 BY WALLER 2002 AND RESPONSE2000

Figure 7.17 shows the moment-curvature diagram of SP2 obtained by Waller2002. When the steel strain at the bottom steel layer reaches the ultimate steel strain (ε_{su} = 0.025), the steels in the bottom layer ruptured. The moment and curvature values are 187.9 kNm and 13.51 rad/km, respectively. Steel layers in the tension side ruptured consecutively.

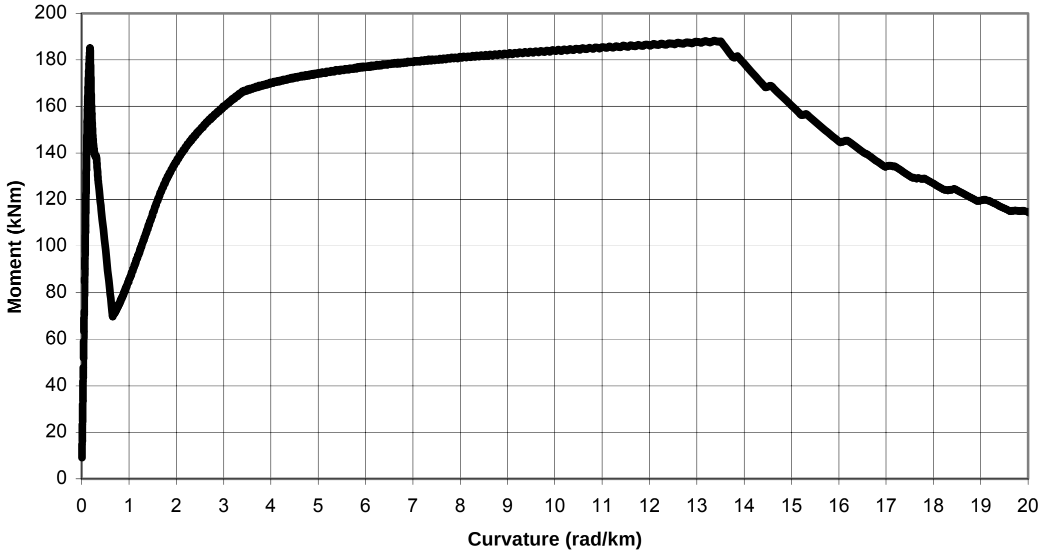

Figure 7.17 Moment-curvature diagram of SP2 obtained by Waller2002.

Figure 7.18 shows the moment-curvature diagram of SP2 obtained by Response2000. Ultimate strain of the reinforcing is steel taken as ε_y = 0.025 again in the moment-curvature program Response2000. Figure 7.19 shows the comparison of moment-curvature diagram of SP2 obtained by Response2000 and Waller2002 when the ultimate strain of the reinforcing steel is 0.025. The same problem explained in the previous part occurred again in Response2000. Ultimate curvature of SP2 obtained by Response2000 is again occurring at the half of the rupture strain value (0.025/2=0.0125). Ultimate strain of the reinforcing steel is taken as ε_y = 0.025, again in the moment-curvature program Response2000. However, when the steel strain at the bottom steel layer in the tension side reaches the half of the rupture strain value (0.025/2=0.0125) steels in this layer seem to rupture at the moment and curvature values of 176.37 kNm and 7.03 rad/km, respectively.

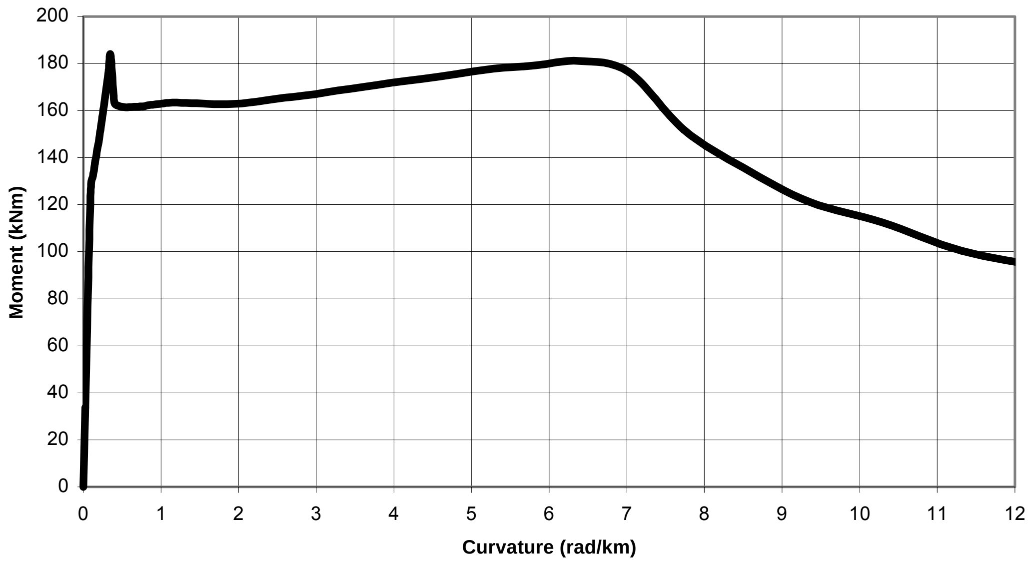

Figure 7.18 Moment-curvature diagram of SP2 obtained by Response2000 (ultimate strain of reinforcing steel is 0.025).

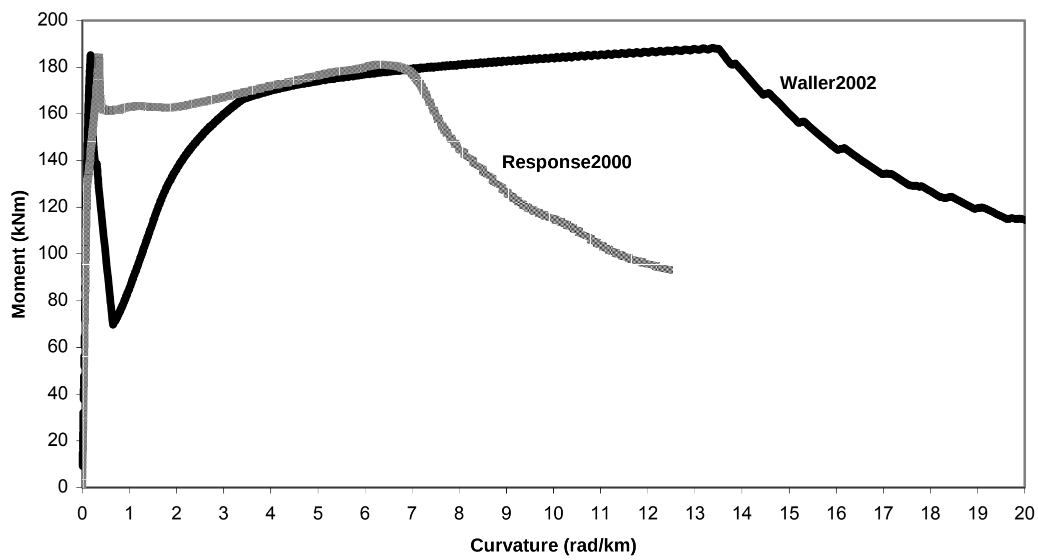

Figure 7.19 Comparison of moment-curvature diagram of SP2 obtained by Response2000 and Waller2002 (ultimate strain of the reinforcing steel is 0.025).

The same procedure explained in the previous part is redone again. Moment-curvature diagram of SP2 is analyzed again by multiplying the ultimate strain of reinforcing steel by a factor of two ($2 \times 0.025 = 0.05$) and Figure 7.20 shows the moment-curvature diagram of SP2 obtained by Response2000.

Figure 7.21 shows the comparison of the moment-curvature diagram of SP2 obtained by Response2000 and Waller2002. It is obvious that from the comparison of the moment-curvature diagrams of SP2 obtained by Response2000 and Waller2002, the moment-curvature responses obtained by these two programs are identical, provided that the rupture strain of the reinforcement steel is increased twice the measured value in Response2000.

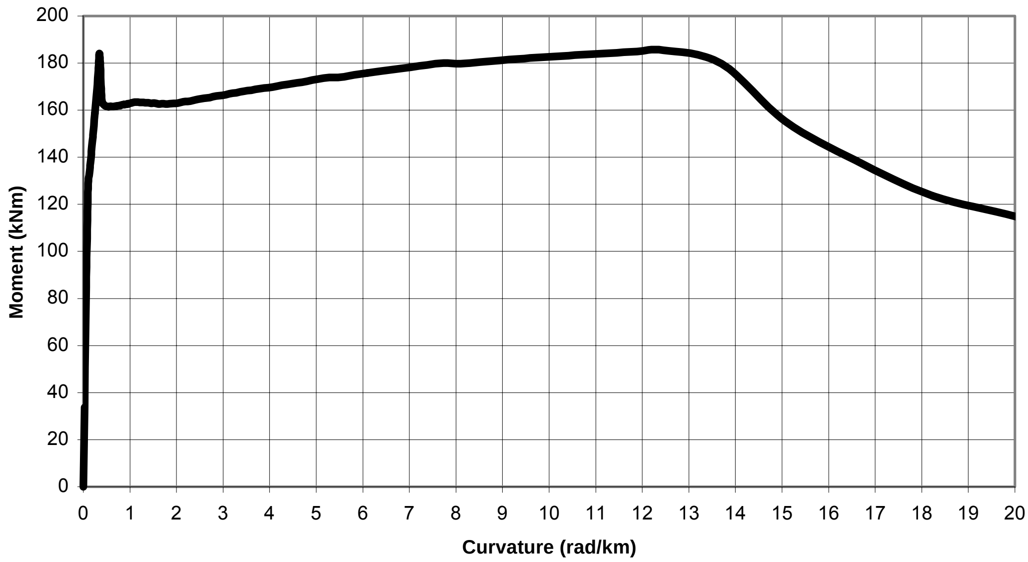

Figure 7.20 Moment-curvature diagram of SP2 obtained by Response2000 (ultimate strain of reinforcing steel is $2 \times 0.0250 = 0.050$).

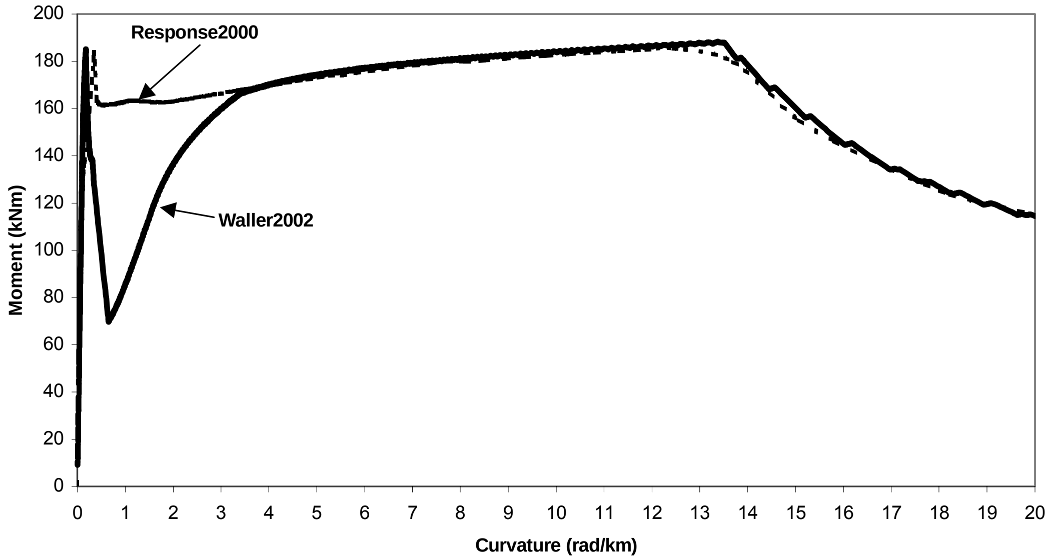

Figure 7.21 Comparison of moment-curvature diagrams of SP2 obtained by Response2000 and Waller2002.

CHAPTER 8

DISCUSSION AND EVALUATION OF THE TEST RESULTS

8.1 GENERAL

In this chapter, the experimental results of the static tests are evaluated and discussed by considering strength, stiffness, response, energy dissipation and drift characteristics of the test specimens.

Figure 8.1 General view of the panel form test specimens SP1 and SP2.

Figure 8.1 shows the general view of the panel form test specimens SP1 and SP2. The test specimen which was tested in the short dimension is called SPECIMEN1 (SP1) and the one which was tested in the long dimension is called SPECIMEN2 (SP2). SP1 is located at the right hand side and SP2 is located at the left hand side in Figure 8.1. The weigths of the panel form test specimens SP1 and SP2 are 24.66 kN and this value is used in all the calculations. The axial load compressive stress (N/A_g) was 0.128 MPa corresponding to an axial load ratio of $N/f_{ck}A_g = 0.00367$.

8.2 PROPERTIES OF THE TEST SPECIMENS

Concrete compressive strength of the panel form test specimens is 35 MPa. In the new Turkish Code (TS-500, 2000), the direct tensile strength is expressed as a function of the square root of the compression strength:

$$f_{ctk} = 0.35\sqrt{f_{ck}} = 2.07 \text{ MPa} \tag{8.1}$$

In the Turkish Code (TS-500, 2000), it is also specified that the tensile strength obtained from flexure tests are 2 times the direct tensile strength:

$$f_{ctf} = 0.7\sqrt{f_{ck}} = 4.14 \text{ MPa} \tag{8.2}$$

Concrete is not a linearly elastic material. Therefore, it is difficult to justify any definition for the modulus of elasticity of concrete. Since the slope of the σ-ε curve of concrete is not constant, one has to describe modulus of elasticity, E_c, before defining such a term. In general the modulus of elasticity defined for concrete is the instantaneous E_c, which is not influenced by the time effect. The instantaneous modulus of elasticity of concrete can be defined in three different ways as stated below (Ersoy and Özcebe, 2001):

a) Initial modulus (Tangent to the curve at the origin)
b) Secant modulus (slope of the secant at a given stress; usually 0.5 f_c)

c) Tangent modulus (Tangent to the σ-ε curve at a given stress, usually 40% to 50% of the compressive strength).

The most commonly used one and the one referred to codes is the "Secant Modulus". Instantaneous modulus of elasticity (in this case Secant Modulus) was calculated using three different codes:

ACI 318: $E_c = 4750\sqrt{f_c} = 4750\sqrt{35} = 28{,}101$ MPa

TS 500: $E_c = 3250\sqrt{f_c} + 14000 = 3250\sqrt{35} + 14000 = 33{,}227$ MPa

CEB: $E_c = 9500(f_c + 8.0)^{1/3} = 9500(35 + 8.0)^{1/3} = 33{,}282$ MPa

If the modulus of elasticity values obtained from the Turkish Code and CEB are compared, it seen that the difference is not significant. However, as can be seen, modulus of elasticity values obtained from the ACI is significantly different. Therefore, elastic modulus of concrete was chosen as 33,227 MPa for the panel form test specimens.

TS-500 recommends the use of E_s = 200 GPa for the modulus of elasticity for nonprestressed reinforcement, so in the calculations 200 GPa is used for the elastic modulus of steel.

8.3 FLEXURAL CRACKING STRENGTH

As explained in Chapter 4 and Chapter 5, panel form test specimens SP1 and SP2 failed as soon as the concrete cracked; followed by immediate yielding and rupturing of the longitudinal steel. The cracking strength is important for SP1 and SP2. The procedure of calculation of cracking strength by using mechanics of materials is explained below.

For a reinforced concrete section subjected to bending, the prediction of the flexural cracking load is important. Beyond the flexural cracking strength, the behavior of the reinforced concrete member changes from linear-elastic to nonlinear and the stiffness decreases. Assuming linear elastic response, flexural cracking stress of a reinforced concrete section subjected to bending and axial load can be calculated using the following equation:

$$\sigma = \frac{N}{A} \pm \frac{M \cdot y}{I} \tag{8.3}$$

The cracking moment M_{cr}, can be calculated by substituting $M = M_{cr}$ and $\sigma = f_{ctf}$ into Equation (8.3):

$$M_{cr} = \left(f_{ctf} - \frac{N}{A} \right)\left(\frac{I}{y} \right) \tag{8.4}$$

where

f_{ctf} : flexural tensile strength of concrete, $f_{ctf} = 0.7\sqrt{f_{ck}}$ (MPa)

I : moment of inertia of the concrete section

y : distance between the centroid and extreme tension fiber

N : total axial load applied on the section

A : gross cross-sectional area

The lateral load corresponding to the flexural cracking (V_{fcr}) could be calculated by assuming the panel form test specimens as a cantilever.

$$V_{fcr} = \frac{M_{cr}}{H} \tag{8.5}$$

where

H : Distance between the lateral load and the cracking surface of the test specimens.

8.4 PROPERTIES OF SP1

Figure 8.2 shows the reinforcement pattern and loading direction of the shear walls of the panel form test specimen SP1.

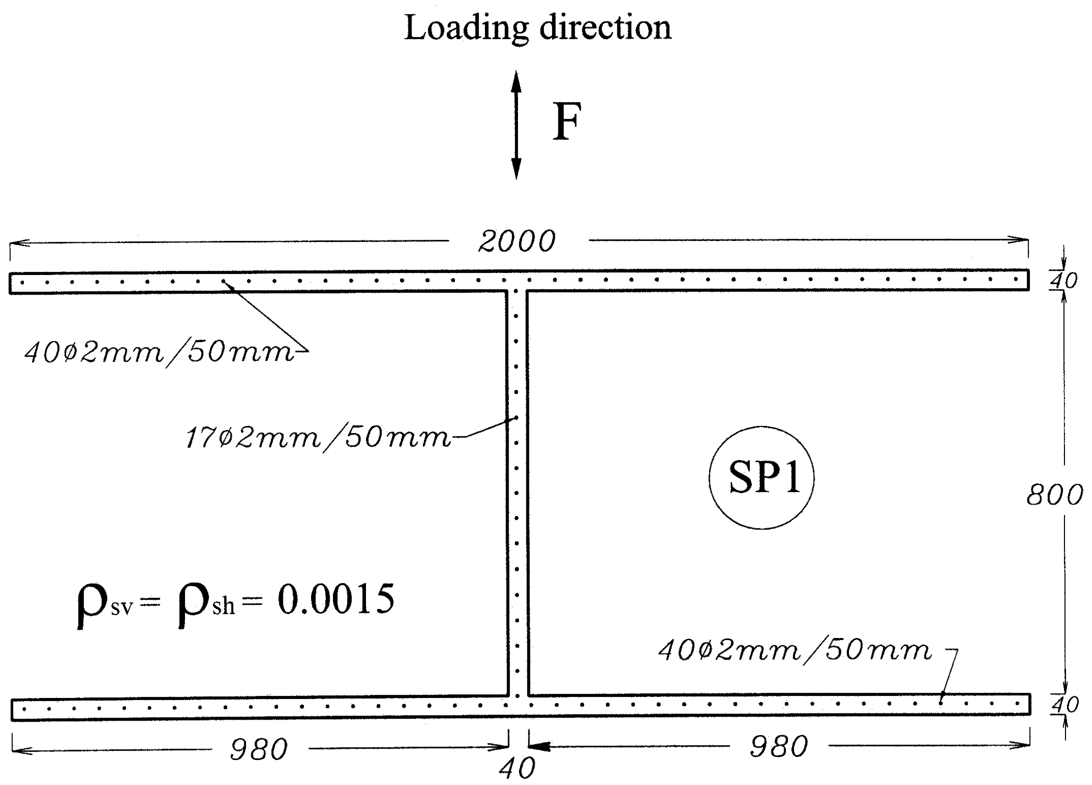

Figure 8.2 Reinforcement pattern and loading direction of SP1. (All dimensions are in mm).

The modular ratio, the total area of the wall reinforcement in the longitudinal direction, the cross-sectional wall area, the longitudinal reinforcement ratio, the transformed area, the gross and transformed moment of inertia and the flexural rigidity of SP1 are summarized in the following.

The modular ratio for SP1 is calculated as shown in the following

$$n = \frac{E_s}{E_c} = \frac{200{,}000\ \text{MPa}}{33{,}227\ \text{MPa}} = 6.0$$

Total area of the wall reinforcement in the longitudinal direction for SP1 is

$$A_{steel} = 305\ \text{mm}^2$$

Cross-sectional wall area for SP1 is

$$A_{concrete} = 192{,}000\ \text{mm}^2$$

Longitudinal reinforcement ratio for SP1 is

$$\rho_s = \left(\frac{A_s}{A_c}\right) = \left(\frac{305\,\text{mm}^2}{192{,}000\,\text{mm}^2}\right) = 0.00159$$

The transformed area of SP1 is calculated by considering the individual steel layers and found as

$$A_{trans} = 193{,}524\ \text{mm}^2$$

Gross and transformed moment of inertia along the short dimension of SP1 is calculated as

$$I_{SP1gross} = 2.995 \times 10^{-2}\ \text{m}^4$$
$$I_{SP1trans} = 3.019 \times 10^{-2}\ \text{m}^4$$

Flexural rigidity for the transformed case of SP1 is

$$E_c \times I_{SP1trans} = = 1{,}003{,}121\ \text{kNm}^2$$

It is seen that the gross and transformed moment of inertia of SP1 are very close to each other because longitudinal reinforcement ratio is low. For simplicity gross moment of inertia can be used in practice but in this study transformed moment of inertia will be used.

From Equation (8.4), moment corresponding to the flexural cracking was calculated and found as

$$M_{cr} = 275.3\ \text{kNm}$$

From Equation (8.5), shear force corresponding to the flexural cracking was calculated as

$$V_{fcr} = \frac{M_{cr}}{H} = \frac{275.3\text{kNm}}{2.67\ \text{m}} = 103.1\ \text{kN}$$

During the static tests of SP1, the horizontal flexural crack, which caused the failure, was observed at 35 kN load level. These differences were due to probability of defects (like voids, large aggregates, local cracks etc.) and the low reinforcement ratio.

8.5 PRESENTATION OF THE STATIC TEST RESULTS FOR SP1

The observed behavior of SP1 is presented in this section. Lateral load-displacement curves for the 1st and 2nd static tests for SP1 were given separately in Chapter 4. In this chapter the 1st and 2nd static tests are combined, considered and presented as a single test.

Lateral load displacement curves of the 1st, 2nd, 3rd and 4th stories are given in Figures 8.3, 8.4, 8.5 and 8.6, respectively. The maximum applied lateral load was 40 kN for SP1. Maximum lateral-displacements are 2 mm, 4 mm, and 6 mm, for the 1st, 2nd and 3rd story levels, respectively. The maximum displacement and yield displacement are 3.5 mm and 8.6 mm, respectively, at the fourth story level as seen in Figure 8.6. The displacement ductility factor for SP1 is $\mu_\Delta = 2.46$.

$$\mu_\Delta \text{ (SP1)} = 2.46 < \mu_\Delta \text{ (required)} = 4{\sim}5$$

The displacement ductility of SP1 is lower than the required displacement ductility. It is obvious from the above equation that SP1 shows brittle failure.

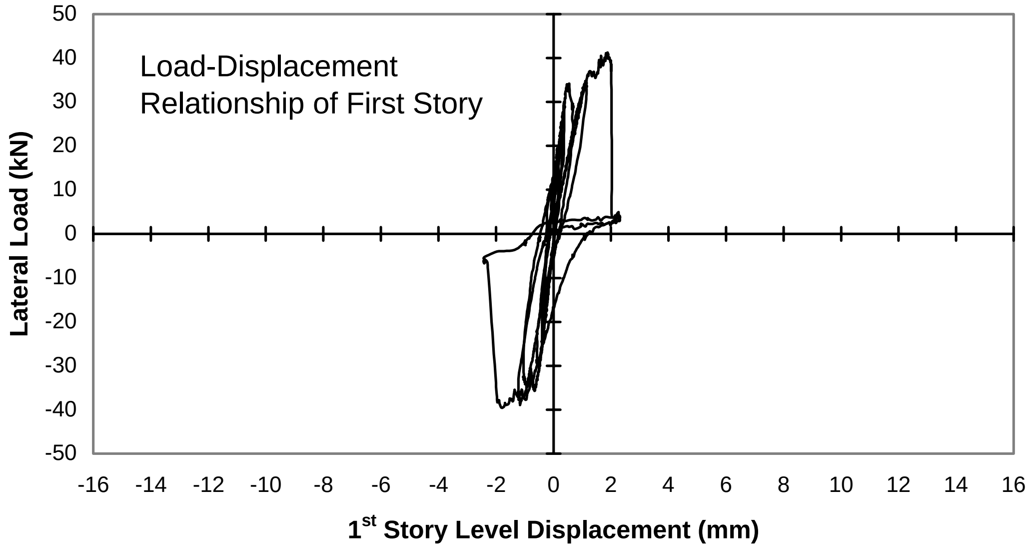

Figure 8.3 Lateral load-displacement curve of the 1st story for SP1.

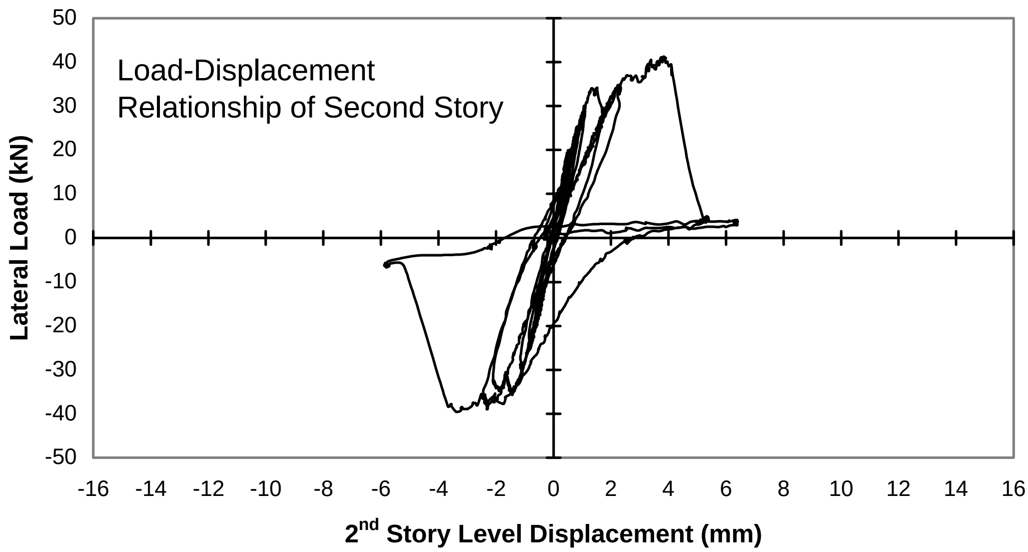

Figure 8.4 Lateral load-displacement curve of the 2nd story for SP1.

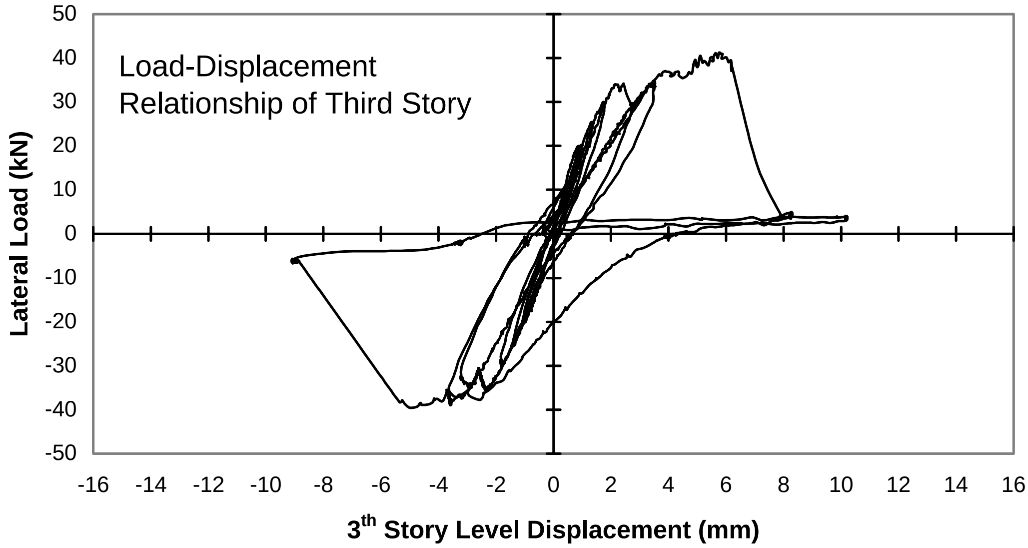

Figure 8.5 Lateral load-displacement curve of the 3rd story for SP1.

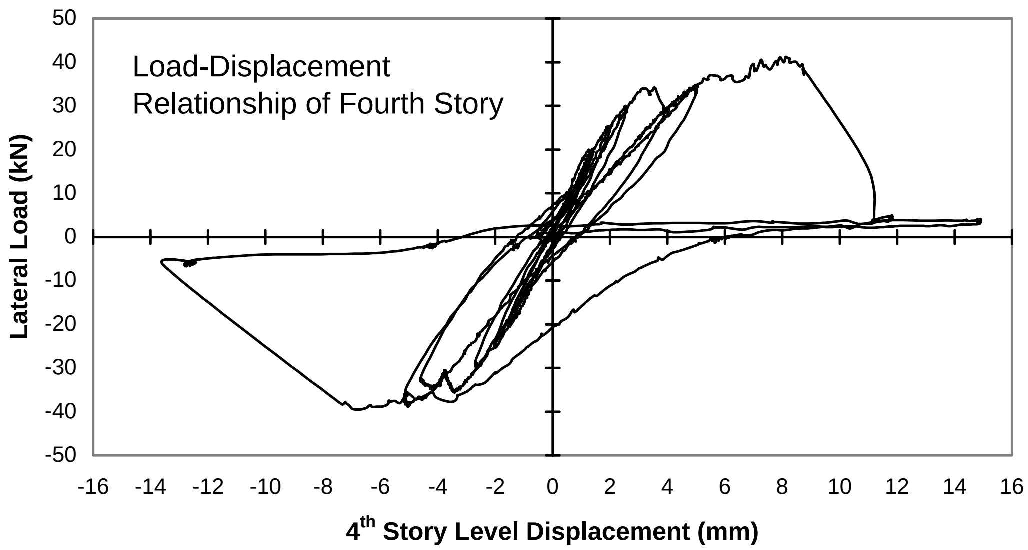

Figure 8.6 Lateral load-displacement curve of the 4th story for SP1.

The observed behavior of SP1 in the static tests can be summarized as follows:

- SP1 exhibits horizontal tension cracking at the flanges.
- As the concrete cracks, longitudinal reinforcements yield at the crack location.
- SP1 fails, as soon as the concrete cracks followed by yielding and then rupturing of the longitudinal steel.
- Crushing of the concrete is not observed.
- The cracking moment and yield moment are very close to each other.
- Unloaded tension force in the flanges after cracking cannot be carried by the minimum amounts of reinforcement.

The observations of the laboratory tests demonstrate that SP1 is susceptible to a brittle material failure. This brittle mode of flexural failure is directly linked to the low-reinforcement ratio of SP1.

8.6 STRENGTH AND CURVATURE DUCTILITY OF SP1

The ultimate flexural capacities of SP1 and SP2 were calculated using the computer program, Response-2000. The analytical interaction diagram for SP1 is shown in Figure 8.7.

It is seen from Figure 8.7 that the axial tension load capacity of SP1 is 183 kN and axial compression load capacity of SP1 is 5880 kN. Constant axial load on SP1, which is -24.66 kN, is shown as a bold horizontal line. At the balanced case, the axial load and moment are 1133 kN and 2980 kNm, respectively. It is seen from the analytical interaction curve that the axial load level on SP1 is very low.

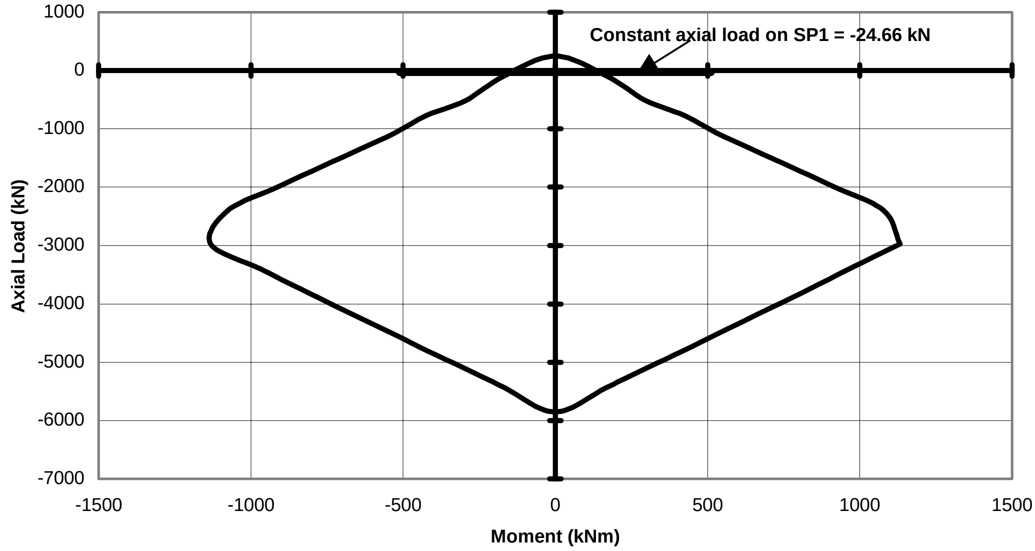

Figure 8.7 Analytical interaction curve of SP1.

Figure 8.8 shows the moment-curvature diagram of SP1 obtained by Waller2002. In Chapter 7 it was shown that Response2000 obtained the same moment-curvature diagram by a modification of the input data (multiplying rupture strain of reinforcement steel with a modification factor of two) because Response2000 has problems with elastic-to-rupture materials.

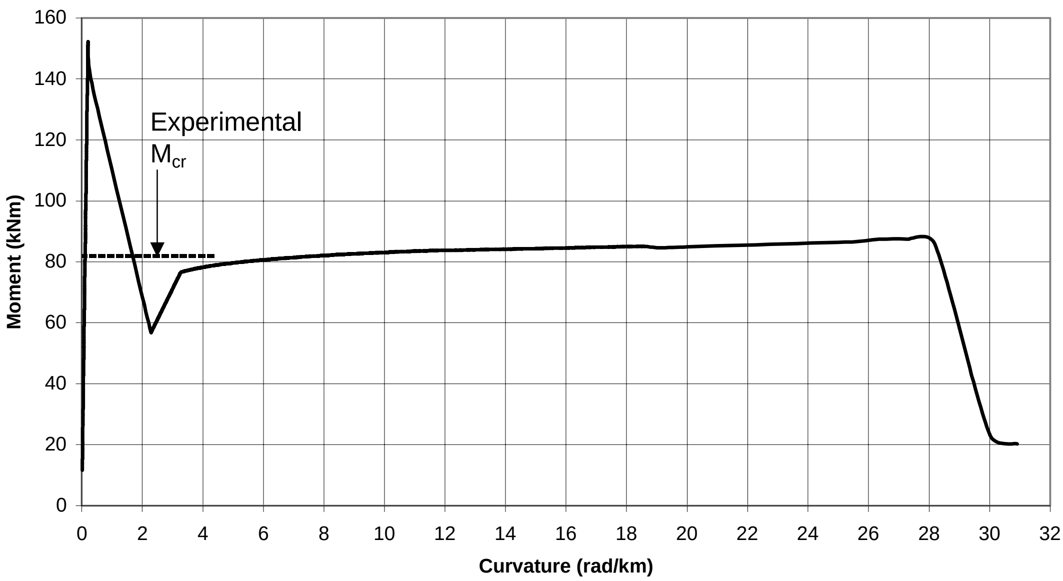

Figure 8.8 Moment-curvature diagram of SP1 obtained by Waller2002.

For a large moment range, up to 152.3 kNm, SP1 remains uncracked. When the extreme tension concrete fiber strain reaches 0.0001, the moment reaches 152.3 kNm. This moment value is the maximum moment value where the curvature is 0.205 rad/km at this stage. Cracking marks the point where the moment-curvature relationship falls down sharply. It is seen that from the moment curvature diagram cracking moment is 1.8 times greater than the ultimate moment. When the extreme tension concrete fiber strain reaches 0.0002, the moment reaches 140.2 kNm and the curvature is 0.298 rad/km. After tension cracking, the moment value falls down from 152.3 kNm to 57.07 kNm value. When the moment value is 57.07 kNm, the curvature and bottom steel strain values are 2.3 rad/km and 0.00194, respectively. As soon as the concrete cracks all the longitudinal flange reinforcement in the tension flange yields. Then the moment values start to increase again and when the moment and curvature values reach 76.57 kNm and 3.275 rad/km, respectively, the bottom steel yields, 2nd and 3th layer reinforcements yield consecutively. Nominal yield is found as 3.57 rad/km and the corresponding moment values are found as 77.34 kNm, as explained in Chapter 7. All the web reinforcements yield consecutively. Moment-curvature diagram is horizontal at that level. It is seen from Figure 8.8 and Table 8.1 that when the steel strain value at the flange of SP1 reaches the rupture strain of the reinforcement (0.025), all the steels at the tension side flange rupture. Ultimate moment and ultimate curvature are 86 kNm and 28.2 rad/km, respectively.

Table 8.1 The summary of the calculated response of SP1.

ε_{top}	ε_{bottom}	ϕ(rad/km)	M(kNm)	Comments
-0.000081	0.0001	0.205	152.3	Bottom Strain=0.0001
-0.000082	0.0002	0.298	140.2	Bottom Strain=0.0002
-0.000083	0.00194	2.3	57.07	Minimum moment
-0.00011	0.00277	3.275	76.57	Bottom steels yield
-0.00011	0.00284	3.35	76.82	2nd layer reinforcement yields
-0.00012	0.00302	3.57	77.34	3rd layer reinforcement yields
-0.00012	0.00302	3.57	77.34	Nominal yield
-0.00012	0.00324	3.82	77.88	4th layer reinforcement yields
-0.00013	0.0035	4.11	78.371	5th layer reinforcement yields
-0.00014	0.0037	4.44	78.95	6th layer reinforcement yields
-0.00014	0.0041	4.83	79.45	7th layer reinforcement yields
-0.00015	0.0045	5.29	79.97	8th layer reinforcement yields
-0.00016	0.0049	5.86	80.49	9th layer reinforcement yields
-0.00018	0.0056	6.55	81.05	10th layer reinforcement yields
-0.00019	0.0064	7.44	81.67	11th layer reinforcement yields
-0.00021	0.0074	8.58	82.4	12th layer reinforcement yields
-0.00024	0.0087	10.17	83.2	13th layer reinforcement yields
-0.00027	0.0106	12.37	83.81	14th layer reinforcement yields
-0.0003	0.0136	15.79	84.48	15th layer reinforcement yields
-0.00035	0.02525	28.2	86.0	Bottom steels ruptured
0.00024	0.02616	30.0	23.36	After bottom steels ruptured

The yield moment was found as M_y = 77.34 kNm, the ratio of the yield moment to the cracking moment is calculated as

$$\frac{M_y}{M_{cr}} = \frac{77.34\ \text{kN}}{152.3\ \text{kN}} = 0.507$$

Ultimate moment is 86 kNm and the ratio of the ultimate moment to the cracking moment is calculated as

$$\frac{M_u}{M_{cr}} = \frac{86\ \text{kN}}{152.3\ \text{kN}} = 0.565$$

In fact this ratio must be greater than 1.25 to prevent the brittle behavior. As a summary, as soon as SP1 cracks under tension, the moment values fall down and the steel in the tension flange yield. After yielding of the second web reinforcement, moment-curvature diagram shows plastic deformation under almost constant moment.

Ultimate curvature and yield curvature (nominal) were found to be 28.3 rad/km and 3.57 rad/km, respectively. The curvature ductility ratio for SP1 was calculated as

$$\mu_\phi = \frac{\phi_u}{\phi_y} = \frac{28.3}{3.57} = 7.89$$

The calculated value of the curvature ductility ratio of SP1 is 7.89. The displacement ductility factor will be calculated in the following section.

From the observations of the moment-curvature graph of SP1 the following conclusions can be drawn:

- The panel form test specimen SP1 has reached its ultimate strength as soon as the concrete cracked; followed by immediate yielding and rupturing of the longitudinal steel in the flanges.
- From the results of the moment curvature graph, SP1 shows very brittle behavior. From the results of the moment-curvature relationship, the ratio of the ultimate moment to the racking moment is much more smaller than 1.25.

$$\frac{M_u}{M_{cr}} = 0.565 < 1.25$$

This is an indication of very brittle type of behavior due to under-reinforcement.

8.7 EFFECTS OF TACK WELDING

In this section of the study, effects of tack welding are investigated. As mentioned in Chapter 3, the horizontal and vertical mesh reinforcement is welded with 50 mm spacing in the horizontal and vertical directions. The diameter of the horizontal and vertical mesh reinforcement is 2 mm. To determine stress-strain relationship of reinforcing steel, randomly taken test coupons were tested under tension. The longitudinal and horizontal mesh reinforcements were plain bars. Yield and ultimate strengths of reinforcing steel are f_{sy} = 550 MPa and f_{su} = 600 MPa, respectively.

In shear walls, steel bars with 2 mm diameter and in the slabs, steel bars with 2.5 mm diameter are used as reinforcing bars. To obtain the characteristic values of mesh reinforcement, randomly taken six specimens were tested under uniaxial tension test before the welding process. From the visual observations, it can be concluded that after tack welding there is no decrement in the area of the mesh reinforcement. The lengths of the reinforcements are 2 m before tack welding process. Test specimen lengths of the reinforcement bars are 100 mm. Table 8.2 shows the mechanical properties of the reinforcing bars before the tack welding process.

Table 8.2 Mechanical properties of the reinforcing bars before tack welding.

Steel No	f_{sy}(MPa)	f_{su} (MPa)	ε_{sy}	ε_{su}
ϕ2	550	650	0.0027	0.03
ϕ2.5	550	650	0.0027	0.03

After obtaining the mechanical properties of the reinforcement, tack welding process is applied to the reinforcements. The spacing of the mesh reinforcement is 50 mm in horizontal and vertical directions. Table 8.2 shows the mechanical properties of the reinforcing bars after tack welding process.

Table 8.3 Mechanical properties of the reinforcing bars after tack welding .

Steel No	f_{sy}(MPa)	f_{su} (MPa)	ε_{sy}	ε_{su}
ϕ2	540	600	0.0027	0.025
ϕ2.5	540	600	0.0027	0.025

From the comparisons of Table 8.2 and Table 8.3 it is seen that the ultimate strength of the reinforcing steel decreases 7.7 % and the ultimate strain of the reinforcing steel decreases 16 % due to tack welding process. Yield strength of the reinforcing steel decreases 1.82 % due to tack welding process.

After the tension test of the mesh reinforcement, the following observation is obtained. Rupturing of the mesh reinforcement does not occur exactly at the tack welding point, but occurs 5~10 mm away from the tack welding point.

In the following section ductility and strength reduction due to tack welding of the reinforcing steel are investigated by changing the yield strength and yield strain, ultimate strength and ultimate strain values. To improve the brittle behavior, boundary reinforcement is provided at the boundary regions of the test specimen. The boundary reinforcement is provided according to the Turkish Seismic Code (AY-1997).

8.8 EFFECTS OF TACK WELDING ON SP1

8.8.1 Ductility Reduction

In this section ultimate strain of the reinforcing steel is changed and the obtained moment-curvature behavior is discussed. The moment-curvature diagram of SP1 is drawn by assuming for ultimate steel strain ϵ_{su} = 0.01, ϵ_{su} = 0.015, ϵ_{su} = 0.020, ϵ_{su} = 0.025, ϵ_{su} = 0.030, ϵ_{su} = 0.035, ϵ_{su} = 0.040 ϵ_{su} = 0.045 and ϵ_{su} = 0.050. Figure 8.9 shows the effects of ultimate strain of reinforcing steel on the moment-curvature behavior of SP1. It is seen from Figure 8.9 that the general behavior is the same when the rupture strain of reinforcing steel is changed from 0.01 to 0.05. Observed cracking moment in the static tests of SP1 is 81 kNm.

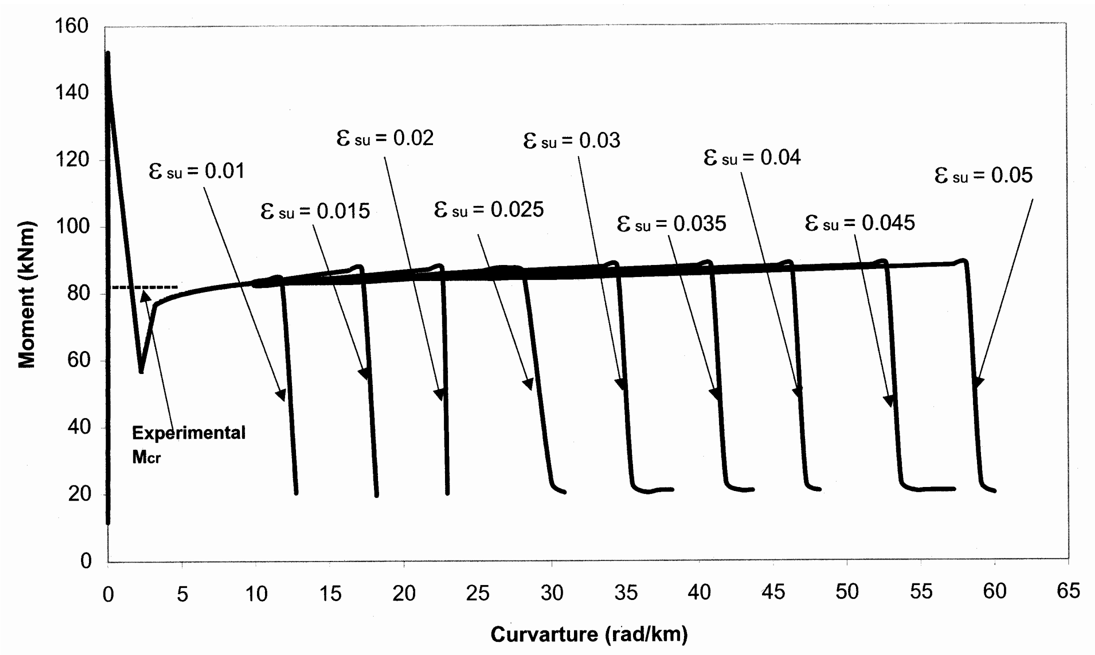

Figure 8.9 Effects of ultimate strain of reinforcing steel on the moment-curvature behavior of SP1.

Cracking moment is found to be 153 kNm theoretically. After cracking, the moment-curvature diagrams fall down sharply and all the longitudinal reinforcement in the tension side flange yield simultaneously in all cases. Rupturing of the longitudinal reinforcement in the tension flange causes dramatic falls in the moment values. The ultimate moment capacity in all cases is approximately 87 kNm. The ratio of the ultimate moment to the cracking moment is calculated as

$$\frac{M_u}{M_{cr}} = \frac{86\,\text{kNm}}{153\,\text{kNm}} = 0.562 < 1.25$$

If more ductile mesh reinforcement were used, the behavior would not be changed. Effect of tack welding does not change the general behavior.

8.8.2 Strength Reduction

In this section, ultimate strength of the reinforcing steel is changed. The moment curvature diagram of SP1 is drawn by assuming for ultimate steel strength value f_{su} = 600 MPa (measured ultimate strength), to be $0.9f_{su}$ = 540 MPa and $0.8f_{su}$ = 480 MPa. Figure 8.10 shows the effects of ultimate stress of reinforcing steel on the moment-curvature behavior for SP1. After cracking, the longitudinal reinforcements in the tension flange yield and rupture. Yield and ultimate curvatures are not changed. The ultimate moment values are 85.0 kNm, 77.5 kNm and 70.0 kNm for f_{su}, $0.9f_{su}$ and 0.8 f_{su}, respectively. Yield and ultimate moment values decrease by a factor of 0.1 and 0.2 as a result of decreasing the ultimate stress of the reinforcing steel by a factor of 0.1 and 0.2, respectively. The general behavior is the same for three cases. It is obvious from Figure 8.9 and Figure 8.10 that the change in the ultimate steel strain and ultimate steel stress does not change the behavior of SP1 because such a low longitudinal steel ratio as 0.0015 is not enough to prevent the brittle behavior.

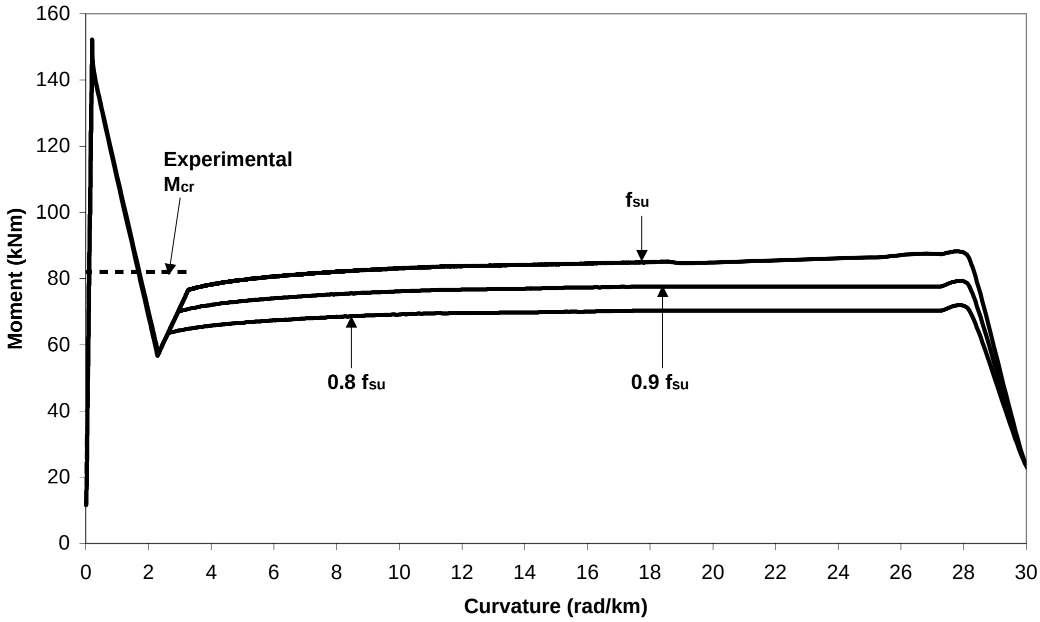

Figure 8.10 Effects of ultimate stress of reinforcing steel on the moment-curvature behavior of SP1.

8.9 BOUNDARY REINFORCEMENT EFFECTS ON SP1

The Turkish Earthquake Code AY-1997, imposes certain regulations and restrictions on structural walls. The plastic hinge region is typically located at the base of a cantilever wall where significant flexural deformations occur. The primary longitudinal reinforcement used to develop the resisting moment is concentrated at both ends of the wall. For slender structural walls $(H_w / l_w > 2)$, which are categorized as the high ductility class, the critical wall length is defined as (h_{cr} = max [l_w, $H_w/6$]). In the critical wall length, confined boundary elements have to be provided at a distance of $l_u \geq 0.2 \times l_w$ from each end of the wall. In this region the longitudinal reinforcement ratio must be at least 0.2% of the gross section. For non-ductile shear walls or outside the critical wall length, boundary elements have to be provided at a distance of $l_u \geq 0.1 \times l_w$ from each end of the wall. In this region the longitudinal reinforcement ratio must be at least 0.1% of the gross section. Figures 8.11 and 8.12 show the reinforcement pattern and loading direction of SP1 with boundary reinforcement ratios of 0.001 b_w l_w and 0.002 b_w l_w, respectively. Boundary reinforcement that is used in this study is assumed to be S420 type reinforcement, which has ultimate strain and strength values of ϵ_{su} = 0.1 and f_{su} = 0.525 MPa, respectively.

Three cases are compared in Figure 8.13. The boundary regions are provided at a distance of $l_u \geq 0.1 \times l_w$ and $l_u \geq 0.2 \times l_w$, boundary reinforcement ratio is 0.1% and 0.2%, respectively for the gross wall area in the direction of loading.

Placing the boundary reinforcement only in the web direction does not change the behavior. The same brittle behavior is observed again. Longitudinal flange reinforcements yield as soon as the section cracks. After the rupturing of the mesh reinforcement in the flange, moment values fall down sharply again as in the previous case.

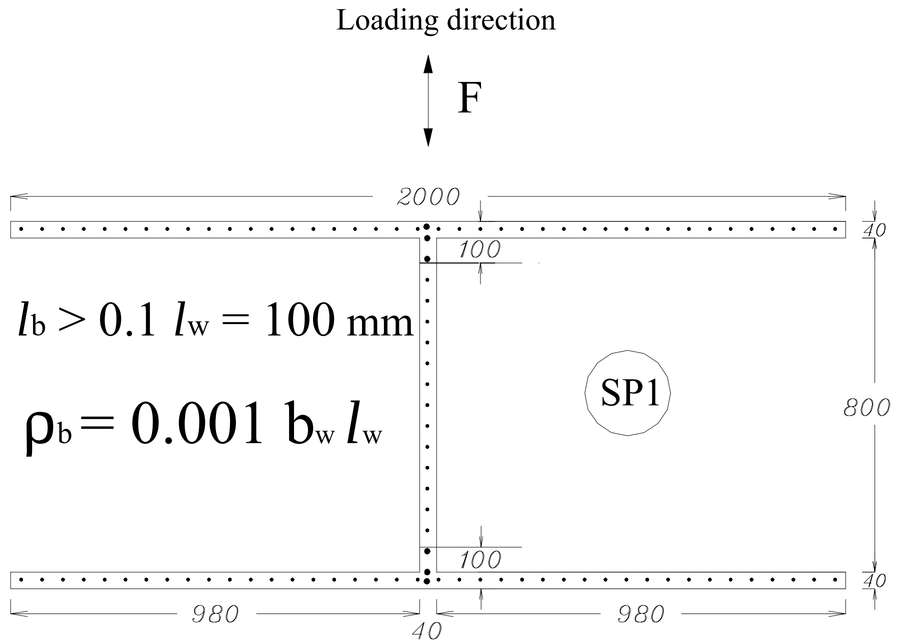

Figure 8.11 Reinforcement pattern and loading direction of SP1 with boundary reinforcement ratio of 0.001 b_w l_w.

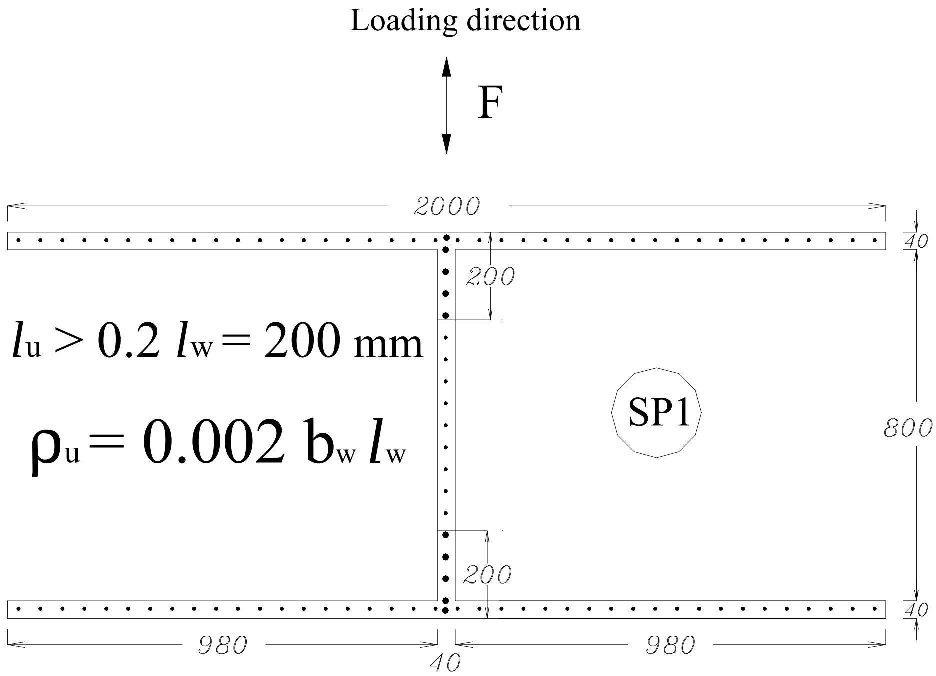

Figure 8.12 Reinforcement pattern and loading direction of SP1 with boundary reinforcement ratio of 0.002 b_w l_w.

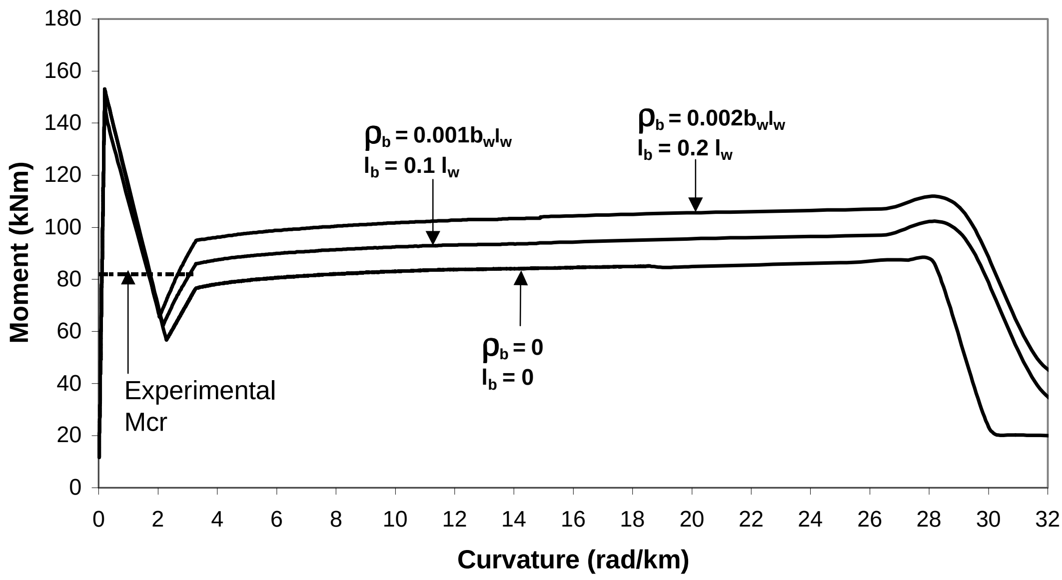

Figure 8.13 Comparison of the moment-curvature diagram by providing concentrated boundary reinforcement in the web wall.

In this stage, it is assumed that boundary reinforcements are placed along the short and long dimensions of the panel form test specimen SP1. Figures 8.14 and 8.15 show the reinforcement pattern and loading direction of SP1 with boundary reinforcement ratio of 0.001 b_w l_w and 0.002 b_w l_w, respectively, in both directions. Figure 8.16 shows the comparisons of the moment-curvature diagram by providing boundary reinforcement along both dimensions. Placing the boundary reinforcement along the short and long dimensions change the behavior of the test specimen SP1. When the rupture strains of the mesh reinforcements in the tension flange reach its rupture strain, these mesh reinforcements rupture and moment values fall down. Moment values for this case are 197.7 kNm and 140.7 kNm and reduction in moment values are 16% and 33% when boundary reinforcement is placed at a distance of $l_b \geq 0.1 \times l_w$ with boundary reinforcement ratio of $\rho_b = 0.001 b_w l_w$ and $l_u \geq 0.2 \times l_w$ with boundary reinforcement ratio of $\rho_b = 0.002 b_w l_w$, respectively. In both cases when the rupture strain of the longitudinal boundary reinforcements (S420) in both directions in the flanges reaches the ultimate strain, the reinforcement rupture, the ultimate curvature and ultimate moment values are obtained. M_u / M_{cr} = 140.7 kNm / 155 kNm = 0.9 and M_u / M_{cr} = 197.7 kNm / 160.5 kNm = 1.23 when boundary reinforcement is placed at a distance of $l_u \geq 0.1 \times l_w$ and $l_u \geq 0.2 \times l_w$, respectively. It is obvious form Figure 8.16 when the boundary reinforcement is placed at a distance of $l_u \geq 0.2 \times l_w$ with boundary reinforcement ratio $\rho_b = 0.002 b_w l_w$ the behavior is not brittle as in the previous case. Ultimate moment M_u is nearly 1.25 times M_{cr}.

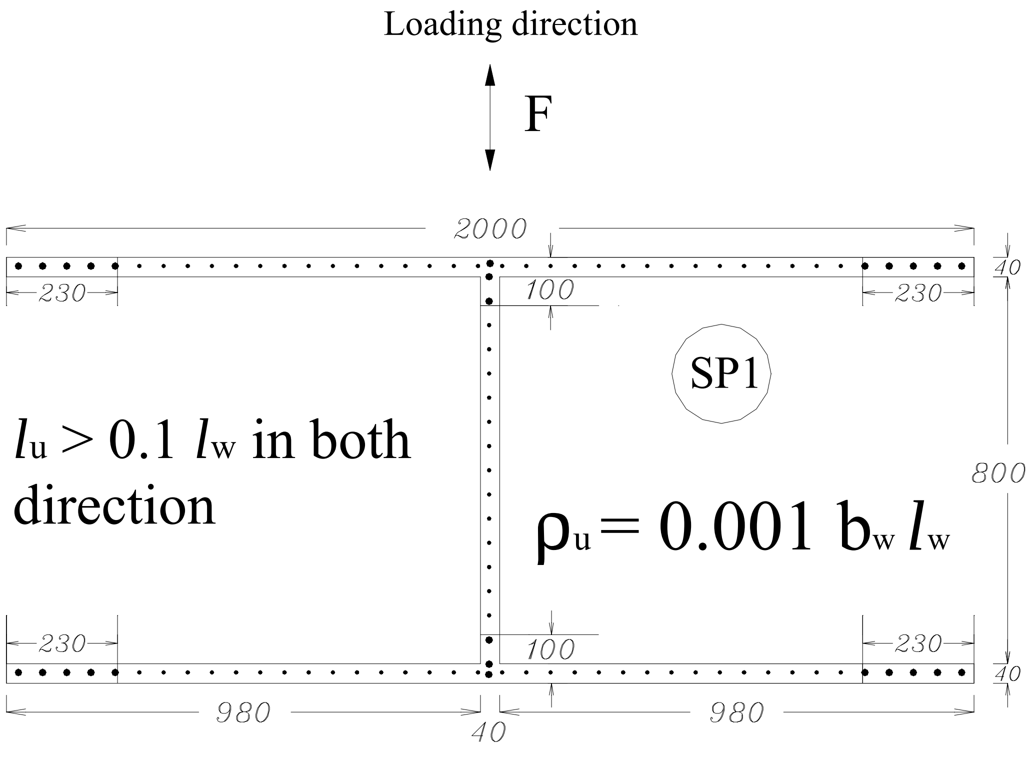

Figure 8.14 Reinforcement pattern and loading direction of SP1 with boundary reinforcement ratio of 0.001 b_w l_w in both directions.

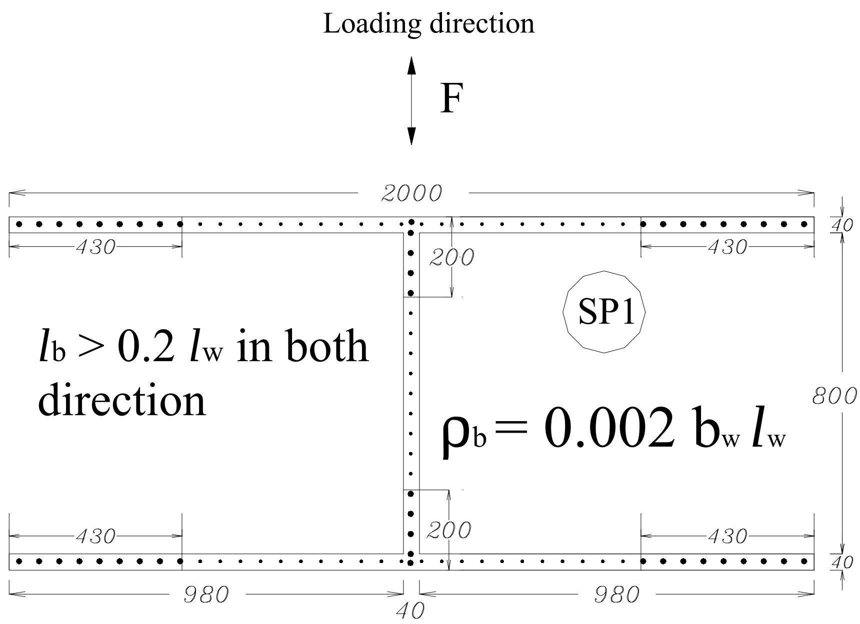

Figure 8.15 Reinforcement pattern and loading direction of SP1 with boundary reinforcement ratio of 0.002 b_w l_w in both direstions.

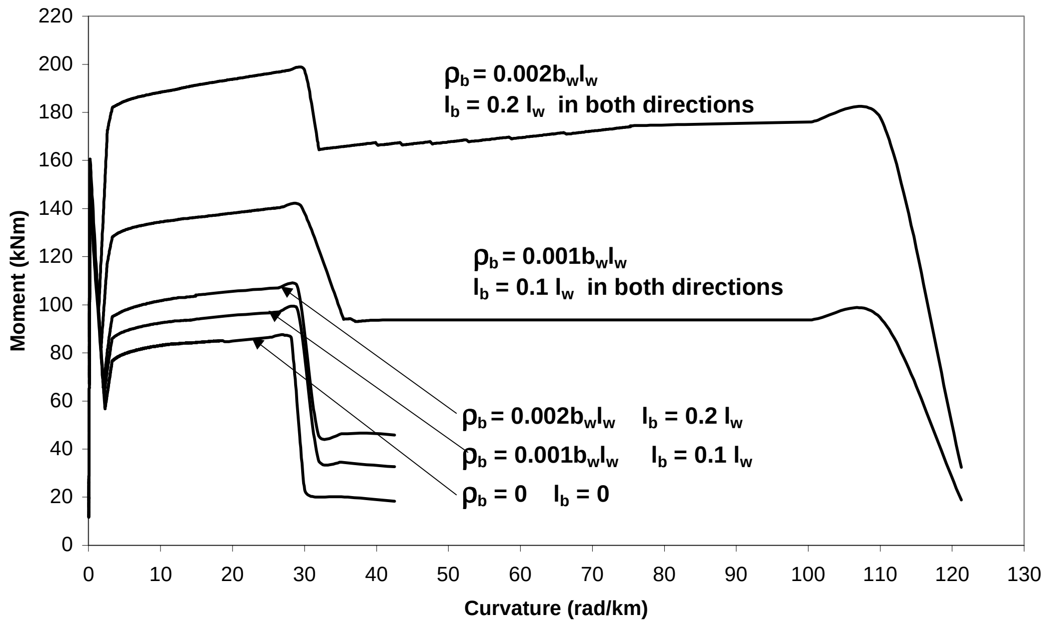

Figure 8.16 Comparisons of the moment-curvature diagram by providing boundary reinforcement along both dimensions.

8.10 PROPERTIES OF SP2

Figure 8.17 shows the reinforcement pattern and loading direction of the shear walls of the panel form test specimen SP2.

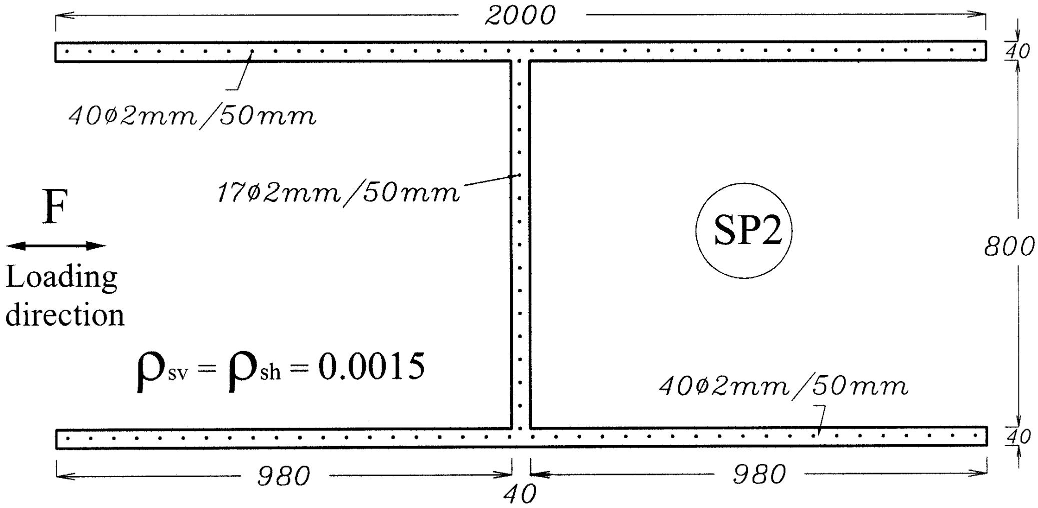

Figure 8.17 Reinforcement pattern and loading direction of SP2. (All dimensions are in mm).

The modular ratio, the total area of the wall reinforcement in the longitudinal direction, the cross-sectional wall area, the longitudinal reinforcement ratio, the transformed area, the gross and transformed moment of inertia and the flexural rigidity of SP2 is summarized in the following.

The modular ratio for SP2 is calculated as

$$n = \frac{E_s}{E_c} = \frac{200{,}000\,\text{MPa}}{33{,}227\,\text{MPa}} = 6.0$$

Total area of the wall reinforcement in the longitudinal direction for SP2 is

$$A_{steel} = 305\,\text{mm}^2$$

Cross-sectional wall area for SP2 is

$$A_{concrete} = 192{,}000 \text{ mm}^2$$

Longitudinal reinforcement ratio for SP2 is

$$\rho_s = \left(\frac{A_s}{A_c}\right) = \left(\frac{305 \text{ mm}^2}{192{,}000 \text{ mm}^2}\right) = 0.00159$$

The transformed area of SP2 is calculated by considering the individual steel layers and found as

$$A_{trans} = 193{,}524 \text{ mm}^2$$

Gross and transformed moment of inertia along the short dimension of SP2 is calculated as

$$I_{SP2gross} = 5.334 \times 10^{-2} \text{ m}^4$$

$$I_{SP2trans} = 5.355 \times 10^{-2} \text{ m}^4$$

Flexural rigidity of SP2 is calculated as

$$E_c \times I_{SP2trans} = 1{,}779{,}217 \text{ kNm}^2$$

It is seen that the gross and transformed moment of inertia of SP2 is very close to each other because longitudinal reinforcement ratio is low as in the case of SP1.

From Equation (8.4), moment corresponding to the first flexural cracking was calculated

$$M_{cr} = 214.88 \text{ kNm}$$

From Equation (8.4), shear corresponding to the first flexural cracking was calculated

$$V_{fcr} = \frac{M_{cr}}{H} = \frac{214.88 \text{ kNm}}{2.67 \text{ m}} = 80.48 \text{ kN}$$

During the static test of panel form test specimen SP2, the crack, which caused the failure of SP2, was observed at about 70 kN load level.

8.11 PRESENTATION OF THE STATIC TEST RESULTS FOR SP2

Figures 8.18, 8.19, 8.20 and 8.21 show the lateral load displacement curves of the 1st, 2nd, 3rd and 4th stories, respectively. In this section the combined 1st and 2nd static tests of SP2 are discussed as it was done for SP1. 80 kN was the maximum applied lateral load for SP2. Maximum lateral-displacements are 0.67 mm, 1.56 mm, and 2.59 mm, for the 1st, 2nd and 3rd story levels, respectively. From Figure 8.21 the maximum displacement and yield displacement are 2.67 mm 4.13 mm at the 4th story level. The displacement ductility factor for SP2 is $\mu_\Delta = 1.55$.

$$\mu_\Delta = \frac{\Delta_u}{\Delta_y} = \frac{4.13}{2.67} = 1.55$$

$$\mu_\Delta \text{ (SP2)} = 1.55 < \mu_\Delta \text{ (required)} = 4\sim5$$

The displacement ductility of SP2 is lower than the required displacement ductility causing SP2 to show brittle behavior, which is also seen from the above equation.

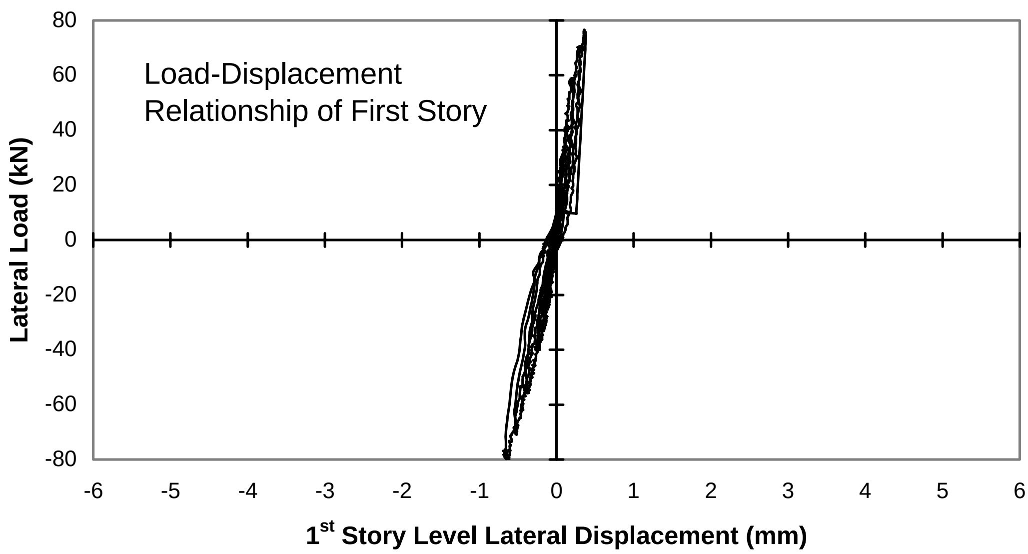

Figure 8.18 Lateral load-displacement curve of the 1st story for SP2.

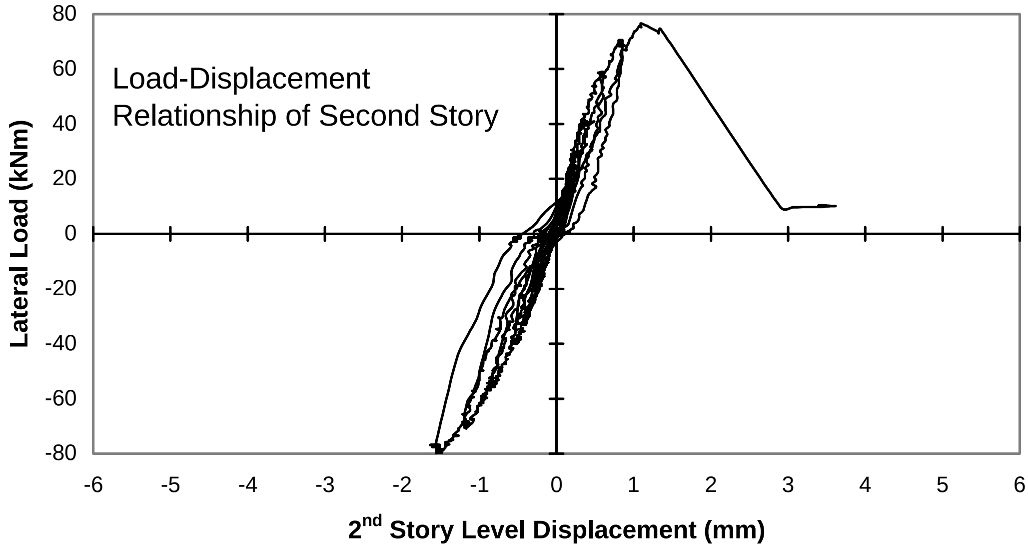

Figure 8.19 Lateral load-displacement curve of the 2nd story for SP2.

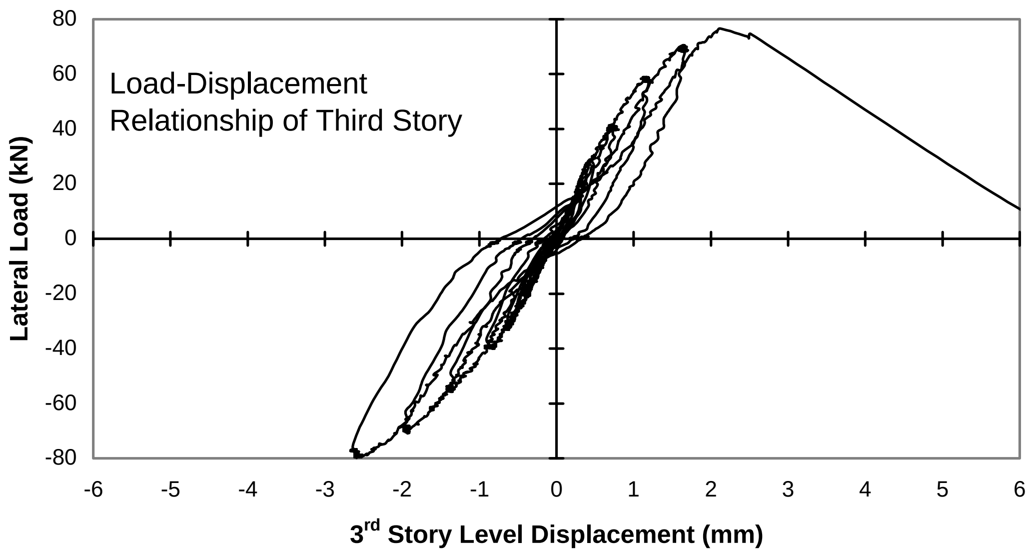

Figure 8.20 Lateral load-displacement curve of the 3rd story for SP2.

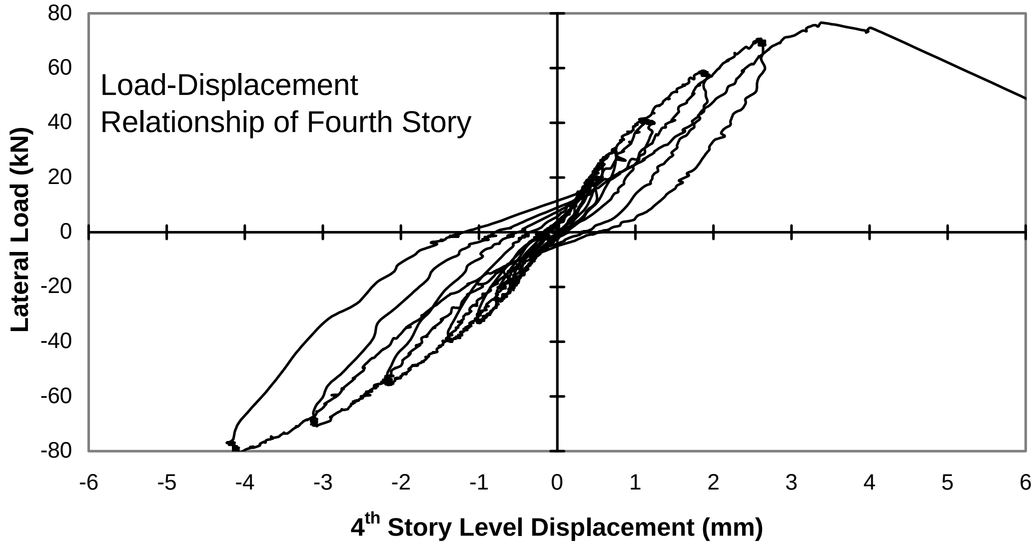

Figure 8.21 Lateral load-displacement curve of the 4th story for SP2.

The observed behavior of SP2 in the static tests can be summarized as follows:

- Horizontal tension cracks occur. These horizontal cracks propagate from boundaries to the center of SP2.
- The longitudinal reinforcement yields as soon as the concrete cracks at the crack location.
- The test specimen SP2 fails, as soon as the concrete cracks, followed by yielding and then rupturing of the longitudinal steel as observed in the static test of SP1.
- Crushing of the concrete is not observed as in the static test of SP1.
- The cracking moment and yield are moment very close to each other.
- Unloaded tension force after cracking cannot be carried by the minimum amounts of longitudinal reinforcement.

The observations of the laboratory tests on SP1 and SP2 indicate that lightly reinforced walls with low axial stress are susceptible to fracture of the longitudinal reinforcement.

8.12 STRENGTH AND CURVATURE DUCTILITY OF SP2

Figure 8.22 shows the analytical interaction diagram of SP2. Axial tension load capacity of SP2 is 183 kN and axial compression load capacity of SP2 is 5880 kN. Axial tension and compression load capacity of SP1 and SP2 are the same because they have the same cross-section but loading direction is perpendicular to each other. Bold horizontal line just below the zero axial load axes shows the constant axial load (-24.66 kN) on SP2. At the balanced case, axial load and moment is 1133 kN and 2980 kNm, respectively. It is seen from the analytical interaction curve that the axial load level on SP2 is very low.

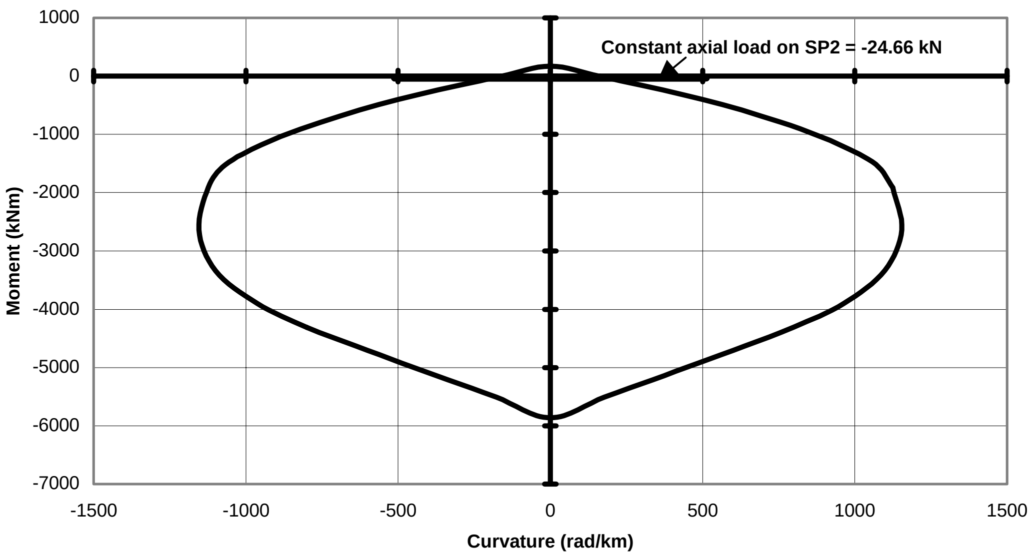

Figure 8.22 Analytical interaction curve of SP2.

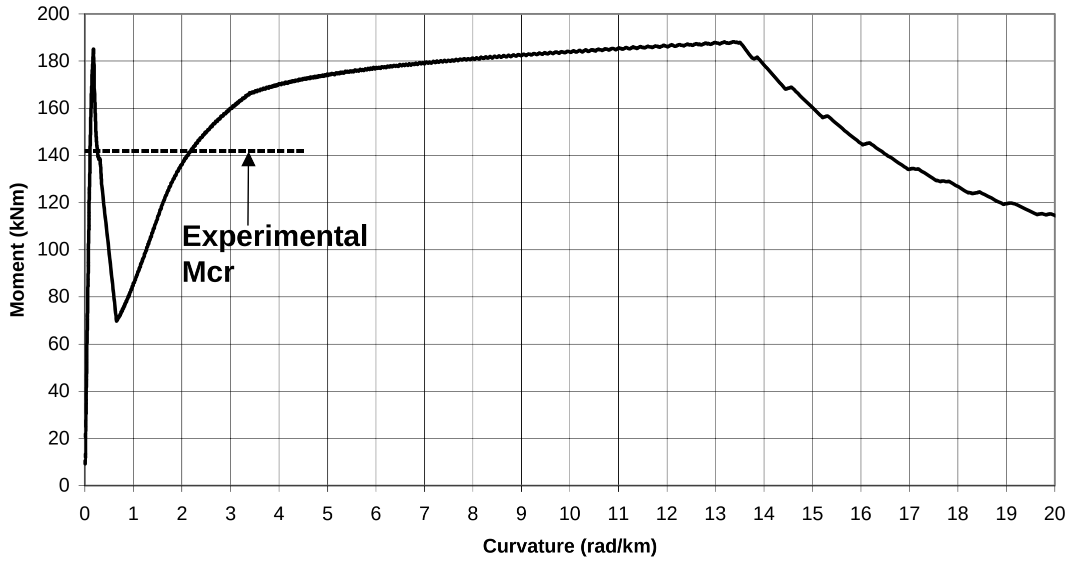

Figure 8.23 Moment-curvature diagram of SP2 obtained by Waller2002.

SP2 remains uncracked for a moment range up to 185.2 kNm. When the extreme tension fiber concrete strain reaches ε_{conbot} = 0.002, the moment value is 185.2 kNm. The curvature is 0.179 rad/km at this stage. After cracking of section the moment falls down. When curvature and moment values are 1.57 rad/km and 147.4 kNm, the outermost layer of longitudinal steel yields. After that the moment values start to increase again. The moment curvature diagram is almost horizontal after that level. Steel layers in the tension part of the section yields consequtively. After yielding of the 23rd layer reinforcement, the moment curvature curve becomes a horizontal curve. The nominal yield curvature and moment values are found as 3.51 rad/km and 167.5 kNm, respectively. It is seen from Figure 8.23 and Table 8.4 that when the steel strain value at the outermost steel layer reaches the rupture strain of the reinforcement steel the longitudianl steels rupture consequtively at the tension side of the section. The moment values start to fall down.

Table 8.4. The summary of the calculated response of SP2.

ε_{top}	ε_{bottom}	ϕ(rad/km)	M(kNm)	Comments
-0.00016	0.0002	0.179	185.2	Concrete cracks
-0.00039	0.00274	1.57	117.4	Bottom steel yields
-0.0004	0.00283	1.61	120.2	2nd layer reinforcement yields
-0.0004	0.00291	1.66	122.9	3rd layer reinforcement yields
-0.00042	0.00302	1.72	125.15	4th layer reinforcement yields
-0.00043	0.0031	1.77	127.65	5th layer reinforcement yields
-0.00045	0.0032	1.83	130.1	6th layer reinforcement yields
-0.00046	0.0033	1.88	132.32	7th layer reinforcement yields
-0.00047	0.0034	1.95	134.8	8th layer reinforcement yields
-0.00048	0.0036	2.02	137.32	9th layer reinforcement yields
-0.00049	0.0037	2.1	139.5	10th layer reinforcement yields
-0.00051	0.00385	2.18	141.7	11th layer reinforcement yields
-0.00052	0.0040	2.27	144.0	12th layer reinforcement yields
-0.00054	0.0042	2.36	146.5	13th layer reinforcement yields
-0.00056	0.0044	2.46	148.9	14th layer reinforcement yields
-0.00057	0.0046	2.57	151.39	15th layer reinforcement yields
-0.0006	0.0048	2.69	154.33	16th layer reinforcement yields
-0.00062	0.00503	2.83	156.5	17th layer reinforcement yields
-0.00064	0.00531	2.98	159.3	18th layer reinforcement yields
-0.00066	0.0056	3.13	161.8	19th layer reinforcement yields
-0.00069	0.00593	3.31	164.9	20th layer reinforcement yields
-0.00072	0.0063	3.51	167.5	21st layer reinforcement yields
-0.00075	0.00673	3.74	168.64	22nd layer reinforcement yields
-0.00078	0.0072	3.99	170.1	23rd layer reinforcement yields
-0.00072	0.0063	3.51	167.5	Nominal yield
-0.00168	0.0253	13.51	187.9	Bottom steel ruptured
-0.00168	0.0258	13.75	181.4	2nd layer reinforcement ruptured
-0.00169	0.0272	14.45	168.13	3rd layer reinforcement ruptured
-0.00171	0.0287	15.21	156.2	4th layer reinforcement ruptured
-0.00172	0.0303	16.03	144.55	5th layer reinforcement ruptured

The curvature ductility ratio for SP2 was found after calculations as 3.85. As soon as the concrete cracks, the longitudinal reinforcements in the tension side yield consecutively. The yield moment was found as M_y = 117.4 kNm, the ratio of yield moment to cracking moment is calculated as 0.634. Ultimate moment is 187.9 kN and the ratio of the ultimate moment to the cracking moment after calculations is found to be 0.507. The curvature ductility ratio for SP2 was calculated as $\mu_\phi = 3.85$.

From the observations of the moment-curvature relationship of SP2 the following conclusions can be drawn:

- The panel form test specimen SP2 reaches their ultimate strength as soon as the concrete cracks; followed by immediate yielding and rupturing of the longitudinal steel in the tension side of the wall.
- From the results of the moment curvature relationship, SP2 shows very brittle behavior due to under-reinforcement. From the results of the moment-curvature relationship, the ratio of the ultimate moment to the cracking moment is smaller than 1.25.

8.13 EFFECTS OF TACK WELDING ON SP2

8.13.1 Ductility Reduction

Ultimate strain of the reinforcing steel is changed and the moment-curvature diagrams are drawn. The effect of ultimate strain of reinforcing steel on the moment-curvature behavior of SP2 is shown in Figure 8.24. The moment-curvature diagram of SP2 is drawn by taking the same ε_{su} values used for SP1. From the moment curvature diagram, it is seen that the cracking moment is 185 kNm. Slight increase is observed at the moment capacity while increasing the ultimate strain of the longitudinal steel. The ultimate moment capacity in all cases is approximately 188 kNm. The ratio of the cracking moment to the ultimate moment is 1.016 and it is smaller than 1.25 for this case as in SP1. When the rupture strain of reinforcing steel is changed from 0.01 to 0.05, the moment-curvature behavior does not change as seen in Figure 8.24.

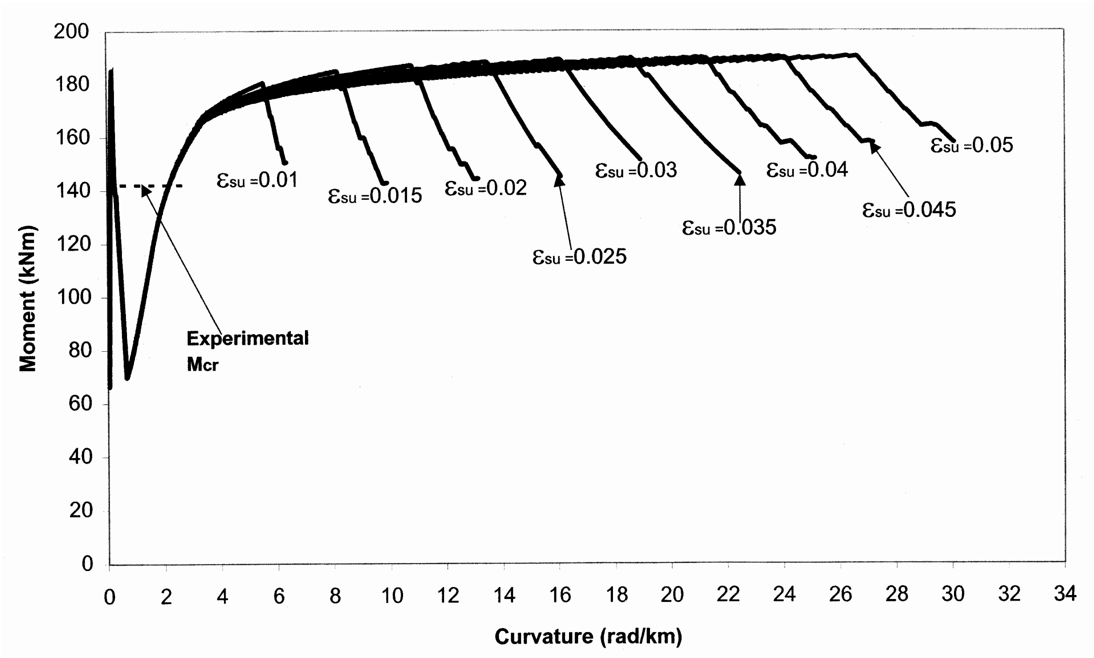

Figure 8.24 Effect of ultimate strain of reinforcing steel on the moment-curvature behavior of SP2.

8.13.2 Strength Reduction

Figure 8.25 shows the effect of ultimate stress of reinforcing steel on the moment-curvature behavior of SP2. As was done for SP1, the ultimate strength of the reinforcing steel was changed and it was seen that the general behavior did not change as seen in the results of SP1.

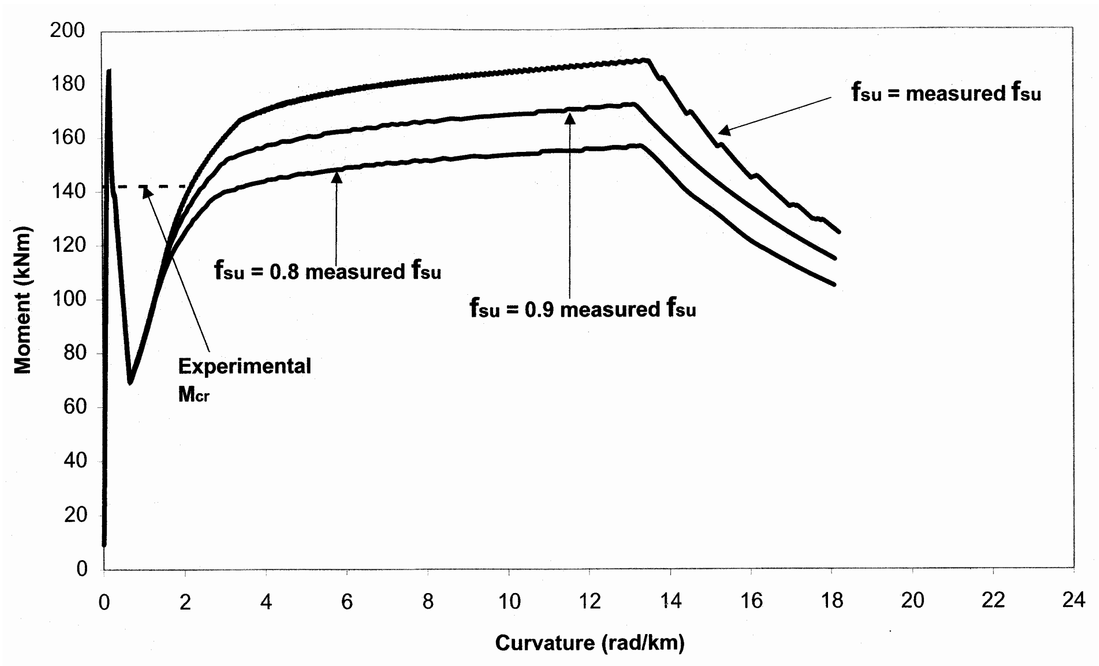

Figure 8.25 Effect of ultimate strain of reinforcing steel on the moment-curvature behavior of SP2.

8.14 BOUNDARY REINFORCEMENT EFFECT ON SP2

The boundary regions are provided at a distance of $l_u \geq 0.1 \times l_w$ and $l_u \geq 0.2 \times l_w$, boundary reinforcement ratio is 0.1% and 0.2%, respectively, for the gross wall area in the direction of loading. Figures 8.26 and 8.27 show the reinforcement pattern and loading direction of SP2 with boundary reinforcement ratio of 0.001 b_w l_w and 0.002 b_w l_w, respectively.

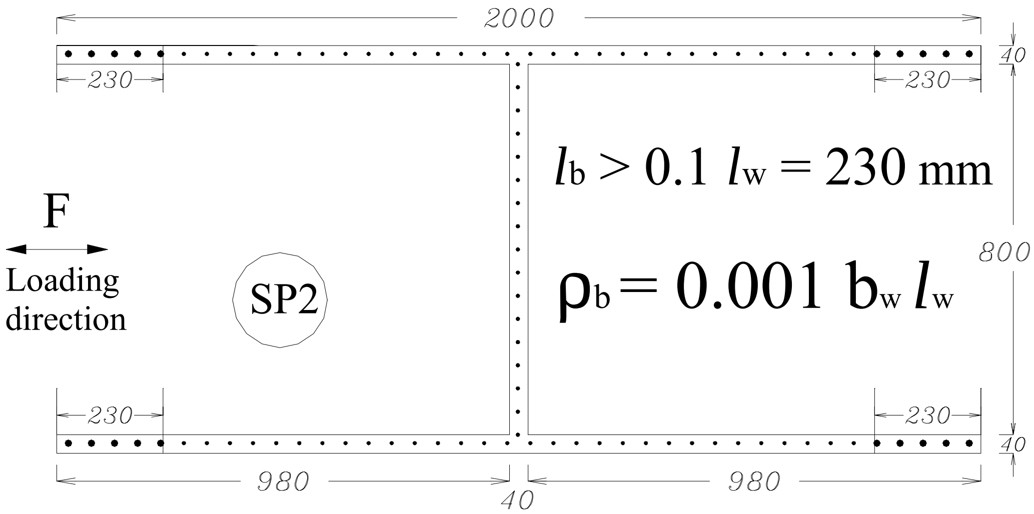

Figure 8.26 Reinforcement pattern and loading direction of SP2 with boundary reinforcement ratio of 0.001 b_w l_w.

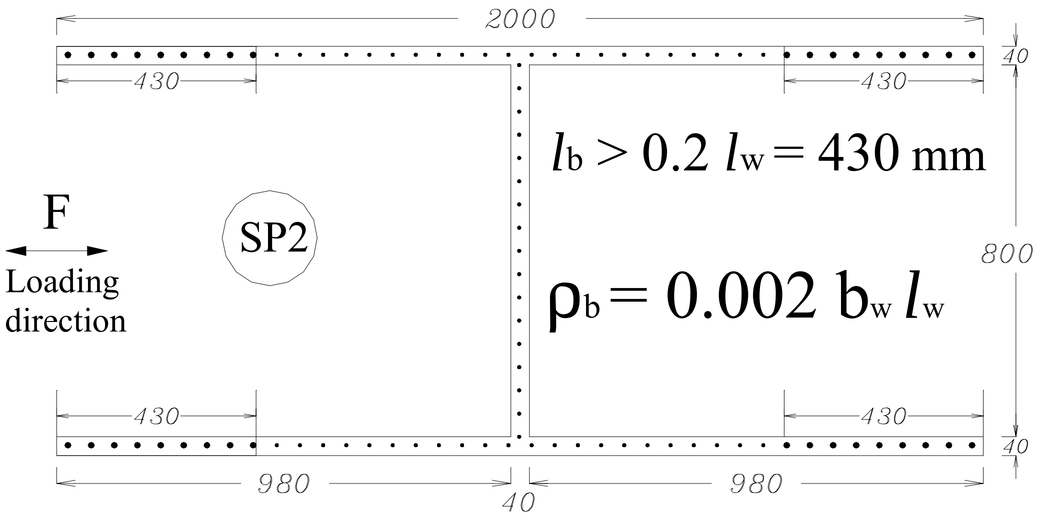

Figure 8.27 Reinforcement pattern and loading direction of SP2 with boundary reinforcement ratio of 0.002 b_w l_w.

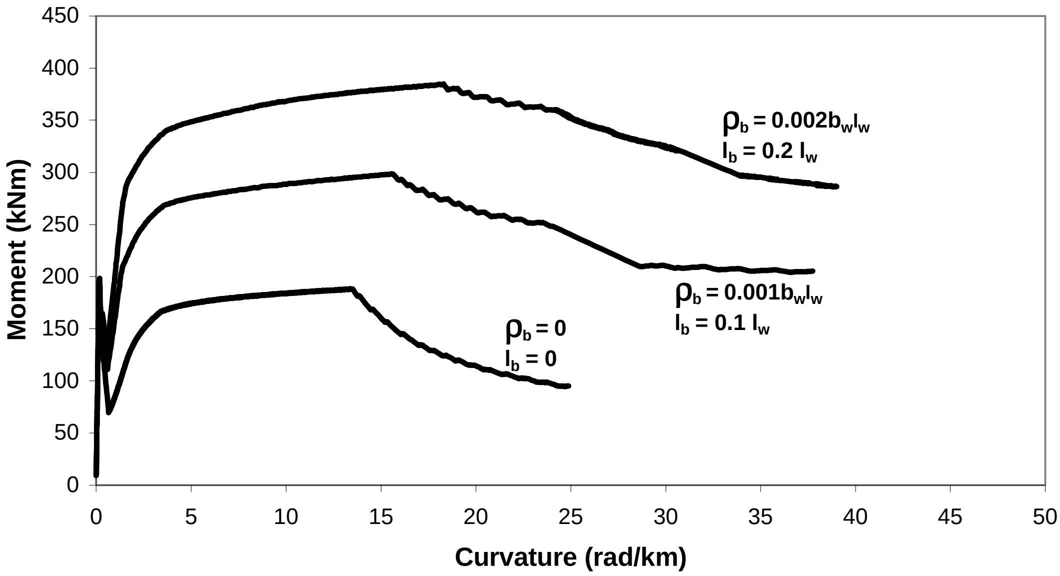

Figure 8.28 Comparison of the moment-curvature diagram by providing concentrated boundary reinforcement.

Three cases are compared in Figure 8.28. The moment-curvature curve at the top shows the concentrated boundary reinforcement is provided at a distance of $l_u \geq 0.2 \times l_w$. In this case the ultimate moment is greater than 1.25 M_{cr}. The behavior in this case is different from the test specimen behavior. When the rupture strain of the mesh reinforcement reaches its rupture value, mesh reinforcement starts to rupture. The crushing of concrete is observed.

8.15 COMPARISONS OF THE LOAD-DISPLACEMENT CURVES AND RESPONSE ENVELOPE CURVES

Comparison of the lateral load displacement curve of SP1 and SP2 for the 1st, 2nd, 3rd and 4th stories are shown in Figures 8.29, 8.30, 8.31 and 8.32. The load carrying capacity of SP2 is two times greater than SP1. SP1 shows more ductile behavior when compared with SP2.

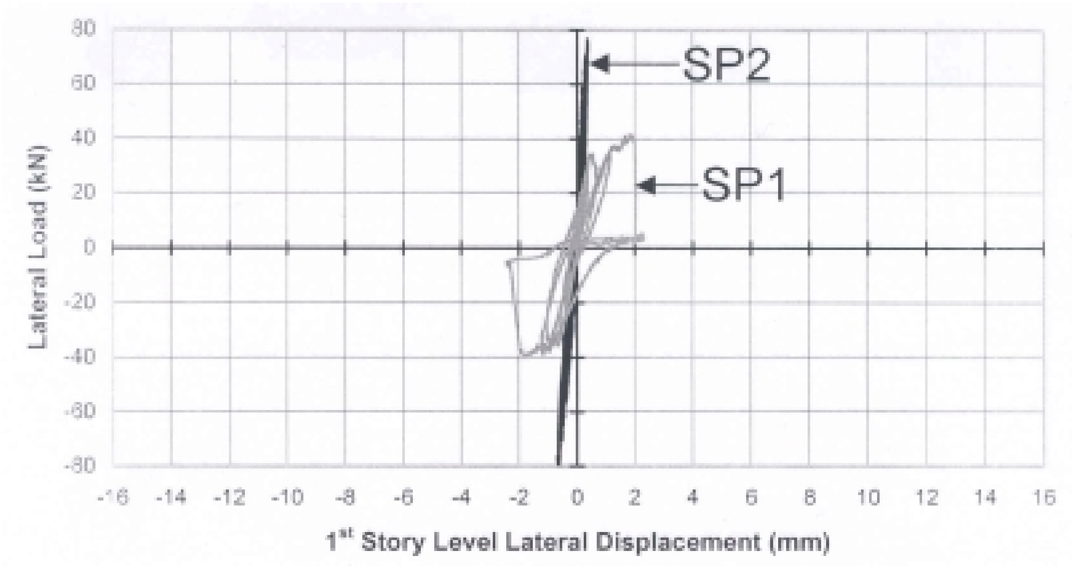

Figure 8.29 Comparison of the lateral load displacement curves of SP1 and SP2 for the 1st story.

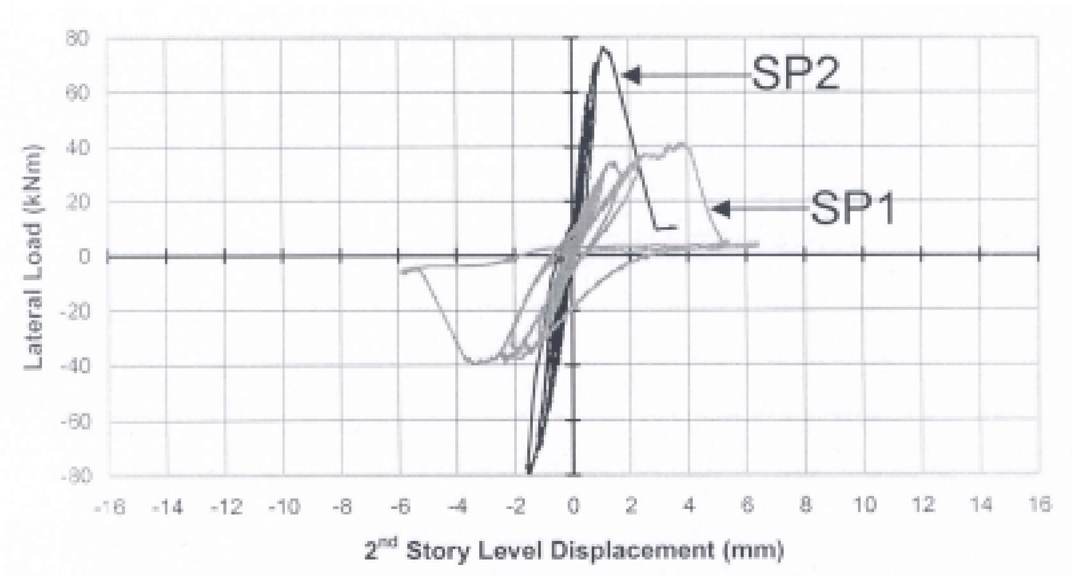

Figure 8.30 Comparison of the lateral load displacement curves of SP1 and SP2 for the 2nd story.

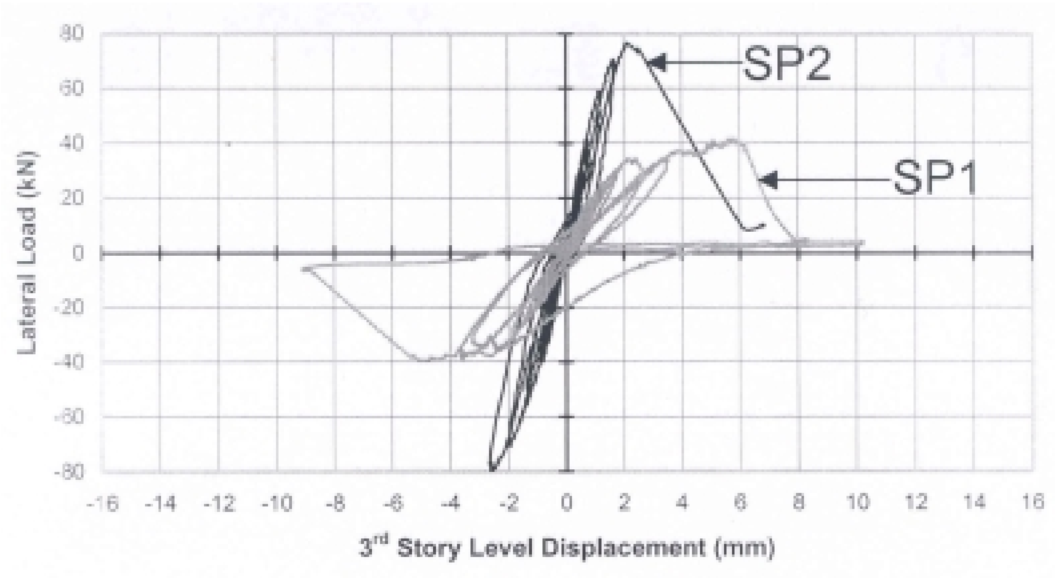

Figure 8.31 Comparison of the lateral load displacement curves of SP1 and SP2 for the 3rd story.

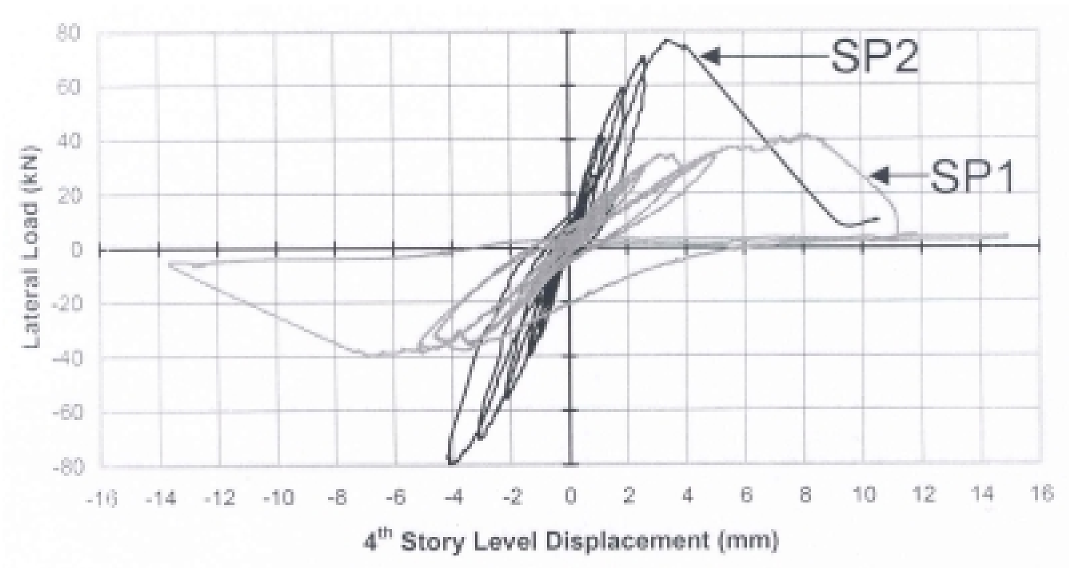

Figure 8.32 Comparison of the lateral load displacement curves of SP1 and SP2 for the 4th story.

Strength and stiffness characteristics of the specimens were evaluated with the help of response envelope curves. The response-envelope curves were obtained by connecting the maximum points of the hysteretic load-displacement curves of the specimens. The response envelopes of SP1 and SP2 were plotted together to bring out the differences of the panel form test specimens.

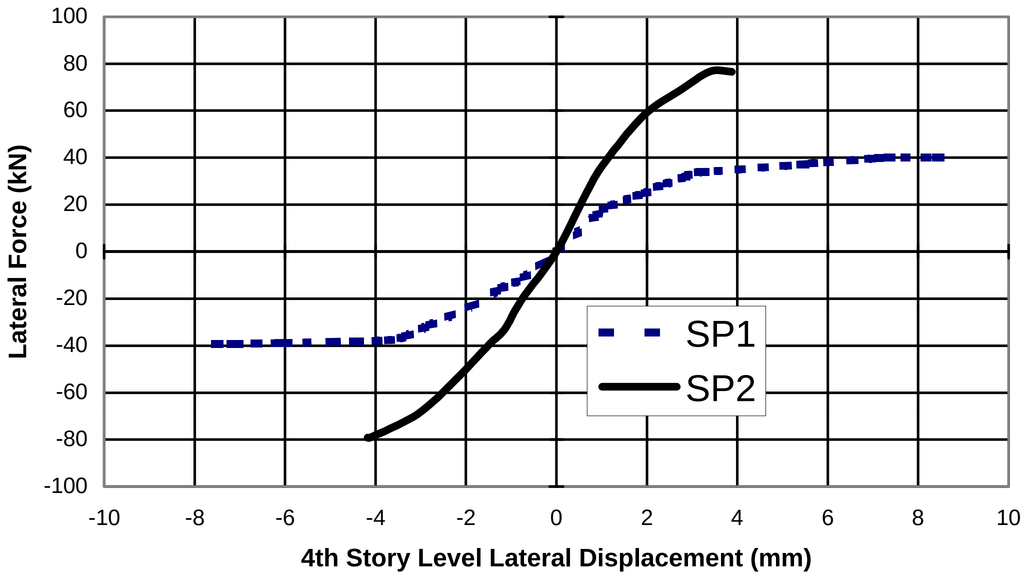

Figure 8.33 Envelope load-displacement curves of SP1 and SP2.

Figure 8.33 shows the response envelopes of SP1 and SP2. From these curves, it can be observed that SP1 behaves more ductile than SP2. Maximum lateral load carried by SP1 and SP2 were 40 kN and 80 kN, respectively. The lateral load carrying capacity of SP2 is two times the value of SP1. The initial stiffness of SP2 is about 2.16 times greater than that of SP1. It should be noted that the maximum lateral displacement of SP1 is two times greater than SP2.

8.16 AN INDICATION OF STIFFNESS

Stiffness can simply be calculated as the slope of the load-deformation curve obtained from the tests. In this study, two types of stiffness were defined; initial stiffness and stiffness prior to failure. The initial stiffness of the specimen k_i, was calculated as the initial slope of the load-deformation curve in the first forward half cycle. "The prior to failure stiffness" of the panel form test specimens was calculated as the average slope of the curve which passes through the origin part of the load-deformation diagram in the last cycle. For the calculation of the stiffness of the specimens, the lateral displacement at the top level was considered. Stiffness properties of the specimens are presented in Table 8.5.

Table 8.5 Stiffness and the stiffness degradation of the test specimens.

Specimen	Initial Stiffness (N/mm)	Prior to Failure Stiffness (N/mm)	Stiffness Degradation (%)
SP1	17550	5850	66.67
SP2	37907	20259	46.56

As can be seen from the Table 8.5, the stiffness degradation of SP1 and SP2 near the failure stage is 3 and 1.87 times lower respectively, which means that the stiffness degradation of SP1 was higher than that of the SP2.

The stiffness reduction of the panel form test specimens near the failure stage was not severe. The prior-to-failure stiffness and the stiffness degradation are related to the maximum displacement during the test. By increasing maximum displacement, "the prior to failure stiffness" decreases and stiffness degradation ratios accordingly increase. However, the maximum displacements of SP1 and SP2 near the failure stage were approximately 8.73 mm and 4.17 mm, respectively. Therefore, one can conclude that the stiffness degradation of SP1 is higher than that of the SP2. As can be seen from Table 8.5 the initial stiffness and prior to failure stiffness of SP2 are 2.16 and 3.46 times that of SP1. The initial stiffness is expected because uncracked moment of inertia and flexural rigidity (EI) of SP2 is two times greater than SP1.

8.17 ENERGY DISSIPATION

The amount of dissipated energy in the specimens was calculated as the area under the experimental load-deformation curves. The work done by the axial load and the energy dissipated by means of the friction forces were neglected since they were small.

The energy dissipation characteristics of the specimens strongly depend on the loading history. Therefore, it would be more meaningful to compare the energy dissipation characteristics of specimens with the same loading history. However, in this experimental study presented in this thesis, the loading histories of SP1 and SP2 were different.

The cumulative displacement was calculated as the addition of absolute maximum displacements in the forward half and backward half cycles (Canbay, 2001). Figure 8.34 shows the cumulative energy dissipation curves of SP1 for the first and second static tests. As can be seen from the Figure 8.34, SP1 dissipated more energy in the 2nd static test as compared to the 1st static test, because the 1st static test was in the elastic range, and the 2nd static test was in the nonlinear range. Figure 8.35 shows the cumulative energy dissipation curves of the static tests of SP1.

Table 8.6 Summary of the absolute cumulative displacement and cumulative energy dissipation of the first test of SP1.

Half cycle No	Maximum top displ. (mm)	Lateral load (kN)	Absolute cumulative displacement (mm)	Energy per cycle (kNmm)	Cumulative energy (kNmm)
1	1.27	20	1.27	12.7	12.7
-1	-1.46	-20	2.73	14.6	27.3
2	1.40	20	4.13	14.0	41.3
-2	-1.52	-20	5.65	15.2	56.2
3	1.96	25	7.61	24.5	81
-3	-2.00	-25	9.61	25.0	106
4	2.53	30	12.14	37.95	143.9
-4	-2.66	-30	14.8	39.9	181.9
5	3.89	35	18.69	77.0	258.9
-5	-4.60	-35	23.29	98.0	356.9

Table 8.7 Summary of the absolute cumulative displacement and cumulative energy dissipation of the second static test of SP1.

Half cycle No	Maximum top displ. (mm)	Lateral load (kN)	Absolute cumulative displacement (mm)	Energy per cycle (kNmm)	Cumulative energy (kNmm)
1	5.32	35	5.32	147	147
-1	-5.37	-35	10.69	157	304
2	8.6	40	19.29	199	503
-2	-7.3	-40	26.59	203	706

Figure 8.36 shows the cumulative energy dissipation curves of SP2 for the first and second static tests. As can be seen from Figure 8.36, SP2 dissipated much more energy in the 2nd static test as compared to the 1st static test. This is reasonable

because in the 1st static test of SP2 maximum applied lateral load was half of the 2nd static test. Figure 8.37 shows the cumulative energy dissipation curves of the static tests of SP2. Figure 8.38 shows the cumulative energy dissipation curves of SP1 and SP2 for the static tests. It is seen from Figure 8.38 that SP1 dissipates more energy than SP2 in the static tests.

It would be misleading to draw generalized conclusions form Figures 8.34, 8.35, 8.36, 8.37 and 8.38, since the load histories were different.

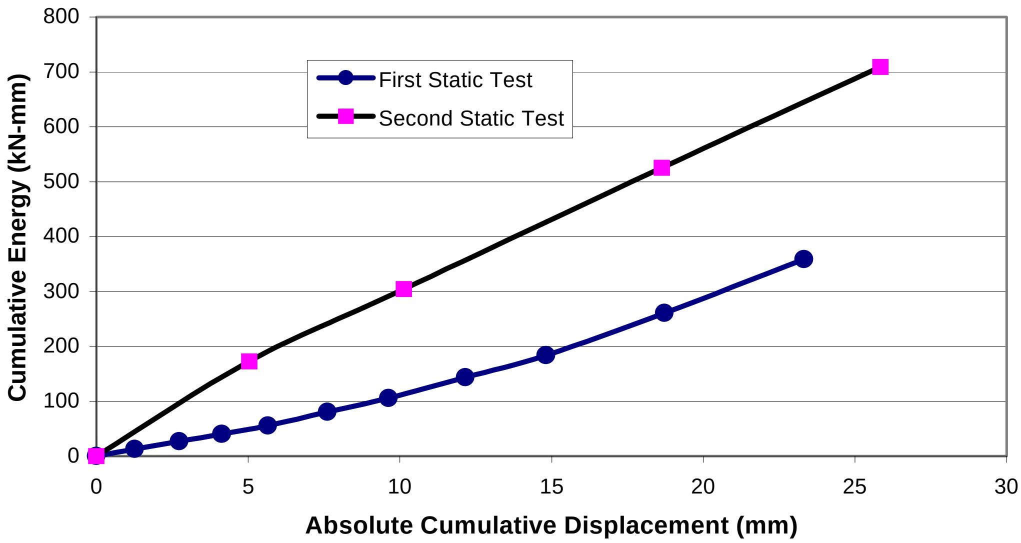

Figure 8.34 Cumulative energy dissipation curves of the SP1 for the first and second static test.

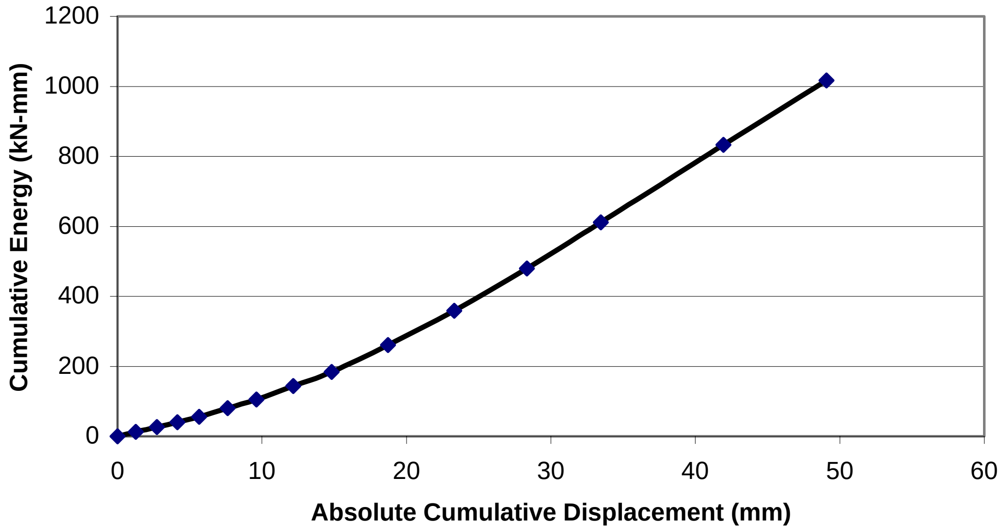

Figure 8.35 Cumulative energy dissipation curve of the static tests of SP1.

Table 8.8 Summary of the absolute cumulative displacement and cumulative energy dissipation of the first static test of SP2.

Half cycle No	Maximum top displ. (mm)	Lateral load (kN)	Absolute cumulative displacement (mm)	Energy per cycle (kNmm)	Cumulative energy (kNmm)
1	0.234	10.0	0.234	1.170	1.170
-1	-0.322	-10.0	0.556	1.610	2.780
2	0.352	15.0	0.908	2.640	5.420
-2	-0.498	-15.0	1.406	3.735	9.155
3	0.498	20.0	1.904	3.735	12.890
-3	-0.664	-20.0	2.568	6.640	19.530
4	0.654	25.0	3.222	8.175	27.705
-4	-0.830	-25.0	4.052	10.375	38.080
5	0.810	30.0	4.862	12.150	50.230
-5	-1.016	-30.0	5.878	15.240	65.470

Table 8.9 Summary of the absolute cumulative displacement and cumulative energy dissipation of the second static test of SP2.

Half cycle No	Maximum top displ. (mm)	Lateral load (kN)	Absolute cumulative displacement (mm)	Energy per cycle (kNmm)	Cumulative energy (kNmm)
1	0.710	20.0	0.710	7.10	7.10
-1	-0.535	-20.0	1.245	5.35	12.45
2	1.390	40.0	2.635	27.80	40.25
-2	-1.220	-40.0	3.885	24.4	64.65
3	-2.195	55.0	6.050	60.36	125.01
-3	-1.976	-55.0	8.026	54.34	179.35
4	3.080	70.0	11.106	107.8	287.15
-4	-2.685	-70.0	13.791	93.98	381.13
5	4.100	80.0	17.891	164	545.13
-5	-3.200	-80.0	21.091	117	662.13

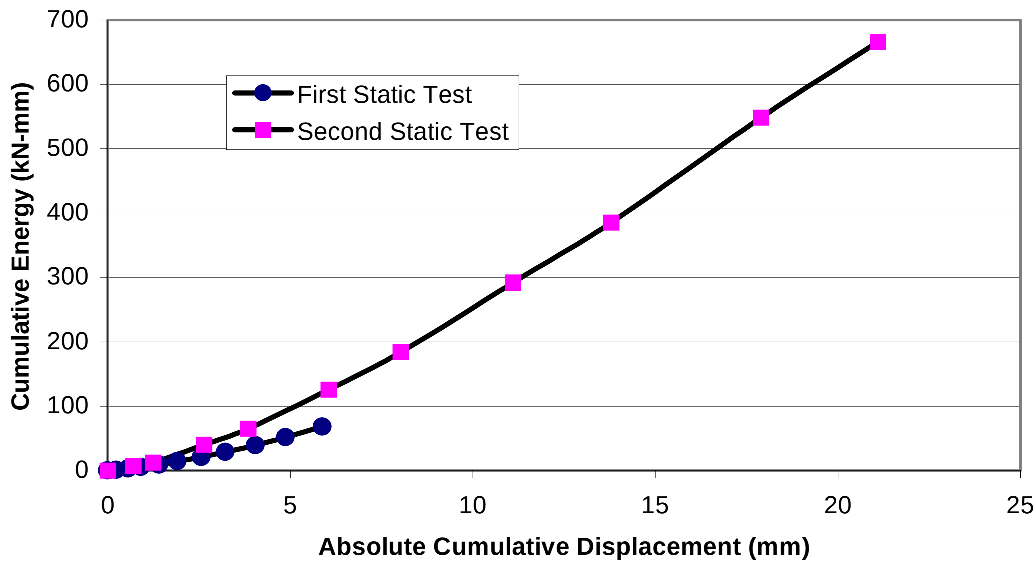

Figure 8.36 Cumulative energy dissipation curves of SP2 for the first and second static tests.

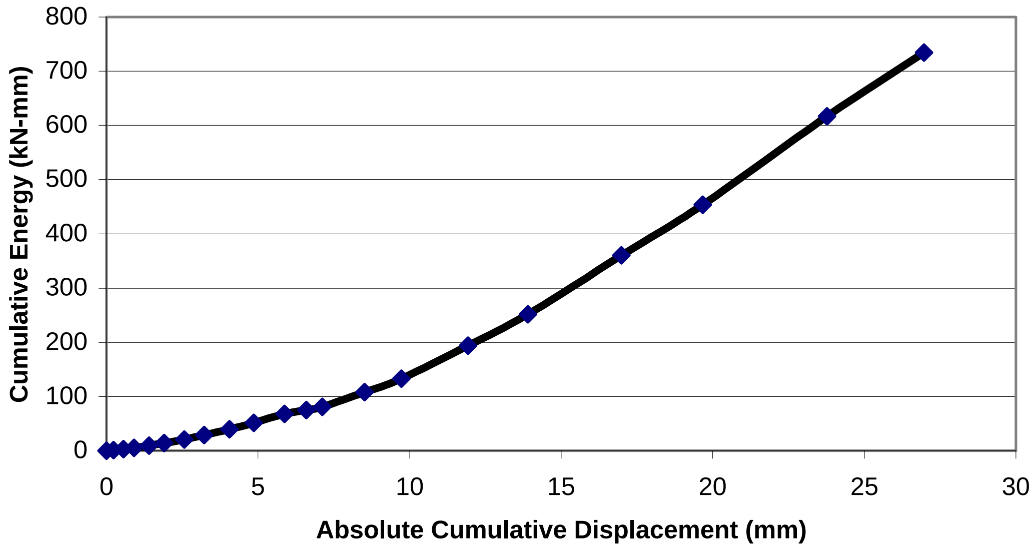

Figure 8.37 Cumulative energy dissipation curves of the static tests of SP2.

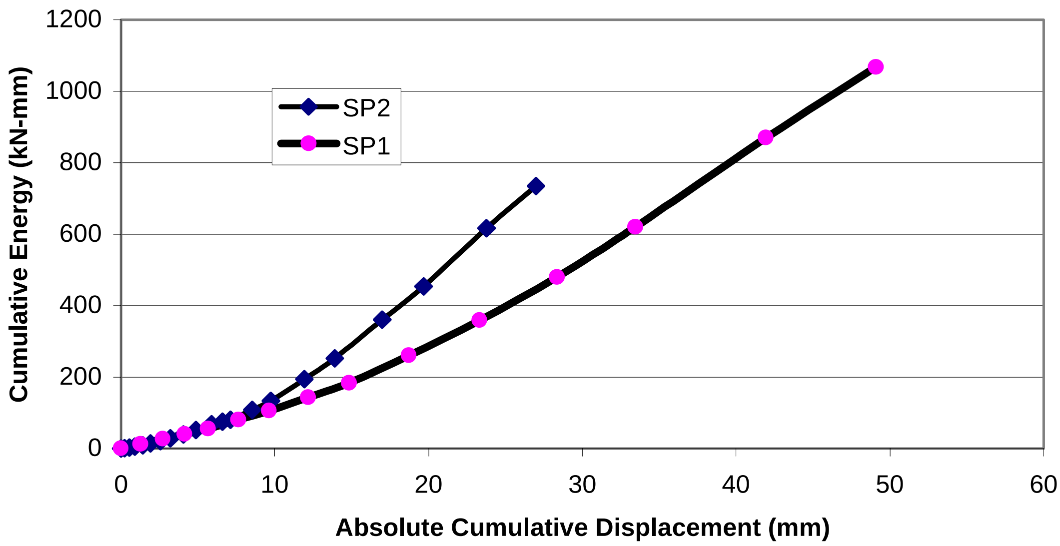

Figure 8.38 Cumulative energy dissipation curves of SP1 and SP2 for the static tests.

8.18 STORY DRIFT INDEX

Story drift index is defined as the relative displacement between the two successive floors dividing the corresponding story height and frequently used in earthquake engineering considering a measure of structural and non-structural damage. Story drift index is not allowed to exceed a certain limit in order to prevent structural and non-structural damage. Additionally for interstory drifts more than 1%, P-Δ effects lead to rapidly increasing augmentation of these drifts (Paulay, 1992). According to the Turkish Seismic Code (AY, 1997), the maximum story drift index is limited to 0.0035 and 0.02/R based on the elastic analysis of the structure. R is the behavior factor and for shear wall structures of normal ductility R = 4. On the other hand, according to (UBC 1997), the maximum story drift index for inelastic analysis is limited to 0.025 for the structures with a fundamental period less than 0.7 seconds, and 0.02 for the structures with a fundamental period greater than 0.7 seconds. As the numbers indicate, the Turkish Seismic Code is more conservative about the amount of story drift index.

Figures 8.39, 8.40, 8.41, and 8.42 show envelope curves of the 1st, 2nd, 3rd and 4th story drift ratios for SP1.

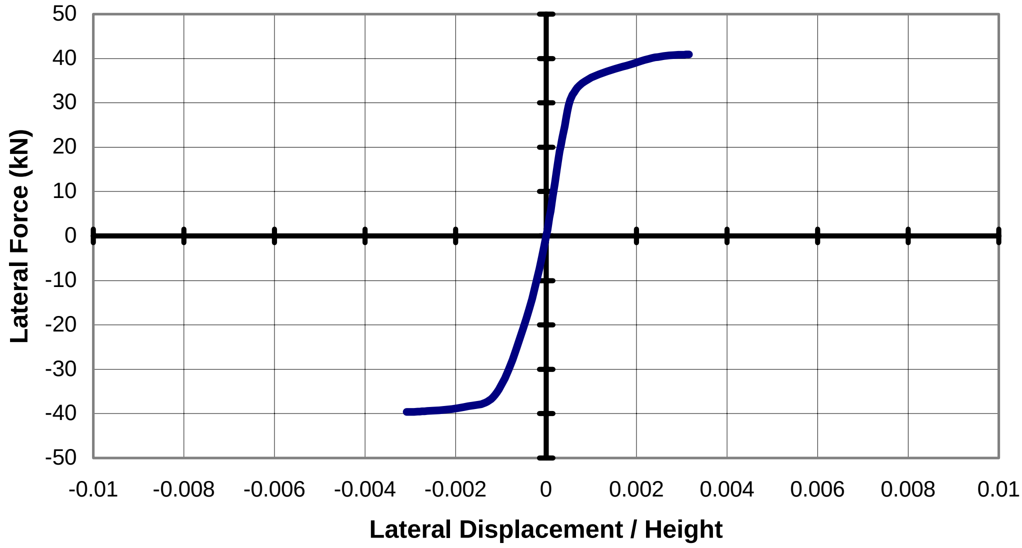

Figure 8.39 Envelope curves of the 1st story drift ratio with the applied load, for SP1.

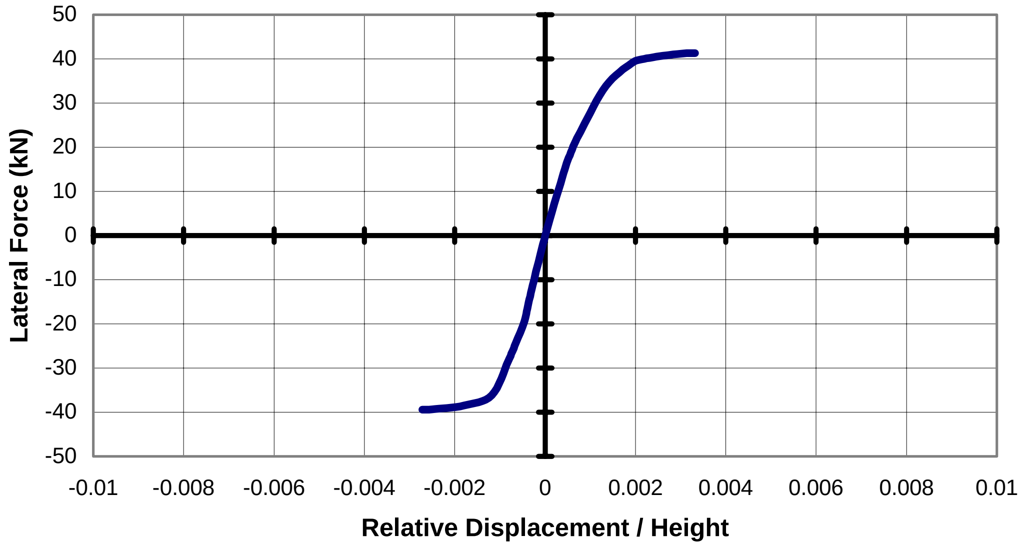

Figure 8.40 Envelope curve of the 2nd story drift ratio with the applied load, for SP1.

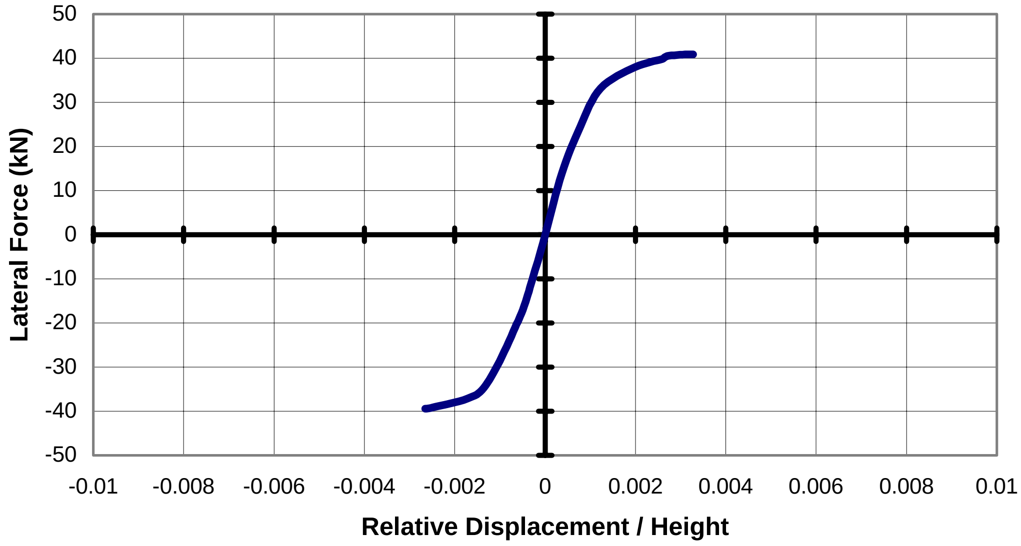

Figure 8.41 Envelope curve of the 3rd story drift ratio with the applied load, for SP1.

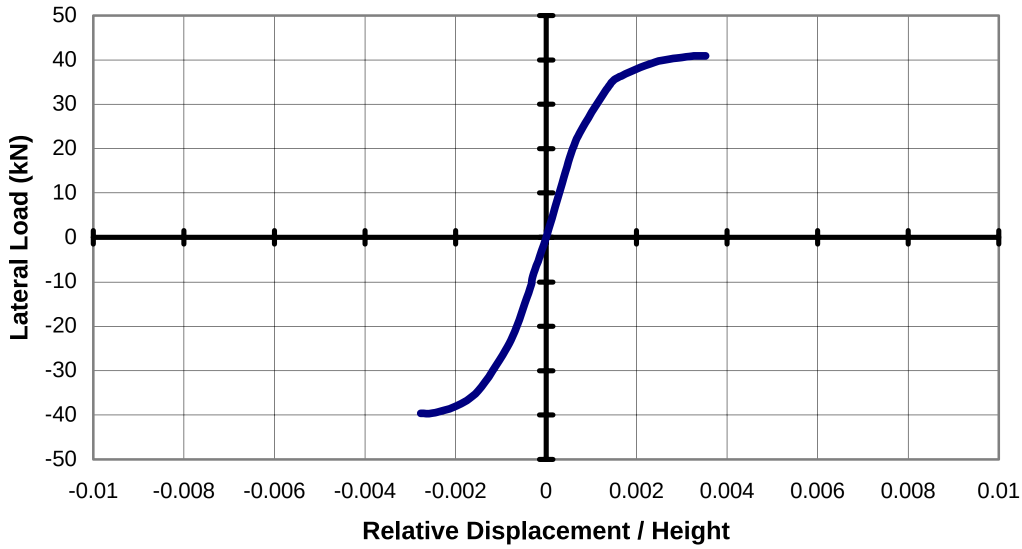

Figure 8.42 Envelope curve of the 4th story drift ratio with the applied load, for SP1.

Envelope curves of the 1st, 2nd, 3rd, and 4th story drift ratios with the applied load for specimen SP1 were almost the same. The reason was that this specimen behaved almost like a cantilever beam above the base. For all stories maximum drift ratio is less than 0.0035. Measured maximum drift ratios for the 1st, 2nd, 3rd, and 4th stories are 0.0032, 0.0033, 0.0033 and 0.0035, respectively. 1997 Turkish seismic code specified maximum drift ratio for this case is 0.0035.

Figures 8.43, 8.44, 8.45, and 8.46 show envelope curves of the 1st, 2nd, 3rd and 4th story drift ratios for SP2. Envelope curves of the 1st, 2nd, 3rd, and 4th story drift ratios with the applied load for specimen SP2 were almost the same. The reason was that this specimen behaved almost like a cantilever beam above the base. For all stories maximum drift ratio is less than 0.003. Measured maximum drift ratios for the 1st, 2nd, 3rd, and 4th stories are 0.0022, 0.00183, 0.0015 and 0.001, respectively. Code specified maximum drift ratio for this case is 0.0035. It is seen that the drift ratio indexes of SP1 and SP2 are in the limits of 1997 Turkish seismic code.

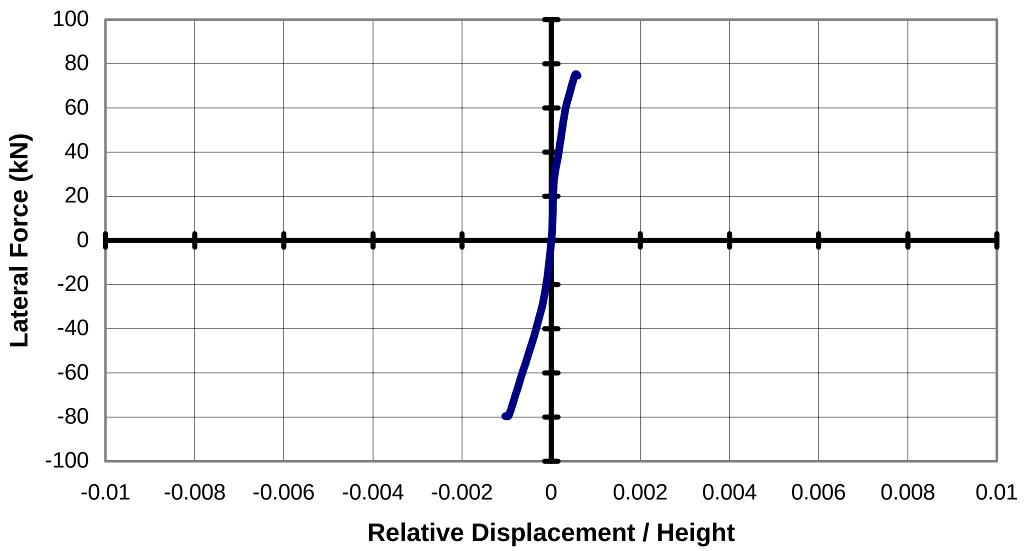

Figure 8.43 Envelope curve of the 1st story drift ratio with the applied load, for SP2.

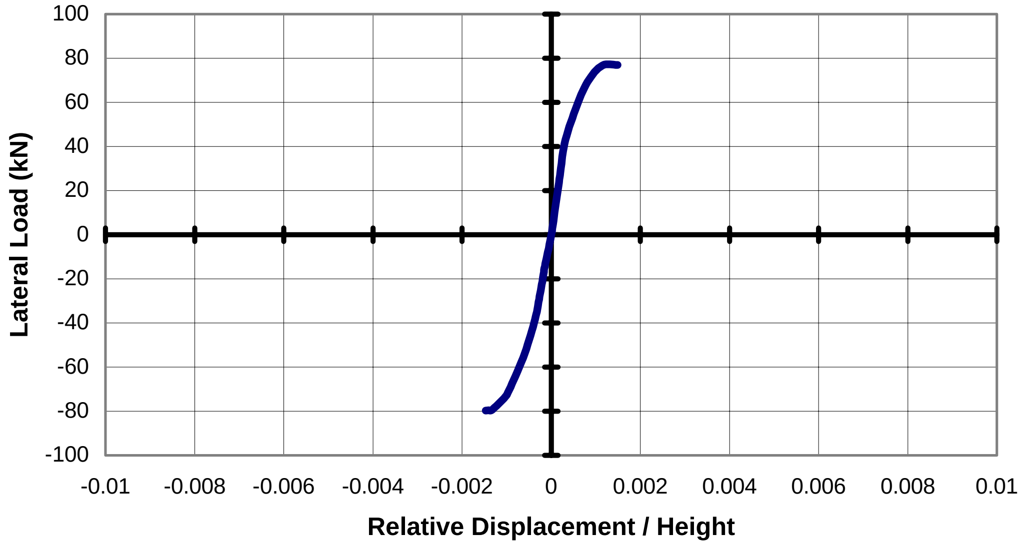

Figure 8.44 Envelope curve of the 2nd story drift ratio with the applied load, for SP2.

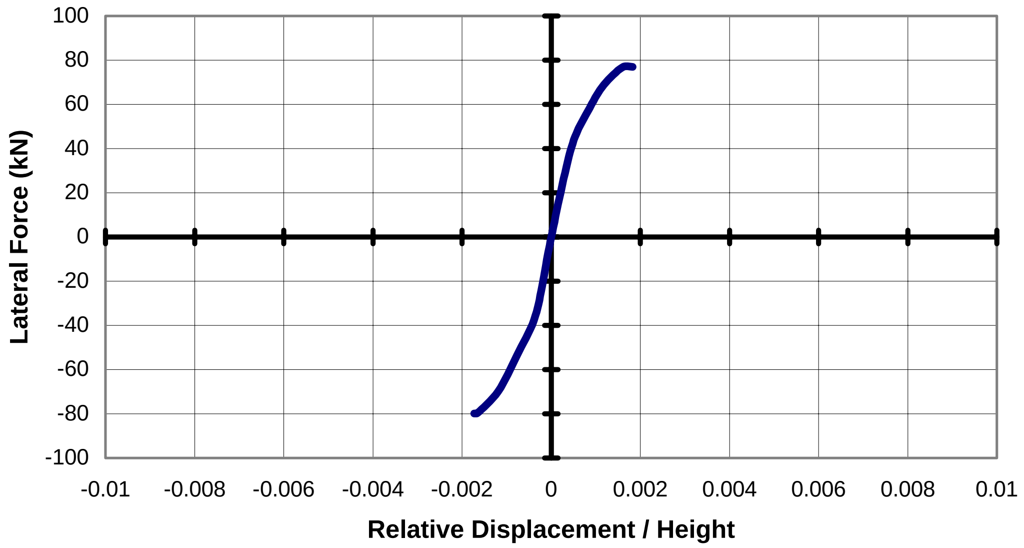

Figure 8.45 Envelope curve of the 3rd story drift ratio with the applied load, for SP2.

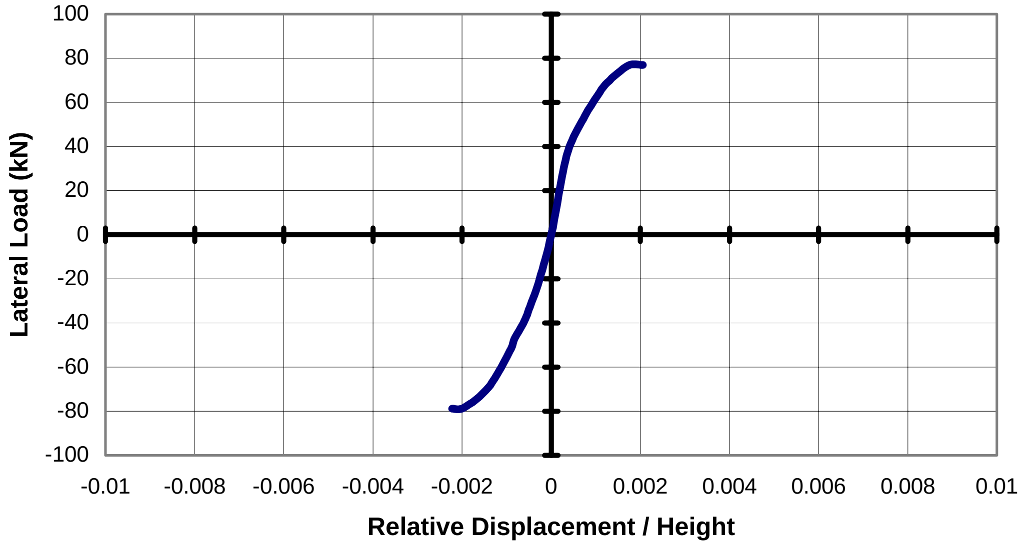

Figure 8.46 Envelope curve of the 4th story drift ratio with the applied load, for SP2.

8.19 THE RELATIONSHIP BETWEEN SYSTEM AND CURVATURE DUCTILITY IN A CANTILEVER SHEAR WALLS

The relationship between curvature ductility and displacement ductility in a simple case can be illustrated with reference to the cantilever shearwall with a lateral point load at the top in Figure 8.47 (The idealized distribution of curvature at the ultimate moment is also shown).

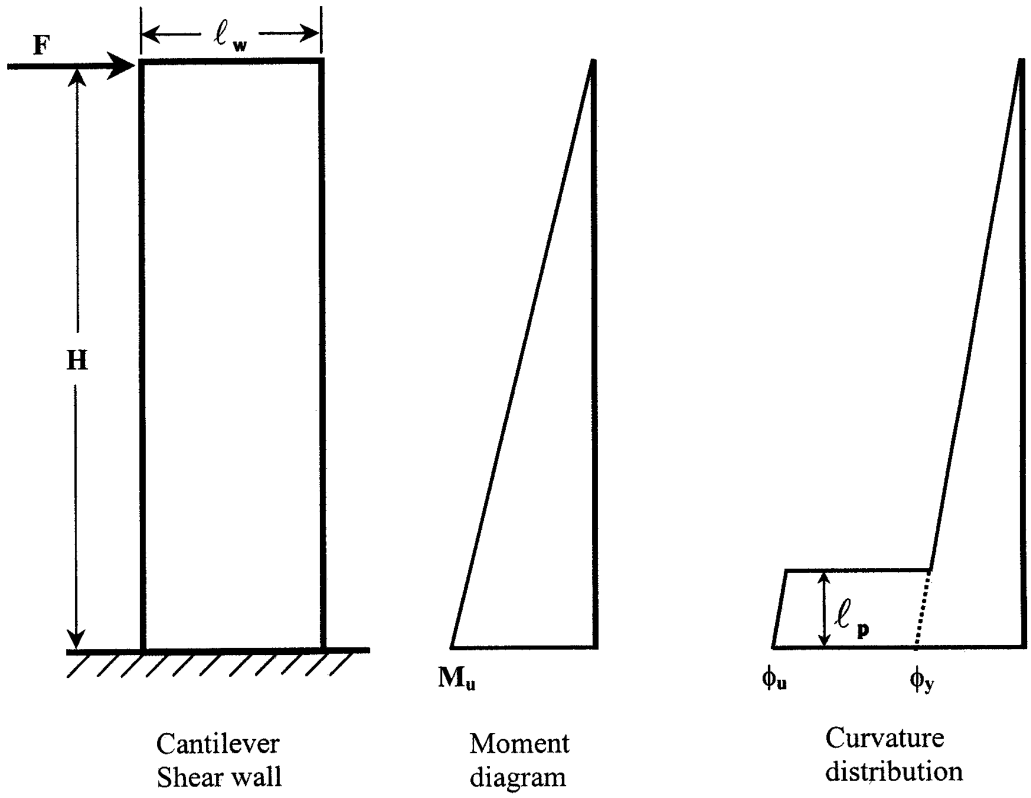

Figure 8.47 Cantilever shear wall with lateral loading at ultimate moment

The lateral yield deflection at the top of the shear wall Δ_y is

$$\Delta_y = \frac{\phi_y \times H^2}{3} \tag{8.6}$$

The plastic hinge rotation θ_p may be assumed to result from uniform plastic curvature ϕ_p in the plastic hinge length ℓ_p shown in Figure 8.47, so that

$$\theta_p = \phi_p \times \ell_p = (\phi_u - \phi_y) \times \ell_p \tag{8.7}$$

Assuming the plastic rotation to be concentrated at midheight of the plastic hinge, the plastic displacement at the top of the shear wall can be calculated by using Equation 8.8.

$$\Delta_p = \theta_p \times (H - 0.5 \times \ell_p) = (\phi_u - \phi_y) \times \ell_p \times (H - 0.5 \times \ell_p) \tag{8.8}$$

The system or displacement ductility for the cantilever shear wall was previously defined as

$$\mu_\Delta = \frac{\Delta_u}{\Delta_y} = \frac{\Delta_y + \Delta_p}{\Delta_y} = 1 + \frac{\Delta_p}{\Delta_y} \tag{8.9}$$

Substituting Equations (8.6) and (8.8) into Equation (8.9) and rearranging yields the relationship between displacement and curvature ductility as in Equation (8.10)

$$\mu_\Delta = 1 + 3 \times (\mu_\phi - 1) \times \frac{\ell_p}{H} \times \left(1 - \frac{\ell_p}{2 \times H}\right) \tag{8.10}$$

or conversely,

$$\mu_\phi = 1 + \frac{(\mu_\Delta - 1)}{3 \times \left(\frac{\ell_p}{H}\right) \times \left[1 - \left(\frac{\ell_p}{2 \times H}\right)\right]} \tag{8.11}$$

Paulay and Priestly (1991) suggest two alternative expressions for the plastic hinge length:

$$\ell_p = 0.2 \times \ell_w + 0.03 \times H \tag{8.12}$$

$$\ell_p = 0.0536 \times H + 0.022 \times d_{bl} \times f_y \tag{8.13}$$

Equation 8.12 includes ℓ_w to the estimate of plastic hinge to account for the influence of plasticity spread due to diagonal cracking. It is felt to be more appropriate for squat walls. Equation 8.13, which was originally developed for columns, is more strongly related to wall height, and includes a term for strain penetration into the foundation, which is depended on diameter d_{bl} and yield strength f_y of the longitudinal reinforcement, and should be more appropriate at higher aspect ratios. Therefore, for the panel form test specimens SP1 and SP2 the plastic hinge length is calculated as follows:

$$\ell_p = 0.0536 \times 2670 + 0.022 \times 2 \times 550 = 167.31\,\text{mm} \approx 170\text{mm}$$

8.20 The Relationship Between System and Curvature Ductility for SP1

By using $\ell_p = 170\,\text{mm}$ and H = 2670 mm and curvature ductility ratio $\mu_\phi = 7.89$ (from the moment curvature relation obtained from Waller2002 and Response2000) the displacement ductility factor can be found as

$$\mu_\Delta = 1 + 3\times(\mu_\phi - 1)\times\frac{\ell_p}{H}\times\left(1-\frac{\ell_p}{2\times H}\right) = 1 + 3\times(7.89-1)\times\frac{170}{2670}\times\left(1-\frac{170}{2\times 2670}\right)$$

$$\mu_\Delta(\text{found}) = 2.274 < \mu_\Delta(\text{required}) = 4 \approx 5$$

It is understood from the above equation that SP1 does not have enough displacement ductility.

By assuming that SP1 has displacement ductility $\mu_\Delta = 4$, we can find the required curvature ductility and compare it with the available curvature ductility found from Waller2002.

$$\mu_\phi = 1 + \frac{(\mu_\Delta - 1)}{3\times\left(\frac{\ell_p}{H}\right)\times\left[1-\left(\frac{\ell_p}{2\times H}\right)\right]} = 1 + \frac{(4-1)}{3\times\left(\frac{170}{2670}\right)\times\left[1-\left(\frac{170}{2\times 2670}\right)\right]}$$

$$\mu_\phi(\text{required}) = 17.23 > \mu_\phi(\text{found}) = 7.89$$

Curvature ductility of SP1 was found as μ_ϕ = 7.89 form the computer programs Waller2002 and Response-2000. The required curvature ductility is 2.18 times greater than the available curvature ductility. It is obvious that SP1 does not have enough curvature ductility capacity either.

8.21 The Relationship Between System and Curvature Ductility for SP2

The displacement ductility factor can be found by using $\ell_p = 170\,\text{mm}$ and H = 2670 mm and curvature ductility ratio $\mu_\phi = 3.85$ (from the moment curvature relation obtained from Waller2002 and Response2000).

$$\mu_\Delta = 1 + 3 \times (\mu_\phi - 1) \times \frac{\ell_p}{H} \times \left(1 - \frac{\ell_p}{2 \times H}\right) = 1 + 3 \times (3.85 - 1) \times \frac{170}{2670} \times \left(1 - \frac{170}{2 \times 2670}\right)$$

$$\mu_\Delta (\text{found}) = 1.527 < \mu_\Delta (\text{required}) = 4 \approx 5$$

SP2 has very limited displacement ductility capacity. Displacement ductility of SP2 is smaller than SP1 as observed from the static tests of SP1 and SP2.

By assuming that SP2 has displacement ductility $\mu_\Delta = 4$, we can find the required curvature ductility and compare it with the available curvature ductility found from Waller2002.

$$\mu_\phi = 1 + \frac{(\mu_\Delta - 1)}{3 \times \left(\frac{\ell_p}{H}\right) \times \left[1 - \left(\frac{\ell_p}{2 \times H}\right)\right]} = 1 + \frac{(4 - 1)}{3 \times \left(\frac{170}{2670}\right) \times \left[1 - \left(\frac{170}{2 \times 2670}\right)\right]}$$

$$\mu_\phi (\text{required}) = 17.23 > \mu_\phi (\text{found}) = 3.85$$

Curvature ductility of SP1 was found as $\mu_\phi = 3.85$ from the moment curvature diagram obtained from the computer programs Waller2002 and Response-2000. It is obvious from the above equation that SP2 has very limited curvature ductility capacity. This brittle behavior is also observed in the static tests of SP2.

It is obvious from the above calculations that the panel form test specimens SP1 and SP2 do not have enough curvature ductility and displacement ductility. Panel form test specimens, subject to reversed loading that causes tension cracking of the concrete, behave in a brittle manner, and thus, do not seem to be earthquake-safe.

8.22 DISPLACEMENT DUCTILITY FACTOR FROM THE ENVELOPE CURVES

The displacement ductility factor μ_Δ is mostly used in the seismic design codes. It has also been called the "global ductility factor" in some publications, since it describes the extent of the post elastic displacement of a whole structure. Figures 8.48 and 8.49 show the envelope curves of the top displacement with the applied load for SP1 and SP2, respectively.

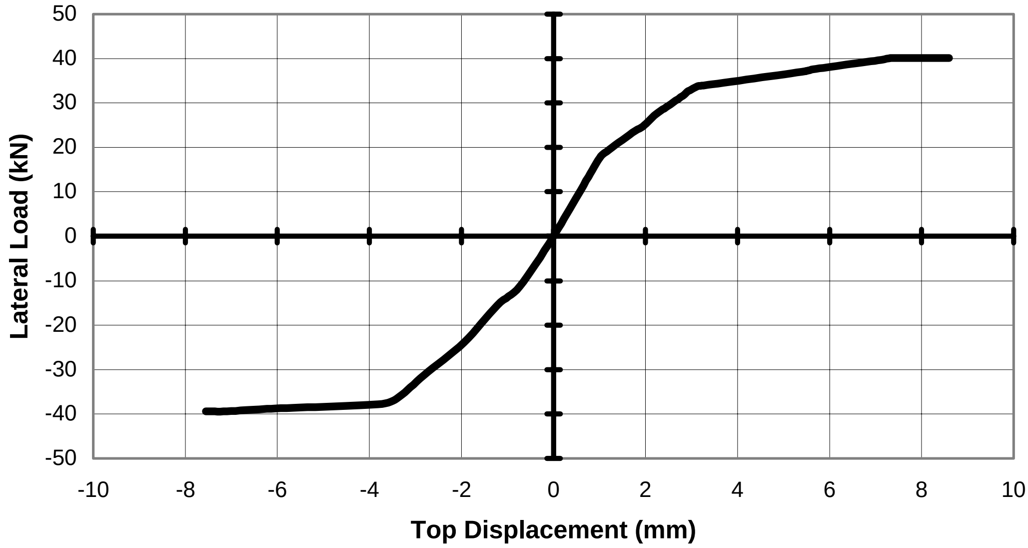

Figure 8.48 Envelope load displacement curve of SP1.

It is seen from the envelope curve that Δ_u is 8.6 mm and Δ_y is 3.5 mm. Displacement ductility factor for SP1 was calculated as

$$\mu_\Delta = \frac{\Delta_u}{\Delta_y} = \frac{8.6}{3.5} = 2.46 < 4 \approx 5 \tag{8.14}$$

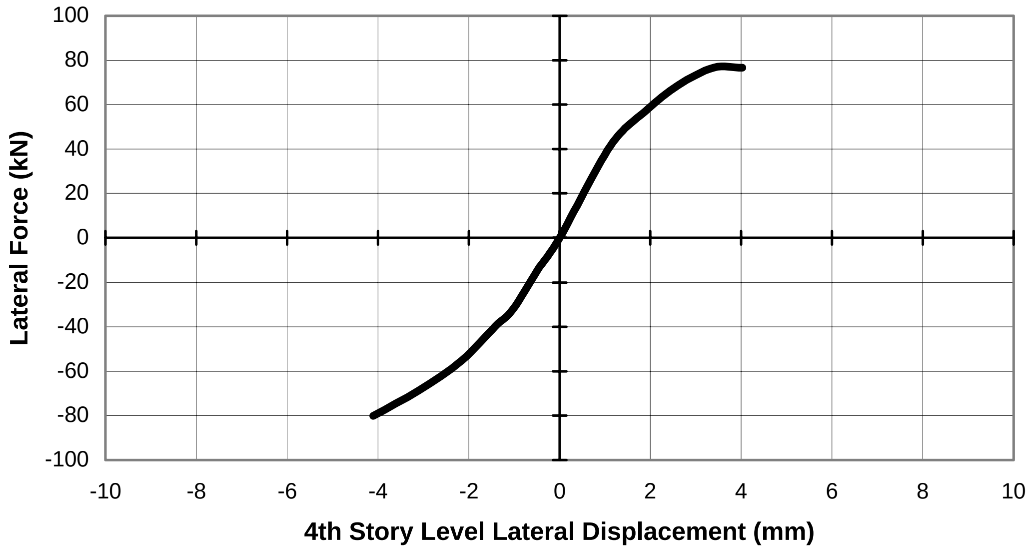

Figure 8.49 Envelope load displacement curve of SP2.

It is seen from the envelope curve that Δ_u is 4.13 mm and Δ_y is 2.67 mm. Displacement ductility factor for SP2 was calculated as

$$\mu_\Delta = \frac{\Delta_u}{\Delta_y} = \frac{4.13}{2.67} = 1.55 < 4 \approx 5 \tag{8.15}$$

It can be concluded that from the Equation 8.14, Equation 8.15 and also Sections 8.20 and 8.21 both SP1 and SP2 show very brittle behavior due to under-reinforcement. Panel form structures possess potential brittleness when subject to earthquake loading. This brittleness springs from excessively low under-reinforcement.

CHAPTER 9

CONCLUSIONS AND RECOMMENDATIONS

9.1 CONCLUSIONS

1) Multi-story panel buildings (buildings built by tunnel-form) which were constructed before the Turkish Earthquake Code (AY-1997) was published are subject to severe earthquake risks of failing in a brittle mode.

2) The risk of failing in a brittle mode springs from the fact that the longitudinal steel ratio is very low as $\rho_{sv} = 0.0015$.

In the Turkish Earthquake Code (AY-1997), for structures in which the total earthquake force is carried by shear walls, the longitudinal steel ratio can be reduced to $\rho_{sv} = 0.0015$ from $\rho_{sv} = 0.0025$, which is the normal minimum.

3) The standard practice in structures built by tunnel-form is to use mesh reinforcement to provide longitudinal steel ratio of $\rho_{sv} = 0.0015$. Before the publication of (AY-1997), no end zones in walls were formed.

4) The brittle failure occurs due to the big difference between the moment corresponding to the tension cracking of concrete and the ultimate moment provided by the longitudinal steel

$$M_{cr} >> M_u$$

As soon as cracking occurs, concrete can carry no tension force. This tension force is unloaded to the tension steel. The minimum amount of longitudinal steel ($\rho_{sv} = 0.0015$) cannot carry the unloaded tension force. It immediately yields and elongates until rupture. The result is a brittle failure.

5) As reinforced by $\rho_{sv} = 0.0015$, the tunnel-form units dissipates very small amount of earthquake energy.

6) Addition of steel to the end of wall cross-section and forming end zones, as required by Turkish Earthquake Code (AY-1997) improves the failure behavior to acceptable standards.

7) In the cross-section of the test unit, as reinforced according to Turkish Earthquake Code (AY-1997)

Ultimate moment capacity of the cracked cross-section is greater than the moment corresponding to the tension cracking of concrete

$$M_u >> M_{cr}$$

The failure mode of the cross-section with end zones is ductile.

8) The effect of tack welding on the failure mode is investigated and found to be insignificant in the brittle failure mode.

9) Tension tests of the 2 mm diameter wires used as reinforcement are performed before and after tack welding. Approximately the same failure loads are found (10% difference). Additionally, the rupture points on the tack-welded wire are almost never exactly on the tack welding. The rupture points occur at some distance away from the tack weld.

10) A special Axial Load-Moment-Curvature (N-M-ϕ) computer program is developed theoretically to analyze the experimentally tested tunnel form units. Computer analyses show the same brittle failure mode, as observed in the laboratory tests.

11) For considering the possibility of the negative effect of tack welding, by reducing both the strength and ductility of the reinforcement, the parametric study obtained by both Response-2000 and Waller-2002 (N-M-ϕ) programs produce the same behavior of brittle failure. It is interesting to note that, the same brittle failure behavior would occur, even if the ultimate strength and ductility of the reinforcing wire were higher.

12) Dynamic tests are performed on panel form units to determine the natural periods in X and Y directions of the cross-section.

13) The panel form test units are modeled by the computer by using the Finite Element Technique and the Wide Column Analogy Technique. Theoretical natural periods are calculated.

14) Experimentally found and theoretically calculated natural periods are almost the same. This fact proves a very important point that the computer models used satisfactorily reflect the realistic dynamic behavior of panel structures.

15) The Finite Element Model is commonly accepted to be realistic, but the wide column analogy is not as readily accepted. The dynamic analysis prove that the wide column analogy could also determine natural periods very close to the experimentally found correct values.

The wide column analogy is a very valuable analytical tool for structural analysis. It reduces the two-dimensional panels to one-dimensional structural elements. Thus the panel structure can be modeled and analyzed as a framed structure. The framed structure, of course, is a method of analysis, which the design engineers are very familiar with.

16) A special purpose computer program is developed (named Waller2002) to develop the accurate N-M-ϕ relationship of reinforced concrete cross-sections. N-M-ϕ program, known as RESPONSE-2000, exists on the Internet. However, it has many weaknesses and aspects, which cannot be handled. Waller-2002 is developed as an improvement of the program RESPONSE-2002.

17) From the observations of the moment-curvature relationship of panel form test specimens, they have reached their ultimate strength as soon as the concrete cracked; followed by immediate yielding and then rupturing of the longitudinal steel.

Subject to an earthquake, the panel walls initially exhibit tension cracking of the concrete. The unloaded moment after tension cracking immediately makes the reinforcement yield.

Rapid unloading of the moment after tension cracking of concrete is terminated by fracture of the distributed longitudinal steel. After longitudinal reinforcement fractures, moment carrying capacity of the wall section is totally lost.

18) From the moment-curvature relationship, which is obtained by Waller2002, the panel form test specimens SP1 and SP2 show very brittle behavior. From the results of the moment-curvature relationship, the ratio of the ultimate moment to the cracking moment is much smaller than 1.25 for both SP1 and SP2. This is an indication of very brittle type of behavior of SP1 and SP2.

19) The failure of SP1 and SP2 provides convincing field evidence that brittleness of reinforced concrete members caused by excessive under-reinforcement cannot be ignored when designing for seismic resistance.

20) Panel structures (buildings built by tunnel-form) possess potential brittleness when subject to earthquake loading. This brittleness springs from excessively low under-reinforcement.

21) Panel buildings, subject to earthquake excitation that causes tension cracking of the concrete, behave in a brittle manner, and thus, do not seem to be earthquake-safe.

22) It should be made as a Turkish Earthquake Code (AY-1997) requirement that, the ultimate moment capacity of a shear wall M_u, be at least 1.25 times greater than the moment that corresponds to concrete cracking, M_{cr}. A similar regulation occurs for prestressed concrete beams: $M_u > 1.25\ M_{cr}$.

9.2 RECOMMENDATIONS

Almost no structural damage was reported on buildings built by tunnel-form in the Marmara Earthquake (1999).

However, the peak ground accelerations in the Marmara Earthquake were rather small as 0.4g-0.43g. As a result, small inertia forces were generated. On the other hand, ground displacements were very large, in the order of 2.5-3.0 m.

If an earthquake producing greater ground accelerations occurs, what is the seismic safety of tunnel-formed structures with walls containing no specially reinforced end zones?

1) Three-dimensional computer models of different panel buildings, which exist in practice, should be developed and be subjected to dynamic analysis according to AY-1997.

2) Each panel should be checked for concrete cracking.

3) N-M-ϕ relationships of panels should be developed by the computer program Waller-2002.

4) The possibility of the occurrence of brittle failure must be carefully investigated.

5) Methods of seismic strengthening must be developed to bypass the occurrence of brittle failure. The developed strengthening method must enable the panel building to dissipate seismic energy.

6) A detailed and organized program of analysis should be done to determine the minimum reinforcement requirements of panels in buildings built by tunnel-form structures. This analytical study must cover all possible wall designs.

7) The minimum reinforcement requirements focusing on amount and distribution of steel within the cross-sections should be experimentally tested to provide the validity of the analytical relationships developed.

8) Providing end zones in tunnel form units increase the ultimate moment capacity M_u as

$$M_u > 1.25\ M_{cr}$$

In doing so, the lateral force, which the unit is subjected, to also increases. It should be verified experimentally that the increased lateral force does not lead to a premature occurrence of shear failure.

9) The effect of wall design geometry should be investigated.

10) Minimum reinforcement amount and distribution of the boundary reinforcement should be investigated for different wall design geometries.

11) The axial load level of the panel form test specimens should be increased.

12) In this study, H wall design that is numbered as 1 was tested under reversed lateral loading. Typical wall design geometry that is shown in Figure 9.1 as 2, 3 and 4 should be tested under reversed cyclic lateral loading.

Figure 9.1 Panel form test specimens wall geometry.

13) Energy dissipation requirements should be determined for typical floor plans and height of the buildings.

14) In this study 1/5 scale panel form test specimens were constructed. Such a small scale caused local construction mistakes. The scale should be increased.

REFERENCES

ACI-318 (1971), “Building Code Requirements for Reinforced Concrete,” American Concrete Institute, Detroit, Michigan, 1971.

ACI-318 (1977), “Building Code Requirements for Reinforced Concrete,” American Concrete Institute, Detroit, Michigan.

ACI-318 (1983), “Building Code Requirements for Reinforced Concrete,” American Concrete Institute, Detroit, Michigan.

Aktan, A. E., Bertero V. V., (1985) “Structural Walls: Seismic Design for Shear” ASCE Journal of Structural Engineering V.111, No.8, August, 1985.

Atımtay, E., (1991) “Seismic design of bridges to relate ductility and sway” Evaluation and Rehabilitation of Concrete Structures and Innovations in Design, American Concrete Institute, SP-128.

Atımtay, E., Tuna, M.E. (2001) “Designing the concrete dual system” Structural Engineering, Mechanics and Computation Vol.2, pp. 1009-1015.

Atımtay, E., (2003) “Tünel kalıplı Yüksek Binaların Deprem Davranışı ve Güvenliği” TÜBİTAK, İNTAG Proje No:561, Ankara, 2003.

AY-1997, Afet Bölgelerinde Yapılacak Yapılar Hakkında Yönetmelik, (1997), T.C. Bayındırlık ve İskan Bakanlığı Deprem Araştırma Enstitüsü Başkanlığı, Ankara, 85 pages.

Balkaya, C., Kalkan, E., (2002) "Nonlinear seismic response evaluation of tunnel form building structures" Computers and Structures V.81, pp. 153-165.

Balkaya, C., Kalkan, E., (2003) "Estimation of fundamental periods of shear-wall dominant building structures" Earthquake Engineering and Structural Dynamics V.32, pp. 985-998.

Bentz, E., and Collins, M., 1998, RESPONSE 2000, Version 0.7.5 (Beta) University of Toronto.

Bertero, V.V., Popov, F.P., Wang, T.V., and Wallenas, T., (1977) "Seismic Design Implications of Hysteretic Behavior of Reinforced Concrete Structural Walls" 6th World Conference on Earthquake Engineering, New Delhi, Vol.5, pp. 159-165.

Bertero V. V., EERI M. (1986) "Lessons Learned Recent Earthquakes and Research and Implications for Earthquake-Resistance Design of Buildings Structures in the United States" Earthquake Spectra, Vol. 2, No.4, pp. 825-858.

Canbay , E. (2001) "Contribution of RC Infills to the Seismic Behavior of Structural Systems", A doctor of Philosophy Thesis in civil Engineering, Middle East Technical University, December 2001.

Cardenas, A. E., Magura, D.D. (1973), "Strength of high-Rise Shear Walls-Rectangular Cross Section," Response of Multistory Concrete structures to Lateral Forces, SP-36, American Concrete Institute, Detroit, pp. 119-150.

Cardenas, A. E., Hanson, J. M., Corley, W.G., and Hognestad E., (1982) “Design Provisions for Shear Walls” Portland Cement Association, Research and Development Bulletin RD028.01D, February 25, 1982, U SA.

Chopra, A.K.(1995), Dynamic of Structures, Theory and Applications to Earthquake Engineering, University of California at Berkeley Prentice Hall, USA.

Clough, R.W., and Penzien, J., (1193) Dynamics of Structures, Mc Graw Hill, New York, 1993.

Coull, A., and Choudhury, J.R. (1967) “Analysis of Coupled Shear Walls”, ACI Structural Journal, Vol.64, September 1967, pp. 587-593.

Diker, Y. (2000) “Seismic Analysis and Design of Tunnel Form Buildings”, Master Thesis Submitted to Graduate School of Natural and Applied Sciences of the Middle East Technical University, May 2000.

Earthquake Effects on Reinforced Concrete Structures: U.S.-Japan Research, SP-84, American Concrete Institute, Detroit, 1985, USA.

Elnashai, A.; Pilakoutas, K.; and Ambraseys, N.N., (1990) “ Experimental Behaviour of Reinforced Concrete Walls under Earthquake Loading,” Earthquake Engineering and Structural Dynamics, V.19, No.3, Apr 1990.

Ersoy, U., Özcebe, G., (1998) “Sarılmış Betonarme Kesitlerde Moment-Eğrilik İlişkisi-Analitik Bir İrdeleme”, İMO Teknik Dergi, No. 129, pp. 1779-1827.

Ersoy, U., Özcebe G., 2001, Betonarme, Evrim Yayınevi, Ankara, 818 pp.

Fintel, M. (1991). “Shearwalls-An Answer for Seismic Resistance?“ Concrete. International, Vol.3, No.7, pp.48-53.

Grupta, A., and Rangen, B. V., (1998) “High-Strenght Concrete (HSC) Structural Walls” ACI Structural Journal, V.95, No.2, March-April, 1998.

Hognestad, E., (1951), A study of combined Bending and axial load in R/C Members, University of Illinois, Engineering Exp. Sta. Bull., No. 399. pp. 42-65.

Kaya, Y. M., (2000) “Capacity Design Considerations of Tunnel Form Buildings”, Master Thesis Submitted to Graduate School of Natural and Applied Sciences of the Middle East Technical University, May 2000.

Kowalsky, M.J., (2001) “RC structural Walls Designed According to UBC and Displacement-Based Methods” Journal of Structural Engineering, V.127, No. 5, Paper No. 22137, pp. 506-516.

Lefas, I.; Kostovos, M.D.; and Ambraseys, N.N., (1990) “Behavior of Reinforced Concrete Structural Walls: Strength, Deformation Characteristics, and Failure Mechanism,” *ACI Structural Journal*, V. 87, No.1, Jan.-Feb. 1990, pp. 23-31.

Lomnitz, C. (1970), “ Major Earthquakes and Tsunamis in Chile during the Period 1935 to 1955,” Geologische Rundschau, Vol. 59, No. 3, 1970, pp. 938-960.

Matacchoine, A., (1991), “Equivalent Frame Method Applied to Concrete Shear Walls”, Concrete International, 65, November, 1991.

Turkish Seismic Code, Ministry of Public Work, Ankara, July 1975.

Park, R., and Paulay, T., (1975) Reinforced Concrete Structures, New York, John Wiley& Sons.

Paulay, T., and Üzümeri, S. M., (1975) " A Critical Review of the Seismic Design Provisions for Ductile Shear Walls of the Canadian Code and Commentary," Canadian journal of Civil Engineering, Vol.2, No.4 1975, pp. 592-601.

Paulay, T., Earthquake-Resisting Shearwalls (1980) "A New Zealand Design Trend." ACI Journal Vol. 77, No. 18, May-June 1980, pp. 144-152.

Paulay, T., Priestley, M.J.N., and Synge, A.J. (1981)."Ductility in Earthquake-Resisting Squat Shearwalls". American Concrete Inst. Structural J., Vol. 79, No. 4, pp. 257-269.

Paulay, T., Priestley, M.J.N., 1992, Seismic Design of Reinforced Concrete and Masonry Buildings, John Wiley&Sons, Inc., New York, USA, 744pp.

Paulay, T., Priestley M. J. N., (1993) "Stability of Ductile Structural Walls" ACI Structural Journal, V.90, No.4, July-August, 1993 pp.385-392.

Paulay, T., E., (1999) "Seismic Displacement Compatibility in Mixed Structural System", Uğur Ersoy Symposium on Structural Engineering, Procedings, METU-Department of Civil Engineering, Ankara, Turkey, July 1999. pp: 275-292

Pilakoutas, K., Elnashai, A., (1993) "Interpretation of testing Results for Reinforced Concrete Panels," *ACI Structural Journal*, V.90, No.6, Nov-Dec. 1993, pp. 642-645.

Pilakoutas, K., Elnashai, A., (1995) "Cyclic Behavior of Reinforced Concrete Cantilever Walls, Part I: Experimental Results," *ACI Structural Journal*, V.92, No.3, May-June 1995, pp. 271-281.

RESPONSE-2000 Reinforced Concrete Sectional Analysis, Response-2k Version 0.8.5.2, Evan C. Bentz and Michael P. Collins, 1999, Canada.

Rüsch, H, und Hilsdorf, H., 1963, Verformungseigenschaften von Beton Unter Zwischen Zugspannangen, Materialprüfungsamt für das Bauwesen der Technischen Hochschule München, Rep. No. 44.

Saatçioğlu, M. and Ravzi, S.R., 1992, Strength and Ductility of Confined Concrete, J. Struct. Engrg, ASCE V.118, No. 6, pp. 1590-1607.

Sittipunt, W., and Wood, S.L. (1995). "Influence of Web Reinforcement on the Cyclic Response of Structural Walls". American Concrete Ins. Structural J., Vol.92, No.6, pp.745-756.

Sonuvar, M. O., (2001) "Hysteretic Response of Reinforced Concrete Frames Repaired by Means of Reinforced Concrete Infills", A Doctor of Philosophy Thesis in Civil Engineering, Middle East Technical University, June 2001

Stark, R. (1988), "Evaluation of Strength, Stiffness, and Ductility Requirements of Reinforced Concrete Structures using Data from Chile (19859 and Michoacan (1985) Earthquakes." Ph.D. Thesis, Department of Civil Engineering, University of Illinois, Urbana.

Subedi, N. K. "RC-Coupled Shear Wall Structures I: (1991) Analysis of Coupling Beams" ASCE Journal of Structural Engineering V.117, No.3, March, 1991 pp. 667-680.

Subedi, N. K. (1991) " RC-Coupled Shear Wall Structures. I: Analysis of Coupling Beams" ASCE Journal of Structural Engineering V.117, No.3, March, 1991 pp. 681-698.

Takeda, T., Sözen M. A., and Nielsen, N.N. (1970), " Reinforced Concrete Response to Simulated Earthquakes, " ASCE, Journal of the Structural Division, Vol. 96, No. ST12, December 1970, pp.2557-2573.

Tegos, I.A. and Penelis, G. Gr. (1988) " Seismic Resistance of Short Columnsand Coupling Beams Reinforced With Inclined Bars", ACI Structural Journal V.93, No.6, November-December, 1988.

Theodosios, P. T., Moretti, M., Bezas, (1996)A. "On the Behavior and Ductility of Reinforced Concrete Coupling Beams of Shear Walls" ACI Structural Journal V.93, No.6, November-December, 1996 pp.711-720.

Thomas P., EERI M. (1986) "The Design of Ductile Reinforced Concrete Structural Walls for Earthquake Resistance" Earthquake Spectra, Vol. 2, No.4, pp. 873-822.

TS-500, (1984) Building Code Requirements for Reinforced Concrete, Turkish Standards Institution, Ankara, April 1984.

TS-500, (2000) Building Code Requirements for Reinforced Concrete, Turkish Standards Institution, Ankara, February 2000.

Wallace, J.W., EERI, M.,Moehle, J.,P. and EERI, M. (1993) "An Evaluation of Ductility and Detailing Requirements of Bearing Wall Buildings Using Data from the March 3, 1985, Chile Earthquake," Earthquake Spectra, Vol. 9, No.1, 1993 pp.137-156.

Wallace, B., and Krawinkler, H., (1985)"Small Scale Model Tests of Structural Components and Assemblies," Earthquake Effects on Reinforced Concrete Structures: U.S.-Japan Research, SP-84, American Concrete Institute, Detroit, 1985, pp. 305-346.

Wight (1988), "Research In Progress," Department of Civil Engineering, University of Michigan, Ann Arbor.

Wood, S., Wight, J., and Moehle, J (1987), "The 1985 Chile Earthquake, Observations on Earthquake-Resistant Construction in Viña del Mar," Civil Engineering Studies, Structural Research Series No 532, Universities of Illinois, Urbana, February 1987.

Wood, S.L. (1989) "Minimum Tensile Reinforcement in Walls, " ACI Structural Journal, Vol.86, No.4, September – October 1989, Detroit, Michigan, USA.

Wood, S.L. (1990) "Shear Strength of Low-Rise Reinforced Concrete Walls," ACI Structural Journal, Vol.87, No.1, January– February, 1990, pp.99-107.

Wood, S. L., EERI M. (1991) " Performance of Reinforced Concrete Buildings During the 1985 Chile Earthquake: Implications for the Design of Structural Walls" Earthquake Spectra, Vol. 7, No.4, 1991 pp. 607-638.

Wyllie, L. et al. (1986), "The Chile Earthquake of March 3, 1985," Earthquake Spectra, Vol. 2 No. 2 April 1986.

Specifications for the Structures to be Built in Disaster Regions The Turkish Seismic Code), Ministry of Public Work and Settlement, Ankara, 1997.

1997 UNIFORM BUILDING CODE, 5360 Workman Mill Road, Whittier, California 90601-2298, 1997, USA.

Ünay, A.İ.,. Tuna., M.E., Atımtay, E., (2002) "Seismic Strength of Panel Structures: Observations on Marmara and Chile Earthquakes", Fifth International Congress on Advances in Civil Engineering, 25-27 September 2002, Istanbul Technical University, Istanbul, Turkey.

Üzümeri, Ş. M., Tankut, T., Özcebe, G., Atımtay, E., (1999) "Assessment, Repair/Strengthening of Moderately Damaged Reinforced Concrete Buildings in Ceyhan Earthquake (1998)", Uğur Ersoy Symposium on Structural Engineering, Procedings, METU-Department of Civil Engineering, Ankara, Turkey, July 1999 pp 413-441.

Yüksel, B., (1997) "A Comparative Study on Seismic Codes " Master Thesis in Civil Engineering, Middle East Technical University, September 1997.

Yüksel, B., Atımtay, E., (2001) "Tünel Kalıplı Yüksek Binaların Deprem Davranışı ve Güvenliği".Yapı Mekaniği Laboratuvarları Toplantısı Bildiriler ve Laboratuvar Olanakları, 5-6 Kasım 2001, Ankara pp. 97-104.

Yüksel, B., Atımtay, E., (2003) "Tünel Kalıplı Yüksek Binaların Yatay Yük Altında Davranışı ".Yapı Mekaniği Laboratuvarları Toplantısı II, 19-20 Haziran 2003, Konya pp. 21-26.

APPENDIX A

CASE STUDY: 13 STORY HIGH PANEL BUILDING

A.1 INTRODUCTION

In this study the three-dimensional dynamic analysis of a 13-story panel form building that has already been constructed is performed. Moment-curvature diagrams of structural walls were drawn by using the computer program Waller-2002. In the first case minimum amount of mesh reinforcement (ρ_{sv} = ρ_{sh} = 0.0015) was used along the wall depth for all structural walls. Spacing of longitudinal and horizontal mesh reinforcements is 150 mm. To provide 0.15% mesh reinforcement ratio in the vertical and horizontal directions along the wall depth, 5.5 mm diameter two-layer mesh reinforcement (S500) was used along the wall depth for shearwalls. In the second case, end zones were provided at the boundaries of the structural walls according to the Turkish Earthquake Code (AY-1997). In all cases boundary elements are provided at a distance of l_u = 0.2 l_w from each end of the wall. The longitudinal boundary reinforcement ratio is 0.2 % for each shearwall. Spacing of longitudinal boundary reinforcement is 150 mm. Web reinforcement ratio is taken as 0.15% for shearwalls. To provide 0.15% web reinforcement ratio in the vertical and horizontal directions, 5.5 mm diameter two-layer mesh reinforcement (S500) was used in the web regions for shearwalls. The spacing of longitudinal and vertical web reinforcement is 150 mm. Moment curvature diagrams for mesh reinforcement and for end zones were plotted on the same graph to be able to compare the behavior of these two cases for structural walls.

In the dynamic analysis of the 13-story high panel building, the fundamental assumptions are considered as stated below:

1. Foundation is assumed to be infinitely rigid, so that the load transfer from superstructure to ground can be provided without allowing deformations.

2. Rigid diaphragm is assumed to distribute horizontal inertia forces at each floor level to vertical resisting elements. In terms of in plane loading, rigid diaphragms are assumed to remain elastic in all times.

3. 1G+1Q+1E is generated as load combination applied to the sample structure where;

G : dead load

Q : live load

E: earthquake load

4. All concrete members behave linearly elastic, so loads and displacements are proportional and the principle of super-position applies.

5. Dead weight of concrete is assumed to be 25 kN/m^3, and 2.5 kN/m^2 of live load is uniformly distributed along the slab.

6. Characteristic cylindrical strength of concrete is 25 MPa. Sectional properties, modulus of elasticity and poisson ratio are kept constant along the height of the sample structure.

7. 13-story panel form structure is subjected to vertical loads and dynamic lateral loads due to earthquakes. Sample structure is analyzed using earthquake loads specified as a response spectrum with a load reduction factor (R) as one.

8. In order to construct the response spectrum curve, the procedure defined by Turkish Earthquake Code (AY-1997) is followed. The panel form building is assumed to be located in Seismic Zone-I in Turkey. Therefore, an effective ground acceleration coefficient (Ao) of 0.4g is applied simultaneously in two mutually perpendicular directions in the X-Y plane. Modal acceleration coefficients T_A and T_B have the values of 0.15 and 0.6 seconds, respectively, by assuming soil type as Zone-

3 (Z3). Response spectrum curve was applied to X and Y directions for dynamic analysis of the 13-story panel form building.

9. Periods, modal shapes, modal forces and modal displacements are obtained as output data associated with the response spectrum dynamic analysis. The effect of higher modes of vibration is included in the root mean square method, ie, the resulting quantity is determined as the square root of the sum of the squares of the partial effects of modal components (SRSS).

The plan view of the 13-story panel form building is shown in Figure A.1. Thickness of shearwalls is 200 mm. This building is modeled with 2.95 m floor height. It has uniform rectangular slabs with 150 mm slab thickness. The sample tunnel form building is modeled according to the wide column analogy and analyzed by the application of the response spectrum in X and Y directions separately. Ten modes of vibration are considered in order to satisfy adequate mass participation.

In generation of equivalent frame, heights of connecting short beams are taken as 1.65 m and 0.75 m for windows and door openings, respectively. Where interaction is only provided with slab, beams with 150 mm depth and 200 mm width are defined between walls.

Response spectrum analysis is performed in each X and Y direction for dynamic analysis of the 13-story panel form building. Earthquake action will be investigated first along global X direction then for global Y direction.

All the moment curvature diagrams in this chapter have two curves, one curve corresponding to minimum amount of mesh reinforcement (ρ = 0.0015) and named as (ρ = 0.0015). The other curve corresponding to minimum amount of mesh reinforcement in the web (ρ = 0.0015) and end zones, which were provided at the boundaries of the structural walls according to the AY-1997 and named as ρ = 0.0015 and boundary reinforcement (AY-1997). Therefore, these moment curvature diagrams are called comparisons of the moment curvature diagrams.

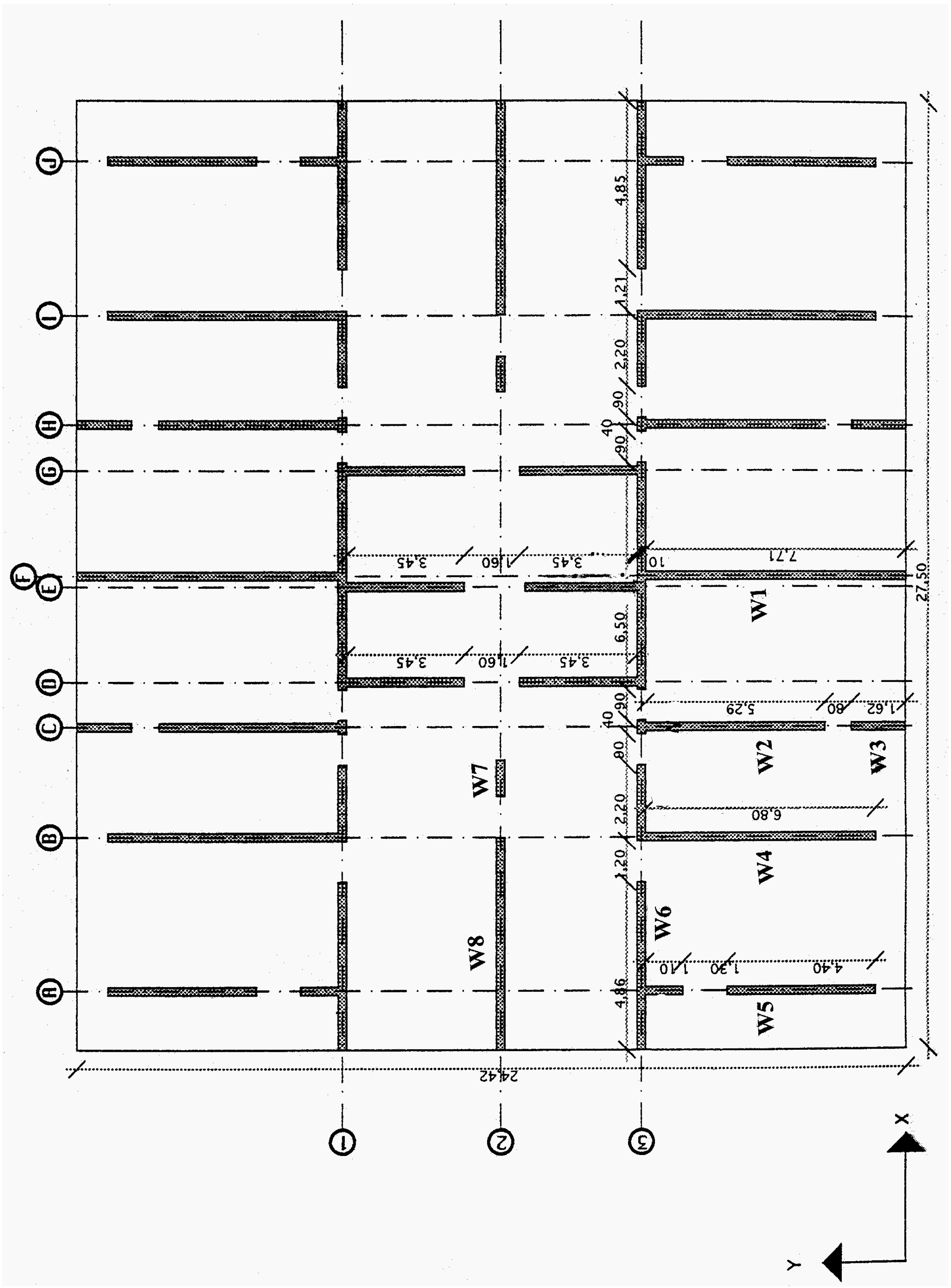

Figure A.1 Plan view of the 13-story panel form building.

A.2 INVESTIGATION OF THE 13-STORY PANEL BUILDING ALONG X DIRECTION

Structural analysis and moment-curvature results of structural walls along X direction are given in Table A.1. Figures A.2, A.3 and A.4 show the comparison of moment curvature diagrams of W1, W6 and W8 when the earthquake action is along the global X direction.

Table A.1 Structural analysis and moment-curvature results of structural walls along X direction.

Wall No	Structural Analysis Results	Minimum Amount of Mesh Reinforcement (ρ_{sv},ρsh =0.0015)			End Zones at the boundaries of the walls according to (AY-1997)		
W	M(kNm)	M_{cr}	M_u	M_u / M_{cr}	M_{cr}	M_u	M_u / M_{cr}
1	170307	12835	12166	0.95	15490	35395	2.291
6	23204	2058	2016	0.979	2288	5675	2.48
8	42613	3759	4427	1.178	4075	8769	2.15

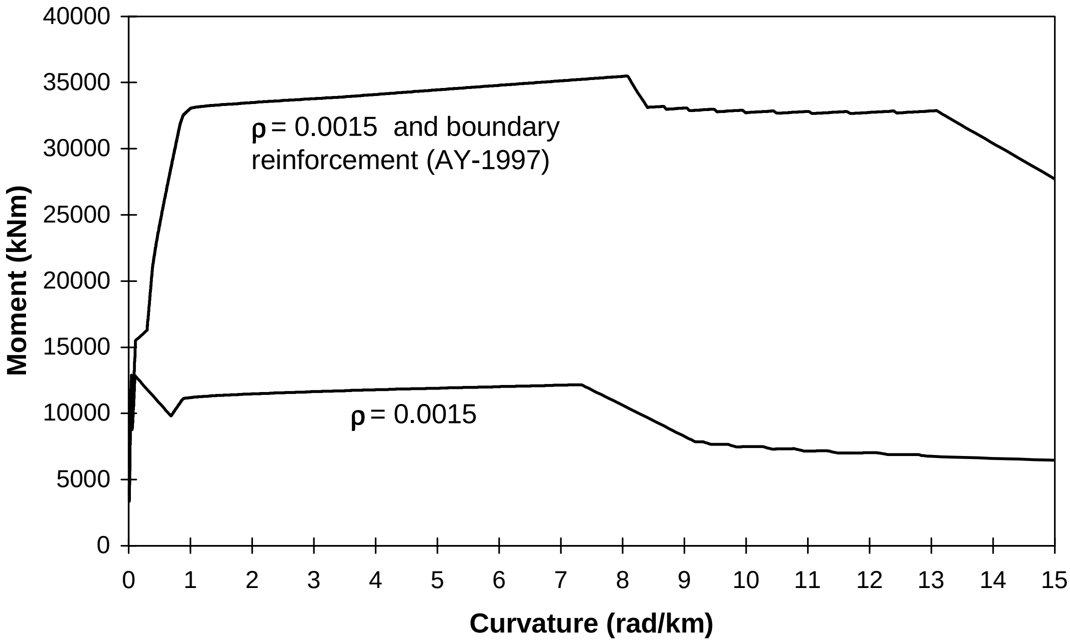

Figure A.2 Comparison of moment curvature diagrams of W1 along X direction.

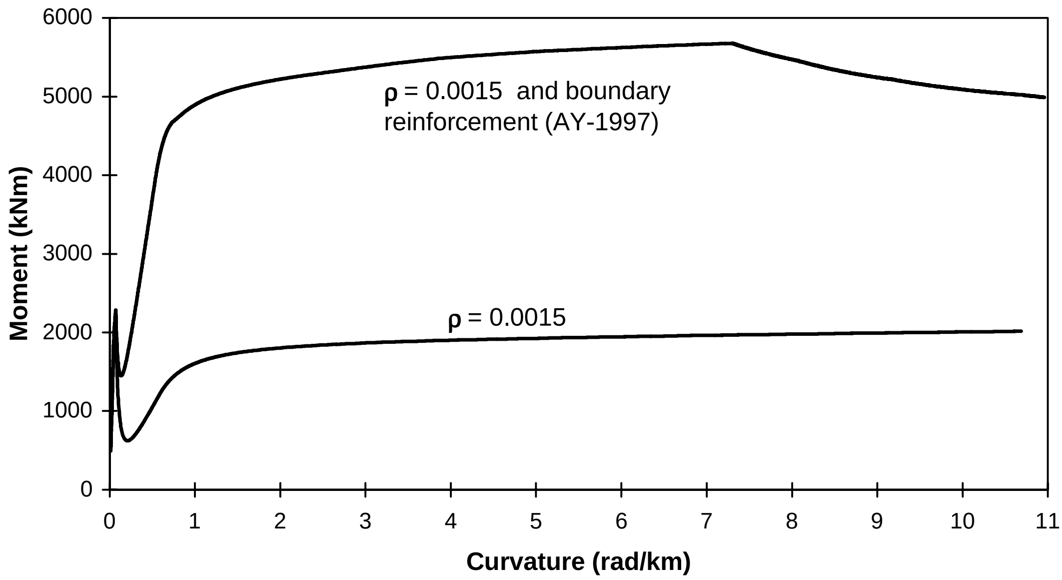

Figure A.3 Comparison of moment curvature diagrams of W6.

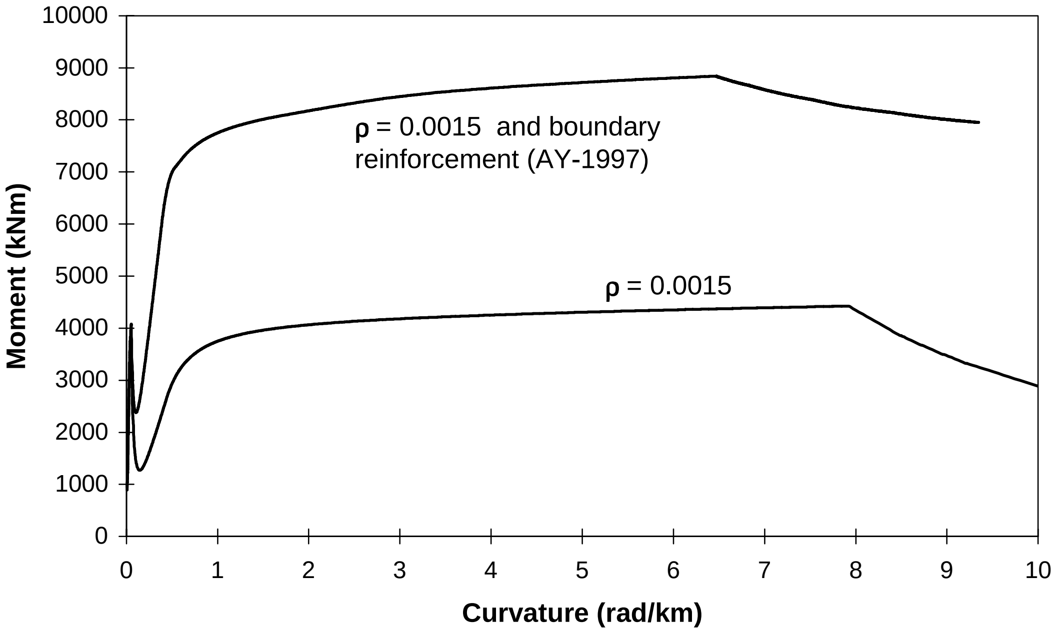

Figure A.4 Comparison of moment curvature diagrams of W8.

A.3 INVESTIGATION OF THE 13-STORY PANEL BUILDING ALONG Y DIRECTION

Structural analysis and moment-curvature results of structural walls along Y direction are given in Table A.2. Figures A.5 and A.6 show the comparison of moment curvature diagrams of W1 when the earthquake action is along Y and –Y of the cross section, respectively. In Table A.2 it is named as 1Y and –1Y when the earthquake action is along Y and –Y of the cross section, respectively. Figures A.7, and A.8 show the comparison of moment curvature diagrams of W2 and W3 along Y direction, respectively. Moment curvature diagram of SW4 is drawn for the flange, which is in tension and compression. In Table A.2 it is named as SW4T and SW4C when the flange of SW4 is in tension and compression, respectively. Figures A.9 and A.10 show the comparison of moment curvature diagrams of SW4 when the flange is in tension and compression, respectively. Comparison of moment curvature diagrams of W5 is shown in Figure A.11.

Table A.2 Structural analysis and moment-curvature results of structural walls along Y direction.

Wall No	Structural Analysis Results	Minimum Amount of Mesh Reinforcement (ρ_{sv},ρsh =0.0015)			End Zones at the boundaries of the walls according to (AY-1997)		
W	M(kNm)	M_{cr}	M_u	M_u / M_{cr}	M_{cr}	M_u	M_u / M_{cr}
1Y	133262	13163	15301	1.162	14265	49453	3.47
-1Y	233262	21778	25809	1.185	24546	57662	2.349
2	14536	2497	2422	0.969	2758	6589	2.389
3	878	226	234	1.035	255	685	2.68
4c	31617	5478	3863	0.705	5920	11201	1.892
4t	31617	6856	5961	0.869	7582	16280	2.148
5	9278	1811	1728	0.955	1984	4341	2.188

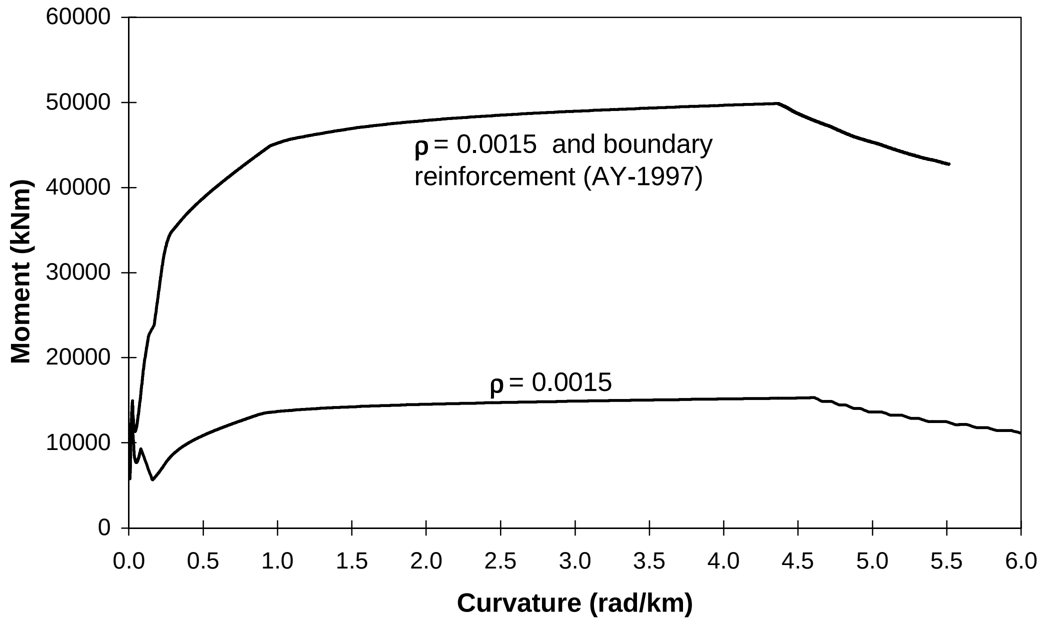

Figure A.5 Comparison of moment curvature diagrams of W1 when the earthquake action is along Y of the cross section.

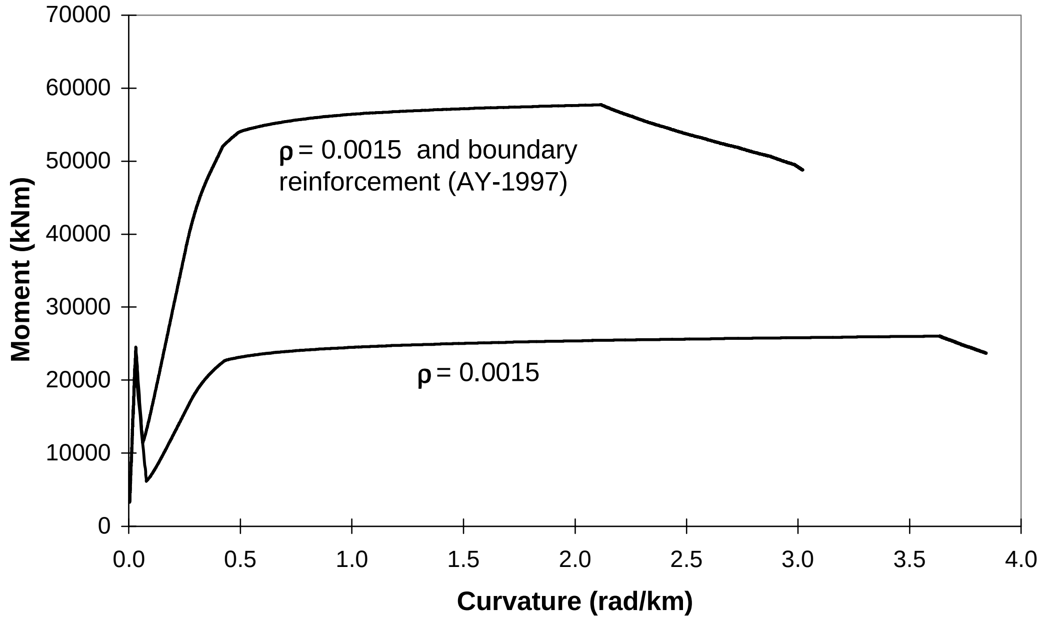

Figure A.6 Comparison of moment curvature diagrams of W1 when the earthquake action is along -Y of the cross section dimension.

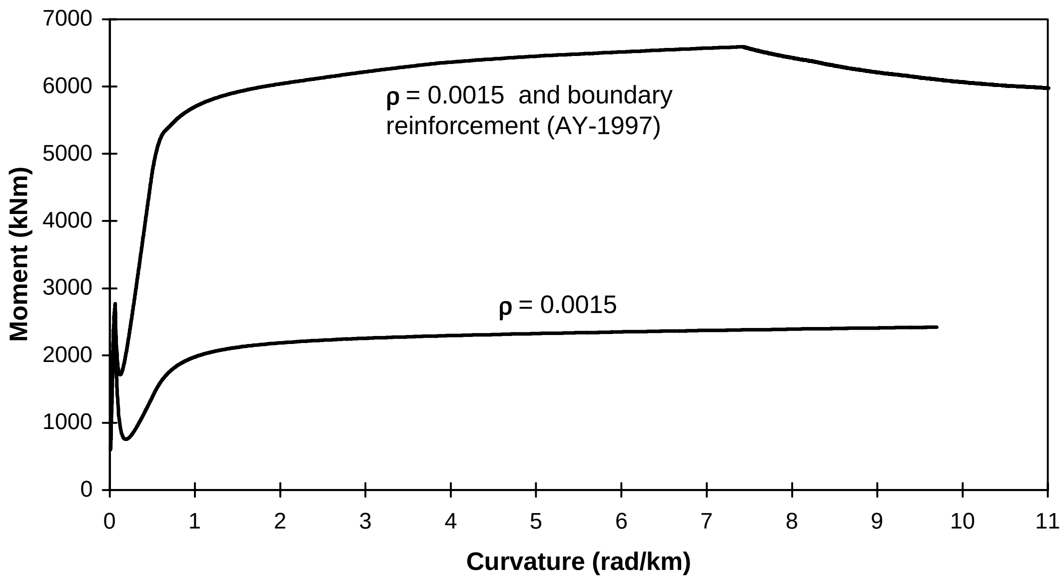

Figure A.7 Comparison of moment curvature diagrams of W2.

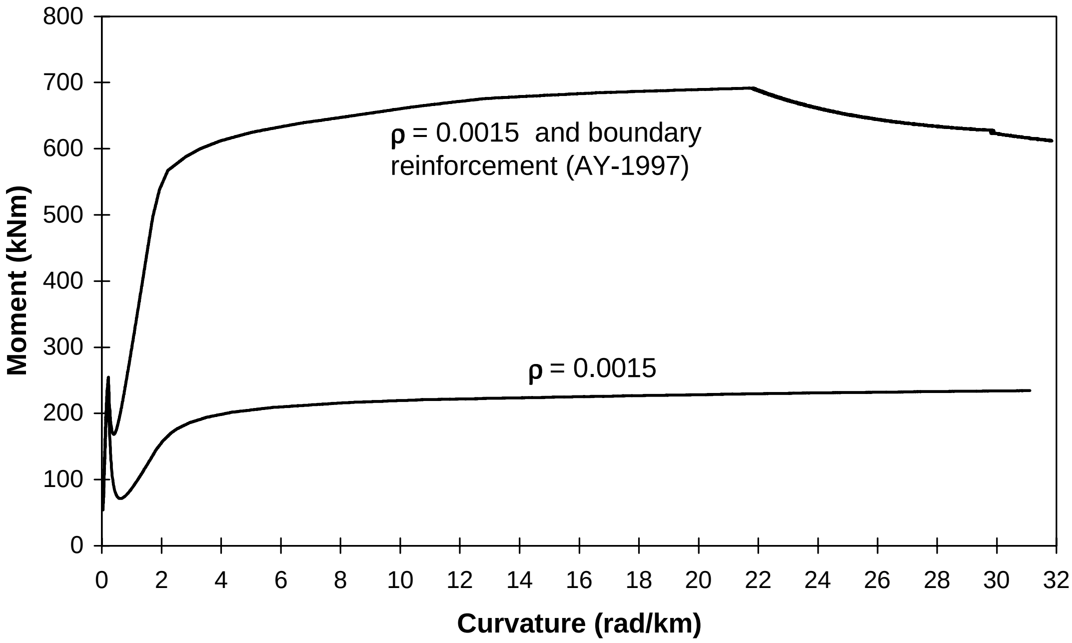

Figure A.8 Comparison of moment curvature diagrams of W3.

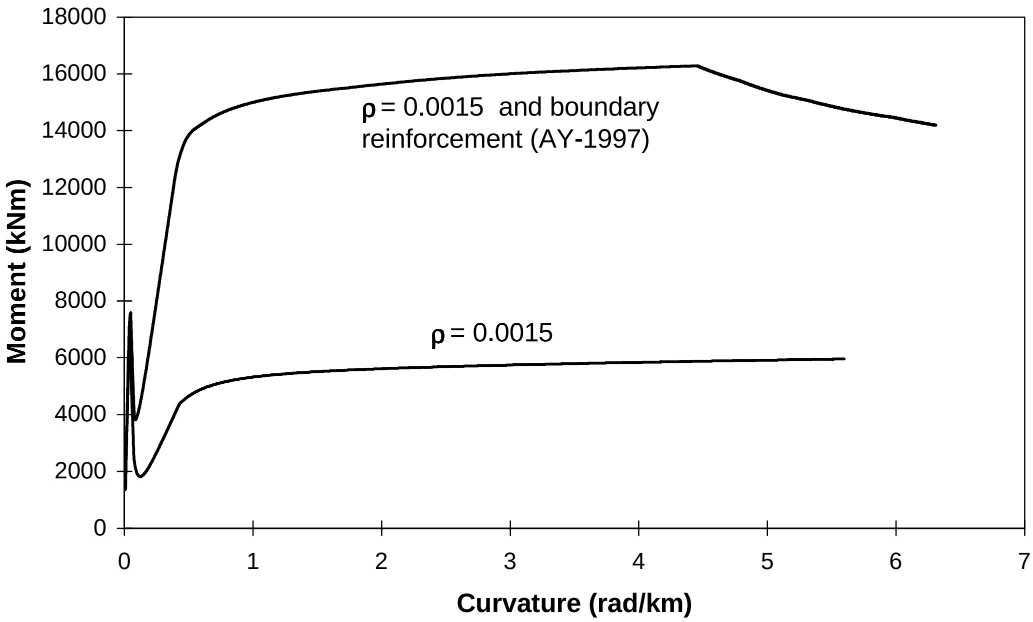

Figure A.9 Comparison of moment curvature diagram of W4 when the flange is in tension.

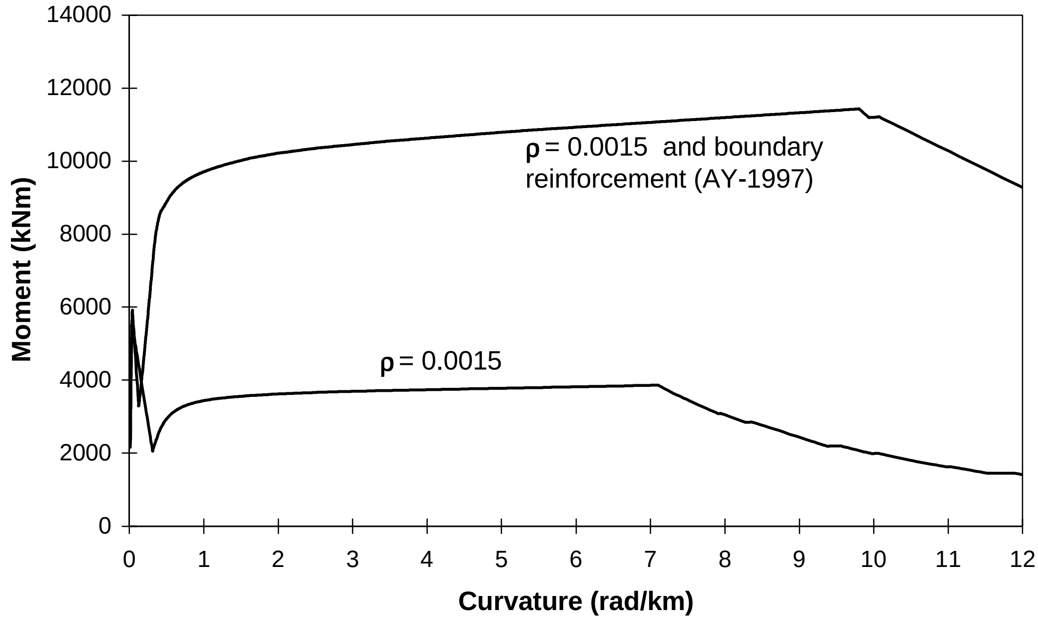

Figure A.10 Comparison of moment curvature diagrams of W4 when the flange is in compression.

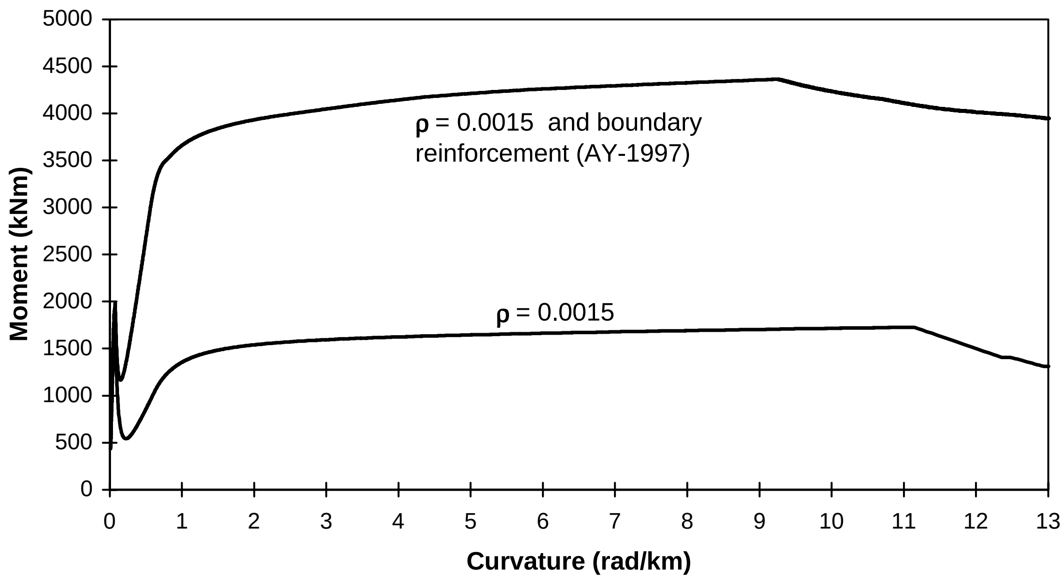

Figure A.11 Comparison of moment curvature diagrams of W5.

Moment curvature diagrams of structural walls were drawn for minimum amount of mesh reinforcement and also for end zones, which were provided at the boundaries of the structural walls according to the Turkish Earthquake Code (AY-1997). When the minimum amount of mesh reinforcement was used, the ratio of the ultimate moment to the cracking moment (M_u / M_{cr}) is less than 1.25 for all structural walls. When the end zones were provided at the boundaries of the structural walls according to the Turkish Earthquake Code (AY-1997), the ratio of the ultimate moment to the cracking moment (M_u / M_{cr}) is greater than 1.25 for all structural walls. It is obvious that when end reinforcement is placed at the boundaries of the structural walls, brittle failure does not occur. It is clear from the Tables A.1 and A.2 the moments which is developed due to load combination of 1G + 1Q + 1E are greater than the ultimate and cracking moments of the shearwalls.

APPENDIX B

EARTHQUAKE FORCES ON THE MODELS AND PROTOTYPES

B.1 INTRODUCTION

In this part of the study 1/5-scale panel form test specimens are called models and real size i.e. 1/1-scale panel form specimens are called prototypes. Equivalent lateral earthquake forces on the 1/5-scale panel form test specimens are calculated and compared with the applied lateral loads in the static tests. Also equivalent lateral forces and overturning moments on the 1/1 real size panel form specimens (prototype) are calculated and compared with the maximum load and moment carrying capacity.

Dead weight of concrete is assumed to be 25 kN/m^3, and 2.5 kN/m^2 of live load is uniformly distributed along the slab. Additional dead and live load is also considered which is coming from the tributary area. Characteristic cylindrical strength of concrete is 35 MPa. Models and prototypes are assumed to be located in Seismic Zone-I in Turkey, so an effective ground acceleration coefficient (A_o) of 0.4g. Load reduction factor (R) is taken as one. Spectrum characteristic periods T_A and T_B have the values of 0.10 and 0.3 seconds, respectively, by assuming soil class as Z1.

B.2 EQUIVALENT LATERAL FORCES ON THE MODELS

In the static test of the models SP1 and SP2 maximum applied lateral loads were 40 kN and 80 kN, respectively. Equivalent lateral force procedure is applied and total design base shear of the 1/5-scale panel form test specimens (models) SP1 and SP2 are calculated as follows. The weight of the 1/5-scale panel form test specimens is 50 kN including additional dead weight from the tributary area and live load. Earthquake load reduction coefficient $R_a(T)$ is taken as one.

Total Design Base Shear of the 1/5 scale panel form test specimen (model) SP1

$$V_t = WA(T_1)/R_a(T_1) = 31\text{kN} < F_{experimental} = 40\text{kN} \quad \text{(B.1)}$$

Total Design Base Shear of the 1/5 scale panel form test specimen (model) SP2

$$V_t = WA(T_1)/R_a(T_1) = 27\text{kN} < F_{experimental} = 80\text{kN} \quad \text{(B.2)}$$

It is understood from Equations B.1 and B.2 that total design base shears due to earthquake of the 1/5-scale panel form test specimens are smaller than the applied lateral load in the static tests ($F_{experimental}$).

Total Design Base Shear due to earthquake of the 1/5 scale panel form test specimen (model) does not represent the actual case. To determine actual earthquake loads 1/1 scale prototype models will be considered.

The ratio of the moment of inertia of the prototype to the moment of inertia of the model (I_{prot} / I_{model}) for SP1 and SP2 is 625. The ratio of the weight of the prototype to the weight of the model (W_{prot} / W_{model}) for SP1 and SP2 is 125.

The ratio of the moment of inertia of the prototype to that of the model is 625 for both SP1 and SP2, however the ratio of the weight of the prototype to the weight of the model is 125 for SP1 and SP2. Since the ratio of the moment of inertias and the ratios of weights (mass) for the prototype to model are not equal, it is not appropriate to compare the equivalent lateral earthquake force and lateral force applied in the static test by using the model. Therefore, the prototype will be used to calculate the equivalent earthquake forces. From the equivalent earthquake forces the moment at the base will be calculated and compared with the moment carrying capacity of the sections.

In the prototypes cross section two-layer minimum amount of mesh reinforcement is used. Spacing of the longitudinal mesh reinforcement is 150 mm.

To provide 0.15% mesh reinforcement ratio in the vertical and longitudinal directions along the wall depth, 5.5 mm diameter two-layer mesh reinforcement was used.

Figures B.1 and B2 show the moment curvature diagram of 1/1 scale (prototype) SP1 and SP2, respectively. For the prototype SP1 and SP2 the ratio of ultimate moment to cracking moment is 0.597 and 1.12, respectively. Moment due to earthquake is 41158 kNm for both SP1 and SP2, respectively. It is understood from Figures B1 and B2 that moment due to earthquake is greater than the moment carrying capacity of the prototype panel form specimens SP1 and SP2.

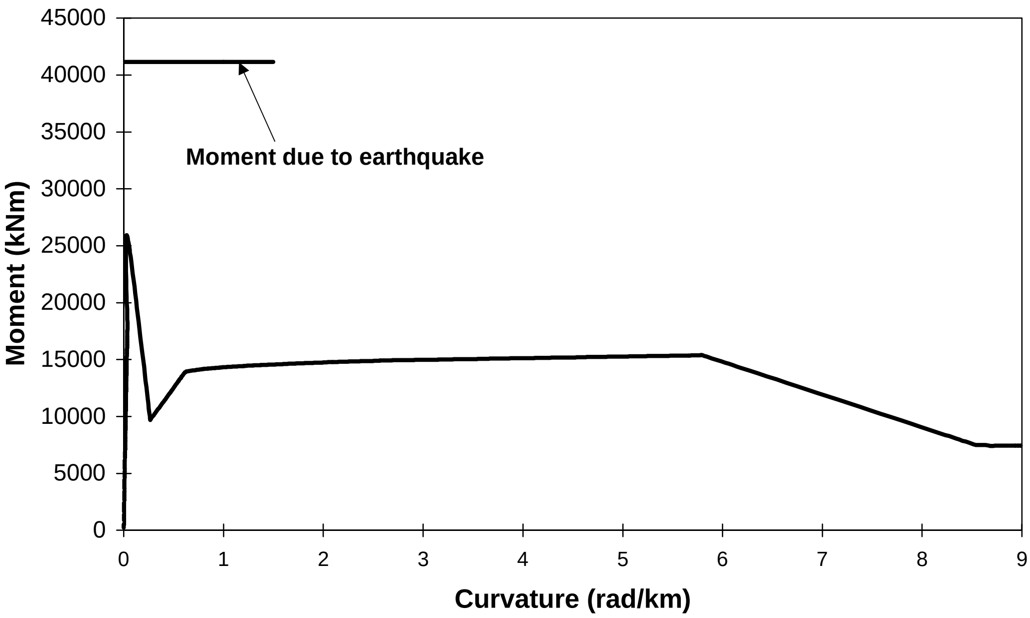

Figure B.1 Moment curvature diagram of 1/1 scale (prototype) SP1.

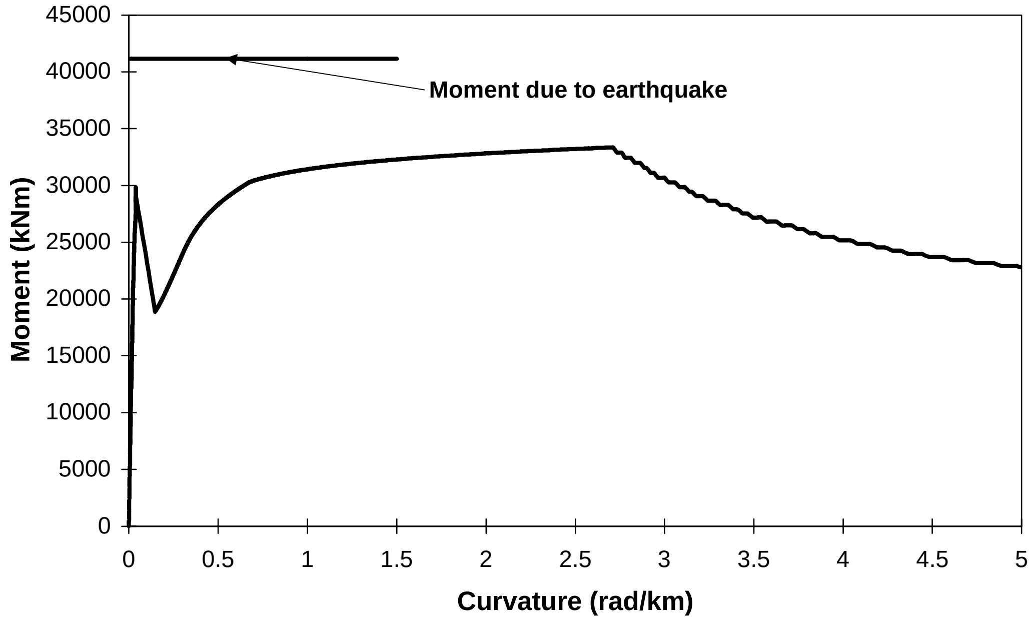

Figure B.2 Moment curvature diagram of 1/1 scale (prototype) SP2.

VITA

S. Bahadır YÜKSEL was born in Ankara on November 24, 1971. He received his B.Sc. degree from Selçuk University in 1994 and M.Sc. degree from Middle East Technical University in 1997. His main area of interest is panel form structures.

EDUCATION

September 1997- present	:	Middle East Technical University, Ankara, Turkey Civil Engineering, PhD, GPA: 3.84/4.00
February 1994- June 1997	:	Middle East Technical University, Ankara, Turkey Civil Engineering, Master of Science GPA: 3.84/4.00
September 1989- June 1993	:	Selçuk University, Konya, Turkey Civil Engineering, Bachelor of Science GPA: 82.00/100

EXPERIENCE

October 1994-March 2003 RESEARCH ASSISTANT(involves teaching). Department of Civil Engineering, Division of Structural Mechanics, Middle East Technical University, Turkey. Have been responsible for the following courses (teaching assist): CE384 Structural Analysis, CE382-Reinforced Concrete Fundamentals, CE483 Advanced Structural Analysis, CE481-Reinforced Concrete Structures, CE222-Engineering Mechanics II.

COMPUTER SKILLS

- Use of Finite Element program SAP, nonlinear inelastic dynamic analysis program DRAIN.
- Development of softwares using BASIC, FORTRAN.
- Several editing, graphical and spreadsheet programs.
- MS-DOS and Windows-2000 Operating Systems.
- Many Internet Applications.

LANGUAGES

English

LIST OF PUBLICATIONS

Yüksel, B., Atımtay, E., (2001) "Tünel Kalıplı Yüksek Binaların Deprem Davranışı ve Güvenliği".Yapı Mekaniği Laboratuvarları Toplantısı Bildiriler ve Laboratuvar Olanakları, 5-6 Kasım 2001, Ankara pp. 97-104.

Yüksel, B., Atımtay, E., (2003) "Tünel Kalıplı Yüksek Binaların Yatay Yük Altında Davranışı ".Yapı Mekaniği Laboratuvarları Toplantısı II, 19-20 Haziran 2003, Konya pp. 21-26.

Yüksel, B., (1997) "A Comparative Study on Seismic Codes " Master Thesis in Civil Engineering, Middle East Technical University, September 1997.

HONORS

Award for being best undergraduate study in Selçuk University (1994).